THE BIOMECHANICAL RESPONSE OF THE EYE, FACE, AND ORBIT TO PRIMARY BLAST OVERPRESSURE

VANESSA DAWN ALPHONSE

Dissertation submitted to the faculty of the
Virginia Polytechnic Institute and State University
in partial fulfillment of the requirements for the degree of

Doctor of Philosophy

In

Biomedical Engineering

Stefan M. Duma, Chair
Andrew R. Kemper
Pamela J. VandeVord
Joel D. Stitzel
Ian P. Herring

09 Sep 2015
Blacksburg, VA

Keywords: Eye, Injuries, Blast, Shock Waves

Copyright 2015, Vanessa D. Alphonse

THE BIOMECHANICAL RESPONSE OF THE EYE, FACE, AND ORBIT TO PRIMARY BLAST OVERPRESSURE

Vanessa Dawn Alphonse

Abstract

Combat-related blast injuries are occurring more frequently with the increased use of improvised explosive devices in current military conflicts. Though much research has focused on how the body responds to the relatively low loading rates associated with blunt trauma, little is known regarding the response of the body to the higher loading rates associated with blast trauma. While soldiers are surviving once-lethal blast events due to enhanced protective equipment, injuries such as those to the eye and face that were once considered inconsequential, can now be detrimental to long-term healthcare costs and quality of life. Although it is suggested primary blast overpressure (i.e., the shock wave) can cause severe eye injuries, there remains few empirical data in the literature that confirms this. Adding to this, there are currently no testing standards to assess the effectiveness of personal protective equipment during blast exposure. Expanding upon traditional research techniques within the field of injury biomechanics, the research in this dissertation focuses specifically on developing experimental and physical models of the eye, face, and orbit for blast overpressure exposure. Foremost, a porcine eye model is used to quantify eye injury risk from blast overpressure exposure. Subsequently, these biomechanical data are used to develop a physical model of the eye that can be used in lieu of cadaver specimens for blunt and blast loading. Lastly, military spectacles and goggles are examined for effectiveness at protecting the eye during blast exposure. Combined with detailed computer-aided design geometries, these data can be used to validate computational models of the eye, orbit, and face to blast loading. Results from these tests support one theory that shock waves may enter the skull through the orbit, alluding to future work that is essential to more fully understanding the physiological response of the brain and ocular motor system to blast exposure. Ultimately, the experimental methods and analysis techniques disseminated herein serve as a framework for future experimental work related to blast and other high-rate loading scenarios.

Acknowledgements

A great many thanks go to my mom, dad, and sister for providing a foundation for education and continually supporting my decision to go to graduate school. I attribute my achievements to their love and support throughout the years, and would not have been able to make it this far without them.

Thank you to all my friends who taught me so many important lessons outside the classroom. I would like to especially thank Justin, Nicole, Evon, Shaylen, Stephanie, Dave, Craig, Pat, Brooke, Terri, Ray, Anna, and Devon. You have all filled my days with laughter and love.

Dean Karen DePauw and Dr. Shelli Fowler inspired me to approach higher education in new ways and I am thankful for their lessons. Thank you to Tess Sentelle, Pam Stiff, and Amanda Covey for their behind-the-scenes work that made my time as a student run smoothly.

Thank you to Dr. Stefan Duma, Dr. Andrew Kemper, Dr. Pamela VandeVord, Dr. Joel Stitzel, and Dr. Ian Herring for your various efforts getting the research projects off the ground. My committee has been instrumental in educating and mentoring me throughout my studies. Conducting this work has been a blast!

Table of Contents

Abstract ii
Acknowledgements iii
Table of Contents iv
List of Figures vi
List of Tables viii
Introduction 1
  Literature Review 12
  Research Objectives 25
Chapter 1: Membrane characteristics for blast overpressure testing using blast simulators 26
  Introduction 26
  Methods 27
  Results 28
  Discussion 30
  Conclusions 31
Chapter 2: Effects of filtering on blast overpressure measurements 32
  Introduction 32
  Methods 32
  Results 34
  Discussion 38
  Conclusions 40
Chapter 3: Eye injury risk to the unprotected eye during primary blast 41
  Introduction 41
  Methods 42
  Results 54
  Discussion 65
  Conclusions 70
Chapter 4: Protective effects of spectacles and goggles during primary blast 71
  Introduction 71
  Methods 72
  Results 78
  Discussion 89
  Conclusions 93
Chapter 5: Pressure propagation within the orbit and around the face during primary blast 94
  Introduction 94
  Methods 94
  Results 97
  Discussion 107
  Conclusions 110
Chapter 6: Evaluating the FOCUS headform eye during blast overpressure 111
  Introduction 111
  Methods 112
  Results 115
  Discussion 120
  Conclusions 121

Chapter 7: An area-sensitive synthetic eye that differentiates between blunt and blast 122
Introduction 122
Methods 123
Results 126
Discussion..... 131
Conclusions 134
Conclusions 135
Research Summary 135
Dissemination of Knowledge 138
Acknowledgements 139
References 140
Appendix A: Overpressure profiles and corridors for porcine eye tests 145
Appendix B: Shock wave parameters for porcine eye tests 214
Appendix C: Porcine eye injury summary 224
Appendix D: MATLAB® script 230

List of Figures

Figure 1. Human eye structures, left eye, top-view. 3
Figure 2. Idealized blast overpressure response represented by the Friedlander waveform. 5
Figure 3. Schematic (side view) of a gas-driven Advanced Blast Simulator (ABS). 8
Figure 4. Photograph of the small VT ABS, side view. 9
Figure 5. Eye injury risk curves. 17
Figure 6. Correlations between intraocular pressure and normalized energy. 18
Figure 7. FOCUS headform and biofidelic synthetic eye. 20
Figure 8. Rupture patterns of each membrane type. 28
Figure 9. Average peak overpressure, positive duration, and positive impulse for all tests 29
Figure 10. Exemplar pressure traces for the three membrane materials. 29
Figure 11. Raw and filtered pressure-time histories for Empty Tube Test 01. 35
Figure 12. Raw and filtered frequency spectra for Empty Tube Test 01. 36
Figure 13. IOP Test 01 raw and filtered pressure-time histories. 37
Figure 14. Normalized frequency spectrum showing the raw and filtered data for IOP Test 01 . 38
Figure 15. Photographs of the three test setups, shown inside the ABS. 43
Figure 16. Isolated eye boundary condition. 44
Figure 17. Synthetic orbit boundary condition. 45
Figure 18. Negative mold used to add gelatin around eye in 3D orbit. 46
Figure 19. 3D orbit boundary condition. 46
Figure 20. Plane of symmetry and occlusion area overlaid on image of GHMBC. 47
Figure 21. Orbit biofidelity test conditions using the synthetic orbit. 48
Figure 22. Pressure measurement locations for experimental setups. 49
Figure 23. CAD geometries of experimental test setups. 53
Figure 24. Pressure-time histories for the synthetic orbit biofidelity tests. 55
Figure 25. Static (in flow), total, and reflected overpressure - unprotected porcine eye tests. 57
Figure 26. Intraocular overpressure for unprotected porcine eye tests with correlations. 58
Figure 27. Correlations between static overpressure measured at two locations. 59
Figure 28. Typical photographs from high speed video analysis for synthetic orbit. 59
Figure 29. Still images from high-speed video of the 30 psi blast with the unprotected eye. 60
Figure 30. Typical photographs from porcine eye dissection. 61
Figure 31. Retinal folds in control eyes. 61
Figure 32. Peak shock wave parameters for three ocular boundary conditions. 63
Figure 33. Injury risk for hyphema for three boundary conditions. 64
Figure 34. Facial pressure sensor locations for 3D orbit. 73
Figure 35. Spectacles and goggles used for protected porcine eye blast tests. 74
Figure 36. Experimental test setups for protected porcine eye tests. 75
Figure 37. Eyewear contact with face. 76
Figure 38. Intraocular overpressure for porcine eye tests – unprotected and spectacles. 79

Figure 39. Intraocular overpressure for porcine eye tests – unprotected and goggles. 80
Figure 40. Intraocular overpressure for porcine eye tests – spectacles and goggles. 81
Figure 41. Peak IOP for unprotected and protected porcine eyes during blast. 83
Figure 42. Positive duration for unprotected and protected porcine eyes during blast. 84
Figure 43. Positive impulse for unprotected and protected porcine eyes during blast. 85
Figure 44. Correlations between peak intraocular pressure and peak overpressure. 86
Figure 45. Correlations between static overpressure measured at two locations. 87
Figure 46. Still images from high-speed video of 30 psi blast with spectacle. 88
Figure 47. Still images from high-speed video of 30 psi blast with goggles. 89
Figure 48. Lens shape for spectacles and goggles. 91
Figure 49. Intraorbital pressure sensor locations for synthetic and 3D orbits. 96
Figure 50. Corridor plots for the nasal sensor. 98
Figure 51. Pressure traces for intraorbital sensors at the 30 psi test level. 99
Figure 52. Facial sensor response at the 30 psi test level. 100
Figure 53. FOCUS headform blast test setup. 113
Figure 54. FOCUS headform sensor locations. 114
Figure 55. Correlation between average FOCUS eye load and average human IOP. 115
Figure 56. Shock wave velocity based on standoff distance. 116
Figure 57. Load cell traces for FOCUS eye tests. 116
Figure 58. Eye injury risk for FOCUS eye tests predicted using peak load. 117
Figure 59. Peak overpressure around the eye for FOCUS and human eye tests. 118
Figure 60. Total overpressure traces for human and FOCUS eye tests. 119
Figure 61. Static overpressure traces for human and FOCUS eye tests. 119
Figure 62. Projected unspent gunpowder on FOUCS headform after blast testing. 120
Figure 63. Area-sensitive FOCUS eye development. 123
Figure 64. Experimental test setups for the area-sensitive eye for blunt and blast loading. 125
Figure 65. Characteristic responses of area-sensitive FOCUS eye to blunt loading. 127
Figure 66. Characteristic responses of area-sensitive FOCUS eye to blast loading. 127
Figure 67. Pulse parameters for sensor array in area-sensitive FOCUS eye. 128
Figure 68. Normalized peak pressure area-sensitive FOCUS eye tests. 129
Figure 69. Positive duration for area-sensitive FOCUS eye tests. 130
Figure 70. Comparison between area-sensitive FOCUS eye and isolated porcine eye tests. 131

List of Tables

Table 1. Shock wave parameter definitions. 5
Table 2. Definitions and common symbols of pressure types. 11
Table 3. Summary of experimental eye tests using animal and human cadaver eyes. 15
Table 4. Mylar and acetate membranes. 27
Table 5. Aluminum membrane characteristics. 27
Table 6. Considerations for membrane choice in future shock tube or ABS studies. 31
Table 7. Cutoff frequencies (3 dB) for a 4th order low pass Butterworth filter. 34
Table 8. Average shock wave parameters for empty tube data (n=5). 34
Table 9. Average shock wave parameters for IOP test data (n=3). 37
Table 10. Unprotected eye test matrix 44
Table 11. Pressure Sensors used for Experimental Tests. 49
Table 12. Predicted injury risk percent using 11.15 mm diameter aluminum rod correlation 64
Table 13. Predicted injury risk percent using 9.25 mm diameter aluminum rod correlation. 65
Table 14. Projected injury risk percent using 6.35 mm BB diameter correlation. 65
Table 15. Predicted percent injury risk for porcine tests with spectacles and goggles. 88
Table 16. Average shock wave parameters for intraorbital sensors - synthetic orbit. 102
Table 17. Average shock wave parameters for intraorbital sensors - unprotected 3D orbit. 103
Table 18. Average shock wave parameters for intraorbital sensors - 3D orbit with spectacles. 103
Table 19. Average shock wave parameters for intraorbital sensors - 3D orbit with goggles. 104
Table 20. Average shock wave parameters for facial sensors - unprotected 3D orbit. 105
Table 21. Average shock wave parameters for facial sensors - 3D orbit with spectacles. 106
Table 22. Average shock wave parameters for facial sensors - 3D orbit with goggles. 107
Table 23. Normalized peak pressure thresholds for area-sensitive FOCUS eye. 129
Table 24. Positive duration thresholds for area-sensitive FOCUS eye. 130
Table 25. Predicted percent injury risk for area-sensitive eye using peak load. 131
Table 26. Anticipated publication and conference topics from the proposed research. 138

Introduction

Research Motivation

Annually, approximately two million people in the United States suffer from eye injuries that require treatment [1]. Common sources of eye injuries include automobile accidents, sports-related impacts, misuse of consumer products, and military combat. These events result in nearly 500,000 cases of lost eyesight in the United States each year [2]. Eye injuries affect quality of life and are expensive to treat, given an estimated annual cost of $51.4 billion associated with adult vision problems in the United States [3, 4]. Furthermore, vision is one focus of the Congressionally Directed Medial Research Programs (CDMRP). Since its inception in 2009, nearly $50 million was awarded to research projects through the CDMRP Vision Research Program. Mitigating eye trauma and reducing injury risk requires knowledge of the specific injury mechanisms underlying injuries. Previous research documented various etiologies of eye injuries, studied parameters that affect eye injury risk, and developed computational and physical models of the eye that can assess eye injury risk during various loading schemes. However, much of the historical research has focused on blunt trauma to the eye from automobiles, sports, and consumer products, and human injury thresholds and tolerances are established for various body regions.

Eye injuries caused by military conflicts account for an increasing percentage of all reported war injuries. Compared to the American Civil War (1861-1865) where 0.57% of all injuries were to the eye, this percentage steadily increased to 2% for both World War I (1914-1918) and World War II (1941-1945), 2.8% for the Korean War (1950-1953), 5-9% for the Vietnam War (1962-1972) [5]. Presumably, the increased rate of eye injuries is related to advancements in modern western medicine, better documentation and medical reporting, and the type of combat typical of each conflict.

Combat-related blast injuries are occurring more frequently with the increased use of explosives and improvised explosive devices (IEDs) in current military conflicts. Explosive events accounted for more than 75% of combat-related fatalities in Operation Iraqi Freedom and Operation Enduring Freedom (OIF/OEF) [6]. Reduced fatality rates during recent military conflicts have been linked to the increased use of personal protective equipment (PPE) [7].

While unprotected air-filled organs such as the lung are most susceptible to blast injury, the use of improved PPE has left the face and eyes disproportionally vulnerable to concomitant blast injuries [8, 9].

Despite the availability of protective eyewear, eye injuries have been reported with and without documented use of protective eyewear at the time of injury. A review of over 3000 patients treated for combat-related trauma during OIF/OEF between March 2003 and September 2006 reported injuries to the eye in 17% of cases where protective eyewear was used, and jumped to 26% when protective eyewear was not used [10]. These included both closed-globe and penetrating injuries, which could have been caused by various mechanisms, including blast exposure. Studies have reported more than 80% of all severe ocular injuries sustained during military combat are the result of munitions fragmentation and debris [11, 12]. Many military explosives are buried or impregnated with shrapnel, thereby increasing the risk of injury from projectiles. The high incidence of eye injuries that occur even when protective eyewear is used further motivates the need to more fully understand primary blast overpressure as an eye injury mechanism.

Although many eye injuries do not pose a high threat to life (a globe rupture, which often results in enucleation and therefore total functional loss of the eye, would likely only be classified as a moderate injury), the economic and psychological effects are alarming. Injuries to the eye and visual system are particularly debilitating from a military perspective because they can severely decrease the ability of a soldier to achieve return-to-duty standards required for service. Notwithstanding, the time and finances invested in training is ‘lost’ when a solider cannot return to duty. Similarly, lack of adequate vision limits the type of jobs that can be acquired following return to civilian life. Decreased quality of life compared to pre-injury levels can leave a veteran feeling depressed and anxious about their current state, and long-term consequences of survivable injuries are still being characterized. Post-traumatic stress disorder (PTSD), which continues to be an increasing concern for health care providers, affected over 100,000 deployed soldiers between 2000 and 2012, a rate that exceeded their non-deployed counterparts by over three times [9]. An understanding of primary blast overpressure injuries and injury mechanisms may shed light on the role of injury to the eye and brain with such outcomes. Aside from military combat, blast events occur in daily civilian life in the form of mass-casualty events and

industrial accidents. The blast events at the 2013 Boston Marathon (commonly referred to as the Boston Marathon Bombing) and the fertilizer plant explosion in West, Texas, which happened within 48 hours of each other resulted in eye injuries that required medical treatment [13]. Both military and civilian triage units serve to benefit from understanding blast eye injuries.

Eye Anatomy and Injuries

The eye serves as a visual sensory organ with many structures within the eye that allow it to function properly. Though the eyes only represent a fraction of the total volume of the human body, their function is critical visual sensory perception. Briefly, light passes through the clear cornea, is focused through the lens, and projected to the light-sensitive retina at the back of the eye, which transmits neural signals to the brain for image processing.

Figure 1 shows a cross-sectional view of a human eye, indicating the major structures within the eye. Structures that are assessed through gross dissection in the studies presented in this dissertation include the sclera, cornea, iris, ciliary body, zonules, lens, and retina.

Human Eye Structures

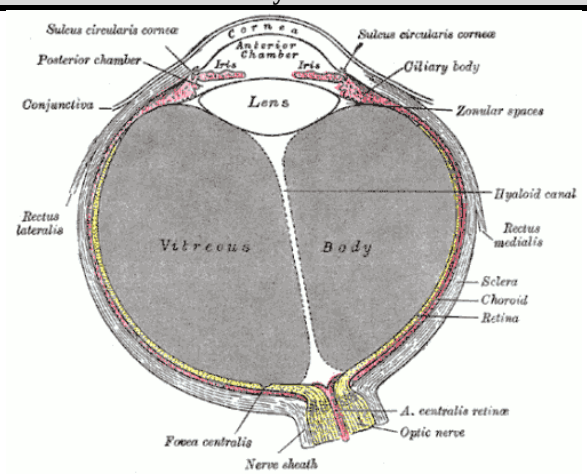

Figure 1. Human eye structures, left eye, top-view.
Gray's figure #869 [14].

Eye injuries range in severity, and though many are not life-threatening, they are often debilitating in terms of economic and psychological costs. Prominent eye injuries assessed experimentally include corneal abrasion, hyphema, lens damage, retinal damage, and globe rupture. The research proposed herein will focus on these injuries. Corneal abrasion (or corneal ulceration) is the scraping off of the top layer cells of the cornea. This often occurs when enough

force is applied to the cornea that epithelia detach. However, epithelial cells can regenerate and as such, corneal abrasions often heal on their own in a few days. Hyphema is bleeding into the anterior chamber of the eye. Unless the volume of blood is sufficiently large, the eye can generally drain this extra fluid without treatment. Lens damage, in terms of trauma, often describes lens dislocation or opacification. Lens dislocation occurs when force tears the zonules, the small fibers that hold the lens in place. Lens trauma can lead to cataract formation. Dislocated lenses and lenses with cataracts may require surgical intervention for removal and replacement with artificial lenses. Retinal damage, often a retinal tear or detachment, requires prompt surgical intervention to preserve eyesight. The retina is the light-sensitive layer of cells at the back of the eye and requires contact with the choroid (blood supply) to maintain function. When the retina detaches from the choroid, reattachment must be performed to preserve function. Globe rupture is a severe eye injury that occurs when the sclera and/or cornea tears, exposing the inside of the eye. Blunt trauma can cause severe equatorial and meridional expansion that results in scleral tearing. Penetrating trauma can compromise scleral integrity and leave intraocular foreign bodies (IOFB) in the eye. Unless promptly treated, this and other traumatic mechanisms of injury may be related to sequelae, including infection and eventual enucleation. Lastly, often related to eye trauma is the temporary increase in intraocular pressure due to the impact. This might be related to sequela including the development of glaucoma, which is characterized by sustained elevated intraocular pressure. Glaucoma is one of the leading eye diseases that result in vision loss.

Primary Blast

A blast wave follows the detonation of a high explosive (e.g., trinitrotoluene (TNT), composition B (Comp-B), composition-4 (C-4)) in which the supersonic explosion in a fluid creates a shock wave. The nearly instantaneous increase in pressure, temperature, and density cause the wave to move faster than the speed of sound in the fluid, and waves “shock up” as molecules are compressed increasingly faster upon each other. As such, shock waves are compression (longitudinal) waves and their propagation depends on the pressure, temperature, and density of the medium through which they travel.

The Friedlander waveform represents an idealized blast overpressure response for a free-field (i.e., no reflective surfaces) explosion (**Figure 2**). It is mathematically represented by an equation that specifies the peak overpressure (P_s) and positive duration (t*) of the wave [15]. This overpressure trace is characterized by an instantaneous rise above ambient pressure, followed by an exponential decay below ambient pressure, with an eventual return to ambient pressure. Ambient pressure is typically atmospheric pressure. Shock wave characteristics that can be determined from the pressure-time history are time of arrival, peak overpressure, positive and negative durations, and positive and negative impulses (**Figure 2**, **Table 1**). These shock wave characteristics are calculated throughout this dissertation, and may factor in blast-specific injury mechanisms. The degree to which each parameter alone or various combinations of parameters affects injury risk is a focus of current research.

Friedlander Waveform

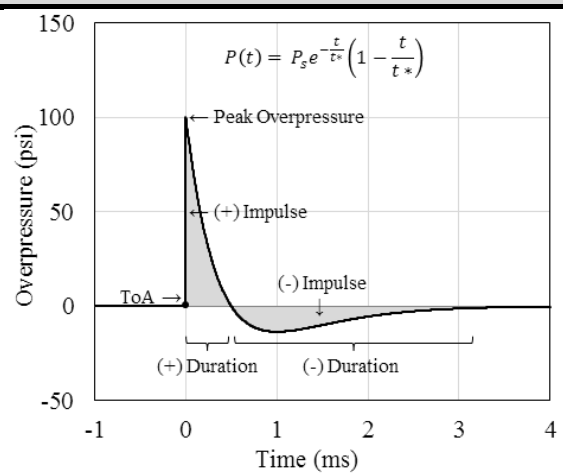

Figure 2. Idealized blast overpressure response represented by the Friedlander waveform.

Table 1. Shock wave parameter definitions.

	Definition
Time of Arrival (ToA)	Time at which the trace initially rises above ambient pressure.
Peak Overpressure	Maximum pressure recorded.
Positive Duration	Time interval between the time of arrival and the time at which overpressure returns to zero.
Negative Duration	Time interval between immediately following the positive duration and ends when the trace rises above ambient pressure.
Positive Impulse	Area under the trace (calculated using trapezoidal integration); positive impulse is calculated over the positive duration.
Negative Impulse	Area under the trace (calculated using trapezoidal integration); negative impulse is calculated over the negative duration.

Potential Primary Blast Injury Mechanisms

Blast loading often provides complex injury mechanisms due to the high-rate nature of these events. Blast-related injuries can be characterized by primary, secondary, tertiary, or quaternary mechanisms. Primary blast injuries are caused solely by the pressure wave (blast overpressure) that passes an object. Air-filled organs (i.e., the lung and bowel) are most susceptible to primary blast injury due to the large difference in acoustical impedance at the interface between these organs [16-18]. Secondary blast injuries are caused by projected material (kinetic energy) that impacts an object. Military explosives and especially IEDs often have fragments in them or are buried, thus increasing the amount of projected material. Projected material can cause penetrating or perforating injuries that require prompt medical attention. Tertiary blast injuries are caused by falls and impacts associated with objects impacting other objects. Regarding military combat, tertiary blast injuries are most often observed when the injured person fell or was located in a structure that collapsed [16]. Quaternary blast injuries encompass the remaining injuries that do not fall into primary, secondary, or tertiary blast injury mechanisms, and include thermal and chemical injuries sustained due to blast. The underlying injury mechanisms for blunt trauma and thermal/chemical burns are well documented in the literature. Therefore, the research described in this dissertation focuses the primary blast injury mechanisms.

Spalling, cavitation, and brisance are well-defined destructive mechanisms for building construction materials such as glass, metal, and concrete. Spalling refers to the process of surface failure that results in flakes of material being broken off a larger body when a shock wave contacts a material. It is often observed in modern combat anti-tank tactics as a method of breaching armored vehicles whereby high explosives are attached to the outside of the vehicle that upon detonation, cause damage as the shock waves conducts through the vehicle hull [19]. Fragments from the material become high-speed projectiles that can cause penetrating or perforating injuries. When applied to biological specimens, spalling is thought to cause tissue damage at air-tissue interfaces [17]. Cavitation refers to the almost instantaneous formation and implosion of small bubbles in a fluid that is generally caused by a rapid change in pressure. It has been hypothesized that cavitation of fluids *in vivo,* caused by a decrease in pressure, can result in tissue injury [20]. The threshold for cavitation is affected by temperature, surface tension, dissolved gases, impurities, and viscosity of the fluid [21, 22]. A previous study

modeled cavitation in the brain due to blast overpressure using a cavitation threshold of -14.5 psi [23]. Brisance refers to the shattering effect of a high explosive and is related to the detonation pressure of the explosive. The shock wave caused during detonation of a high explosive can be transmitted through solid objects; this wave can cause the material to fragment. A highly brisant explosive material will project smaller fragments than a lower brisant explosive, though the velocity of the resulting fragments may be the same. The fragments caused by spalling and brisance can cause secondary blast injuries.

The near-instantaneous pressure differential caused by blast overpressure may provide another method of bodily injury. The destructive potential of pressure differentials is commonly observed during tympanic membrane rupture. The tympanic membrane is a thin tissue in the ear that often serves as an (albeit unreliable) indicator of exposure to primary blast injury due to its low rupture threshold of approximately 5 psi [24]. Furthermore, it is thought that conjunctival hemorrhage (bleeding in the white of the eye) is one of the most common injuries caused by blast overpressure exposure [17, 25]. This specific injury is plausible because incredibly small vasculature that coats the sclera is potentially susceptible to damage at low pressure levels. Lastly, the body is susceptible to damage from the inertial effects of blast.

Shock Tubes and Advanced Blast Simulators (ABS)

Shock tubes and ABSs are commonly used to simulate free-field blasts without the use of live-fire high energy explosives such as TNT, Comp-B, and C-4. One advantage of using such a device instead of free-field testing is that it allows for the study of isolated, idealized shock waves and therefore, the isolated effects of primary blast overpressure exposure. While some systems use combustion to provide the energy for a shock wave, most are gas-driven. Due to its low molecular weight, helium is typically used as the driving gas.

A standard gas-driven shock tube consists of equally shaped “driver” and “driven” sections separated by a frangible membrane. The driver section is pressurized with the gas until the membrane ruptures (either passively or actively) and sends a burst of gas down the driven section. As the gas compresses upon itself, a shock-front forms and the shock wave propagates through the tube. An ABS differs from a shock tube because it is designed to provide a more realistic pressure pulse. An ABS is designed for wave-shaping, which allows the resulting wave

to be more representative of a free-field shock wave from a spherical charge. The goal for a shaped wave is to observe both the primary and subsequent shocks in the pressure trace, which is similar to the pressure trace observed for spherical charges [26]. An ABS has a contoured driver section, which is typically linear but can also be positively or negatively curved, mated with a convergent driven section [27]. An end-wave eliminator (EWE) at the open end of the driven section serves both as a shock diffuser and energy dump tank. Regardless of the system used, test specimens are placed inside tube at a point where the shock wave is fully developed. **Figure 3** is a computer-aided design side view schematic of an ABS with an EWE.

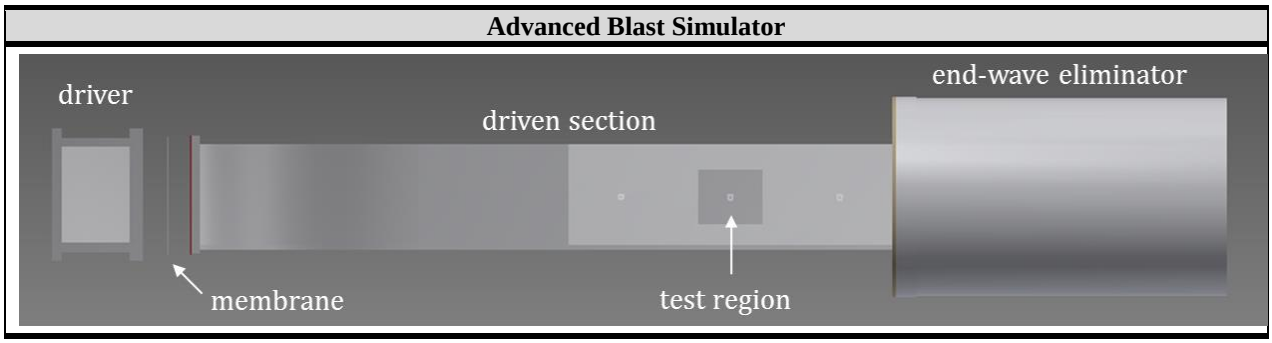

Figure 3. Schematic (side view) of a gas-driven Advanced Blast Simulator (ABS).

All blast overpressure tests described in this dissertation were conducted using the small VT ABS (Figure 4). This is a helium gas-driven tube with a 12 in x 12 in cross-sectional test area, specifically designed for testing small specimens. It has a linear driver section mated with a convergent driven section, a clear window that allows access to samples inside the tube, and an end-wave eliminator with plates angled at 15° to diffuse and absorb energy from the shock wave. This ABS is currently able to produce initial peak overpressures at the test region up to approximately 30 psi (static overpressure) with a positive duration around 2.5 ms. Depending on the membrane material used, a secondary peak overpressure that follows the initial peak overpressure could be as high as 40 psi. Chapter 1 examines various membrane materials and peak overpressures. Higher peak overpressures and various positive durations could be achieved by further modifying the ABS. A fully planar flow can exist with a specimen that occludes up to 20% of the cross-sectional area before the test specimen creates a turbulent flow that is not representative of realistic shock wave propagation *in theatre*. Therefore, all specimens tested inside this tube will have a cross-sectional area no larger than the 20% occlusion area, or approximately 30 in^2.

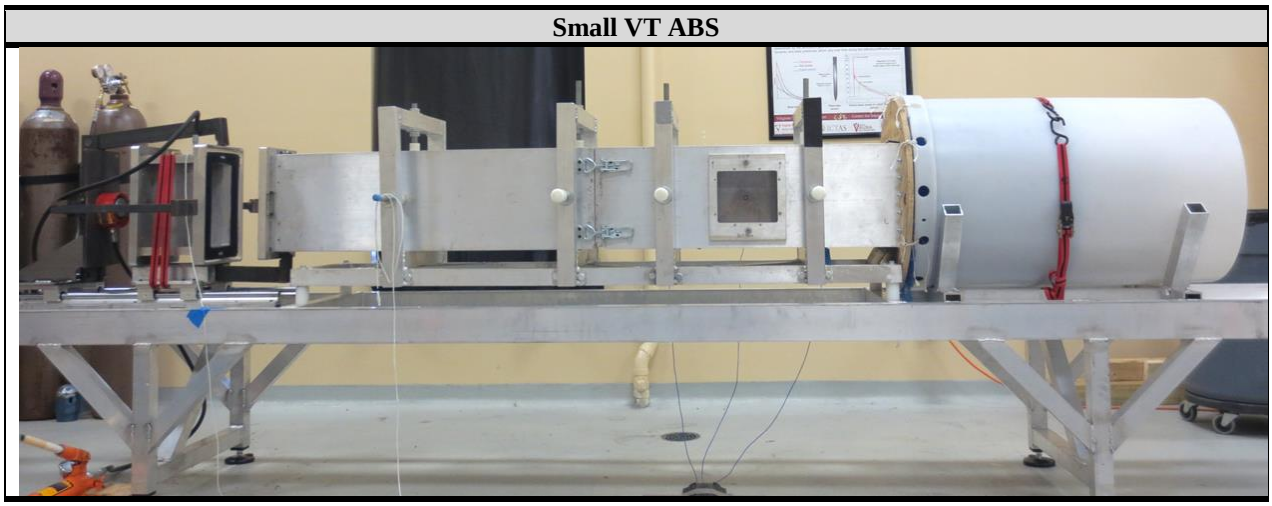

Figure 4. Photograph of the small VT ABS, side view.

The driver and driven sections are separated by a 9 in x 13 in rectangular opening. A piece of rubber on the driver side creates a seal and a piece of rubber on the driven side provides friction between the driven section and the membrane. This rubber does not protrude into the driven section, as this often causes lower test pressures. Similarly, cleaning the rubber with rubbing alcohol before testing ensures that dust does not affect this seal. Membranes are then placed in the opening and sealed with a pneumatic clamping system with a 7000 psi clamping pressure. All tests conducted with the VT ABS were performed with a minimum helium gas tank pressure of 1000 psi. The driver is pressurized using compressed helium until the membrane passively bursts, sending the gas down the tube and thereby simulating a blast event. The characteristic responses of various membrane materials are quantified in Chapter 1.

Three high frequency response pressure sensors (Model 102B15, PCB Piezotronics, Depew, NY) are mounted flush to the inside wall of the tube. These sensors are located 12 in apart from each other, with the middle sensor located at the test region. Shock wave velocity can be quantified using the time of arrival of the shock wave at these sensors. Properly choosing instrumentation is critical to accurately assessing blast conditions. Due to the high loading rates associated with blast, instrumentation should have the highest sampling rate possible (>>100 kHz) to properly capture the blast event. Blast rise times are often on the order of tens of microseconds, and can be easily missed or greatly distorted at sampling rates less than 100 kHz. Similarly, instrumentation should be chosen for its ability to capture these high rates, and should have high frequency responses (>500 kHz) and fast rise times (<5 μs) to avoid distortion of the signal. Low-pass hardware filters should be avoided, as these may further attenuate frequencies that may

be important to blast loading. The effects of filtering high-rate data are further examined in Chapter 2.

Pressure Measurements and Definitions

The main output measure of the experimental blast overpressures tests presented herein is pressure. As such, specifically denoting the type of pressure measured during testing is of utmost concern as ambiguity often leads to confusion. Pressure refers to a normal force applied to a surface of an object per unit area over which the force is applied, and is used to define the state of a fluid. Gauge pressure refers to a pressure measurement relative to ambient pressure (i.e., a change in pressure). Many sensors are designed to be 'zeroed' at ambient pressure, and therefore measure gauge pressure. Blast overpressure (a gauge pressure) refers to a pressure measurement above atmospheric pressure caused by a shock wave. Blast overpressure measurements are further described as static overpressure or reflected overpressure based on the orientation of the sensor that measures blast overpressure as well as the surface around the sensor. Static ("side-on") pressure is the pressure experienced by a point within the flow (that does not obstruct the flow) and describes the state of the flow. Static pressure is measured with a sensor oriented parallel to fluid flow propagation. Reflected ("face-on") pressure is the pressure experienced by a reflective surface within a flow. Reflected overpressure occurs when an object obstructs the flow. Reflected pressure is measured with a sensor oriented perpendicular to fluid flow propagation. Dynamic pressure is a free-stream parameter that characterizes the kinetic energy of the flow and does not refer to an actual loading on a surface. Stagnation pressure is the pressure measured when fluid velocity is zero. Stagnation pressure accounts for both the static and dynamic components of the free-stream pressure, and is measured with a pitot tube. Total pressure is equivalent to the stagnation pressure for isentropic, compressible flows. **Table 2** indicates these pressures and their definitions.

Table 2. Definitions and common symbols of pressure types.
Modified from [27].

Pressure Type	Symbol	Definition
Pressure	p	A normal force applied to a surface of an object per unit area over which the force is applied that is used to define the state of a fluid.
Gauge Pressure	Δp	A pressure measured relative to ambient pressure. Gauge pressure can be higher or lower than ambient pressure. Sensors measure gauge pressure relative to ambient or atmospheric pressure.
Blast Overpressure	BOP	A gauge pressure measured above atmospheric pressure caused by a shock wave.
Static Pressure	p_s	Pressure experienced by a point within the flow that does not obstruct the flow. This is often referred to as a "side-on" pressure.
Reflected Pressure	p_r	Pressure experienced by a reflective surface within a flow. This is often referred to as a "face-on" pressure.
Dynamic Pressure	p_d	Describes the local specific kinetic energy of the flow. This cannot be directly measured, but can be deduced using a pitot-static probe (i.e., the difference between the measured stagnation and static pressures).
Stagnation Pressure (Total Pressure)	p_t	Pressure measured when fluid velocity is zero. This is measured with a pitot tube. Stagnation pressure is equivalent to total pressure when the flow is isentropic.

Literature Review

Previous research has investigated ocular injuries from projectile impacts for a variety of blunt objects with known projectile characteristics to determine the eye injury tolerance. These studies comprise much of the historical experimental eye tests that are currently used to assess and predict eye injuries from blunt impacts. Data from these experiments have been used as motivation for further experimental studies and the development and validation of a number of computational, finite element, and physical models of the eye for various loading schemes. As many eye injuries are physiologic in nature, and because it is unethical to test human volunteers in potentially injurious conditions, live or anesthetized animals have been used to model human eye injury. Human cadaver eyes and postmortem animal eyes can, however, be used to assess gross injury such as corneal abrasion and globe rupture. Injury risk for physiologic injuries can be predicted using injury risk functions developed based on these experimental studies. Therefore, this section is split into subsections to cover historical experimental animal and human cadaver eye tests, creating eye injury risk functions, and developing physical, computational and finite element models of the eye for various loading scenarios. **Table 3** at the end of this section summarizes results from studies mentioned herein.

Experimental Animal Eye Studies

Historical experimental data using various animal models have reported eye injuries caused by blunt trauma. Weidenthal conducted blunt impact tests on 28 anesthetized *macaca mulatta* (rhesus) monkeys using a brass rod projected at the eye at various energy levels. Hyphema, contusion deformity, and globe rupture were reported [28]. Ten of the 28 eyes had hyphema, five of the 28 eyes had contusion deformity, and five of the 28 eyes had globe rupture. The eyes that sustained a globe rupture may have rendered assessment of other intraocular injuries difficult, if not impossible. Weidenthal later eye mounted in various materials [29]. Some of the porcine eyes were tested *in situ* before enucleation for comparison with enucleated eyes mounted in a 10% gelation solution or in a stone mold. Additionally, eyes were mounted in plasticene and 20% gelatin solution. Most of the data are insufficient to account for specific test conditions and injury pathologies. However, it was concluded that eyes mounted in a 10% gelatin solution best matched the response of eyes tested before enucleation. Delori conducted blunt impact tests on

75 enucleated porcine eyes using a BB projected at the eye mounted in a 10% gelatin solution [30]. Unfortunately, the data presented are insufficient to account for the specific injury pathologies and frequency at which these injuries occurred. However, this study presented the time-history of anterior pole, posterior pole, and corneal deformation due to impact by analyzing high-speed video of each test. McKnight conducted blunt impact tests on 20 anesthetized cats that had previously undergone radial keratotomy (RK) in one eye (three cats had bilateral RK) using a BB projected at the eye [31]. Twenty-three eyes were impacted with BBs at various velocities. The remaining 17 eyes were tested as controls. While all eyes suffered a hyphema, only four of the operated eyes ruptured; none of the unoperated eyes ruptured. Green conducted blunt impact tests on 11 anesthetized *macaca fascicularis* monkeys to observe fracture of the orbital floor [32]. This was done by dropping a brass cylinder down a tube to directly impact the globe. These tests resulted in 16 eyes with blow-out fracture, and six eyes with no blow-out fracture. Globe rupture was observed in five of the 16 eyes with blow-out fracture. Duma conducted blunt impact tests on 13 porcine eyes using foam objects projected at the eye *in situ* [33]. This study presented injury results for corneal abrasion by quantifying the area of the cornea damaged due to impact. Eight of the 13 eyes resulted in corneal abrasions affecting between 10% and 75% of the cornea. Scott conducted blunt impact tests on 21 enucleated porcine eyes using three steel rods projected at eyes mounted in a 10% gelatin solution [34]. These tests presented injury results for corneal abrasion, hyphema, lens damage, retinal damage, and globe rupture. Injuries were categorized as: Level 0 (no injury), Level 1 (injury to the iris or ciliary body, disruption of anterior chamber angle, lens injury without dislocation), Level 2 (lens dislocation or retinal damage), Level 3 (lens dislocation and retinal damage, possibly with iris or ciliary body injury), or Level 4 (globe rupture). Five tests resulted in Level 0 injury; two tests resulted in Level 1 injury; six tests resulted in Level 2 injury, six tests resulted in Level 3 injury, and no tests resulted in Level 4 injury. Two tests had no injury level listed. An interesting observation of this study was that injury outcome suggested lens damage occurred concurrently with retinal injury 100% of the time, but that the reciprocal was not true; i.e, retinal injury did not always occur concurrently with lens damage. Kennedy conducted blunt impact tests on 65 enucleated porcine eyes using various objects (airsoft pellets, BBs, paintballs, foam particles, plastic rods, aluminum rods) projected at eyes mounted in a 10% gelatin solution [35]. These tests presented injury results for globe rupture. Twenty-three of the 65 tests resulted in globe

rupture. Duma conducted a series of 36 blunt impact tests on 12 enucleated porcine eyes using metal rods and BBs [36]. These tests presented injury results for globe rupture. Four of the 36 tests resulted in globe rupture. Duma later conducted a series of 38 tests on 8 porcine eyes using two water streams and various stream velocities to investigate the safety of water streams (i.e., water toys and water park streams) [37]. Globe rupture was not observed in this study.

Experimental Human Cadaver Eye Studies

Historical experimental data using cadaveric eye models have reported eye injuries caused by blunt trauma. Delori conducted blunt impact tests on two enucleated human cadaver eyes using a BB projected at eyes mounted in a 10% gelatin solution [30]. Unfortunately, the data presented are insufficient to account for the specific injury pathologies and frequency at which these injuries occurred, with the exception of a single test on a human cadaver eye which resulted in globe rupture. Vinger conducted blunt impact tests on two enucleated human cadaver eyes using baseballs projected at eyes mounted in 10% gelatin solution [38]. One eye was impacted by a CD-25 baseball at 75 mph and did not rupture. The other eye was impacted by a CD-250 baseball at 55 mph and did rupture. Stitzel conducted blunt impact tests on 22 enucleated human cadaver eyes using foam projectiles, BBs, and baseballs projected at eyes mounted in a 10% gelatin solution [24]. These tests presented injury results for globe rupture. Specifically, four of the eight BB tests and four of the five baseball tests resulted in globe rupture. None of the foam particles resulted in globe rupture. Kennedy conducted blunt impact tests on 61 enucleated human cadaver eyes using various objects (airsoft pellets, BBs, paintballs, foam particles, plastic rods, aluminum rods) projected at eyes mounted in a 10% gelatin solution [21]. These tests presented injury results for globe rupture. Twenty-two of the 61 tests resulted in globe rupture. Alphonse studied the response of the human eye to impact with a toy helicopter blade [39]. Minor corneal abrasions were observed, but no globe ruptures were observed. Alphonse later studied the response of the human eye to firework overpressure [40]. Six human eyes were exposed to a charge that simulated fireworks at three standoff distances (22 cm, 12 cm, 7 cm). While corneal abrasions were observed to be caused by projected, unspent gunpowder, it was concluded that the pressure wave itself did not cause injury at this energy level.

Table 3. Summary of experimental eye tests using animal and human cadaver eyes.

Study	Eye Model	Test Conditions	Outcomes
Weidenthal 1964	20 anesthetized monkey eyes	Brass rod projectile (1.26 J – 2.96 J)	10/28 eyes resulted in hyphema 5/28 eyes resulted in globe rupture
Weidenthal 1966	235 (*in situ* and enucleated) pig eyes	Air rifle BB projectile (0.78 J)	Insufficient data to account for specific test conditions and injury pathology 10% gelatin solution best matched response of *in situ* eyes
Delori 1969	75 enucleated pig eyes 2 enucleated human cadaver eyes	Air rifle BB projectile (0.68 J)	Insufficient data to account for specific test conditions and injury pathology High-speed video of each test used to track anterior pole, posterior pole, and corneal deformation
McKnight 1988	20 anesthetized cat eyes (radial keratotomy performed in one or both eyes)	BB gun (0.34 J – 0.99 J)	4/23 operated eyes ruptured 0/17 unoperated eyes ruptured
Green 1990	11 anesthetized monkey eyes	Brass rod drop test (0.89 J – 3.56 J)	5/16 eyes resulted in globe rupture
Vinger 1999	2 enucleated human cadaver eyes	Baseball projectile (46.4 J & 82.2 J)	1/2 eyes resulted in globe rupture
Duma 2000	13 (*in situ*) pig eyes	Foam particle projectile (0.034 J – 1.446 J)	8/13 eyes resulted in corneal abrasion covering 10%-75% of the cornea
Scott 2000	21 enucleated pig eyes	Steel rod projectile (0.36 J – 1.89 J)	5/21 eyes had no injury 2/21 eyes had injury to iris/ciliary body, anterior chamber angle disruption, or lens damage without dislocation 6/21 eyes had lens dislocation or retinal damage 6/21 eyes had lens dislocation and retinal damage 2 eyes had no specific injuries listed
Stitzel 2002	22 enucleated human cadaver eyes	BB, foam particle, and baseball projectile (0.004 J – 134.5 J)	8/22 eyes resulted in globe rupture
Kennedy 2006	65 enucleated pig eyes 61 enucleated human cadaver eyes	Airsoft pellet, paintball, delrin impactor, plastic rod, foam particle, aluminum rod, BB projectile (0.01 J – 20.75 J)	23/65 pig eye tests and 22/61 human eye tests resulted in globe rupture
Duma 2012a	12 enucleated pig eyes	Aluminum rod, BB projectile (0.047 J – 2.257 J)	4/36 eyes resulted in globe rupture
Duma 2012b	8 enucleated pig eyes	Water streams	No globe ruptures observed
Alphonse 2012a	6 enucleated human cadaver eyes	Toy helicopter blades	No globe ruptures observed
Alphonse 2012b	6 enucleated human cadaver eyes	Consumer fireworks	Minor corneal abrasions were observed in all tests; no globe ruptures observed

Injury Risk Functions for the Eye

Injury risk functions are tools that relate measurable parameters to injury outcomes. The development of accurate injury risk functions relies on compiling experimental injury data and quantifiable test parameters. Many of the historical experimental eye impact studies report data that can be utilized for this purpose. Several experimental studies, in addition to providing injury results and measured parameters, also presented injury risk models for eye injuries. Each of these studies investigated the development of injury risk models based on various parameters and their relationship to injury outcome.

Duma determined kinetic energy was the most significant parameter related to injury among univariate models (mass, velocity, energy) using linear logistic regression of data from experimental impact tests with foam particles [19]. This study presented an injury risk function that used kinetic energy to predict the probability of corneal abrasion. Similarly, Scott correlated kinetic energy to resulting injury. Using a chi-square analysis, this study showed a strong association between kinetic energy and lens dislocation, and a strong association between kinetic energy and retinal damage [20]. This study also correlated projectile momentum to resulting injury; however, a chi-squared analysis indicated no association between projectile momentum and injury. Duma presented an analysis of eight previous experimental eye impact studies. Projectile mass and velocity were shown to be poor predictors of injury. This study presented injury risk curves that used either normalized energy or kinetic energy to predict the probability of corneal abrasion, lens dislocation, retinal damage, and globe rupture [27]. It was determined that normalized energy was a better predictor than kinetic energy because it accounts for the size of the projectile. Additionally, confidence intervals and 50% risk of injury values were determined for corneal abrasion, hyphema, lens dislocation, retinal damage, and globe rupture, for both kinetic and normalized energy. Kennedy presented binary logistic regression injury risk functions that used either kinetic energy or normalized energy of a projectile to predict the risk of globe rupture for porcine eyes and human cadaver eyes [28]. This study corroborated the findings of Duma that normalized energy is a better predictor than kinetic energy. Based on resistance to globe rupture, it was determined that porcine eyes were significantly stronger (2x) than human cadaver eyes for projectile impacts ($p=0.01$). Kennedy presented a comprehensive meta-analysis of over 250 eye impacts reported in the literature [29]. This study presented injury

risk functions for hyphema, lens damage, retinal damage, and globe rupture. However, in contrast to earlier efforts to develop eye injury functions with logistical regression, the final risk functions presented in this study were determined using a more robust survival analysis. The final recommended risk functions employ survival analysis using the maximum likelihood method to estimate parameters. A Weibull distribution was assumed for all injury types. Using this methodology, final risk functions and 5%-95% confidence intervals were presented for hyphema, lens damage, retinal damage, as well as globe rupture. **Figure 5** shows the injury risk curves based on normalized energy as an injury predictor [29].

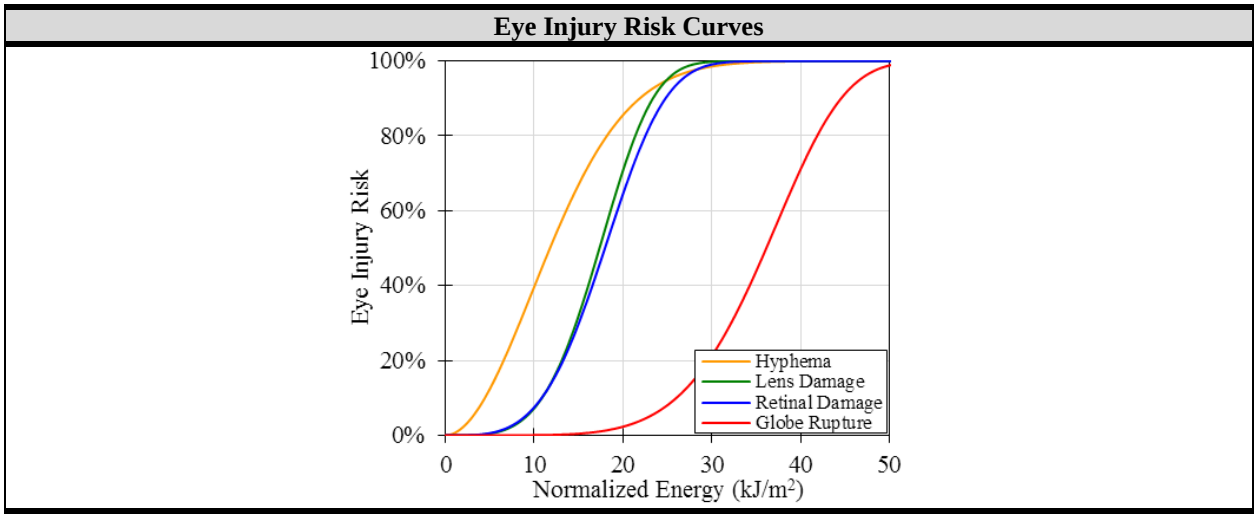

Figure 5. Eye injury risk curves.
Image modified from [29].

When projectile characteristics are unknown or there is no known projectile impact (i.e., water streams, pressure wave loading), it becomes necessary to use a parameter other than normalized energy for injury risk assessment. Previous work has indicated that intraocular pressure (IOP) can be used to predict injury risk in these cases. Kennedy determined a static loading threshold for human eye rupture to be 0.36 ± 0.2 MPa [41]. This and another study by Bisplinghoff determined a dynamic loading threshold for human globe rupture to be 0.91 ± 0.29 MPa [30] and 0.97 ± 0.29 MPa [31]. Internal pressurization was used as a method to both statically and dynamically load the eye. A small pressure sensor was inserted into the eye to measure IOP for these tests. Bisplinghoff also conducted experimental tests to determine the failure threshold of the eye due to an increase in IOP and to determine the material properties of the eye under high-rate loading [32]. This study calculated an average maximum true stress of 18.89 ± 4.81 MPa for both equatorial and meridional directions of the eye, an average maximum true strain along the

equator of 0.041 ± 0.014, and an average maximum true strain along the meridian of 0.058 ± 0.018. Intraocular pressure measurements were used to calculate stress. High speed video analysis of markers printed on the sclera were used to calculate strain. Overall, these experimental studies illustrate that measuring IOP during experimental tests provides another parameter for injury risk analysis. Duma investigated the correlation between IOP and kinetic energy and the correlation between IOP and normalized energy [2]. Intraocular pressure was measured throughout each test and normalized energy was calculated for each projectile. Overall, kinetic energy showed better correlation to IOP than normalized energy for all points. However, when separated by projectile type, there was a higher correlation between IOP and normalized energy than between IOP and kinetic energy for both cylinders. Three separate correlation curves were presented for IOP and normalized energy, one for each projectile (**Figure 6**) [36]. Normalized energy was previously determined to have a stronger correlation with injury than kinetic energy. The correlation between IOP and normalized energy presented in this study can be used with previously developed injury risk curves based on normalized energy to determine injury risk for eye injuries in cases where projectile characteristics are unknown or incalculable.

Correlations between IOP and NE

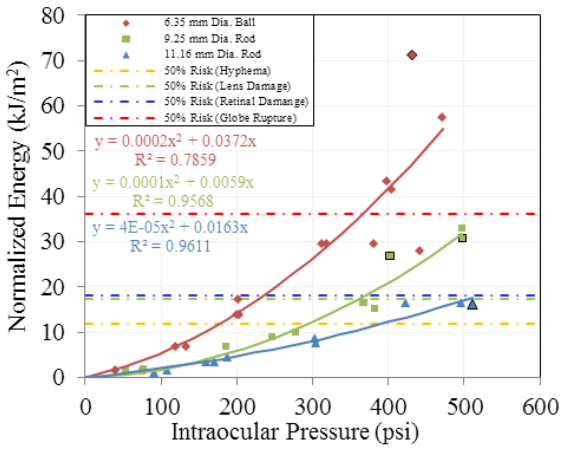

Figure 6. Correlations between intraocular pressure and normalized energy.
Image modified from [35].

Duma conducted a series of 38 tests on eight porcine eyes using two water streams and various stream velocities to investigate the safety of water streams (i.e., water toys and water park streams) [22]. As water streams flow continually they do not have a tangible mass associated with them; therefore, kinetic and normalized energy cannot be directly quantified for these cases.

This study implemented the correlations from Duma using the 6.35 mm projectile to predict eye injury risk from water streams based on IOP [2]. The 6.35 mm diameter projectile correlation was used because the water stream diameters were approximately 3.2 mm and 6.4 mm. Globe rupture was neither predicted nor observed in this study. Risk for hyphema was predicted to be as high has 20.7%; however, because cadaver tissue cannot be properly perfused, hyphema could not be directly assessed. Risk for lens dislocation and retinal damage was less than or equal to 1.3% for all tests. Alphonse et al. conducted a series of 30 tests on six human cadaver eyes using five remote control toy helicopter blades to investigate the safety of these toys [39]. This study implemented the correlations from Duma using the 6.35 mm projectile to predict eye injury risk from toy helicopter blades based on IOP [2]. The 6.35 mm diameter projectile correlation was used because the impacting area of the toy helicopter blades was less than 0.1 mm. Globe rupture was neither predicted nor observed in this study. Risk for hyphema was predicted to be a maximum of 0.2%. Risk for lens dislocation and retinal damage was 0.0% for all tests. Alphonse studied the response of six human cadaver eyes to firework overpressure at three standoff distances (22 cm, 12 cm, 7 cm) [26]. As firework explosions do not have a calculable mass, this study implemented the correlations from Duma using the 11.16 mm projectile to predict eye injury risk from commercial fireworks based on IOP [2]. The 11.16 mm diameter projectile correlation was used because it most closely matches the exposed area of an unprotected eye. While corneal abrasions were observed to be caused by projected, unspent gunpowder, it was concluded that the pressure wave itself did not cause injury at this energy level. Injury risk for hyphema, lens damage, retinal damage, and globe rupture was less than or equal to 0.01% for all tests.

Physical Models of the Eye

Many anthropomorphic test devices (ATDs) do not have the capability to specifically assess eye injuries. However, the Facial and Ocular CountermeasUre Safety (FOCUS) headform is an advanced anthropometric test device (ATD) specifically designed to quantify and assess injury risk due to facial and ocular loading (**Figure 7**). It has eight segments that represent facial bones (two frontal, two zygoma, two maxilla, one mandible, one nasal) and two eyes (**Figure 7**). Each bone segment and eye is instrumented with a load cell, allowing the FOCUS to quantify the load

applied to each region during an impact. Currently, the FOCUS headform is the only ATD that has the sensitivity to detect eye injury during impact to the head and face.

FOCUS Headform	FOCUS Eye and Load Cell
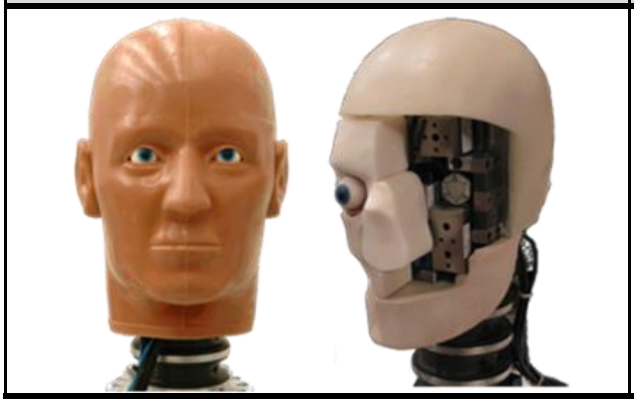	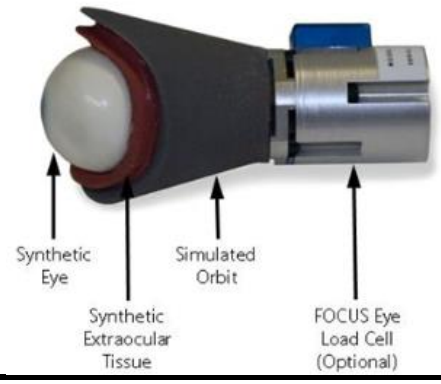

Figure 7. FOCUS headform and biofidelic synthetic eye.
Eye load cells are models 8065J (left) and 8060J (right) by Humanetics ATD.

Experimental Blast Eye Experiments

Hines-Beard used a modified paintball shooter to simulate a blast wave for exposure to mice [42]. Mice were placed with one eye a maximum of 0.5 cm from the end of the barrel and exposed to a single blast at 23.6 psi, 26.4 psi, or 30.4 psi. Preliminary results indicated globe rupture and extraocular muscle tears were caused at two higher test pressure levels (43.8 psi and 35.0 psi), and subsequently tests were not conducted at these pressure levels due to the severity of the injuries observed. Remaining test pressure levels were 23.6 psi, 26.4 psi, and 30.4 psi. Mortality rates within 24 hours of exposure at these levels were 24%, 22%, and 46%, respectively. Intraocular pressure and visual acuity tended to decrease over time following blast exposure at these test pressure levels. Corneal edema was observed in some mice, but was not conclusive. Ultimately, however, this study further corroborates other work in this area, concluding that isolated primary blast overpressure does not cause severe injury to the eye. Zou exposed Sprague-Dawley rats to one of two primary blast pressure levels (~26 psi, ~70 psi) using 5 kg of 2,4,6-trinitrotoluene (TNT) [43]. The rats were examined at 24 h, 72 h, and 2 w post-blast for retinal injury. Results of this study indicate that the retina experienced inflammation, edema, and apoptosis follow blast exposure. Bricker-Anthony also used a modified paintball shooter to simulate a blast wave for exposure of mice to blast overpressures of 23 psi, 26 psi, or 30 psi [44, 45]. Acute injury to the eye and its structures was not noted, however, corneal

edema, hyphema, cataracts, neuronal death, retinal pigment epithelium vacuoles and optic nerve degeneration were present in some eyes up to twenty-eight days following blast, when all animals were sacrificed. Further work by Bricker-Anthony found that blast exposure causes cell death and changes in visual acuity [45]. Sherwood exposed enucleated porcine eyes potted in synthetic orbits to primary blast overpressure and examined injuries to various eye tissues using B-scan and ultrasound biomicroscopy [46]. This study reported injuries including corneal epithelial disruption, scleral delamination, angle recession, chorioretinal detachments, lamellar lacerations, and cyclodialysis clefts. Corneal epithelial disruption and scleral delamination could have been caused by the preparation techniques as noted by the authors. Results of this study indicated that injury severity coincided with increasing peak pressure and impulse. While this study reported retinal damage was caused by blast overpressure exposure, it failed to quantify baseline damage in the enucleated porcine eye model. Choi exposed anesthetized rats to either a single or repeated blasts at approximately 10 psi using a shock tube [47]. Repeated blasts were conducted daily for five days. Both the single exposure as well as the repeated exposure showed retinal damage at the cellular level, with repeated exposure showing significantly higher damage.

While the anesthetized animal models indicate blast overpressure exposure may cause physical injuries to the eye as well as dysfunction of the structures and visual system, many of these models do not account for the anatomic dissimilitude between the animal model and the human eye. As such, these results, while promising for the development and testing of treatments for ocular dysfunction, cannot be directly assumed to be true for the human eye and visual system. Future work in this field may yield scaling techniques between the animal eye and human models that will allow for a better correlation between injuries in both models. Similarly, particular care should be taken when comparing results from various methods of producing blast overpressure waves. Using a modified paintball shooter to replicate a blast wave is somewhat misleading, as the pressure-time histories do not accurately represent a blast wave. The shape of these pulses is more similar to a high-rate blunt impact than a blast wave. Lastly, a combination of shock wave parameters can be used to compare results between studies, where peak overpressure, positive duration, and positive impulse can help scale the pulse from varous studies.

Computational Models of the Eye

Computational models are integral tools used in the field of injury biomechanics to quickly assess many hypothetical loading situations. Numerous computational models of the eye have been developed for dynamic blunt loading, and more recently, blast loading. Many of these models were specifically designed to assess blunt trauma and have been well-validated for their biofidelic response, material properties, and boundary conditions. However, due to the paucity of experimental blast data required to fully validate them, many models of the eye that strive to assess blast loading lack rigorous validation. Therefore, experimental data on the response of the eye and its properties at high loading rates are necessary to validate these models. The research proposed herein will yield data that can be used to validate such models. A brief synopsis of relevant computational models of the eye is mentioned herein. This is by no means exhaustive of the number of computational eye models currently being developed.

Many computational models of the eye have been developed and validated for blunt loading. Uchio developed a model of the human eye and determined material properties of the cornea and sclera using uniaxial tensile tests [48]. The eye was sectioned into three layers for the model: superficial layer of the cornea and sclera, deep layer of the cornea and sclera, iris, ciliary body, choroid, and retina, and inner aqueous humor, lens, and vitreous. Projectile impacts at various diameters and velocities were simulated and suggested that intraocular foreign bodies (IOFB) occur at velocities above 30 m/s, though there was no clinical evidence to support this. Stitzel developed a nonlinear finite element model of the eye, the Virginia Tech Eye Model (VTEM), and validated it with experimental data to accurately predict globe rupture [49]. This model consisted of many eye structures (cornea, sclera, lens, ciliary body, zonules, aqueous humor, vitreous body) in a fluid flow. The model assumes a Lagrangian formulation for the eye and its structures, with an Eulerian formulation for the aqueous, vitreous, and fluid around the eye. These assumptions greatly improved fidelity over prior models. Material properties for various eye structures were pulled from the literature. Higher stresses were predicted than previous models due to the increase biofidelity of the boundary conditions and model assumptions. Corneoscleral stress (>23 MPa) and local pressure (>2.1 MPa) were used to predict globe rupture. While this study increased the biofidelity of the eye and orbit, with the added benefit of validation for globe rupture prediction values based on experimental tests, failure was not

specifically modeled. Weaver evaluated projectile eye impacts using a computational model of the eye and matched experimental impacts from the literature [50]. This study used the VT-WFU Eye Model (an adaptation of the original VTEM). Computational results were shown to match experimental results. Corneoscleral stress (>17.21 MPa) and internal eye pressure (>1.01 MPa) were used to predict globe rupture. It was determined area-normalized kinetic energy was the best single predictor of peak stress and pressure in the eye, indicating that projectile size may be of importance to eye injury prediction. Weaver also studied the effect of orbit anthropometry on eye injury risk [51]. Specifically, this model varied orbital aperture, brow protrusion angle, eye protrusion, and eye location within the orbit and measured the corneoscleral stress and strain, internal eye pressure, and contact forces between the orbit, eye and impactor for 27 anthropometries. Anthropometry measurements were previously determined from CT images of nearly 40 human subjects [51]. Simulations of eye impact with a baseball at 30.1 m/s were run using a Lagrangian-Eulerian fluid flow finite element model for the eye. The models indicated that greater brow protusion, smaller eye protrusion, and smaller orbital apertures were protective characteristics. Overall, this study computationally illustrates the effect of human variation and provides a large dataset for various factors that affect orbital anthropometry that can potentially be protective to the eye for impact scenarios.

Few computational models have been designed specifically for blast loading. Stitzel subjected the VT-WFU Eye Model to a 1 lb charge of TNT at distances of 5 ft and 10 ft directly anterior to and 6 feet offset to the right of the cornea [52]. Peak stress (maximum principal stress in the corneal-scleral shell elements) and pressure (center of the eye in the vitreous) were quantified. Both stress and pressure were used to determine injury risk for hyphema, lens damage, retinal damage, and globe rupture. Stress predicted higher injury risk than pressure in three of the four test conditions, with the closest charge location with respect to the eye having the opposite trend. Esposito developed a Lagrangian-Eulerian finite element model of the eye using simple constitutive models [53]. This model consisted of many eye structures (sclera, cornea, lens, retina, aqueous) as well as the orbital fat around the eye. A TNT explosion was simulated at various distances and charge sizes to determine isodamage and isolethality curves based on Stuhmiller [54]. A maximum anticipated injury was modeled at approximately 50% survival rate for lung injury levels. Isolethality was assessed at a lower level of threshold lung injury. The pressure wave was directed frontally to the eye, and resulted in an oscillating pressure trace in

the eye. Four eye regions were studied and it was shown that the macula was most susceptible to this oscillation. Experimental tests will confirm if this oscillation occurs in theatre. Bhardwaj developed a three-dimensional fluid-structure interaction computational model of the eye to study stresses and deformations of the eye induced by exposure to primary blast overpressure [55]. This study modeled exposure of a human face and eye geometry to an explosion of 2 kg of TNT at a distance of 2.5 m in both a frontal (charge at level of face) and angled (ground charge relative to face). Specifically, this work studied the influence of facial features on wave propagation and predicted an area of maximum pressure in the nasal-side corner of the eye. Watson recently developed a finite element model of the eye that includes many internal structures that is similar to the model previously developed by Stitzel [56]. Computational blast tests were modeled to simulate matched experimental test conditions from a previously published study by one of the authors [56]. Results from these tests indicated high stresses at the interface between the ciliary body and the vitreous fluid, which could possibly account for angle recession and cyclodialysis clefts observed in the experimental studies [46]. However, a major limitation of this this finite element model is that it was only validated using blunt impact data from the literature due to the lack of high-speed video analysis of the response of the eye during blast loading.

Research Objectives

The research in this dissertation aims to examine the response of the eye during exposure to blast overpressure. Chapters 1 and 2 encompass experimental methods and analysis techniques that can be transferred to studies beyond what is reported herein. Chapters 3 and 5 focus on examining the effects of increasing biofidelity of the facial geometry surrounding the eye, with respect to injury risk and overall response to blast overpressure exposure. Chapter 4 expands upon the experimental methods and results presented in Chapter 3 to assess the ability of military spectacles and goggles to mitigate injury risk to the eye from blast loading. Chapter 6 examines the current FOCUS headform for blast loading. Chapter 7 describes the development of an area-sensitive physical model of the eye that can be used to distinguish between blunt and blast loading regimes in the absence of *a priori* knowledge of the injury scenario. The chapter-specific research objectives are as follows:

Chapter 1: Characterize the response of various materials for use in an ABS or shock tube.

Chapter 2: Determine if filtering experimental blast data can simultaneously preserve shock wave parameters and remove experimental artifacts.

Chapter 3: Experimentally quantify injury risk for the unprotected porcine eye exposed to primary blast overpressure using three boundary conditions and three pressure levels.

Chapter 4: Evaluate if military spectacles and goggles affect shock wave parameters measured in the eye, within the orbit, and around the face. Experimentally quantify injury risk for the protected porcine eye exposed to primary blast overpressure.

Chapter 5: Characterize the response of the eye, orbit, and face for the unprotected porcine eye exposed to primary blast overpressure

Chapter 6: Assess the FOCUS headform for eye injury during low-level blast loading.

Chapter 7: Assess the ability of an area-sensitive physical model of the eye to distinguish between blunt and blast loading, as well as various projectile impactor sizes.

Chapter 1

Membrane Characteristics for Biological Blast Overpressure Testing Using Blast Simulators

Introduction

Full-scale blast field trials using actual munitions or military explosives such as tritonol or C4 are important for investigation of certain aspects of blast effects and injury. However, such experiments are highly problematic with respect to repeatability, application of advanced instrumentation, availability, weather, and cost of sites with qualified personnel with potential scheduling constraints. Specially designed gas-dynamic shock tubes that use highly compressed gas as the energy source isolate the effects of pure blast waves without fragmentation and ejecta, and allow for systematic studies in the laboratory in a controlled, repeatable manner. A gas-driven shock tube or blast simulator consists of two chambers separated by a membrane that ruptures passively. One chamber (the 'driving' section) is pressurized until the membrane ruptures, creating a pressure wave that travels down the second chamber (the 'driven' section). The pressure wave "shocks up" as it travels down the tube until it forms a fully planar shock wave at the test region that resembles a free-field blast.

A number of factors affect the performance and output of shock tubes and blast simulators such as size, shape, driving gas, driven gas, temperature, humidity, membrane material, and membrane thickness. The relationship between driving and driven gas and the effect of shock-tube configuration on the resulting pressure trace are well understood [57]. Non-ideal diaphragm rupture was identified from the earliest shock-tube research as described in that reference: "*Despite the wealth of shock-tube literature published in recent years, relatively little information of a systematic nature has been reported on the behaviour and bursting characteristics of suitable diaphragm material*". Three widely used membrane materials are Mylar, acetate, and aluminum, each of which behaves differently. The purpose of this paper is to compare and contrast these three membrane materials at three distinct pressure levels to provide guidance for future studies that use passive rupture membranes in gas-driven shock tubes or blast simulators.

Methods

The gas-driven Advanced Blast Simulator (ABS) at Virginia Tech was used to simulate peak overpressures of 10 psi, 20 psi, and 30 psi. Pressure measurements for the Mylar and acetate membrane tests were recorded at 500 kHz (Dash® 8HF-HS, Astro-Med®, Inc., West Warwick, RI). Pressure measurements for the aluminum membrane tests were recorded at 300 kHz (TDAS PRO, Diversified Technical Systems, Inc., Seal Beach, CA). Goal pressures at the test location were chosen as incremental steps for three distinct pressure levels; 10 psi, 20 psi, and 30 psi. Mylar and acetate sheets were cut to the 9 in x 13 in membrane size using scissors and stacked to thicknesses between 15-60 mil[1] to achieve the desired pressure levels (**Table 4**). Mylar and acetate thickness may vary ± 5 mil depending on temperature. Aluminum sheets were cut to the 9 in. x 13 in. membrane size using a bandsaw. A horizontal "X" pattern was scored in the 5 in. x 9 in. region of the sheet using a CNC milling machine with an accuracy of 1 mil. It was previously shown that scoring metal membranes in this fashion facilitates even and repeatable opening of the membrane upon rupture [58]. The unfinished edges were filed by hand to remove any burrs that could potentially damage the driver/driven interface. Aluminum alloy, sheet thickness, and scoring depth were varied to provide a range of rupture pressures (**Table 5**). All tests were performed with a Helium gas tank with a pressure of at 1000 psi.

Table 4. Mylar and acetate membranes.

Goal Pressure	No. Tests	Material	Sheets Stacked	Thickness
20 psi	(n=3)	Mylar	2 x 10 mil	20 mil
30 psi	(n=1)	Mylar	3 x 10 mil	30 mil
30 psi	(n=2)	Mylar	5 x 10 mil	50 mil
10 psi	(n=10)	Acetate	15 mil	15 mil
20 psi	(n=10)	Acetate	20 mil + 15 mil	35 mil
30 psi	(n=10)	Acetate	3 x 20 mil	60 mil

Table 5. Aluminum membrane characteristics.

Goal Pressure	No. Tests	Material	Thickness	Scoring Depth
10 psi	(n=10)	Aluminum 3003	25 mil	7 mil
20 psi	(n=10)	Aluminum 2024	20 mil	6 mil
30 psi	(n=10)	Aluminum 2024	32 mil	13 mil*

*Note: one test was scored at a depth of 14 mil.

[1] 1 mil = 0.001 in.

A custom MATLAB® (version 7.11.0.584 (R2010b), The MathWorks, Inc., Natick, MA) script was written to determine the peak overpressure, positive duration, and positive impulse for each test. Peak overpressure was defined as the maximum pressure value recorded during the test. Positive duration was defined as the time interval between initiation of positive overpressure and the time at which overpressure returned to zero. Impulse was defined as the area under the positive portion of the pressure- time history. Impulse was calculated using trapezoidal integration of the pressure trace over the positive duration.

Results

A total of 66 tests were conducted; Mylar membranes (n=6), acetate membranes (n=30), and aluminum membranes (n=30). Each membrane material had a unique rupture pattern (**Figure 8**). Peak overpressure, positive duration, and positive impulse were determined for each test (**Figure 9**). The Mylar membranes tended to bulge before rupturing and did not rupture consistently. Data for the Mylar membranes are limited to the 20 psi level due to this inconsistency in rupture. The acetate membrane tended to fragment while the aluminum membranes did not fragment. The acetate and aluminum membranes produced pressure traces representative of the idealized Friedlander waveform (**Figure 10**).

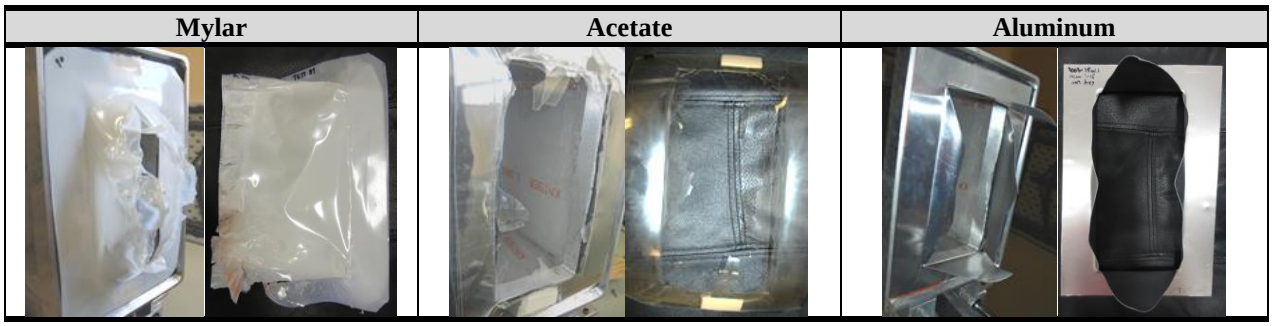

Figure 8. Rupture patterns of each membrane type.
(Left) Bulged and blown out Mylar membranes. (Center) Acetate membranes missing middle portion due to fragmentation. (Right) Typical "petal" rupture pattern of scored aluminum membranes.

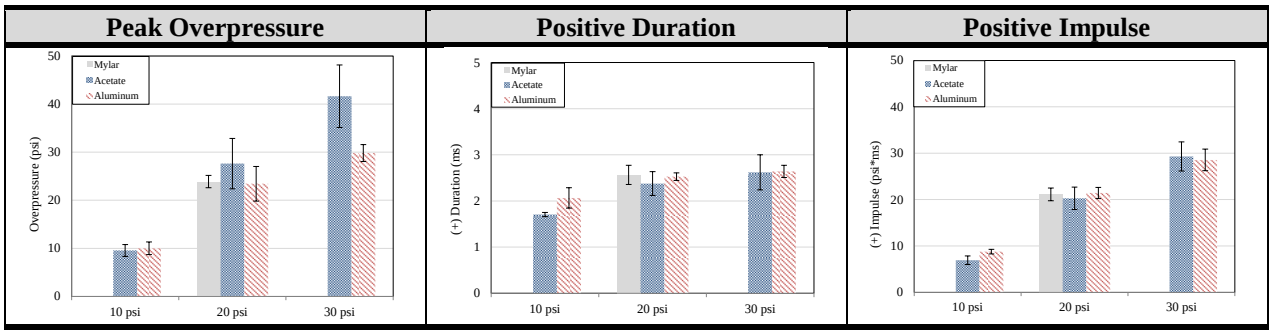

Figure 9. Average peak overpressure, positive duration, and positive impulse for all tests

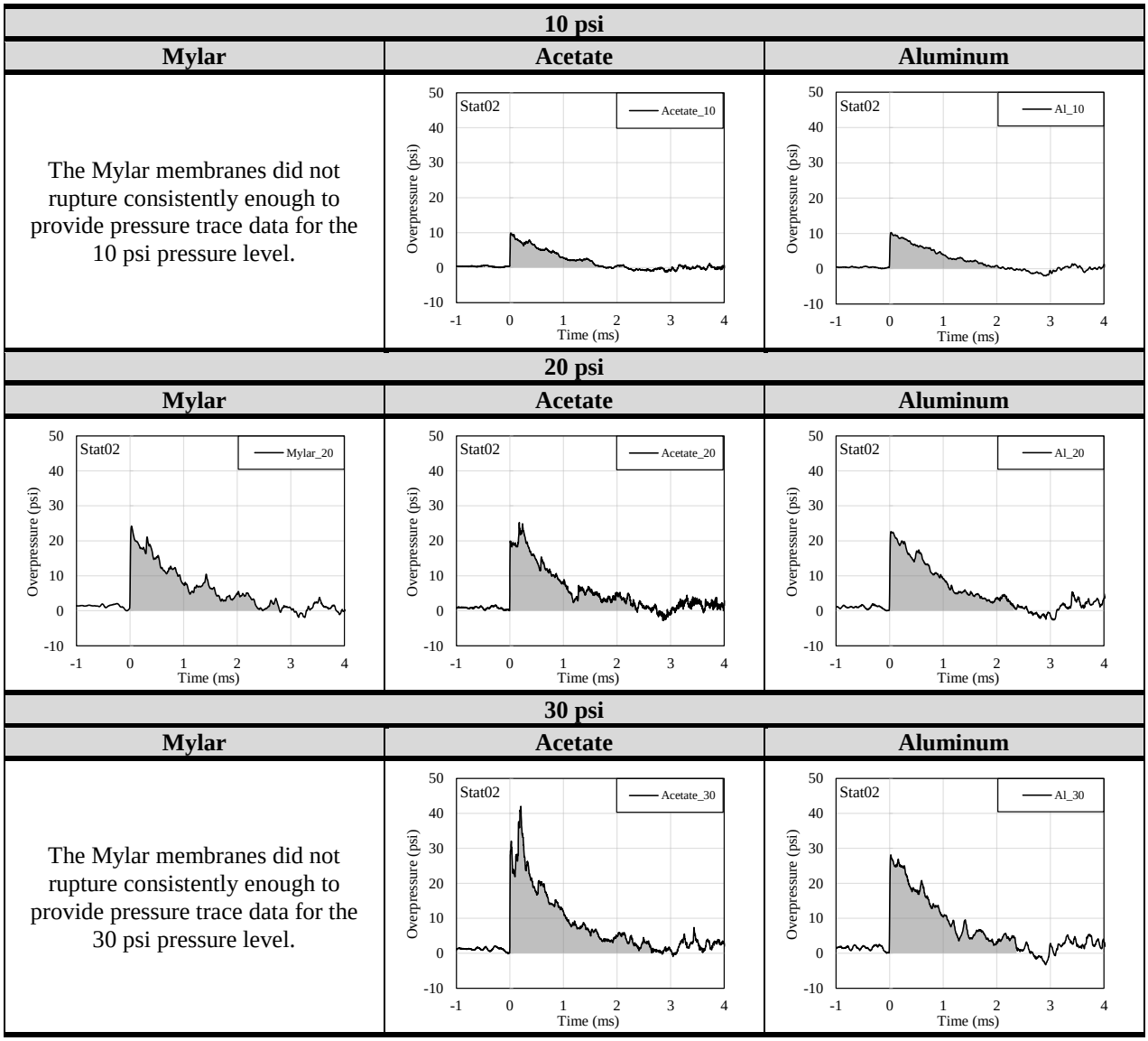

Figure 10. Exemplar pressure traces for the three membrane materials.

Discussion

Each membrane material produced unique rupture patterns and pressure traces at the test region. Ideally, a membrane ruptures instantly with no obstruction of material, thereby producing a clean pressure trace at the test region. The acetate membranes were highly frangible and sent many fragments down the driven section, leaving little material at the driver/driven interface. The aluminum membranes ruptured in a "petaling" pattern with pieces remaining attached at the wall, and being heavier material, involved a relatively slow opening. Despite these nuances, both the acetate and aluminum membranes produced close-to-ideal pressure traces at the test region. Conversely, the Mylar membranes tended to cause leaking at the driver/driven interface, which for a number of tests, resulted in failure to rupture. Failed rupture tests were omitted from the current study. Being highly plastic, when the Mylar membranes did rupture, tears formed near the central bulge but did not 'run'. As such, the flow venting from the driver passed through a small opening, developing a jetting flow which caused poor shock-wave development in the driven section.

A number of factors further affect how the membrane ruptures, which affects the pressure trace at the test location. Helium gas filling rate, which is related to the pressure in the gas tank, can dictate disruption of the shock wave, with lower pressures causing slower filing rates that yield poor or uneven membrane ruptures. Therefore, it is important to monitor helium tank pressure levels during testing. A pressure gauge can be used to ensure a consistent clamping force is applied between the driver and driven sections to minimize potential gas leaks. It is critical to note that the pressure at the test location may vary with changes in temperature.

Ease of use and cost may further affect the choice between Mylar, acetate, and aluminum membranes (**Table 6**). Mylar and acetate membranes are relatively easy to produce, as they only need to be cut to the desired membrane size. As these plastic materials are relatively thin, this can be done with scissors. Conversely, aluminum membranes require more complicated machining and less common equipment. The process of fabricating the aluminum membrane took approximately 20 minutes, about four times as long as preparing the Mylar or acetate membranes. The Mylar membranes cost between $0.3-0$1.3 each and the acetate membranes cost between $0.9-$2 each, depending on sheet thickness. However, stacking multiple acetate membranes to achieve higher pressures will increase the cost per test. Depending on the alloy

and size of sheet stock purchased, the aluminum membranes cost between $3-$9 each for the current study.

Table 6. Considerations for membrane choice in future shock tube or ABS studies.

	Mylar	Acetate	Aluminum
Pros	• Does not fragment • Relatively inexpensive	• Produces good pressure traces • Relatively inexpensive • Easy to manufacture	• Does not fragment • Produces good pressure traces
Cons	• Bulges and may not rupture • Inconsistent rupture	• Numerous large and small fragments	• Relatively expensive • Requires CNC mill

Conclusions

This study provides a number of factors that affect the peak overpressure, positive duration, and positive impulse of pressure traces recorded in an ABS using Mylar, acetate, and aluminum membrane materials. It is recommended that aluminum membranes be used if finances and tools are available to manufacture them, due to their consistency and lack of fragments that could potentially damage biological test specimens. Acetate membranes should be used to ensure consistent results between tests for large scale studies where producing the number of aluminum membranes is not a viable option and fragmentation is not a large concern. As the acetate membranes were highly frangible biological test specimens should be protected from impact from potential membrane fragments. This can be accomplished using fabric or mesh deflector screens upstream of the specimen which do not greatly affect the propagation of the wave. Although Mylar membranes have performed very well with conventional shock tubes, Mylar membranes are not recommended for ABS use due to the inconsistency in rupture and poor representation of an idealized pressure wave when rupture does occur [59]. As the current study focused on individual materials, the role of combining different materials to yield better pressure traces and relative cost effectiveness needs to be further explored in future work.

Chapter 2

Effects of Filtering on Experimental Blast Overpressure Measurements

Introduction

The increased frequency of blast-related injuries in current military conflicts, terrorist events, and industrial accidents has created the need to quantify human injury tolerance to exposure to shock waves. Experimental studies that use laboratory equipment to mimic real-world, free-field blast overpressure events are becoming increasingly common. One approach to examining the effects of blast exposure is to correlate diagnosed injuries to measurable, quantifiable shock wave parameters (e.g., peak overpressure, positive duration, and positive impulse). Here, "overpressure" refers to the pressure wave caused by detonating a high-order explosive. Due to the high-rate nature of blast, low pass hardware and software filters that prevent aliasing for impact and crash data are typically not applied to blast data. Furthermore, signals recorded at the high sampling rates required to capture blast events are especially susceptible to experimental artifacts. Post-processing blast data with a properly designed filter can yield smoother overpressure traces and remove artificial responses of the sensor during shock wave loading. The purpose of this study is to examine if a 4th order low pass Butterworth filter can remove artifacts from overpressure traces while preserving the integrity of the shock wave parameters.

Methods

The small VT ABS **(Figure 4**) was used for this test series. Aluminum membranes (alloy 2024, 32 mil thickness, 7-8 mil "X" pattern) were used to produce shock waves of approximately 30 psi static overpressure measured along the inside wall of the tube at the test region. All data were recorded using a high performance data acquisition system (TDAS PRO, Diversified Technical Systems, Inc., Seal Beach, CA). The internal 8-pole Butterworth low pass hardware anti-alias filter (-3dB of 4300 Hz) for TDAS PRO was bypassed for all tests. The sampling frequency for each channel was 301.887 kHz, which was determined by the maximum bandwidth of TDAS PRO (25 kHz).

Five tests were conducted on the empty ABS. Data were collected using high-frequency response pressure sensors (Model 102B15, 200 psi, PCB Piezotronics, Depew, NY) located flush with the inside wall of the tube at 4 ft and 5 ft from the initiation of the shock wave. The resonance frequency of these pressure sensors was greater than 500 kHz, and the rise time was ≤1.0 μs. The coaxial cables supplied with these sensors had an internal crimp strain relief at the connector, and were shielded for electrical impedance of 50 Ω and insulation resistance >1 TΩ. As these sensors were mounted to the ABS, they were subjected to any mechanical vibrations caused by the propagating overpressure. Therefore, the sensors were snugly inserted in plastic holders that dampened the effects of vibration.

Three tests were conducted on the ABS under the same conditions as the empty tube tests but with a test object inside the tube. The test object consisted of a porcine eye potted in a synthetic orbit that was mechanically coupled to the ABS walls, located 5 ft from the initiation of the shock wave. The preparation methods for eyes in synthetic orbits were previously published [36]. Intraocular overpressure (IOP) was collected using a miniature pressure sensor inserted into the eye (Model 060, 100 psi, Precision Measurement Company, Ann Arbor, MI). As this sensor was designed to be minimally invasive for biological applications, the sensor wire was a simple unshielded Teflon-coated copper wire.

Data were zeroed based on the average value of the first 10,000 points in the trace. Time of arrival (ToA), peak overpressure, positive duration, and positive impulse were quantified at each sensor location for all tests using a custom MATLAB® script (version 7.11.0.584 (R2010b), The MathWorks, Inc., Natick, MA). A 4th order phaseless low pass Butterworth filter was applied to the raw data. The difference equation and constants describing the filter are defined by SAE J211/1[60]. The filter passed data through twice, forward then backward, to avoid phase shift. The channel frequency class (CFC) of the filter was incrementally increased between CFC 1000 and CFC 10k **(Table 7**). The overall shape of the overpressure trace was monitored. The average raw shock wave parameters were quantified and used to establish ±2.5% thresholds for comparison with the filtered data. A Fast Fourier Transform (FFT) was used visualize the frequency spectrum of each channel.

Table 7. Cutoff frequencies (3 dB) for a 4th order low pass Butterworth filter.

CFC	CFC 1000	CFC 2000	CFC 3000	CFC 4000	CFC 5000	CFC 6000	CFC 7000	CFC 8000	CFC 9000	CFC 10k
Cuttoff Freq. (Hz)	1650	3300	4950	6600	8250	9900	11550	13200	14850	16500

Results

Lower cutoff frequencies attenuated the peak to a greater extent than higher cutoff frequencies, effectively decreasing the peak overpressure and increasing the rise time and positive duration. The positive impulse remained relatively constant across the filters tested.

Table 8 reports the average raw data values that were used as a standard for comparison with the average filtered data. Shaded cells indicate that the average filtered value falls within ±2.5% of the average raw value. No filter preserved the rise time. The lowest cutoff frequency to preserve the remaining raw parameter values for both sensors was the CFC 6000 filter. **Figure 11** illustrates the effect of filtering on the raw and filtered Empty Tube test data collected by the two sensors for a single test. **Figure 12** shows the FFT of the empty tube test data for a single test. Many of the peak frequencies are harmonics of 60 Hz, indicating sensitivity to AC-powered equipment in the room.

Table 8. Average shock wave parameters for empty tube data (n=5).
Shaded cells indicate that the average filtered value falls within ±2.5% of the average raw value.

Sensor 01	Raw Data	CFC 1000	CFC 2000	CFC 3000	CFC 4000	CFC 5000	CFC 6000	CFC 7000	CFC 8000	CFC 9000	CFC 10k
Pk. Overpress. (psi)	35.90	26.29	31.20	33.57	34.63	35.14	35.44	35.65	35.82	35.95	36.05
Rise Time (μs)	36.44	324.62	167.61	119.91	96.06	80.82	69.56	62.94	958.64	49.02	45.71
(+) Dur. (ms)	1.88	2.02	1.91	1.88	1.87	1.86	1.86	1.86	1.86	1.85	1.85
(+) Imp. (psi*ms)	22.07	22.16	22.13	22.12	22.11	22.10	22.10	22.09	22.09	22.08	22.08

Sensor 02	Raw Data	CFC 1000	CFC 2000	CFC 3000	CFC 4000	CFC 5000	CFC 6000	CFC 7000	CFC 8000	CFC 9000	CFC 10k
Pk. Overpress. (psi)	28.53	25.21	27.08	27.11	27.43	27.68	27.86	28.00	28.12	28.23	28.31
Rise Time (μs)	31.14	354.44	202.72	143.10	90.10	72.87	60.95	53.00	47.70	43.72	40.41
(+) Dur. (ms)	2.34	2.60	2.42	2.39	2.37	2.36	2.36	2.36	2.35	2.35	2.35
(+) Imp. (psi*ms)	23.40	23.41	23.36	23.38	23.38	23.39	23.39	23.39	23.40	23.40	23.40

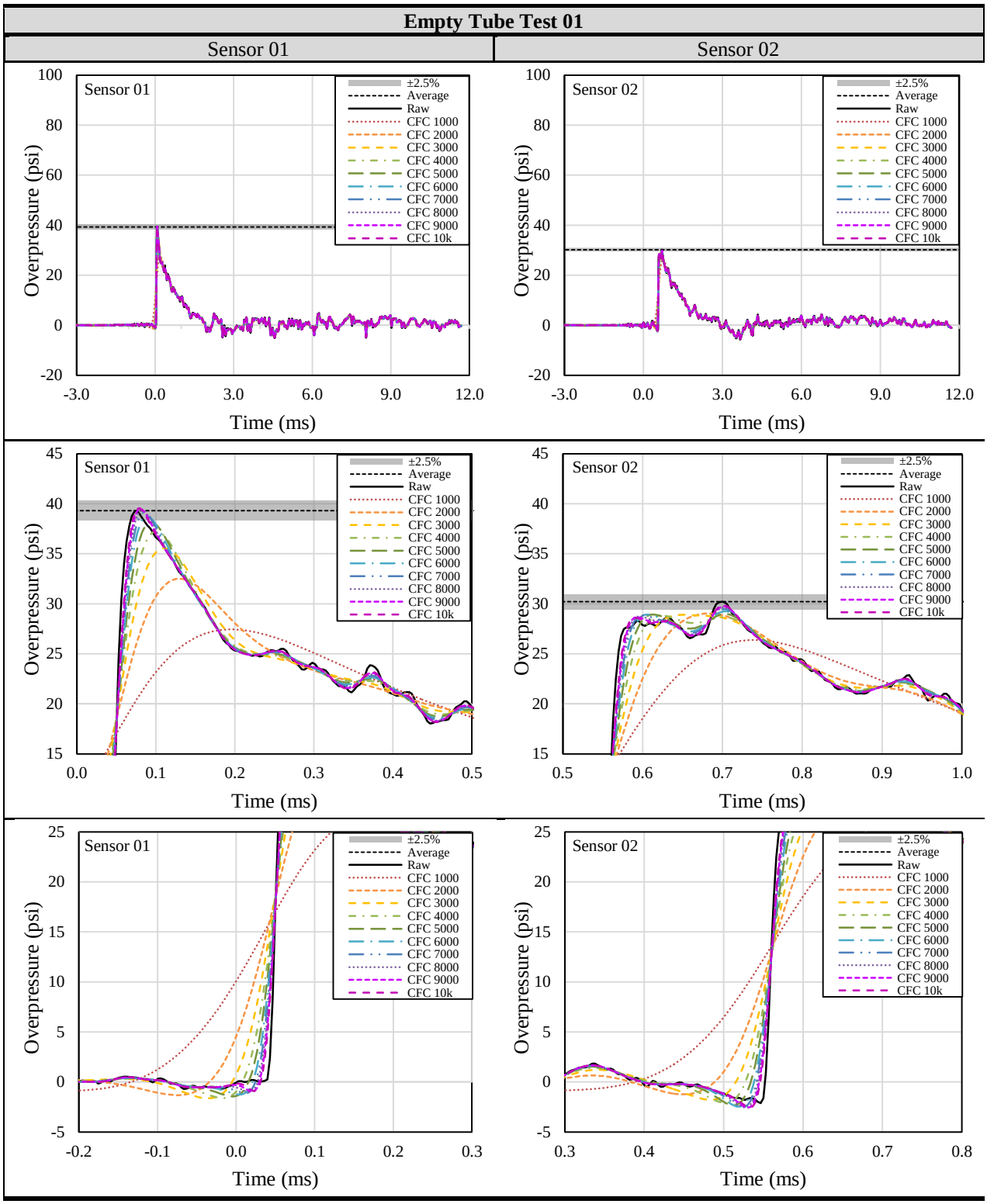

Figure 11. Raw and filtered pressure-time histories for Empty Tube Test 01. Plots show peak overpressure ("Pk."), ±2.5% thresholds for peak overpressure, and data points used to calculate the raw rise time (circles). Note the decreased magnitude and temporal delay of the peak overpressure, and early time of arrival for the lower cutoff frequencies. (Left) Sensor 01 was located 4ft from the bursting membrane. (Right) Sensor 02 was located 5ft from the bursting membrane. (Top) Overpressure traces. (Middle) Zoomed in view of the peak overpressure. (Bottom) Zoomed in view of the time of arrival.

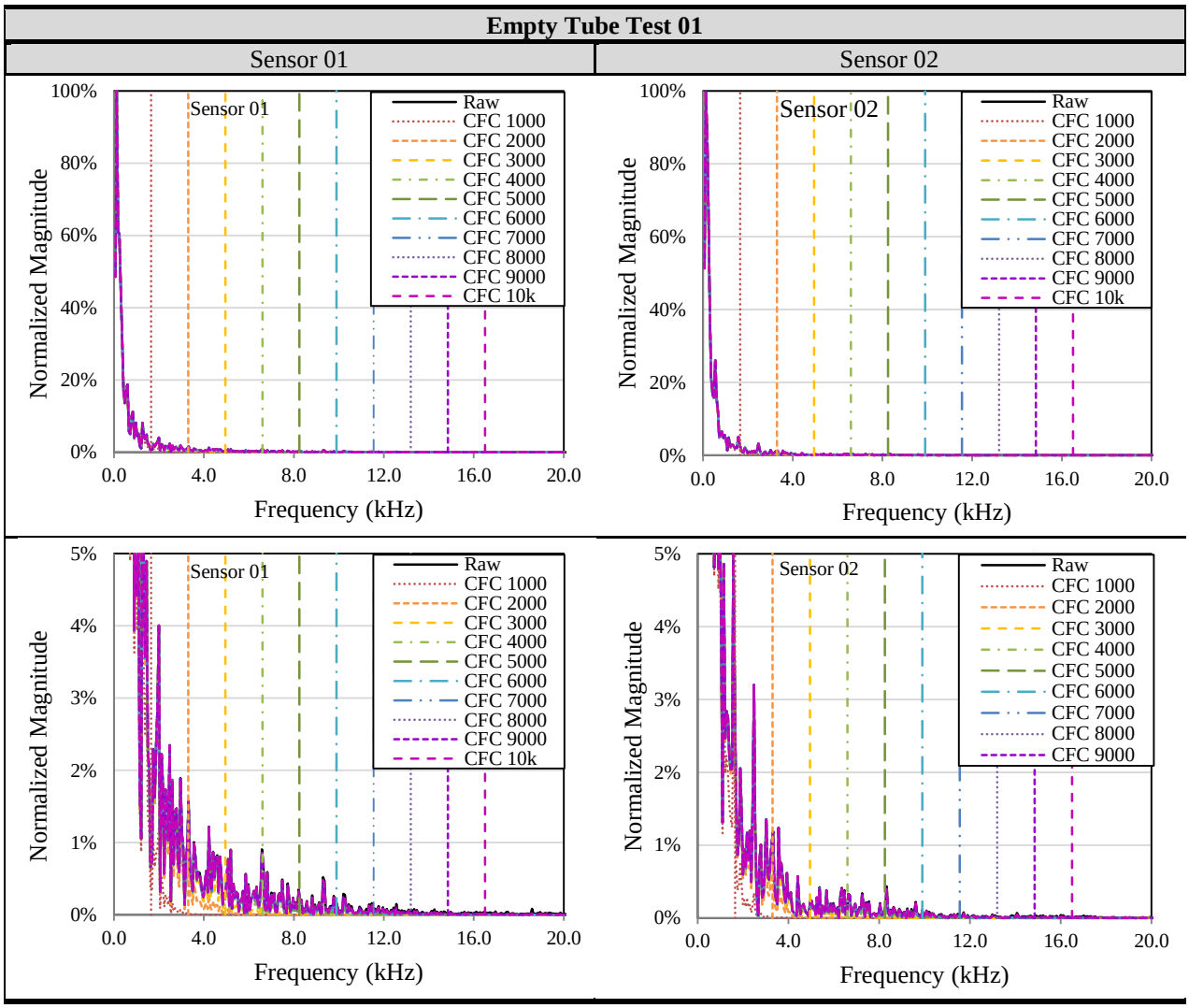

Figure 12. Raw and filtered frequency spectra for Empty Tube Test 01. Axes truncated at 20 kHz for clarity (maximum frequency ~150 kHz). Vertical lines represent the 3 dB cutoff frequency for each of the filters applied to the data, and are color-coded respectively. (Top) Many of the peak frequencies are harmonics of the 60 Hz utility frequency for electrical power in the United States. (Bottom) Zoomed in view to 5% of the normalized magnitude.

Table 9. Average shock wave parameters for IOP test data (n=3). reports the average raw data values that were used as a standard for comparison with the average filtered data. Shaded cells indicate that the average filtered value falls within ±2.5% of the average raw value. No filter preserved the rise time. The lowest cutoff frequency to preserve the remaining raw parameter values was the CFC 7000 filter. **Figure 13** illustrates the effect of filtering on the raw and filtered IOP test data collected for a single test. Note that there is a "spike" in the trace around 4 ms. This high magnitude, short duration spike was likely caused by the unshielded wire whipping due to the shock wave wind. **Figure 14** shows the FFT of the IOP test data for a single

test. Many of the peak frequencies are harmonics of 60 Hz, indicating sensitivity to AC-powered equipment in the room.

Table 9. Average shock wave parameters for IOP test data (n=3).
Shaded cells indicate that the average filtered value falls within ±2.5% of the average raw value.

Sensor 01	Raw Data	CFC 1000	CFC 2000	CFC 3000	CFC 4000	CFC 5000	CFC 6000	CFC 7000	CFC 8000	CFC 9000	CFC 10k
Pk. Overpress. (psi)	80.68	59.34	73.36	77.73	79.09	79.38	79.30	79.15	79.07	79.05	79.06
Rise Time (μs)	53.00	308.06	178.87	132.50	119.25	104.90	99.37	96.06	92.75	93.85	90.54
(+) Dur. (ms)	1.40	1.97	1.87	1.86	1.78	1.77	1.77	1.40	1.40	1.40	1.40
(+) Imp. (psi*ms)	36.68	40.17	40.14	40.10	39.75	39.75	39.76	36.69	36.69	36.69	36.69

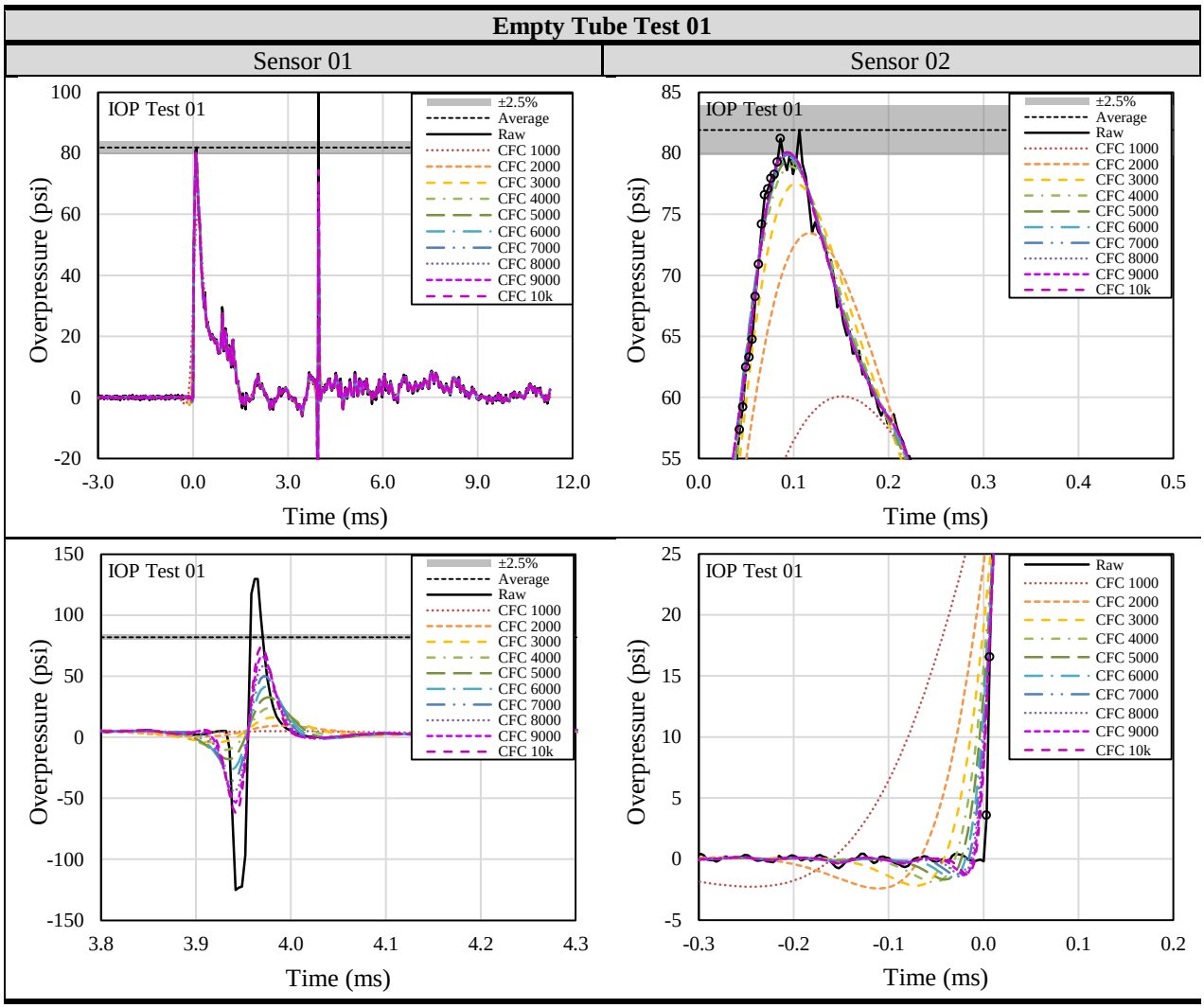

Figure 13. IOP Test 01 raw and filtered pressure-time histories, showing the peak overpressure ("Pk."), ±2.5% thresholds, and data points used to calculate the raw rise time (circles). (Top Left) Overpressure traces. Note the spike in the trace around 4 ms, caused by the wire whipping due to the shock wave wind. (Top Right) Zoomed in view of the spike. (Bottom Left) Zoomed in view of the peak overpressure. (Bottom Right) Zoomed in view of the time of arrival.

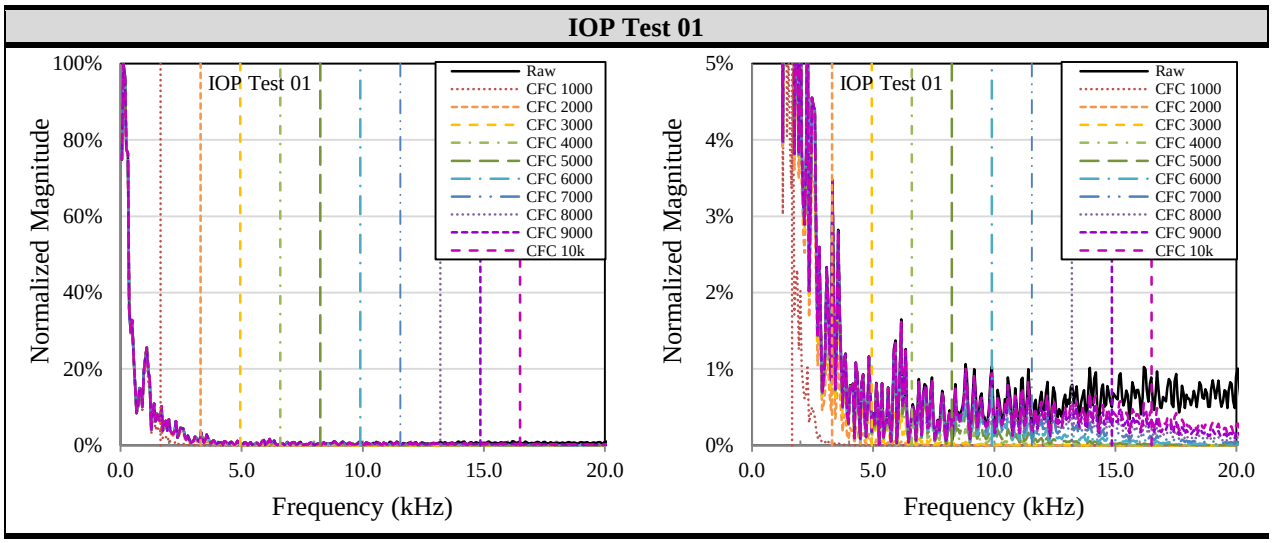

Figure 14. Normalized frequency spectrum showing the raw and filtered data for IOP Test 01, truncated at 20 kHz for clarity (maximum frequency ~150 kHz). Vertical lines represent the 3 dB cutoff frequency for each of the filters applied to the data, and are color-coded respectively. (Left) Many of the peak frequencies are harmonics of the 60 Hz utility frequency for electrical power in the United States. The high frequency noise in the spectra can be attributed to spikes in the overpressure traces caused by the wire whipping from the shock wave wind. (Right) Zoomed in to view 5% of the normalized magnitude.

Discussion

A 4th order phaseless low pass Butterworth filter applied to blast overpressure data during post-processing was able to attenuate the high frequency signals caused by experimental artifacts. However, as the filter cutoff frequency decreased, the raw signal was increasingly rounded. This caused the ToA to occur earlier and increased the positive duration. The peak overpressure decreased and was temporally delayed. The temporal shifts in ToA and the time at peak overpressure caused the rise time to increase. The changes to rise time, peak overpressure, and positive duration, are not surprising. Interestingly, the positive impulse appeared to be less affected by filtering than the other parameters. This can be attributed to an extent by the simultaneous decrease in peak overpressure and increase in positive duration associated with filtering the data and the reliance on both of these parameters in calculating impulse.

Peak overpressure, positive duration, and positive impulse could be preserved within the predefined ±2.5% thresholds of the raw parameter values, using a CFC 6000 and CFC 7000 filter for the Empty Tube tests and the IOP tests, respectively. Rise time was not preserved within the ±2.5% thresholds for either test condition for the cutoff frequencies examined. Although the maximum sampling rate was just over 300 kHz, the extremely fast rise times (< 100 μs) resulted

in a limited the number of data points during the initial loading phase, which made it difficult to obtain rise times within the ±2.5% thresholds.

A number of factors can be attributed to the slower convergence of all parameters for the IOP tests (i.e., the conclusion that higher filters were required to preserve the same parameters for IOP tests as compared to Empty Tube tests). While both the Empty Tube tests and IOP tests were conducted at the same pressure level (30 psi), the wall sensor and intraocular sensor produced characteristic traces. Compared to the Empty Tube tests, the IOP tests tended to have higher peak overpressures, rise times, and positive impulses, but lower positive durations. As the eye in the test setup had a forward-facing orientation to the direction of shock wave travel, the intraocular overpressure measured could be loosely considered a reflected overpressure. Reflected overpressure accounts for both the static and dynamic components of a shock wave, and therefore has a higher magnitude than static overpressure. The IOP test responses exhibited greater variation than the Empty Tube tests, which is likely due in part to the inherent variation between biological tissue samples obtained from different animals.

The FFTs for both the Empty Tube tests and IOP tests indicated that both types of sensors responded to the 60 Hz utility frequency for electrical power in the United States, as many of the peak frequencies observed in the FFTs were multiples of 60. As filtering was able to preserve the general shape of the overpressure trace and most of the shock wave parameters, presumably these frequencies were inconsequential to the overall analysis of the overpressure traces for this study. Future work could examine the effect of removing as many powered electronics as possible from around the test area. A similar analysis can be conducted to examine if the 60 Hz harmonic noise can be reduced by testing outdoors, where AC-powered equipment around the test site may be limited.

The IOP test FFT indicated that the miniature pressure sensor was more sensitive to higher frequencies than the wall sensors used for the Empty Tube tests, as there were numerous peaks well beyond 10 kHz. This high frequency content, which was not present for the Empty Tube test data, can be attributed to the unshielded sensor wire being whipped by the shock wave wind. All three IOP test overpressure traces had at least one artificial “spike” characterized by a peak

overpressure that approached or exceeded the maximum range of the pressure sensor and a total duration around 10 μs.

Engineering controls can be implemented during experimental design to eliminate or minimize the cause of common artifacts. When possible, shielded cables should be chosen; otherwise, unprotected wires can be routed through a grounded braided steel sheath to achieve a similar effect. Frequently used equipment is exposed to mechanical vibrations during testing, and can cause damage or loosening. Connections between sensors and wires and between sensors and the tube should be routinely examined to ensure secure contact. Properly strain-relieving any wires that contact the tube walls can prevent damaging the sensor and minimize high-frequency responses due to physical shaking or whipping during testing. Lastly, electrical cables and wires connected to sensors should not be coiled or placed too close to other powered equipment.

Conclusions

The methods disseminated in this paper serve as an initial investigation of the effects of filtering high rate blast data collected indoors using an ABS and two different pressure sensors. A 4th order phaseless low pass Butterworth filter with increasing cutoff frequencies (CFC 1000 – CFC 10k) was applied to the data. Filtered shock wave parameters were compared to ±2.5% of the raw data parameters. Peak overpressure, positive duration, and positive impulse could be preserved within these thresholds.

These techniques focused on manually assessing filters. A multiobjective optimization routine could be used to more quickly and accurately create an optimal filter that can be used for a wider range of blast applications. This would be especially useful when multiple parameters are used simultaneously to assess injury risk. As with all analyses, caution should be taken to ensure the data are not misrepresented by post-processing techniques, including filtering. Besides altering the overall shape of the recorded signal, changes in quantifying the shock wave parameters caused by post-processing filtering could drastically affect injury prediction that relies on the fidelity of these parameters.

Chapter 3

Eye Injury Risk to the Unprotected Eye due to Primary Blast Overpressure Exposure

Introduction

The increased use of improvised explosive devices (IEDs) in current military conflicts beyond what has been reported in historical military efforts necessitates the need to understand human tolerance to blast overpressure exposure (shock waves). Explosive events accounted for more than 75% of combat-related fatalities in Operation Iraqi Freedom and Operation Enduring Freedom (OIF/OEF) [6]. Reduced fatality rates during recent military conflicts have been linked to the increased use of personal protective equipment (PPE) [7]. While unprotected air-filled organs such as the lung are most susceptible to blast injury, the use of improved thoracic PPE has reduced the incidence of these injuries, leaving the face and eyes disproportionally vulnerable to concomitant blast injuries [8, 9]. Despite the availability of protective eyewear for soldiers involved in OIF/OEF between 2003-2006, eye injuries reportedly occurred in 17% of cases where protective eyewear was used and jumped to 26% when protective eyewear was not used at the time of combat-related injury [10]. These injuries could have been sustained by multiple injury mechanisms, potentially including primary blast overpressure. The incidence of eye injuries that occur even when protective eyewear is used further motivates the need to understand primary blast overpressure as an eye injury mechanism for the unprotected eye.

Studies have reported more than 80% of all severe ocular injuries sustained during military combat are the result of munitions fragmentation and debris [11, 12]. Many military explosives are buried or impregnated with shrapnel, thereby increasing the risk of injury from projectiles. While injury mechanisms for blunt trauma are well understood, the specific injury mechanisms and injuries caused by primary blast overpressure (i.e., the increase in pressure) exposure are not well understood [28-39].

Although many eye injuries do not pose a high threat to life, the economic and psychological effects are alarming. An example of this is that a globe rupture, which often results in enucleation and therefore total functional loss of the eye, would likely only be classified as a moderate injury. Injuries to the eye and visual system are particularly debilitating from a

military perspective because they can severely decrease the ability of a soldier to achieve return-to-duty standards required for service. Notwithstanding, the time and finances invested in training is 'lost' when a solider cannot return to duty. Similarly, lack of adequate vision limits the type of jobs that can be acquired following return to civilian life. Decreased quality of life compared to pre-injury levels can leave a veteran feeling depressed and anxious about their current state. An understanding of primary blast overpressure as an injury mechanism may shed light on the role of injury to the eye with such outcomes.

Due to the paucity of studies in the literature that specifically examine the response of the eye to primary blast overpressure exposure, it is necessary to experimentally quantify the physical response of the eye. Therefore, the purpose of this study is twofold; first, to quantify and predict eye injuries caused by survivable primary blast overpressures, and second, to examine the effect of increasing biofidelity of the boundary conditions surrounding the eye during blast overpressure exposure.

Methods

All tests were conducted using the small VT ABS with aluminum membranes prepared as described in Chapter 1 (**Figure 4**). Briefly, this is a helium gas-driven tube specifically designed for testing small specimens, and is able to produce peak overpressures up to approximately 30 psi (static overpressure) with a positive duration around 2.5 ms using aluminum membranes.

Main Study

A total of 88 porcine eyes were used in this study. Fresh porcine eyes were shipped overnight on wet ice, stored in a refrigerator, and tested within three days of slaughter (Animal Technologies, Tyler, TX, USA). Control eyes were used to assess postmortem effects and damage from tissue procurement. Sham eyes were used to quantify potential injuries from pre-test preparation techniques, including the insertion of a pressure sensor and pressurization tube into the eye through the optic nerve and setting the eye in a rigid concave cup or in gelatin. All eyes were prepared with the following technique. Skin and musculature was removed to expose only the globe and optic nerve. Eyes were identified as left (OS) or right (OD). Cornea clarity was qualitatively assessed (clear, not clear), and visibility of the "Y" suture on the lens was noted. Fluorescein dye was applied to the cornea and a blue light was used to help visualize corneal

abrasions. Any existing corneal abrasions were noted. Control eyes were dissected at this point to assess and quantify baseline damage to the eye caused by postmortem degradation and procurement from the abattoir. The remaining eyes were further prepared by applying a dot pattern on the surface of the sclera using permanent black ink. A miniature pressure sensor (Model 060S, 100 psi, Precision Measurement Company, Ann Arbor, MI) and a small tube were inserted through the optic nerve into the vitreous fluid and secured in place using a cable tie. Normal physiologic intraocular pressure (IOP) was provided throughout the duration of the test using a gravity-fed system. Specifically, a bag of Lactated Ringer's solution was connected to the small tube and suspended 8 in. above the eye to provide normal physiologic pressure to the eye during the duration of testing (0.29 psi or 14.95 mmHg). Intraocular pressure was measured before and after each test using a veterinary tonometer (Tono-Pen AVIA Vet® Veterinary Tonometer, Reichert Technologies, Depew, NY, USA). Due to minor variations, measurements were taken using the tonometer until three sequential measurements recorded the same IOP at a 95% confidence.

Eyes were placed in one of three boundary conditions ("Isolated Eye", "Synthetic Orbit", "3D Orbit") and exposed to a single blast event at 10 psi, 20 psi, or 30 psi static overpressure. The synthetic orbit and the 3D Orbit represented the left orbit geometry. These pressure levels were chosen to examine the effects of increasingly severe, yet survivable blast events [15]. The three boundary conditions surrounding the eye were tested to assess the effects of increasing biofidelity of the orbit and facial geometries. Photographs of these three test setups are shown in **Figure 15**, and **Table 10** summarizes the final test matrix.

Isolated Eye	Synthetic Orbit	3D Orbit
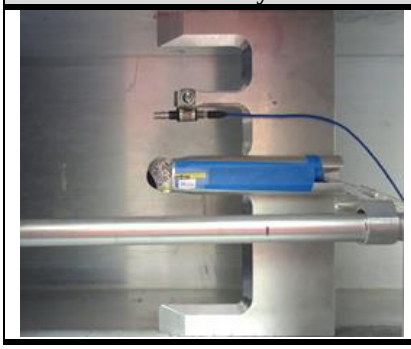	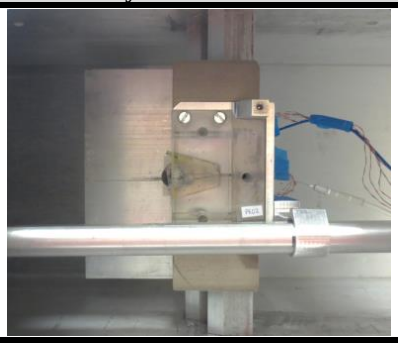	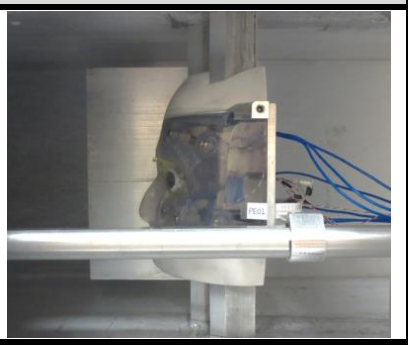

Figure 15. Photographs of the three test setups, shown inside the ABS.

Table 10. Unprotected eye test matrix

Control	Sham	Isolated Eye	Synthetic Orbit	3D Orbit
Quantify damage from postmortem degradation and procurement	Quantify damage from preparation methods	Quantify isolated eye response with no reflected surfaces	Quantify response with simplified orbit using flat reflective surfaces	Quantify response with human orbit using complex reflective surfaces
16 eyes	8 eyes in isolated 16 eyes in gelatin	5 eyes at 10 psi 6 eyes at 20 psi 4 eyes at 30 psi	5 eyes at 10 psi 6 eyes at 20 psi 5 eyes at 30 psi	6 eyes at 10 psi 5 eyes at 20 psi 6 eyes at 30 psi

The isolated eye test condition was designed to isolate the eye from the orbital bones, muscle, and fat. This expanded upon previous work conducted on isolated human eyes exposed to fireworks [40]. The isolated eye test condition consisted of a rigid concave cup with a hole in the back through which the optic nerve, IOP sensor, and pressurization tube could pass. This was designed to provide support for the eye during the test, and provided minimal reflective surfaces around the eye. Approximately one third of the posterior portion of the eye contacted the concave cup. Eyes were prepped with the experimental apparatus oriented vertically, such that the cornea faced the ceiling, so that only gravity affected the eye and no additional tension was placed on the optic nerve or the back of the eye. An alligator clip attached to the cable tie held the eye in place. When the experimental apparatus was rotated such that it was oriented horizontally for testing, the eye loosely rested on a small ledge to prevent drooping. A photograph of the isolated eye in the horizontal orientation is shown in **Figure 16**.

Isolated Eye

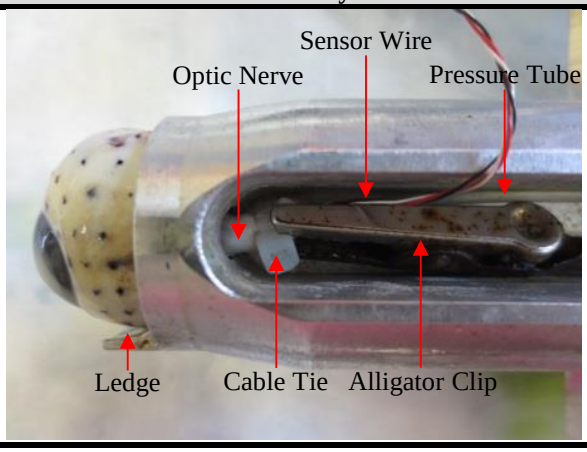

Figure 16. Isolated eye boundary condition.

The synthetic orbit had smooth, flat surfaces that approximated a first-order human orbital geometry. The eye was suspended within the orbit using fishing line, with approximately one

third of the anterior portion of the eye exposed. A 10% Knox® gelatin solution was poured around the eye within the orbit to simulate the fat and muscles within the orbit. The orbit was refrigerated for at least 45 minutes to allow the gelatin to set. A photograph of the synthetic orbit is shown in **Figure 17**.

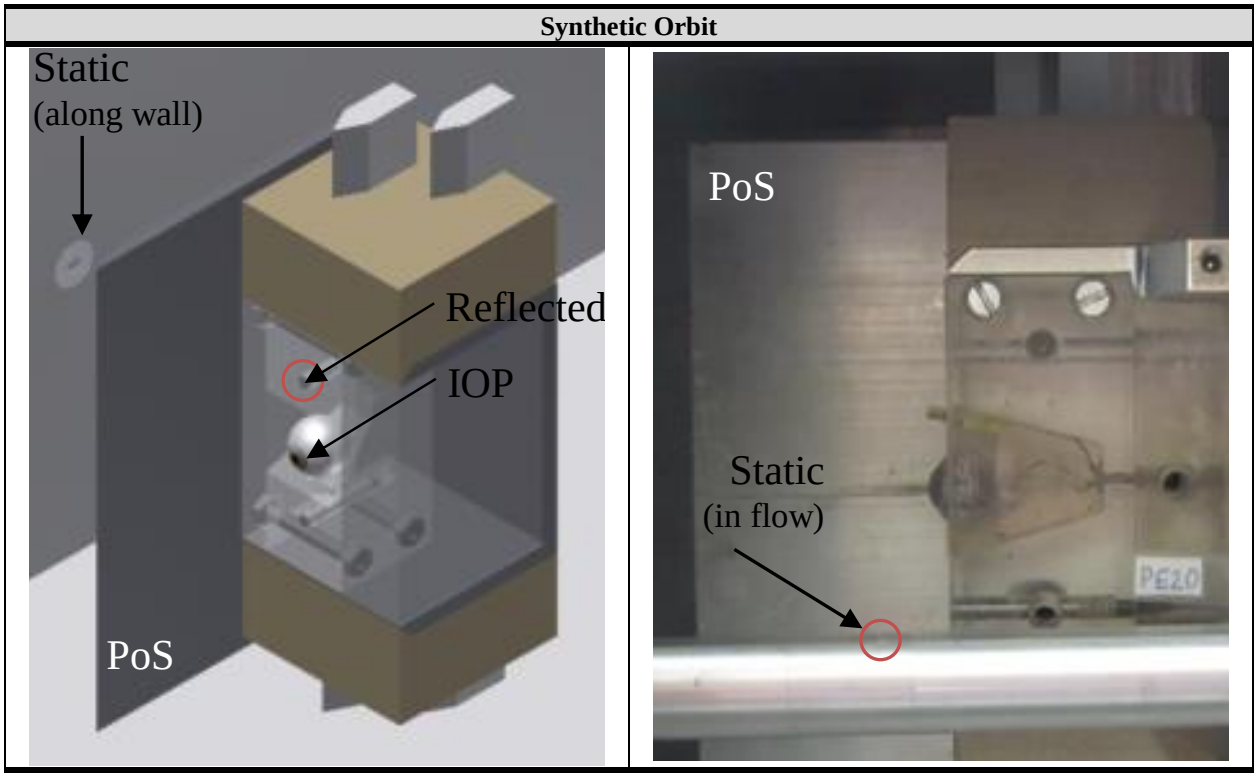

Figure 17. Synthetic orbit boundary condition.

The 3D orbit test condition has the facial geometry, including skin, of the Global Human Body Models Consortium (GHBMC) head [61]. This geometry was used to manufacture a clear rigid plastic orbit using 3D printing. Similar to the synthetic orbit preparation, the eye was suspended within the orbit using fishing line. A negative mold of the eye was required for preparation of the 3D orbit because of the curved surface of the 3D orbit facial geometry. A 10% Knox® gelatin solution was poured around the eye within the orbit to simulate the fat and muscles within the orbit as well as the soft tissue around the eye and eyelid. Photographs of the negative mold and the 3D orbit are shown in **Figure 18** and **Figure 19**, respectively.

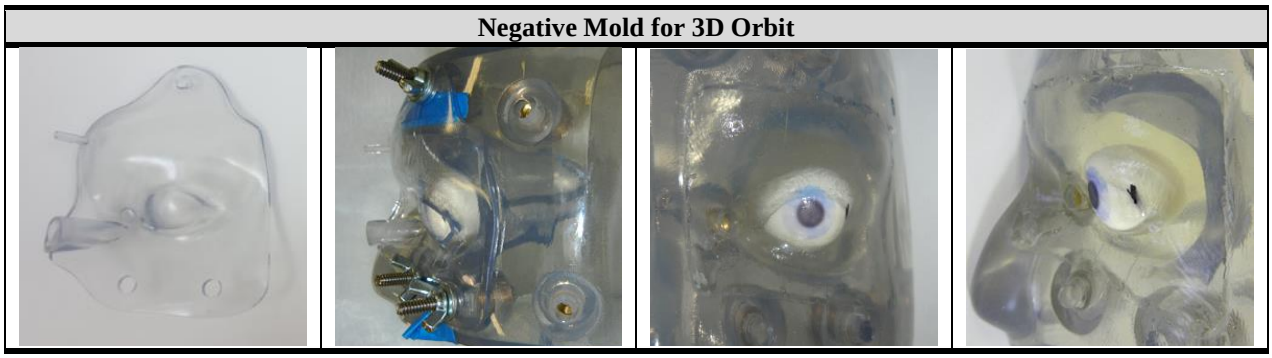

Figure 18. Negative mold used to add gelatin around eye in 3D orbit.
(Images shown with a synthetic eye.)

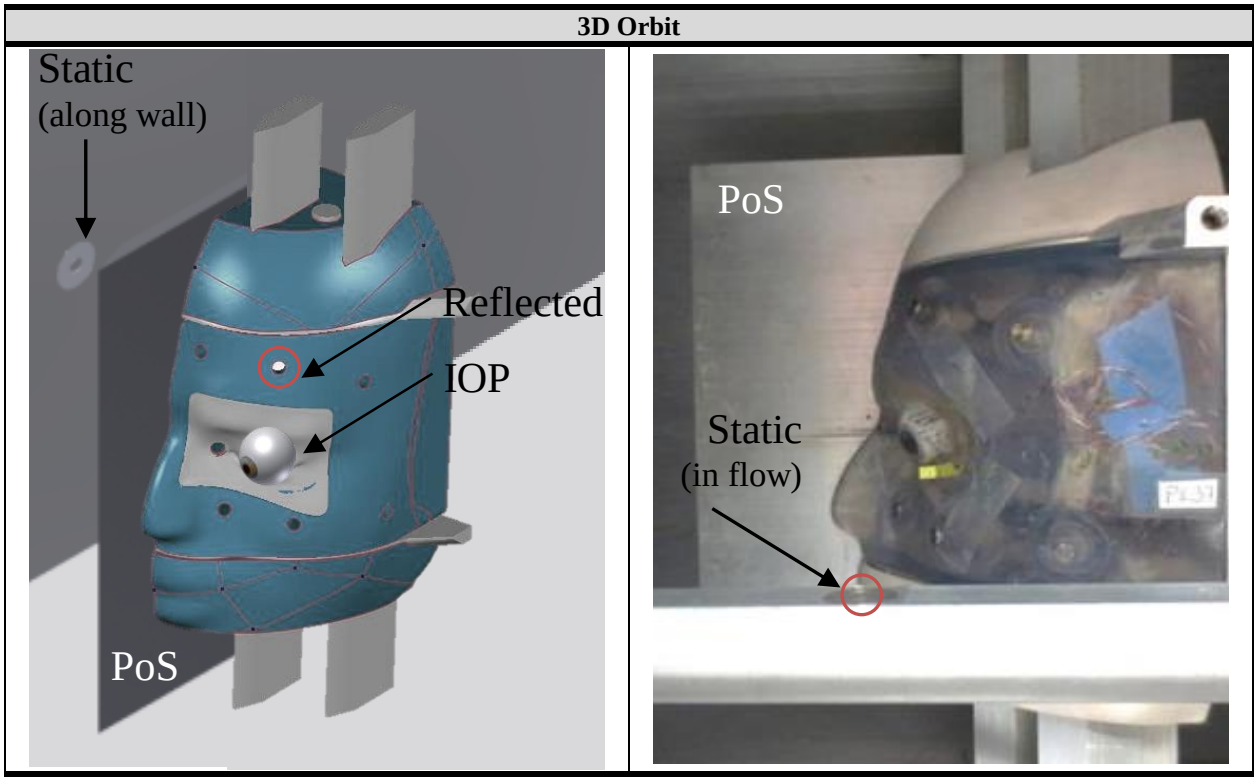

Figure 19. 3D orbit boundary condition.

Evaluation of Test Condition Biofidelty using the Synthetic Orbit

As the synthetic orbit and 3D orbit represented only half the human face and occluded a larger cross-sectional area of the tube than the isolated eye, the biofidelity of these setups was systematically assessed prior to conducting the final tests as described above for this study. Special care was taken to ensure these test conditions did not restrict fluid flow within the test section of the ABS, and two modifications were examined upon recommendation of a blast physicist.

The first modification was a plane of symmetry (PoS) that used created a more realistic condition for the tests conducted with a bisected facial geometry by preventing pressure relief around the nasal side of the face that would not occur *in theatre*. The PoS was evaluated by adding it along the nasal side of the synthetic orbit, which corresponds to the line of symmetry in the human head along the mid-sagittal plane. The PoS was fabricated from a 0.25" thick piece of aluminum and had a beveled leading edge facing away from the nose. This allowed the pressure wave to easily pass around the test orbit, thereby providing a more realistic boundary condition around the bisected portion of the face represented by the orbit. The PoS extended 3" in front of the eye. **Figure 20** illustrates the location of the PoS with respect to the human face and orbit.

The second modification was the addition of forehead and chin blocks around the orbit that allowed for tests to include as much of the human face as possible. Experimental test size based on cross-sectional occlusion area was assessed by testing and comparing the responses of the synthetic orbit with and without extension blocks that simulated a first-order approximation of the forehead and chin. The synthetic orbit without the blocks had a cross-sectional occlusion area of 10% of the tube. The addition of the blocks increased the cross-sectional area to 20% of the tube. **Figure 20** illustrates the area of the face tested with the PoS and with and without the blocks.

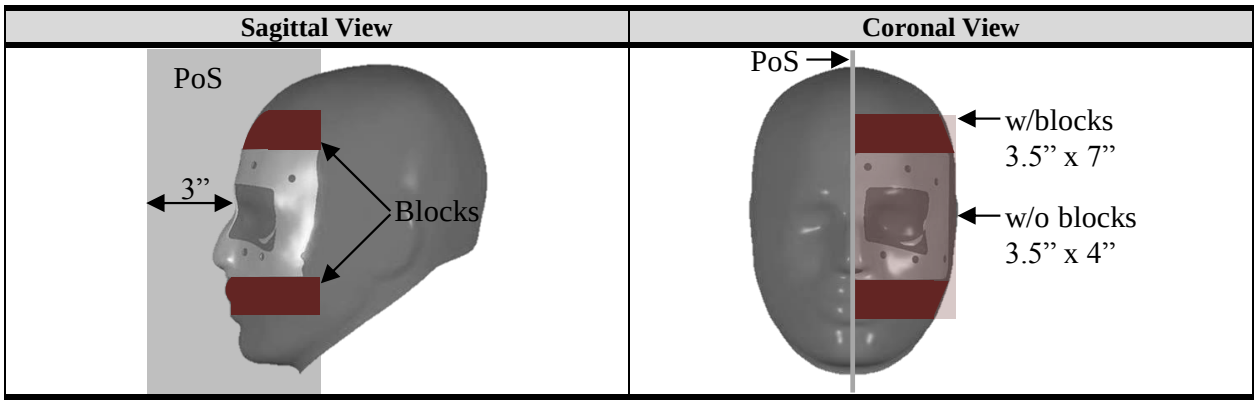

Figure 20. Plane of symmetry and occlusion area overlaid on image of GHMBC.

Tests were conducted in duplicate at each pressure level using four test scenarios: Empty Tube, PoS with 10% occlusion, No PoS with 20% occlusion, and PoS with 20% occlusion (**Figure 21**). Porcine eyes were not used for this. Static overpressure was measured along the wall of the tube at the test region and reflected overpressure was measured at the forehead of the synthetic orbit. The Empty Tube tests provided baseline overpressure profiles for static overpressure measured

along the wall of the tube at the test region for comparison with the biofidelity tests. Adding the synthetic orbit with a 10% occlusional cross-sectional area provided a minimum occlusion that still mimicked a facial geometry. Adding the PoS created a more realistic condition for pressure relief. Lastly, adding "forehead" and "chin" blocks to the synthetic orbit created a 20% cross-sectional occlusion area, and is more realistic because of the addition of the forehead and chin geometry. Testing this last condition with a PoS was the most realistic condition in terms of both size and pressure relief.

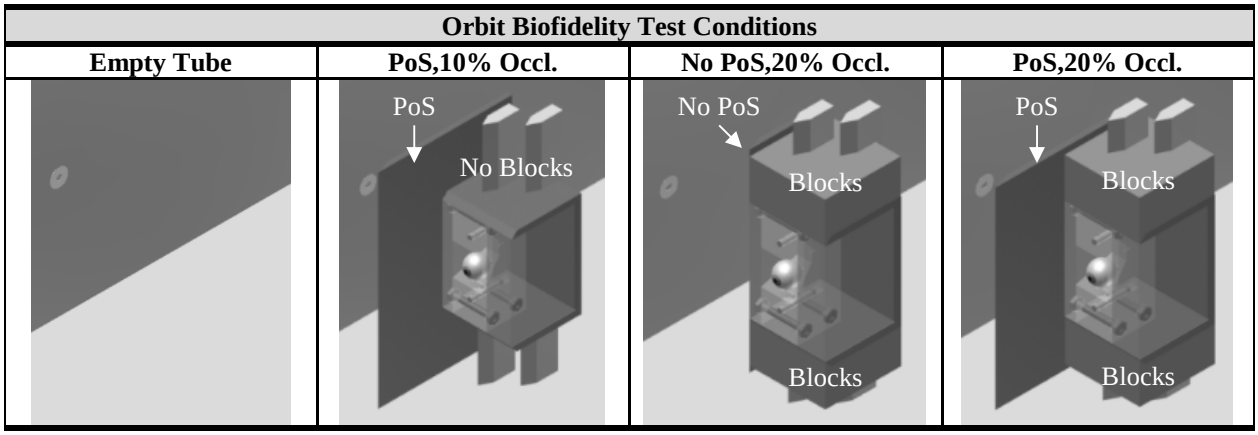

Figure 21. Orbit biofidelity test conditions using the synthetic orbit.

Pressure was measured at a number of locations in and around the eye for the final test matrix. Intraocular pressure (IOP) was measured inside the eye throughout the test using the miniature pressure sensor. Static overpressure in the fluid flow was measured using a "pencil" sensor mounted 2 inches from the temporal side of the orbit. The sensing element of the pencil sensor was aligned with the front of the cornea. Total overpressure was measured for the isolated eye condition using a sensor mounted above the eye. Reflected overpressure was measured for the synthetic orbit condition using a sensor mounted in the forehead of the orbit, flush with the flat surface. Reflected Overpressure was measured for the 3D Orbit condition using a sensor mounted in the forehead of the orbit, flush with surface of the 3D Orbit. **Figure 22** illustrates the locations of these sensors.

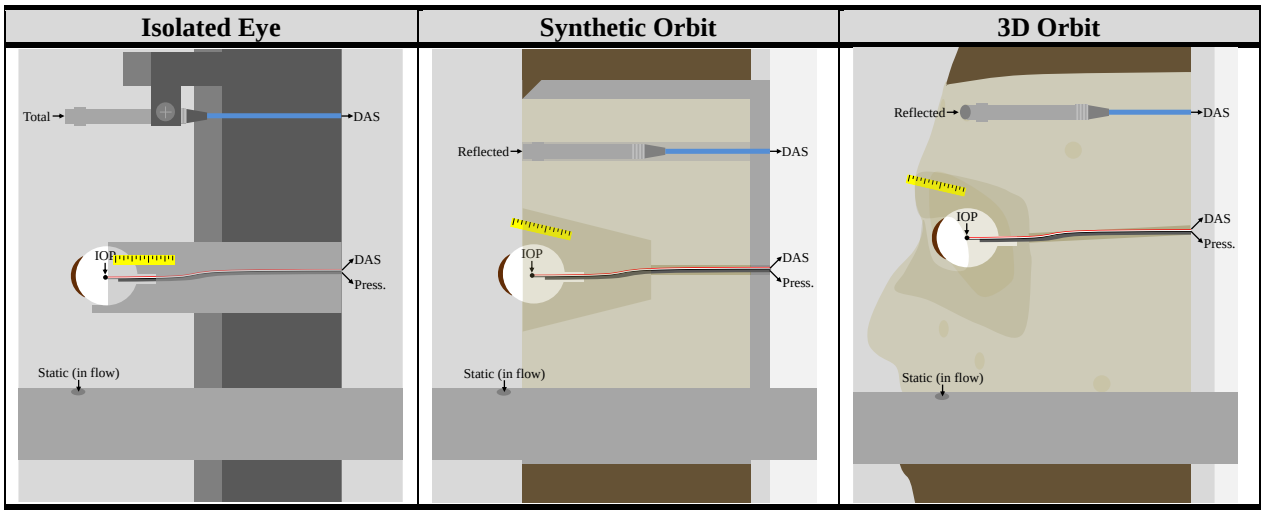

Figure 22. Pressure measurement locations for experimental setups.

Additionally, a pressure sensor inside the driver of the ABS measured membrane rupture pressure, and three sensors were mounted flush with the inside wall of the tube, 12 inches apart from each other, with the middle sensor at the test region to measure static overpressure along the wall of the tube. The middle of these three sensors was used for comparison to "empty tube" tests that were completed before testing each day to ensure the test pressure level was within specification. Information for all sensors used in this test series is summarized in **Table 11**.

Table 11. Pressure Sensors used for Experimental Tests.

Pressure Location	Pressure Sensor Information		
	Company	Model #	Pressure Range (psi)
Intraocular	PMC*	060, 060s	100
Static (in flow)	PCB†	137A24	250
Total, Reflected, Facial	PCB†	113B21	200
Driver	Endevco‡	8510B	500
Static (along wall)	PCB†	102B16	100

*Precision Measurement Company (Ann Arbor, MI, USA)
†PCB Piezotronics (Depew, NY, USA)
‡Meggitt Sensing Systems (Irvine, CA, USA)

All data were collected at 301.887 kHz (TDAS PRO, Diversified Technical Systems, Inc., Seal Beach, CA). The standard TDAS PRO anti-aliasing filter was bypassed because the frequency content of the blast overpressure exceeded the 4,300 Hz cutoff frequency. However, the TDAS PRO sensor input modules (SIMs) bandwidth of 0-25 kHz acts as a low-pass filter with a frequency cutoff of 25 kHz. All pressure data were zeroed prior to the event. High speed video of each test was captured at 20 kfps (v9.1, Vision Research, Wayne, NJ). Movement of a string

hung from the top of the tube located near the eye was used to quantify the time of arrival of the shock wave using high speed video analysis.

A custom MATLAB® (version 7.11.0.584 (R2010b), The MathWorks, Inc., Natick, MA) script was used to quantify the shock wave characteristics of each pressure sensor location (time of arrival, peak overpressure, positive duration, and positive impulse). Pressure measured inside the driver was used to quantify the time at which the membrane burst, which was considered t=0. Time of arrival (ToA) for each sensor location was based on the time of membrane rupture. Peak overpressure was defined as the maximum pressure value recorded during the test. Positive duration was defined as the time interval between initiation of positive overpressure and the time at which overpressure returned to zero. Impulse was defined as the area under the positive portion of the pressure- time history. Impulse was calculated using trapezoidal integration of the pressure trace over the positive duration. **Figure 2** graphically illustrates these parameters using an idealized Friedlander pressure waveform. A one-way ANOVA was conducted on the average peak IOP, positive duration, and positive impulse for each boundary condition with tukey-kramer multiple comparison test to determine significance between groups with a $p < 0.05$.

Peak intraocular pressure was correlated to peak static overpressure measured at the wall and within the flow field. Peak intraocular pressure was also correlated to peak total (isolated eye test condition only) or peak reflected overpressure (synthetic and 3D orbit conditions only). Further, peak static pressure measured at the wall was correlated to peak overpressure measured in the fluid flow. Average ± standard deviation of all the shock wave parameters (time of arrival, peak overpressure, positive duration, and positive impulse) were quantified for each sensor location and are tabulated in **Appendix B**.

Injuries were assessed in two ways. First, gross dissection of each eye following the test was used to quantify physical damage to the tissues and structures of the eye. Second, injury risk for physiologic injuries was calculated using the peak intraocular pressure measured for each test. Specific methods for each of these techniques are described below in further detail.

All eyes were dissected using the following technique. The cornea and sclera were examined for damage. Fluorescein dye was reapplied to the cornea and a blue light was used to help visualize any new corneal abrasions incurred during preparation and testing. The cornea was cut off to

expose the iris and anterior portion of the lens. The iris was cut away to expose the anterior sides of the ciliary body, zonules, and lens. Damage to these structures was noted. Using a surgical microscope, damage to the zonules was further assessed by gently pushing on the lens with a q-tip and tugging on iris flap contralateral to the zonules being examined. The eye was then bisected to expose the retina and the posterior sides of the ciliary body and lens. A dissection microscope was used to magnify and examine these structures in detail, as many were not visible to the naked eye. Photographs were taken of each step of the dissection. Any damage that may have been caused by dissection techniques was noted.

Injury risk curves exist for the prediction of hyphema, lens damage, retinal damage, and globe rupture using normalized energy [62]. Normalized energy is the parameter required to calculate eye injury risk using published injury risk curves developed for projectile impacts. Normalized energy is defined as the kinetic energy of an impacting object divided by the projected area of the object. Neither kinetic energy nor projected area could be calculated for blast scenarios because blast is inherently different from projectile impact. Therefore, NE was quantified using three published correlations between IOP and NE that were developed based on projectile impacts to the eye [36]. Normalized energy was quantified for each of the three correlations based on the projectile diameters: 6.35 mm, 9.25 mm, and 11.15 mm. As the current test series was designed to study the effect of blast on an unprotected eye, the 11.15 mm diameter projectile correlation was used for the final injury risk prediction. This was chosen because the area of an open eye affected by a blast, i.e., the area of the eye not covered by the eyelid, is most similar to the projected area of the 11.16 mm diameter rod. However, the two remaining correlations were also used to predict injury risk for comparison and to provide a more conservative injury risk prediction.

High speed videos were analyzed for displacement of the cornea as well as anterior-posterior translation of the entire orbit. Frame-by-frame analysis of the high speed video was conducted for a handful of tests at each pressure level. A minimum of five ink-printed dots on the sclera (chosen in a cross pattern) as well as several locations along anatomical structures of the surface of the cornea were selected for analysis. The location of these points was manually tracked for the first 3 ms of the test event (30 frames). The movement patterns were plotted on top of the first frame of this analysis.

Computer-aided design (CAD) geometries of the small VT ABS with the Driver and EWE as well as the three boundary conditions used in this experimental study were created for future computational model validation purposes (Autodesk Inventor Professional 2013, Autodesk Inc., San Rafael, CA, USA). These files can be provided by the author upon request. While these did not include the geometry for the eye, they did include the pencil sensor used for static overpressure measured in the flow, as well as the PoS for the synthetic and 3D orbit test conditions. Images of the CAD geometries are shown in **Figure 23**.

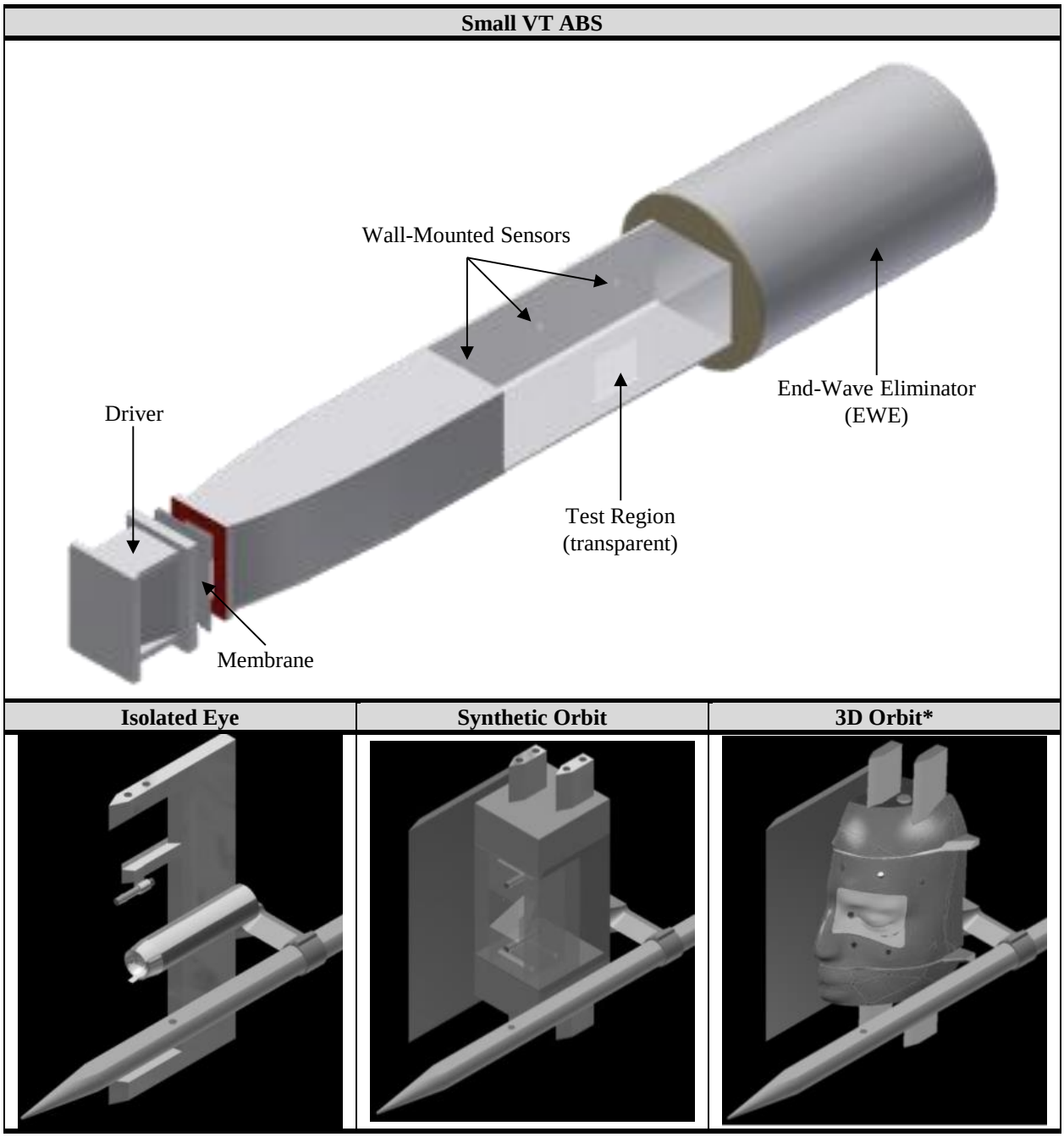

*GHBMC facial geometry from Philip J. Brown.

Figure 23. CAD geometries of experimental test setups.

Results

Evaluation of Test Condition Biofidelty using the Synthetic Orbit

Static and reflected overpressure-time histories for each pressure level of the biofidelity tests using the synthetic orbit are shown in **Figure 24**. The lack of the PoS created the most different response measured by the static sensors as compared to the empty tube tests, as can be seen by the second peak in static overpressure around 0.4 ms for these tests. Neither the addition of the PoS or the extension blocks changes the response of the static overpressure compared to the empty tube tests. Therefore, all final tests were conducted using the PoS and extension blocks.

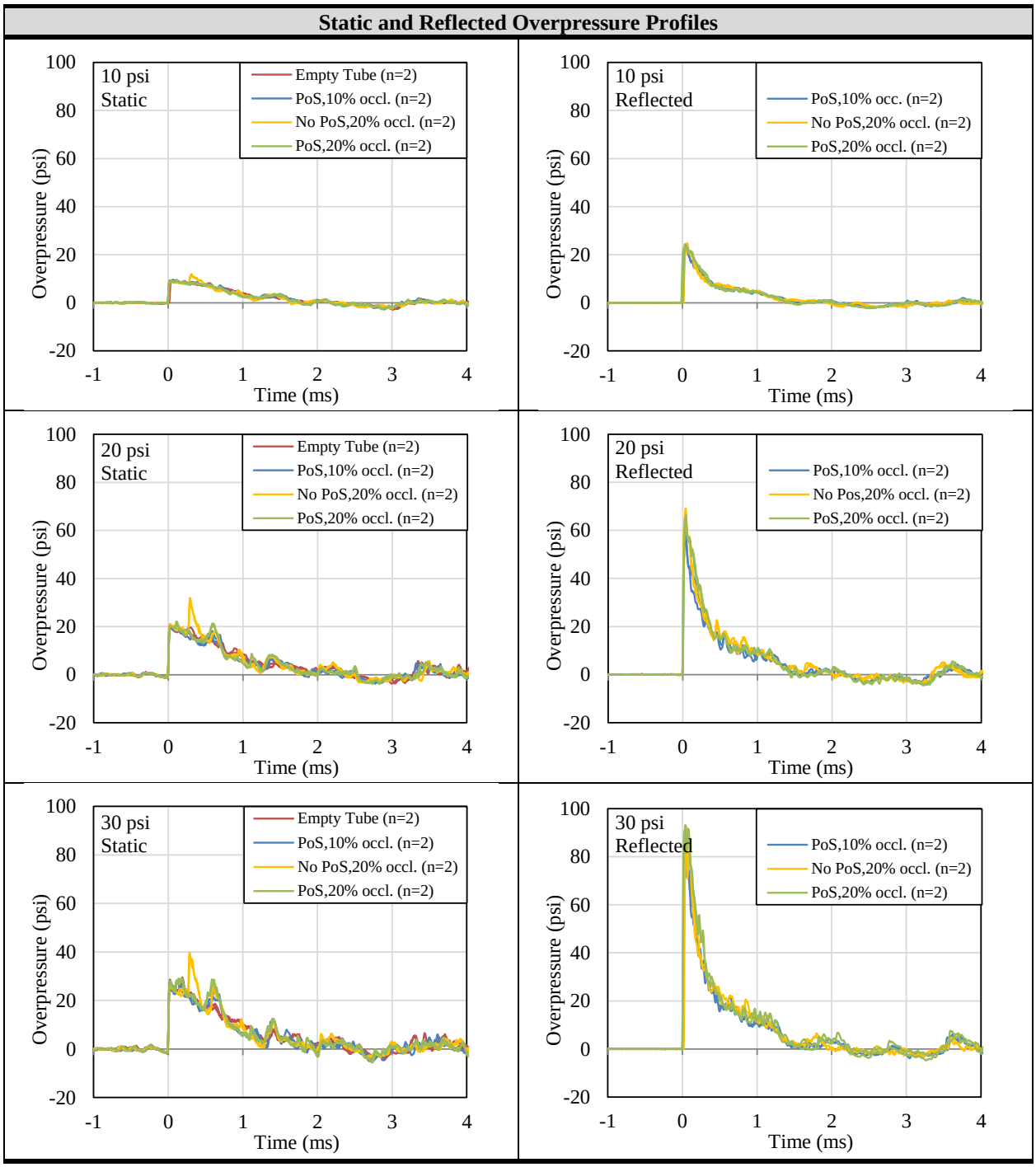

Figure 24. Pressure-time histories for the synthetic orbit biofidelity tests.

Evaluation of Boundary Condition Tests for Final Test Matrix

The PoS and blocks were used for all tests in the final matrix because they did not adversely affect the static or reflected overpressure traces. Overall, peak overpressures increased as the test pressure level increased for all three boundary conditions. Average ± 1 standard deviation pressure-time histories for static (in flow), and total or reflected overpressure are shown for each boundary condition in **Figure 25**. A secondary peak at ~0.25 ms in the static overpressure trace was exacerbated with the addition of the PoS for the synthetic and 3D orbits. Average ± 1 standard deviation pressure-time histories for IOP are shown for each boundary condition in **Figure 26**. Correlations between peak overpressure (static, total, and reflected) and peak IOP are shown for each test condition in **Figure 26**. Correlations between static overpressure measured at the wall and static overpressure measured in the fluid flow are shown in **Figure 27**.

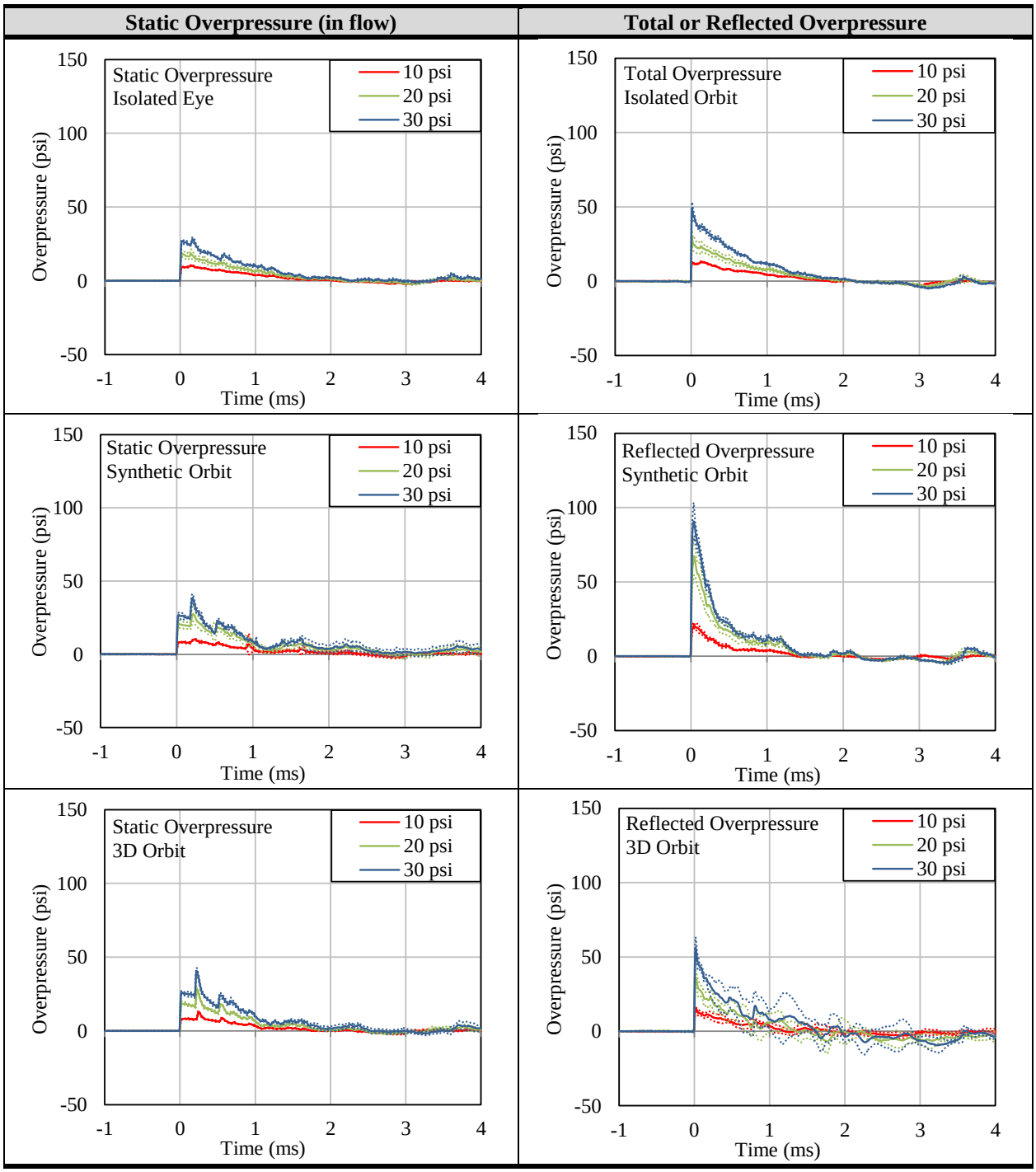

Figure 25. Static (in flow), total, and reflected overpressure - unprotected porcine eye tests.

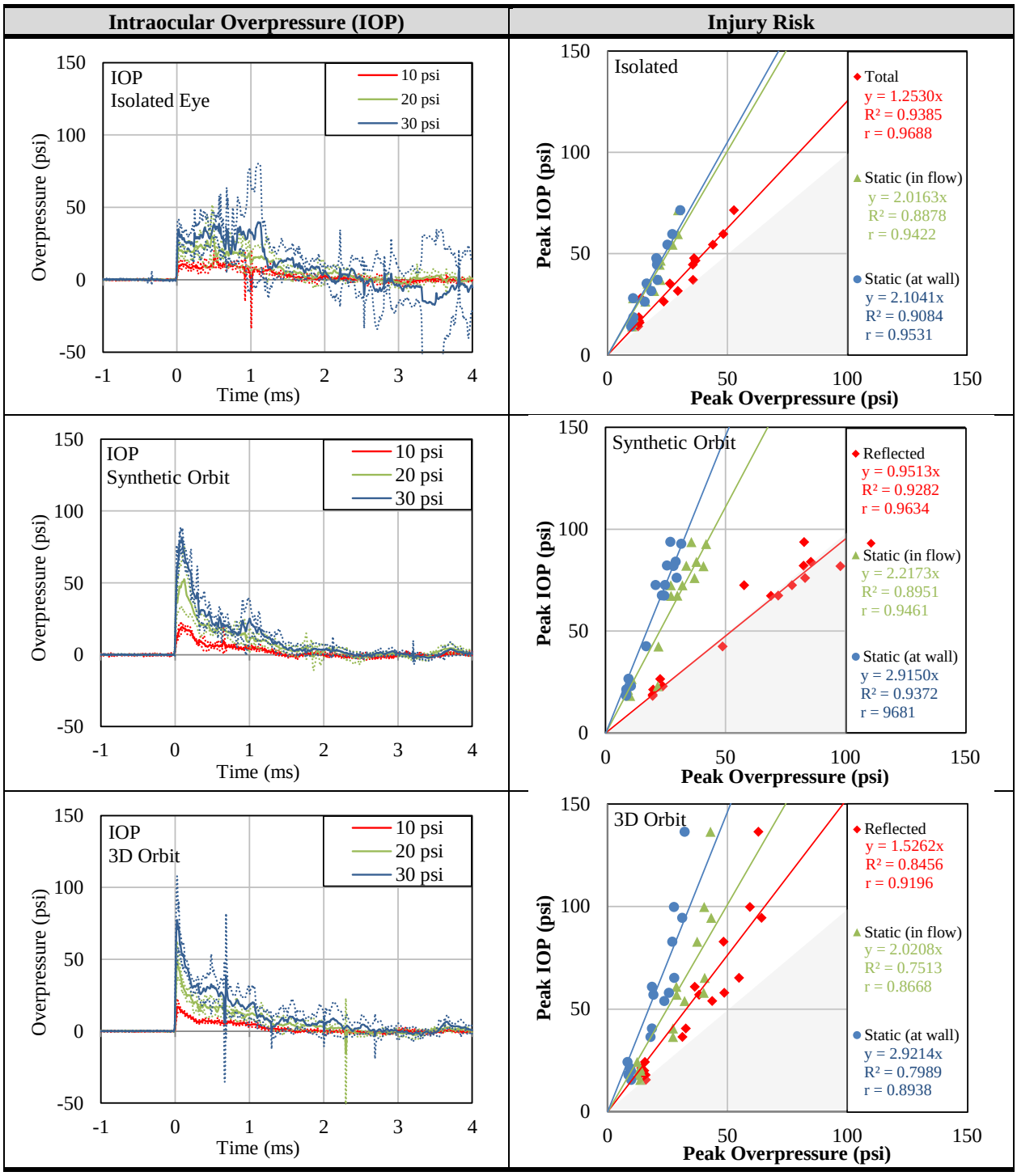

Figure 26. Intraocular overpressure for unprotected porcine eye tests with correlations.

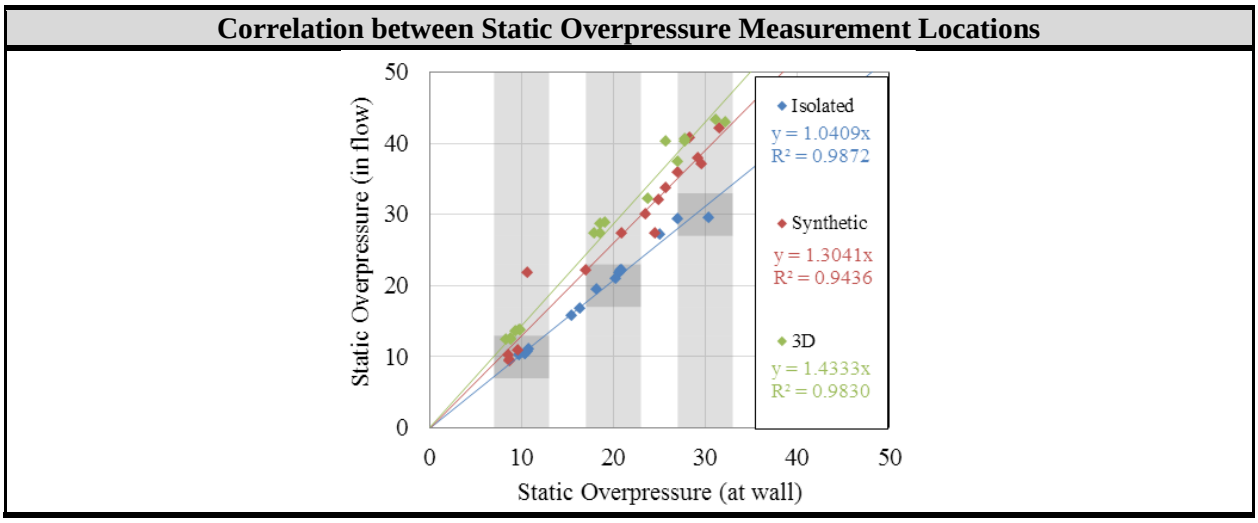

Figure 27. Correlations between static overpressure measured at two locations.

Exemplar images for the synthetic orbit tests showing point tracking are shown in **Figure 28**. Deflection of the cornea was less than 3 mm for all tests. Movement of the gelatin surrounding the eye in the 3D orbits made analysis of the high speed videos for the 3D orbit tests difficult. Notably, there was rippling on the surface gelatin which made it impossible to accurately locate the ink-printed dots on the sclera (**Figure 29**). Overall, results of the video analysis were inconclusive because of the lack of large deformations in the corneal or scleral tissues.

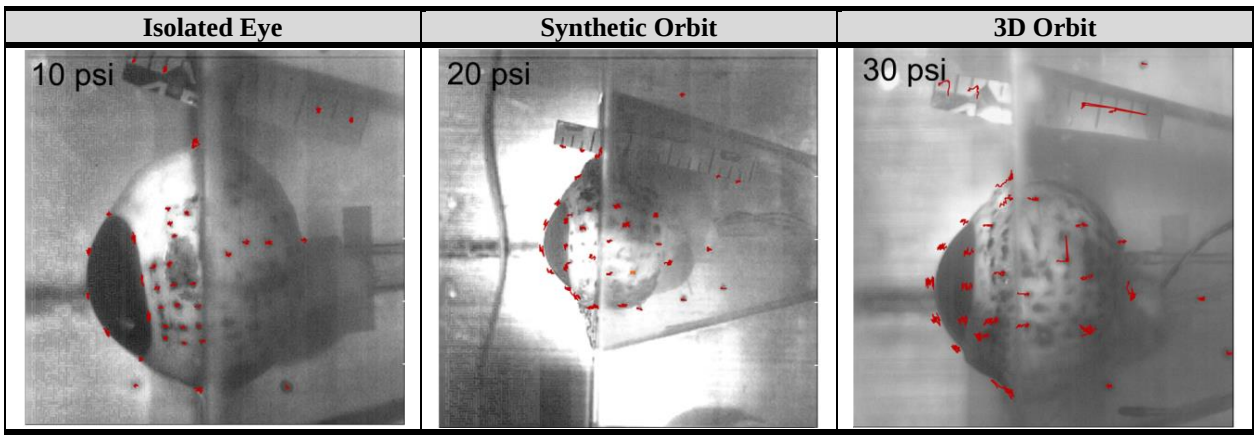

Figure 28. Typical photographs from high speed video analysis for synthetic orbit.

Unprotected Eye		
t = 0μs	t = 400μs	t = 800μs

Figure 29. Still images from high-speed video of the 30 psi blast with the unprotected eye.

Full injury summaries for all tests are tabulated in **Appendix C**. A number of the injuries observed at the lens and ciliary body upon dissection were incurred during dissection, and are noted as such in this summary. Due to the low number of eyes with reported injuries, significant differences between the proportion injured sham eyes and the proportion of injured test eyes could not be accurately quantified. **Figure 30** shows images from a typical dissection. Due to rapid postmortem degradation, retinal damage was present in all eyes and was therefore not correlated to exposure to blast overpressure. **Figure 31** shows three photographs of the retinal folds and partial retinal detachments observed in control eyes. No major injuries were recorded as being caused by primary blast overpressure exposure.

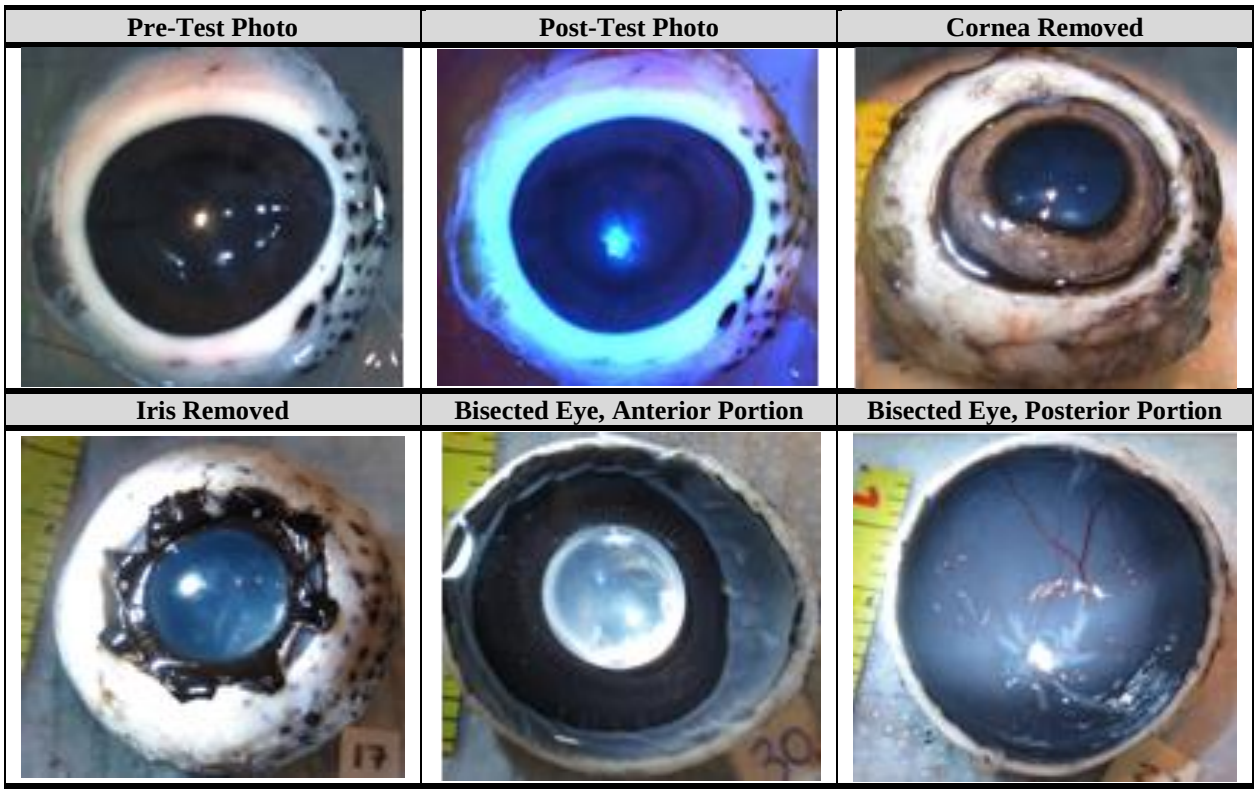

Figure 30. Typical photographs from porcine eye dissection.

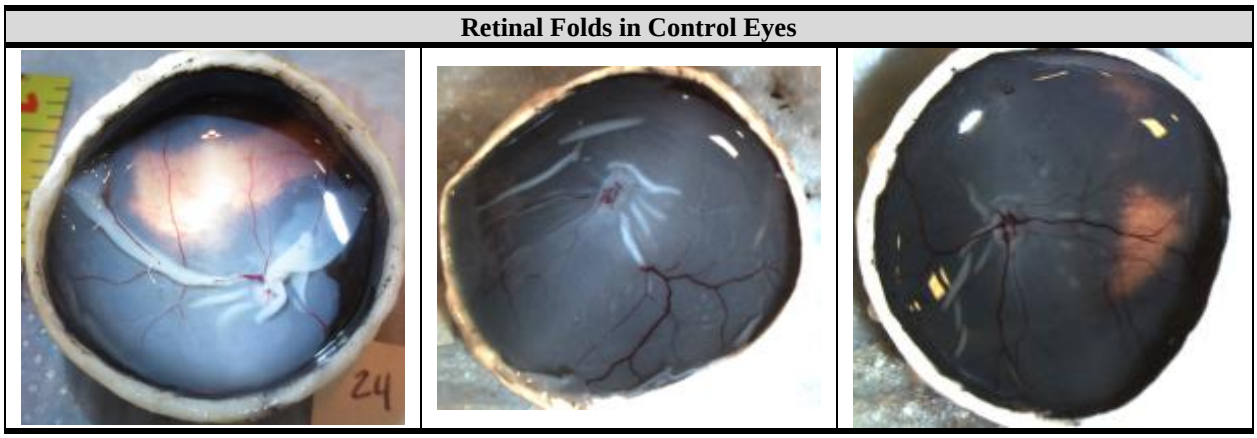

Figure 31. Retinal folds in control eyes.

Predicted injury risk was <5% for all eye injuries in all test conditions at all overpressure levels tested, calculated using peak IOP and the 11.16mm correlation between IOP and NE. **Figure 32** shows the peak shock wave parameters (peak IOP, positive duration, and positive impulse) for all three boundary conditions. Peak IOP was significantly higher for the synthetic orbit than for the isolated eye at the 20 psi level. Positive duration and positive impulse were not significantly different for any of the boundary conditions. **Figure 33** shows the injury risk for hyphema for the three boundary conditions. Significant differences are noted with an asterisk. **Table 13**

shows the average ± standard deviation for injury risk calculated for hyphema, lens damage, retinal damage, and globe rupture using the largest correlation.

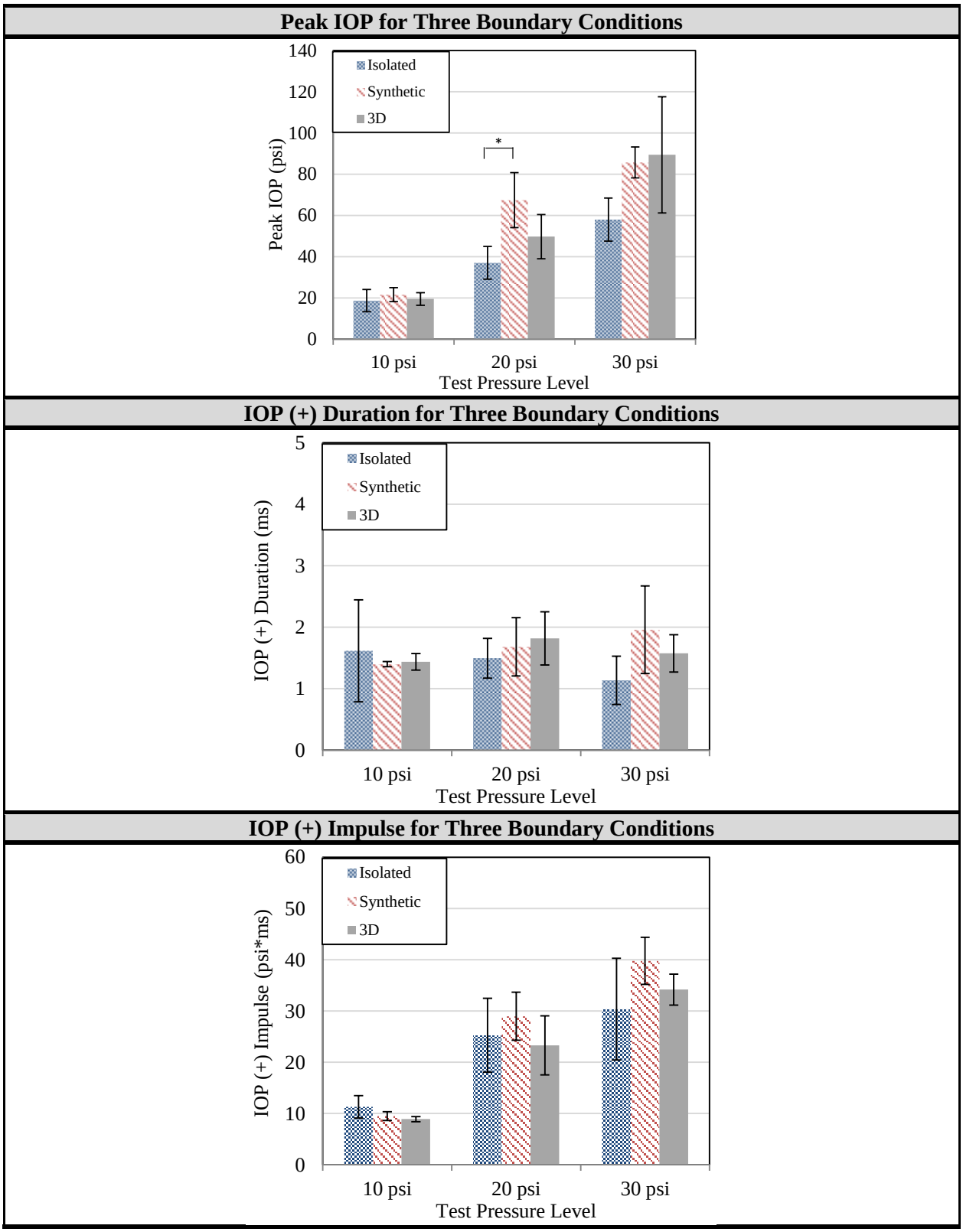

Figure 32. Peak shock wave parameters for three ocular boundary conditions.

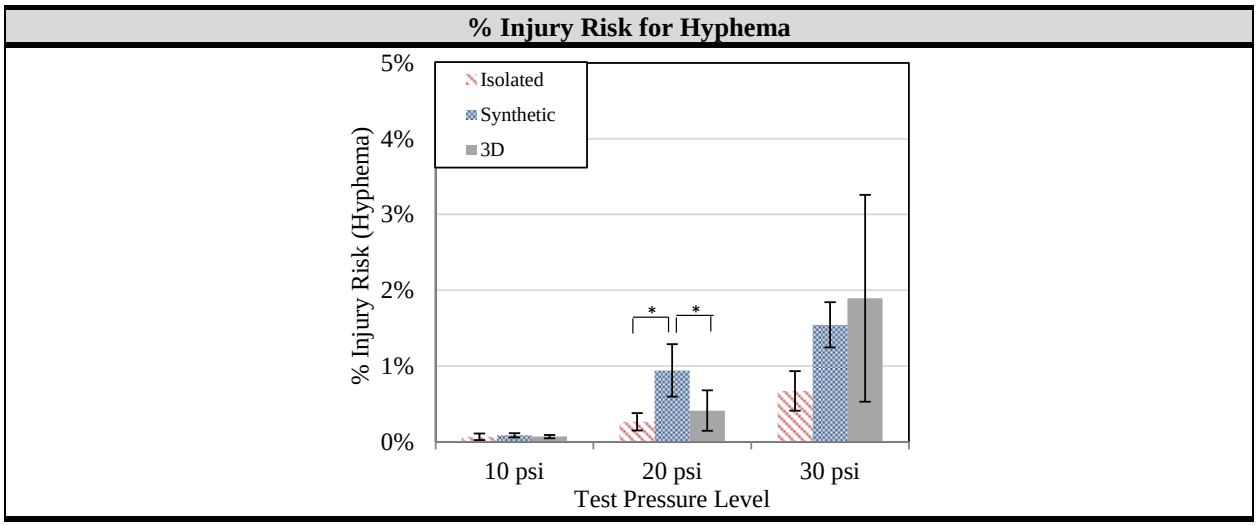

Figure 33. Injury risk for hyphema for three boundary conditions.

Table 12. Predicted injury risk percent using 11.15 mm diameter aluminum rod correlation (avg ± stdev).

	Hyphema	**Lens Damage**	**Retinal Damage**	**Globe Rupture**
	% Injury Risk	% Injury Risk	% Injury Risk	% Injury Risk
Isolated				
10 psi	0.07 ± 0.04	0.00 ± 0.00	0.00 ± 0.00	0.00 ± 0.00
20 psi	0.26 ± 0.12	0.00 ± 0.00	0.00 ± 0.00	0.00 ± 0.00
30 psi	0.67 ± 0.26	0.00 ± 0.00	0.00 ± 0.00	0.00 ± 0.00
Synthetic				
10 psi	0.09 ± 0.03	0.00 ± 0.00	0.00 ± 0.00	0.00 ± 0.00
20 psi	0.94 ± 0.35	0.00 ± 0.00	0.00 ± 0.00	0.00 ± 0.00
30 psi	1.54 ± 0.30	0.01 ± 0.00	0.01 ± 0.00	0.00 ± 0.00
3D				
10 psi	0.07 ± 0.02	0.00 ± 0.00	0.00 ± 0.00	0.00 ± 0.00
20 psi	0.49 ± 0.21	0.00 ± 0.00	0.00 ± 0.00	0.00 ± 0.00
30 psi	1.89 ± 1.37	0.01 ± 0.02	0.02 ± 0.03	0.00 ± 0.00

Only when using the 6.35mm correlation does injury risk increase above 5% (for hyphema only), which is the most conservative prediction. Injury risk for lens damage, retinal damage, and globe rupture are virtually non-existent at these overpressure levels for even the most conservative prediction. **Table 13** and **Table 14** show the average ± standard deviation for injury risk predicted for hyphema, lens damage, retinal damage, and globe rupture using the correlations developed with medium and small impactors for comparison, respectively.

Table 13. Predicted injury risk percent using 9.25 mm diameter aluminum rod correlation.

	Hyphema	Lens Damage	Retinal Damage	Globe Rupture
	% Injury Risk	% Injury Risk	% Injury Risk	% Injury Risk
Isolated				
10 psi	0.02 ± 0.01	0.00 ± 0.00	0.00 ± 0.00	0.00 ± 0.00
20 psi	0.10 ± 0.05	0.00 ± 0.00	0.00 ± 0.00	0.00 ± 0.00
30 psi	0.34 ± 0.18	0.00 ± 0.00	0.00 ± 0.00	0.00 ± 0.00
Synthetic				
10 psi	0.02 ± 0.01	0.00 ± 0.00	0.00 ± 0.00	0.00 ± 0.00
20 psi	0.54 ± 0.25	0.00 ± 0.00	0.00 ± 0.00	0.00 ± 0.00
30 psi	1.06 ± 0.29	0.00 ± 0.00	0.00 ± 0.00	0.00 ± 0.00
3D				
10 psi	0.02 ± 0.01	0.00 ± 0.00	0.00 ± 0.00	0.00 ± 0.00
20 psi	0.22 ± 0.12	0.00 ± 0.00	0.00 ± 0.00	0.00 ± 0.00
30 psi	1.57 ± 1.60	0.01 ± 0.02	0.02 ± 0.03	0.00 ± 0.00

Table 14. Projected injury risk percent using 6.35 mm BB diameter correlation.

	Hyphema	Lens Damage	Retinal Damage	Globe Rupture
	% Injury Risk	% Injury Risk	% Injury Risk	% Injury Risk
Isolated				
10 psi	0.36 ± 0.24	0.00 ± 0.00	0.00 ± 0.00	0.00 ± 0.00
20 psi	1.52 ± 0.70	0.01 ± 0.01	0.01 ± 0.01	0.00 ± 0.00
30 psi	4.11 ± 1.70	0.05 ± 0.04	0.07 ± 0.06	0.00 ± 0.00
Synthetic				
10 psi	0.46 ± 0.16	0.00 ± 0.00	0.00 ± 0.00	0.00 ± 0.00
20 psi	5.89 ± 2.27	0.11 ± 0.07	0.15 ± 0.09	0.00 ± 0.00
30 psi	9.93 ± 2.03	0.30 ± 0.13	0.39 ± 0.16	0.00 ± 0.00
3D				
10 psi	0.37 ± 0.12	0.00 ± 0.00	0.00 ± 0.00	0.00 ± 0.00
20 psi	2.94 ± 1.31	0.02 ± 0.02	0.04 ± 0.03	0.00 ± 0.00
30 psi	12.27 ± 9.10	0.78 ± 1.25	0.91 ± 1.36	0.00 ± 0.01

Discussion

Effects of Plane of Symmetry and Occlusion Area on Pressure Profiles

Neither the addition of the PoS or maximum occlusion area negatively affected the response of the system as compared to the empty tube. Therefore, all tests in the final matrix using porcine eyes in the synthetic and 3D orbits used both the PoS and the maximum allowable occlusion area (20%) in the form of extension blocks that simulated the forehead and chin. Notably, tests conducted with the PoS recorded a secondary peak in static overpressure (in flow) at ~0.25 ms that was not observed in the empty tube tests. This secondary peak is shown in the pressure traces shown in **Figure 25**. This peak was caused by reflection of the pressure wave off the side of the orbit to the wall of the ABS, and back to the orbit. The pressure traces for the 10% and

20% occlusional areas did not vary considerably, indicating that the addition of the forehead and chin blocks did not inhibit the shock wave response.

Pressure Level and Injury Risk

Injury risk increased as test pressure level increased for all three boundary conditions. Injury risk was highest for the synthetic orbit. The low predicted injury risk was consistent with the lack of injuries observed upon dissection.

This study used extreme care to isolate the shock wave to assess primary blast overpressure by preventing fragmentation of the membrane. Many shock tube studies use acetate membranes which are frangible and potentially cause secondary blast injuries in addition to primary blast injuries. High speed video was used to note if anything potentially impacted the eye. Tests in which the eye was "impacted" by a string that was placed near the eye to quantify the shock wave time of arrival. Tests were omitted from the final matrix only in cases where this "impact" resulted in an increase in the IOP, as this increase would not be observed *in theatre*.

This study is the first of its kind to both quantify gross injury to the eye and predict physiologic eye injury risk from primary blast overpressure exposure. A previous study used a similar test matrix to expose enucleated porcine eyes potted in plastic orbits to a single overpressure event at 10 psi, 20 psi, or 30 psi within the expansion cone of a standard gas-driven shock tube [46]. Results from the current study are consistent with results from the published study, i.e., at the pressure levels tested, no severe eye injuries were noted to be caused by primary blast overpressure. Similarly, neither study rules out the possibility that primary blast overpressure exposure could potentially affect the eye and visual system. However, there are discrepancies in the interpretation of the injury results garnered from each study. Notably, retinal damage was observed in eyes used for both studies. While the published study indicated that retinal damage may have been caused by exposure to primary blast overpressure exposure, it was noted in the current study that all eyes, including control eyes, had some degree of retinal folding or detachment at the macroscale level. Furthermore, postmortem retinal degradation has been previously been documented [63]. Despite the use of ultrasound biomicroscopy, which was used to exclude pre-damaged tissue in the published study, the observed damage at the macroscale level makes it difficult, if not impossible, to accurately correlate retinal injury to primary blast

overpressure exposure. Therefore, retinal damage was excluded from potential injuries caused by primary blast for the current study. A notable difference in the current study was the addition of a pressurization system and use of a miniature pressure sensor for constant IOP measurement throughout the duration of the test. This allowed for the prediction of physiologic injuries using published injury risk functions that could not otherwise be quantified in either study. The published study only pressurized the eye through the anterior chamber prior to testing, which could further account for some of the damages observed (e.g., angle recession).

Correlations between Sensor Locations

Peak IOP was more similar to peak total or reflected overpressure than to peak static overpressure for all three boundary conditions. This was due to the forward-facing nature of both the eye and total/reflected sensors, which were perpendicular to the propagation of the shock wave. The measurement of pressure in this orientation accounted for both the static and dynamic components of the shock wave; therefore, both IOP and reflected overpressure should be higher than static overpressure. This trend was observed for all boundary conditions, though the correlation was strongest for the synthetic orbit condition, where the correlation between reflected pressure and IOP was nearly 1:1.

Static overpressure measured at the wall of the tube and within the fluid flow was almost identical for the isolated eye test condition, which was due to minimal obstruction to fluid flow for this condition. Effectively, the small occlusion area of the isolated eye provided a minimal reflective surfaces that produce reflections around the eye. Conversely, for the synthetic orbit and 3D orbit, the wall pressure sensor measured a lower static overpressure than static overpressure in the flow. This was caused by the addition of surfaces upon which the shock wave can reflect. The PoS, while providing a more realistic fluid flow condition for the orbit and face itself, created a surface directly across from the static pressure sensor mounted in the wall, which shielded the wall-mounted sensor from reflections. As such, reflections off the orbit and PoS were observed as secondary peaks approximately 0.1 ms after the initial peak only in the static overpressure (in the flow).

Effects of Boundary Condition Biofidelity on Shock Wave Parameters

This study serves as the first of its kind to examine the effects of increasing orbit biofidelity on porcine eye response during survivable blast overpressure exposure. The isolated eye condition allowed for the greatest amount of pressure relief around the eye, as there were minimal reflective surfaces surrounding the eye in the isolated eye test setup. Consequently, of all three boundary conditions, IOP was lowest for the isolated eye. The synthetic orbit produced the highest reflected of the three test setups test due to the fact that the synthetic orbit consisted of a large perpendicular surface upon which the shock wave must reflect. Similarly, the synthetic orbit produced the highest IOP of the three test setups at the 10 psi and 20 psi test levels. While the synthetic orbit and 3D orbit had matched cross-sectional occlusion areas, the curved surface of the 3D orbit allowed the pressure wave to more easily pass around the face. Therefore, the 3D orbit allowed for more pressure relief, which resulted in the lower reflected pressures for all test levels and lower IOP for the 10 psi and 20 psi test levels.

Limitations

A number of limitations are inherent to the tests conducted in the current study. Using cadaveric tissue provides a model to examine gross injury to the tissue and structures of the eye, but cannot be used to quantify physiologic injuries that may be present *in vivo*. This study attempted to account for this limitation by predicting physiologic injuries using peak IOP measured during the test. However, the injury risk curves used for this purpose were originally developed and validated for blunt loading, and have not been extensively validated for blast loading. However, these risk curves provide the only physiologic injury risk assessment method for the current model at this time. Future work developing blast-specific injury risk curves for the eye will provide a more realistic prediction of physiologic blast-related eye injuries.

A porcine model was chosen for the current study due to its anatomical and geometrical similarities to the human eye. The most important difference between the porcine and human eye models is perhaps their structural properties at various loading regimes. It was previously established that the porcine eye is significantly stronger (nearly twice) than the human eye, which is likely due to the greater scleral thickness of the porcine eye in comparison to that of the human eye [41]. The tests conducted to quantify this difference involved statically and dynamically pressurizing human and porcine eyes and measuring the pressure at rupture. As such, it is possible that a human eye would experience greater deflection than a porcine eye

exposed to the same blast test pressure level. Therefore, results in this study potentially underestimate the risk of human eye injury.

The tests in this study were designed to simulate an eye-level, forward-facing blast event. This only accounts for one loading direction, and does not take into account the effect of oblique loading or ground charges, both of which are possible scenarios during combat.

Future Directions

The current study focused on survivable pressure levels. Although no blast-related injuries were observed at these pressure levels, it remains possible that severe eye injuries could be caused by higher pressure levels. However, it is likely that other more life-threating injuries may be caused at the pressure levels required to cause severe eye injuries, making the presence of eye injury comparatively insignificant. It is critical to the development of blast-specific human eye injury risk curves that tolerances and thresholds for the eye and its structures be quantified. This necessitates testing at higher pressure levels and potentially longer durations. Due to the physical limitations of current shock tubes and ABSs, this may only be possible with live-fire testing using high order explosives such as trinitrotoluene (TNT) or C4. Given that the eye is susceptible to injury from projectiles, care should be taken to minimize debris and fragmentation from live-fire tests.

While high-speed video was taken for each test in the current study, the structural response of the eye could not be quantified due to the fact that there was minimal deflection of the tissue at these pressure levels. It is possible that future work with higher pressure levels would create greater deflection that would provide the necessary strains to quantify material properties of the sclera.

Results of this study can be used to develop and validate computational models of the eye specific for blast loading. As a number of CFD and FE models of the eye have already been developed for this purpose, results from the current study provide critical data to validate these models. Once validated, these computational models could be used to more quickly assess a wider array of blast loading conditions, including higher pressure and oblique loading orientations, thus accounting for some of the limitations of the current experimental study.

Conclusions

This study is the first of its kind to assess eye injuries for a porcine eye model exposed to survivable primary blast overpressure levels with increasing biofidelity of the boundary conditions surrounding the eye. Three boundary conditions ("Isolated Eye", "Synthetic Orbit", "3D Orbit") were tested at 10 psi, 20 psi, and 30 psi to examine the effects of both increasing test pressure level and experimental test setup biofidelity on the response of the eye. Care was taken to ensure the experimental test setups maintained a realistic fluid flow. All test setups occluded <20% of the cross-sectional area of the tube. A plane of symmetry (PoS) was added along the nasal side of the synthetic and 3D orbits to prevent unrealistic pressure relief around the nose. Pressure relief around the eye was greatest for the isolated eye due to the lack of large reflective structures surrounding the eye in this condition. The synthetic orbit produced the highest pressures at each test level due to the flat reflective surfaces perpendicular to shock wave propagation. Despite this, all tests resulted in low predicted injury risk. Furthermore, no injuries could be attributed solely to primary blast overpressure. Therefore, it was concluded that at these test pressure levels, eye injury risk is extremely low. Ultimately, these results indicate that boundary condition fidelity is critical to evaluating, modeling, and predicting eye injuries caused by primary blast overpressure exposure. These results expand the field by providing realistic test conditions that can be repeated or modeled for future studies and by adding the prediction of eye injury risk using intraocular pressure.

Chapter 4

Protective Effects of Spectacles and Goggles during Blast Overpressure Exposure

Introduction

Recent military conflicts have relied heavily on improvised explosive devices (IEDs), that often include shrapnel to maximize injuries. Reduced fatality rates in military conflicts have been linked to the use of advanced personal protective equipment (PPE), which is often designed to minimize the effects of ballistics and shrapnel [7]. Despite the availability of protective eyewear, eye injuries occurred in 17% of cases where protective eyewear was used and jumped to 26% when protective eyewear was not used [10]. The incidence of eye injuries that occur even when protective eyewear is used motivates the need to more fully understand primary blast overpressure as an eye injury mechanism for protected eyes.

The United States Army provides soldiers with protective eyewear for use during training and combat. The Authorized Protective Eyewear List (APEL) supplies information on each of the approved spectacles and goggles that are available to personnel. Each pair of eyewear is tested for protection from ballistic impact using rigorous test procedures from the American National Standards Institute (ANSI Z87.1 2010) for occupational safety as well as specific military standards (MIL-PRF 32432). However, eyewear is not currently evaluated or rated for protection during primary blast overpressure exposure. Consequently, there is a need to develop test methods to evaluate the effectiveness of PPE eyewear during blast overpressure loading events.

While initial experimental and computational models suggest eye protection can reduce peak overpressure exposure to the eye, it is imperative to understand the actual ocular response during blast overpressure exposure [64]. However, there is a paucity of experimental data that can be used to validate computational models. Furthermore, the question remains whether spectacles and/or goggles reduce eye injury risk from primary blast. Therefore, the purpose of this study is to quantify eye injury risk when wearing eye PPE, specifically spectacles and goggles, during

primary blast overpressure exposure and evaluate the effectiveness of these PPE by comparing the results to those obtained for the unprotected eye.

Methods

All tests were conducted using the small VT ABS with aluminum membranes prepared as described in Chapter 1 (**Figure 4**). Briefly, this is a helium gas-driven tube specifically designed for testing small specimens, and is able to produce peak overpressures up to approximately 30 psi (static overpressure) with a positive duration around 2.5 ms using aluminum membranes.

A total of 33 porcine eyes were acquired for this study. Fresh porcine eyes were shipped overnight on wet ice, stored in a refrigerator, and tested within three days of slaughter (Animal Technologies, Tyler, TX, USA). Three eyes were tested at the 10 psi and 20 psi levels and five eyes were tested at the 30 psi level for each piece of eyewear. An additional eleven eyes were used as controls (n=8) and shams (n=3). Control eyes were used to assess postmortem effects and damage from tissue procurement. Sham eyes were used to quantify potential injuries from pre-test preparation techniques, including the insertion of a pressure sensor and pressurization into the eye and setting the eye in a rigid concave cup or in gelatin. All eyes were prepared with the following technique. Skin and musculature was removed to expose only the globe and optic nerve. Eyes were identified as left (OS) or right (OD). Cornea clarity was qualitatively assessed (clear, not clear), and visibility of the "Y" suture on the lens was noted. Fluorescein dye was applied to the cornea and a blue light was used to help visualize corneal abrasions. Any existing corneal abrasions were noted. Control eyes were dissected at this point to assess and quantify baseline damage to the eye caused by postmortem degradation and procurement from the abattoir. The remaining eyes were further prepared by applying a dot pattern on the surface of the sclera using permanent black ink. A miniature pressure sensor (Model 060S, 100 psi, Precision Measurement Company, Ann Arbor, MI) and a small tube were inserted through the optic nerve into the vitreous fluid and secured in place using a cable tie. Normal physiologic intraocular pressure (IOP) was provided throughout the duration of the test using a gravity-fed system. Specifically, a bag of Lactated Ringer's solution was connected to the small tube and suspended 8 in. above the eye. Intraocular pressure was measured before and after each test using a veterinary tonometer (Tono-Pen AVIA Vet® Veterinary Tonometer, Reichert

Technologies, Depew, NY, USA). Due to minor variations, measurements were taken using the tonometer until three sequential measurements recorded the same IOP at a 95% confidence.

Test eyes were placed in the 3D orbit described in Chapter 3. Seven facial pressure sensors located around the eye were used to quantify pressure around the face during the event (**Error! Reference source not found.**). These were labeled 'nasal', 'top medial', 'top middle', 'top temporal', 'bottom medial', 'bottom middle', and 'bottom temporal'. All sensing elements were flush with the external geometry of the 3D orbit. The nasal sensor was located adjacent to the eye. The top and bottom sensors are located on the forehead and chin, respectively.

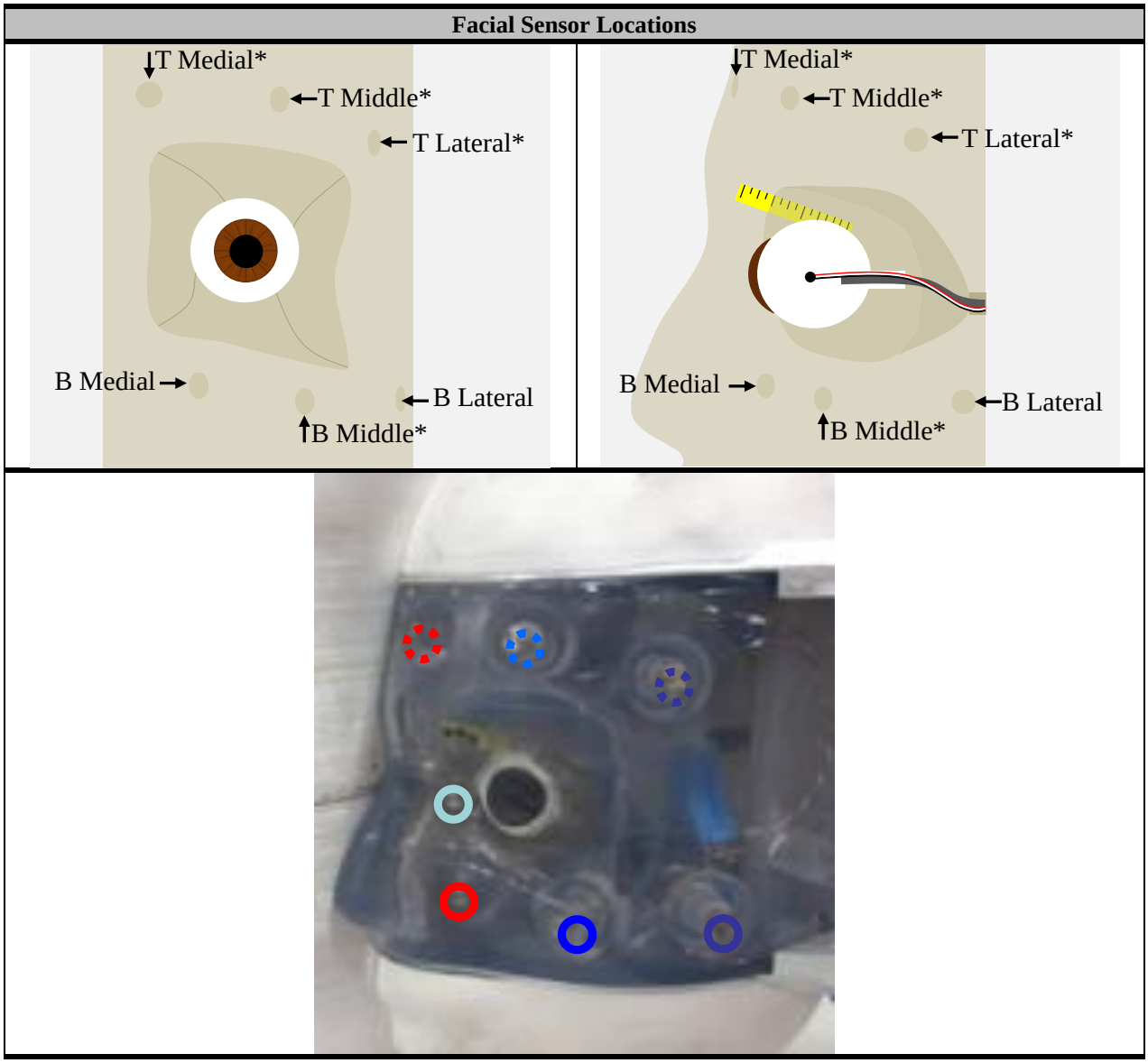

Figure 34. Facial pressure sensor locations for 3D orbit.

One pair of spectacles and one pair of goggles were selected from the Authorized Protective Eyewear List (APEL) provided by the Program Executive Office (PEO Soldier) [65]. The Eye Safety Systems, Inc. (ESS[2]) Crossbow and Profile NVG were chosen because of their popularity as reported through multiple contacts with PEO Soldier (**Figure 35**).

Spectacle: **ESS Crossbow**	**Goggle:** **ESS Profile NVG**
APEL, UPLC Approved	APEL, UPLC Approved
Manufacturer Part Number: 740-0615	Manufacturer Part Number: 740-0127
Cost: $40.00	Cost: $100.00

Figure 35. Spectacles and goggles used for protected porcine eye blast tests.

The spectacles and goggles were placed on the 3D printed orbit that was previously used for the unprotected porcine eye tests (**Figure 36**). A single pair of each the spectacles and goggles was used for all tests. The eyewear was cut in half in order to fit over the 3D orbit and against the plane of symmetry (PoS). As the lens for both the spectacles and goggles was separate from the rim and nosepiece, super glue was used to secure these pieces together. The spectacles and goggles were both rigidly held in place at the bridge of the nose using a screw to attach the lens to a small aluminum block, which was rigidly mounted to the PoS (**Figure 37**). The earpiece of the spectacles was held in place at the temple using a plastic cable fastener. The position of the cable fastener simulated the position above the ear where the spectacles would rest, without the addition of a head strap. The goggles were held in place at the temple by securing the strap to the back of the experimental test setup. Tension on the strap was strong enough for the goggle to remain in contact with the face, but not strong enough to compress the goggles. This preparation technique was developed after a number of users were instructed to adjust the goggles for comfort, as would be done *in theatre*. Additionally, the goggles were placed on the FOCUS headform to compare fit and contact between the goggle and the headforms. While both the ESS

[2] Eye Safety Systems, Inc. (ESS) did not provide financial support for this test series.

Crossbow and ESS Profile NVG are Universal Prescription Lens Carrier (UPLC) compatible, allowing soldiers who require prescription lenses to use this eyewear, all tests were conducted without the prescription lens attachment. The spectacles did not contact any of the seven facial pressure sensors. The goggles contacted five of the facial pressure sensors. The nasal and bottom nasal sensors remain exposed with the goggles in place.

Spectacle: ESS Crossbow	Goggle: ESS Profile NVG

Figure 36. Experimental test setups for protected porcine eye tests.

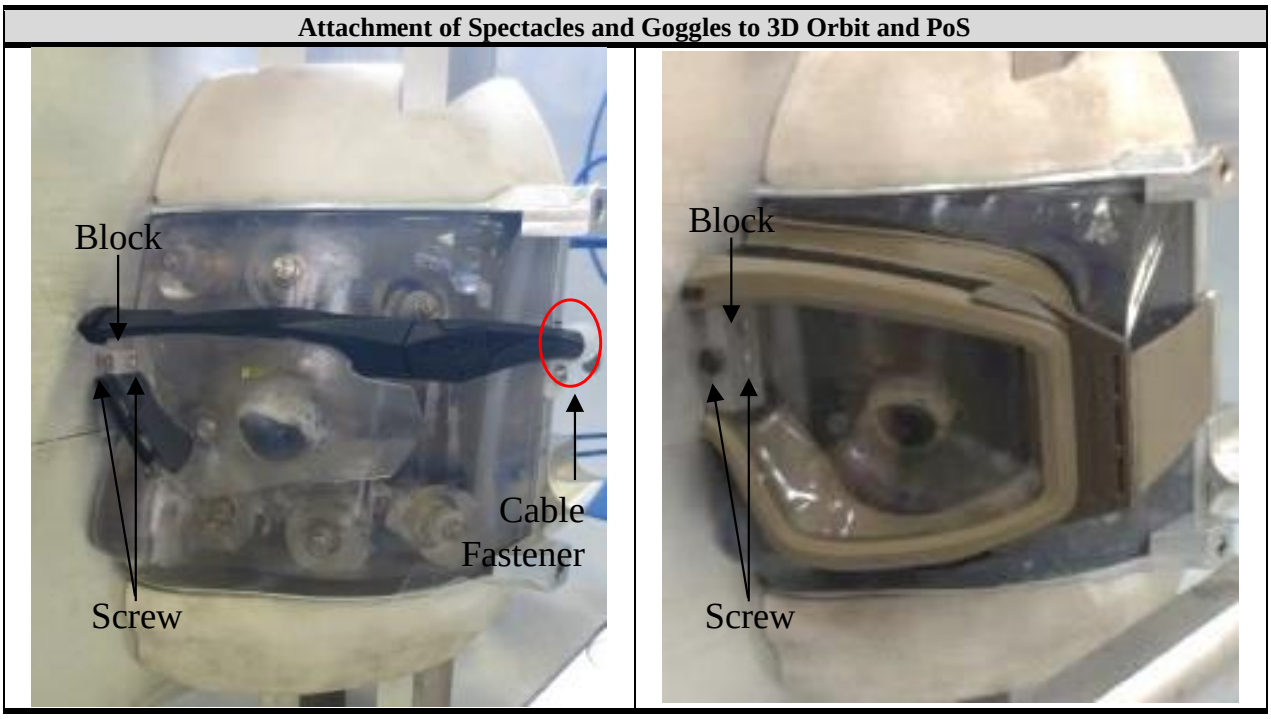

Figure 37. Eyewear contact with face.

Pressure measurement locations are the same as described in Chapter 3. Briefly, static overpressure was measured at three locations along the wall of the tube and at one location in the fluid flow near the test setup, intraocular pressure was measured inside the eye, and intraorbital overpressure was measured at four locations inside the orbit. Additionally, reflected overpressure was measured at six new locations around the face.

All data were collected at 301.887 kHz (TDAS PRO, Diversified Technical Systems, Inc., Seal Beach, CA). The standard TDAS PRO anti-aliasing filter was bypassed because the frequency content of the blast overpressure exceeded the 4,300 Hz cutoff frequency. However, the TDAS PRO sensor input modules (SIMs) bandwidth of 0-25 kHz acts as a low-pass filter with a frequency cutoff of 25 kHz. All pressure data were zeroed prior to the event. High speed video of each test was captured at 20 kfps (v9.1, Vision Research, Wayne, NJ).

A custom MATLAB® (version 7.11.0.584 (R2010b), The MathWorks, Inc., Natick, MA) script was used to quantify the shock wave characteristics at each pressure sensor location (time of arrival, peak overpressure, positive duration, and positive impulse). Using MATLAB®, a one-way ANOVA was conducted on the average peak IOP, reflected overpressure, static overpressure (in the flow), and static overpressure (along the wall) for the spectacles, goggles,

and unprotected 3D orbit tests conducted in Chapter 3 with tukey-kramer multiple comparison test to determine significance between groups with a $p < 0.05$.

Injuries were assessed in two ways. First, gross dissection of each eye following the test was used to quantify physical damage to the tissues and structures of the eye. Second, injury risk for physiologic injuries was calculated using the peak intraocular pressure measured for each test. Specific methods for each of these techniques are described below in further detail.

All eyes were dissected using the following technique. The cornea and sclera were examined for damage. Fluorescein dye was reapplied to the cornea and a blue light was used to help visualize any new corneal abrasions incurred during preparation and testing. The cornea was cut off to expose the iris and anterior portion of the lens. The iris was cut away to expose the anterior sides of the ciliary body, zonules, and lens. Damage to these structures was noted. Using a surgical microscope, damage to the zonules was further assessed by gently pushing on the lens with a q-tip and tugging on iris flap contralateral to the zonules being examined. The eye was then bisected to expose the retina and the posterior sides of the ciliary body and lens. A dissection microscope was used to magnify and examine these structures in detail, as many were not visible to the naked eye. Photographs were taken of each step of the dissection. Any damage that may have been caused by dissection techniques was noted.

Injury risk curves exist for the prediction of hyphema, lens damage, retinal damage, and globe rupture using normalized energy [62]. Normalized energy is the parameter required to calculate eye injury risk using published injury risk curves developed for projectile impacts. Normalized energy is defined as the kinetic energy of an impact divided by the projected area of the impact. As neither the kinetic energy nor the projected area of the impact can be calculated for blast scenarios because blast is inherently different from projectile impact, NE was quantified using published correlations between IOP and NE. Normalized energy was quantified for each of the three correlations based on projectile diameters: 6.35 mm, 9.25 mm, and 11.15 mm [36]. As the current test series was designed to study the effect of blast on an unprotected eye, the 11.15 mm diameter projectile correlation was used for the final injury risk prediction. This was chosen because the area of an open eye affected by a blast is the area of the eye not covered by the eyelid is most closely related to the projected area of the 11.16 mm diameter rod. However, the

two remaining correlations were also used to predict injury risk for comparison and to provide a more conservative injury risk prediction.

Results

Pressure-time histories for all tests with the spectacles and goggles are shown in **Figure 38**, **Figure 39** and **Figure 40**. The unprotected eye IOP time histories from Chapter 3 are included for comparison. Static overpressure time histories for empty tube tests conducted at each pressure level can be found in **Appendix A** for comparison. Peak IOP increased with increasing test level. Compared to the unprotected eye, the recorded pressure pulses for both the spectacles and goggles had a delayed time to peak overpressure. This was observed to a greater extent for the goggles than for the spectacles. Peak IOP decreased with the addition of the spectacles on at the 20 psi and 30 psi test levels. Peak IOP decreased with the addition of the goggles at all three test levels.

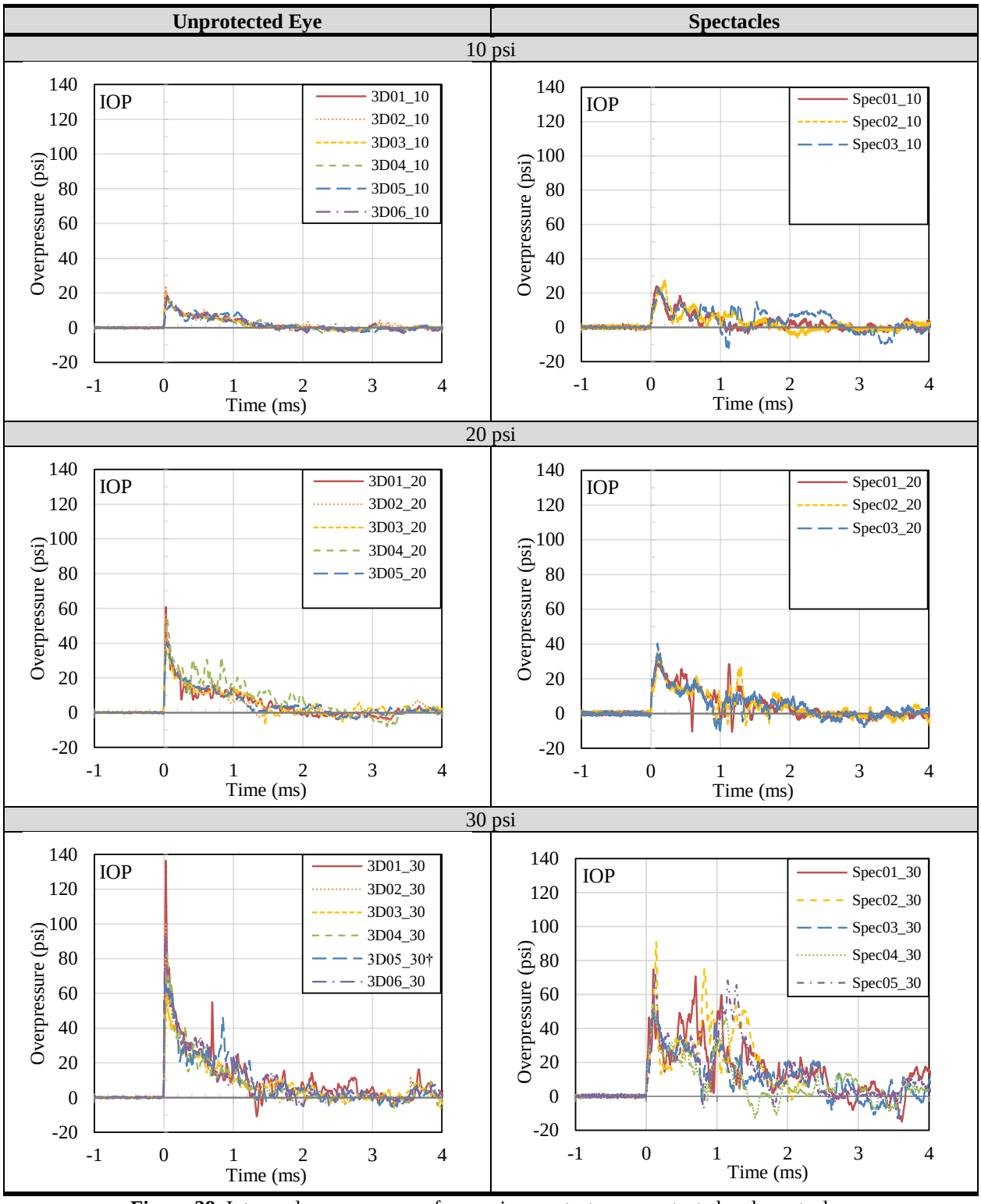

Figure 38. Intraocular overpressure for porcine eye tests – unprotected and spectacles.

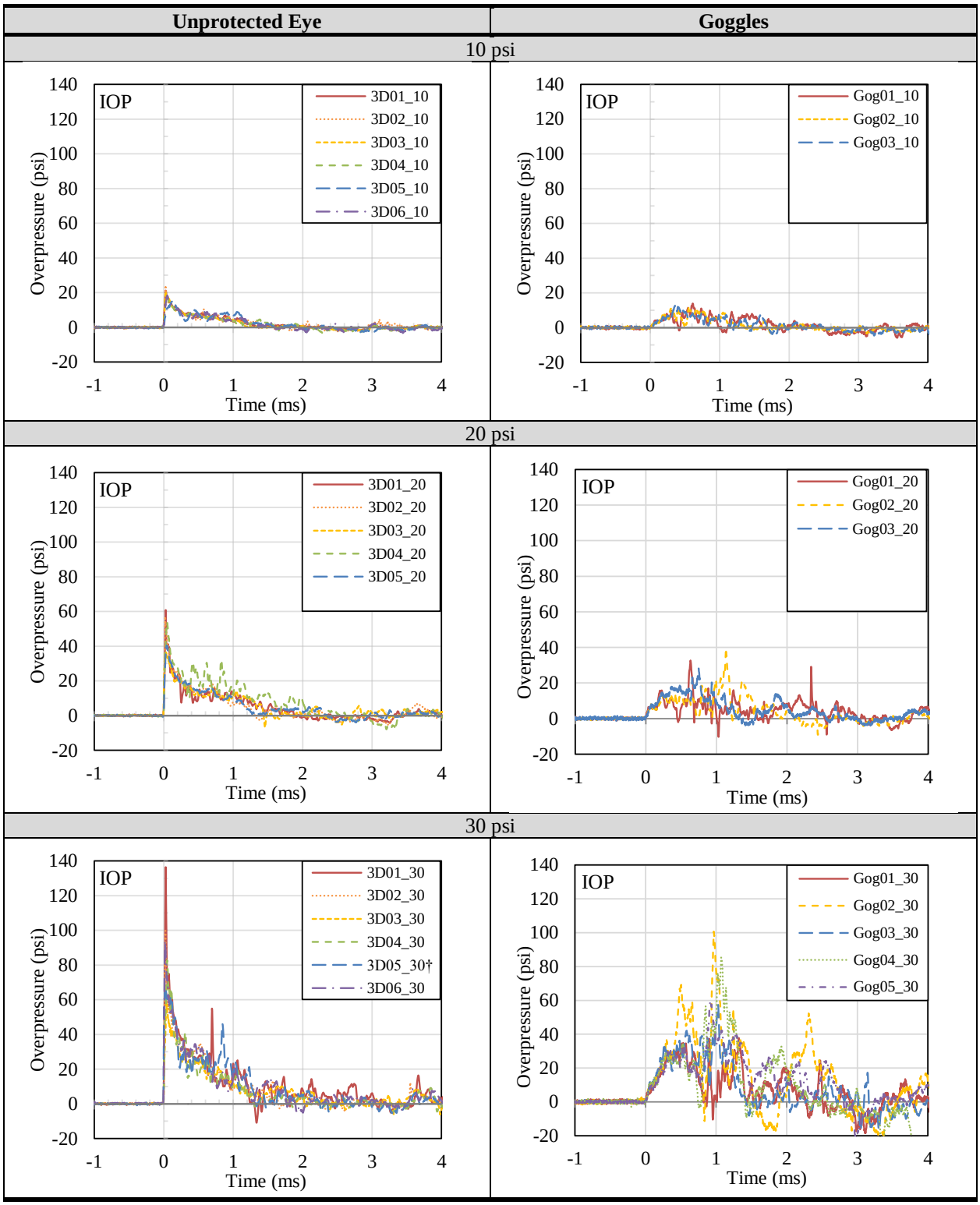

Figure 39. Intraocular overpressure for porcine eye tests – unprotected and goggles.

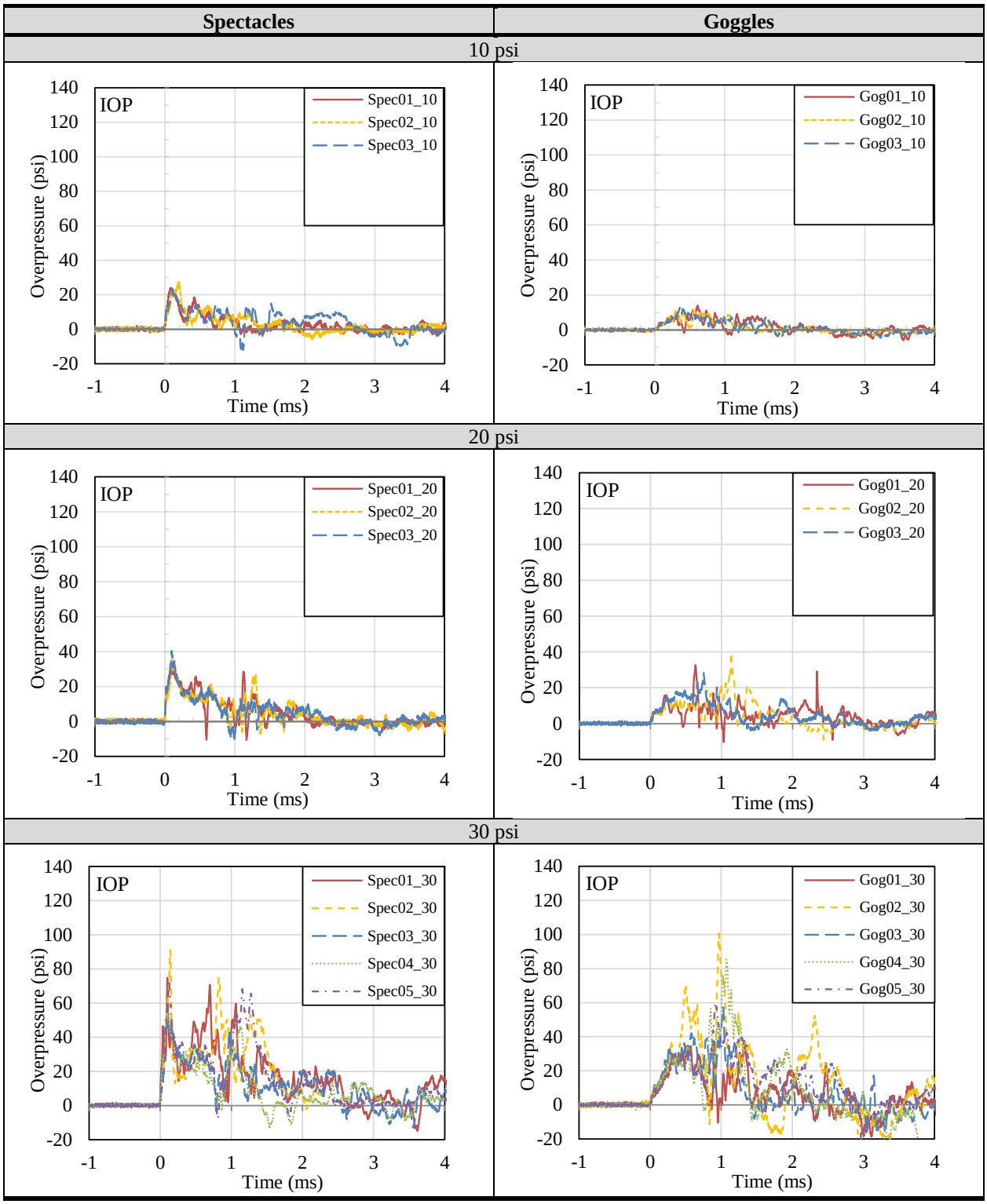

Figure 40. Intraocular overpressure for porcine eye tests – spectacles and goggles.

Figure 41, **Figure 42**, and **Figure 43** respectively show the average peak overpressure, positive duration, and positive impulse for IOP, reflected overpressure, static overpressure (in the flow), and static overpressure (along the wall) for the spectacles, goggles, and unprotected eye test from Chapter 3. Peak overpressure measured at all locations increased with increasing test pressure level for both the spectacles and goggles. The goggles resulted in a greater reduction in peak IOP than the spectacles at all three test levels. Both the spectacles and goggles showed a decrease in peak IOP at the 20 psi and 30 psi levels. However, the reduction in peak IOP at the 20 psi and 30 psi levels was not significantly different from the unprotected eye. The spectacles recorded a significant increase in peak IOP compared to the unprotected eye and the goggles at the 10 psi level. The goggles recorded a significant decrease in peak IOP compared to the unprotected eye and spectacles at the 10 psi level. Generally, positive duration did not vary significantly at each sensor location. Positive duration for the spectacles was significantly lower than the unprotected eye at the 20 psi level for IOP, and significantly higher than the goggles at the 10 psi for reflected overpressure. Similar to peak overpressure, positive impulse showed significant differences at the 10 psi level for all four pressure measurement locations. Positive impulse was higher for the spectacles than the unprotected eye at each pressure measurement location, and was significantly higher than the goggles at the IOP, reflected overpressure, and static overpressure (along the wall) locations.

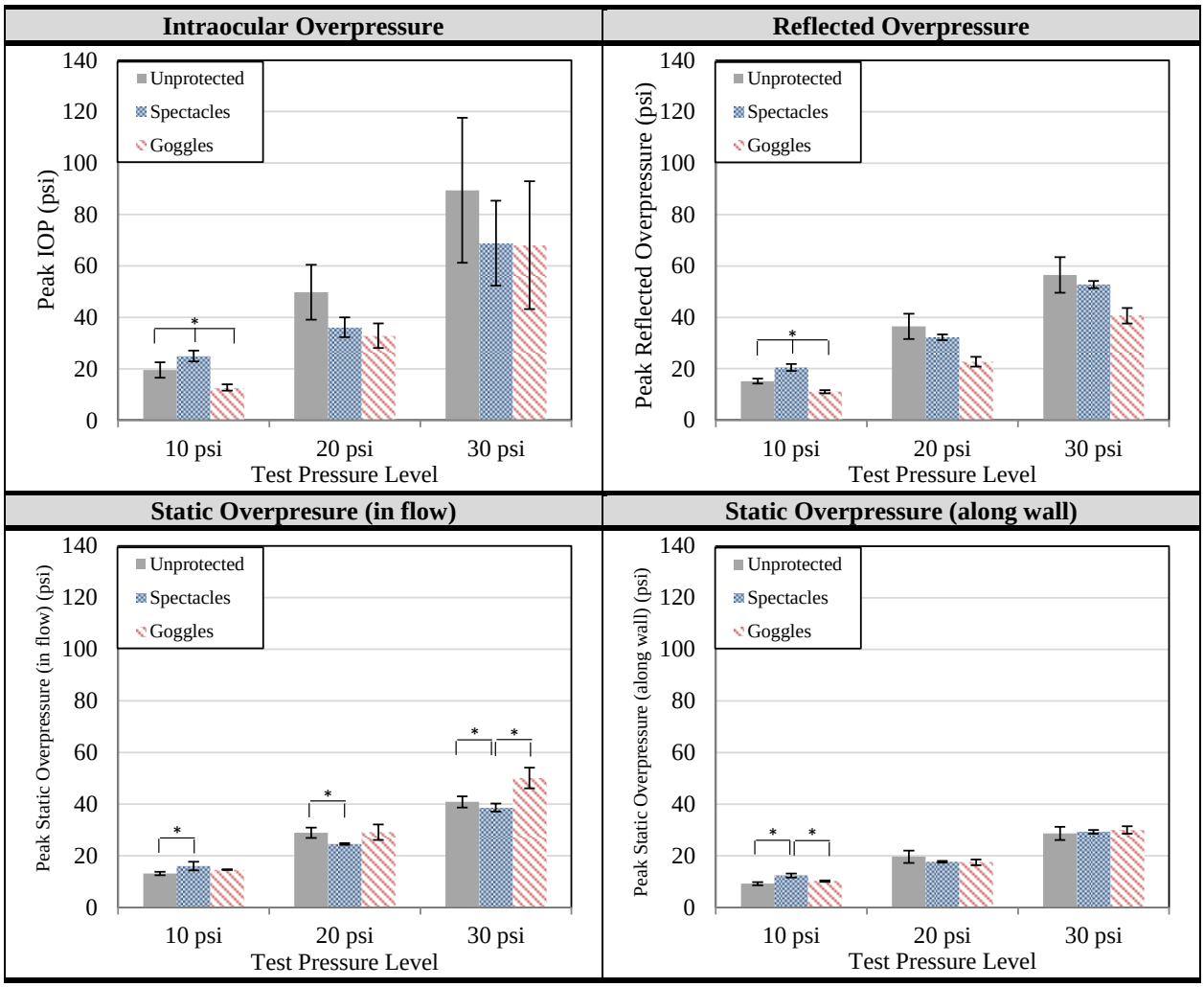

Figure 41. Peak IOP for unprotected and protected porcine eyes during blast.

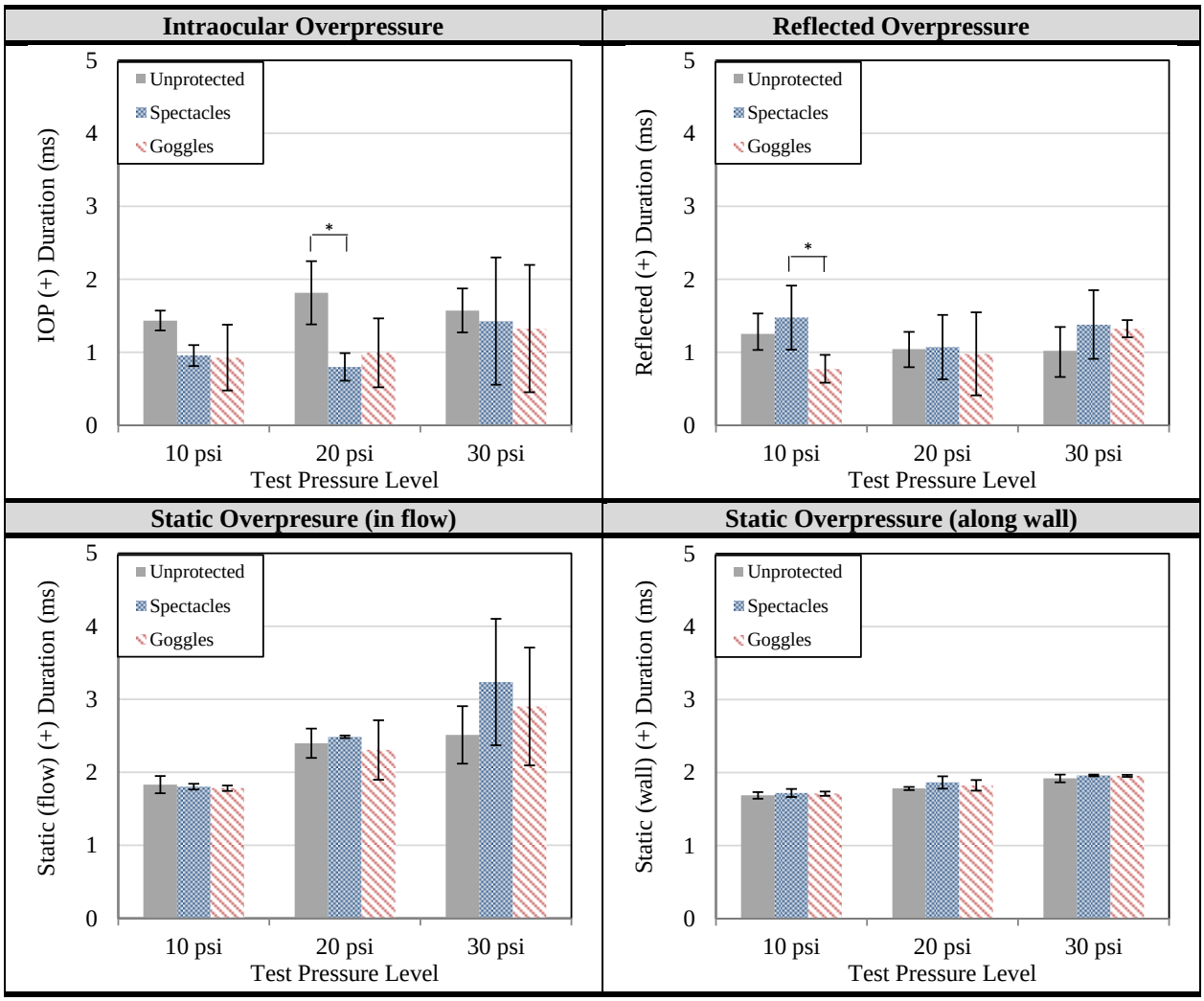

Figure 42. Positive duration for unprotected and protected porcine eyes during blast.

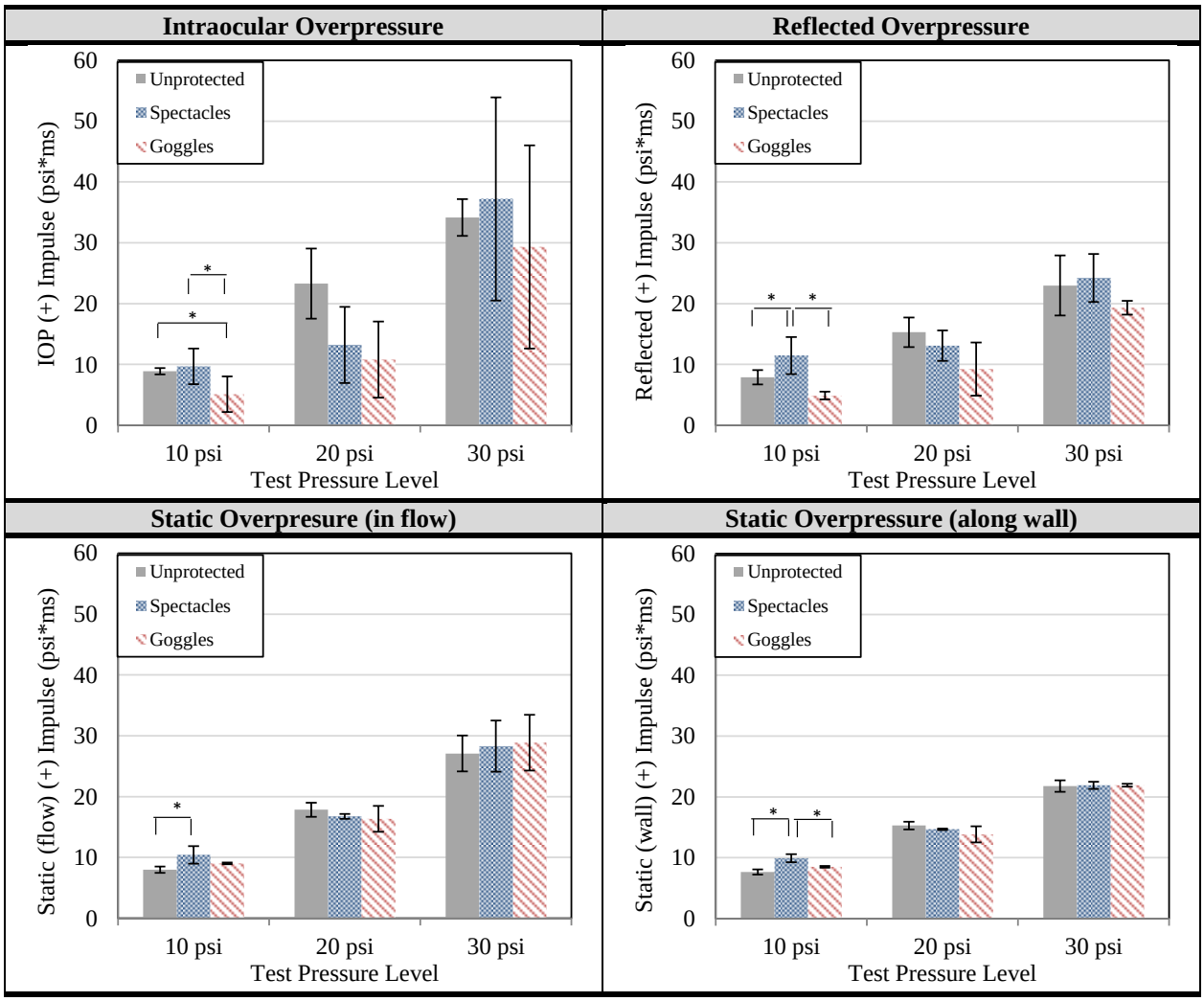

Figure 43. Positive impulse for unprotected and protected porcine eyes during blast.

Peak static overpressure (measured in the flow as well as along the wall) and peak reflected overpressure were plotted against peak IOP for tests with spectacles and googles. The unprotected eye tests were also plotted for comparison. Linear correlations between the peak pressure measured at each location and peak IOP are illustrated in **Figure 44**. Compared to the unprotected eye tests and based on the slopes of these linear regression lines, IOP was most similar (that is, closest to a 1:1 ratio) to reflected overpressure for the unprotected eye and spectacle tests, and to static overpressure measured in the flow for the goggle tests. The Pearson correlation coefficient is greater than 0.8 for all three conditions.

Correlations between static overpressure measured at the wall and static overpressure measured in the fluid flow are shown in **Figure 45**. The correlation for the unprotected eye from Chapter 3 is included again for comparison. Peak static overpressure measured in the flow was higher than

peak static overpressure measured along the wall for the unprotected eye as well as for the addition of the spectacles and the goggles.

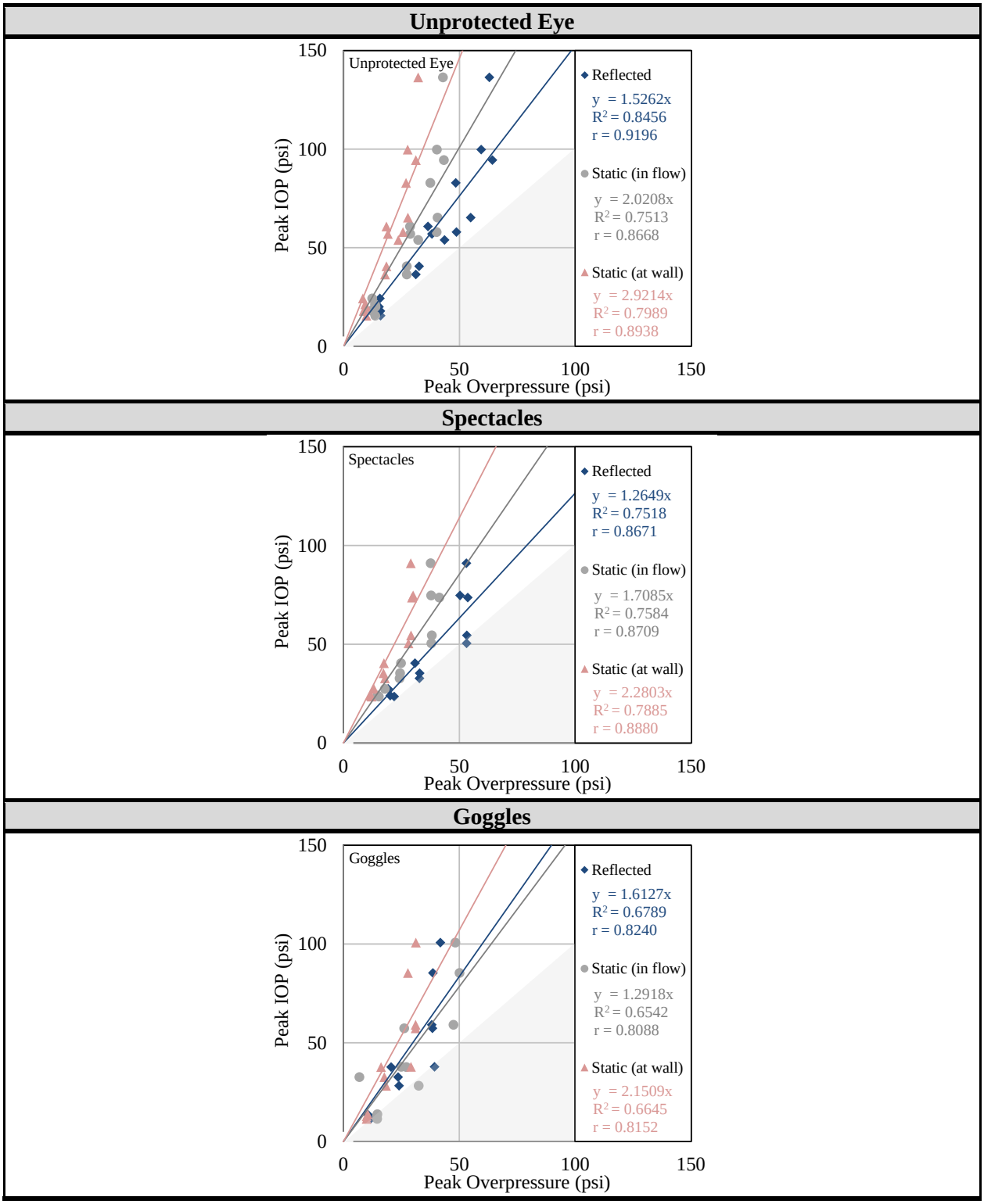

Figure 44. Correlations between peak intraocular pressure and peak overpressure.

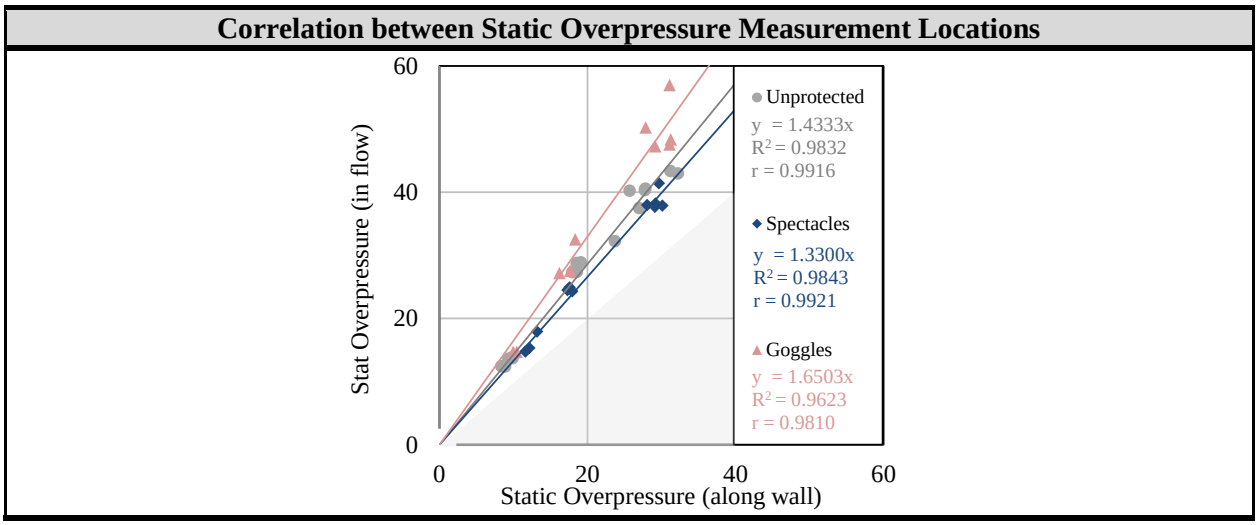

Figure 45. Correlations between static overpressure measured at two locations.

Full injury summaries for all tests are tabulated in **Appendix C**. A number of the injuries observed at the lens and ciliary body upon dissection were incurred during dissection, and are noted as such in this summary. Other than two cases of lens damage, only ciliary body was reported as potentially being independent of preparation techniques. However, using chi-square tests, it was determined that there was no significant difference between the proportion of ciliary body injury observed between sham eyes and any of the unprotected eyes, eyes with spectacles, or eyes with goggles. Therefore, it was concluded that there was a lack of consistently reported injuries caused by exposure to primary blast overpressure.

Predicted injury risk increased with increasing test pressure level (**Table 15**). Injury risk was <2% for all eye injuries for both spectacles and goggles. Predicted injury risk calculated for the spectacles and goggles was lower than the unprotected eye.

Table 15. Predicted percent injury risk for porcine tests with spectacles and goggles.

	Hyphema	Lens Damage	Retinal Damage	Globe Rupture
	% Injury Risk	% Injury Risk	% Injury Risk	% Injury Risk
Unprotected Eye				
10 psi	0.07 ± 0.02	0.00 ± 0.00	0.00 ± 0.00	0.00 ± 0.00
20 psi	0.49 ± 0.21	0.00 ± 0.00	0.00 ± 0.00	0.00 ± 0.00
30 psi	1.89 ± 1.37	0.01 ± 0.02	0.02 ± 0.03	0.00 ± 0.00
Spectacles				
10 psi	0.11 ± 0.02	0.00 ± 0.00	0.00 ± 0.00	0.00 ± 0.00
20 psi	0.24 ± 0.05	0.00 ± 0.00	0.00 ± 0.00	0.00 ± 0.00
30 psi	1.00 ± 0.51	0.00 ± 0.00	0.00 ± 0.00	0.00 ± 0.00
Goggles				
10 psi	0.03 ± 0.01	0.00 ± 0.00	0.00 ± 0.00	0.00 ± 0.00
20 psi	0.20 ± 0.06	0.00 ± 0.00	0.00 ± 0.00	0.00 ± 0.00
30 psi	1.11 ± 0.76	0.00 ± 0.01	0.01 ± 0.01	0.00 ± 0.00

Note: Injury risk calculated using the correlation between an 11.16 mm diameter rod and intraocular pressure.

Still images of high speed video during the first 800 μs of the blast event show a rippling effect on the gelatin surrounding the eye and minor deflection of the lens for both the spectacles and goggles (**Figure 46**, **Figure 47**). The rippling effect was previously observed with the unprotected eyes, and was more noticeable with the spectacles as compared to the goggles. Deflection of the lens could not be accurately quantified from this single side-on view video image due to the fact that deflections occurred in multiple axes. The nosepiece of the goggle which initially contacts the nose moved off the nose during the event, causing a slapping motion on the nose and gelatin. This can be seen in the third frame in **Figure 47**.

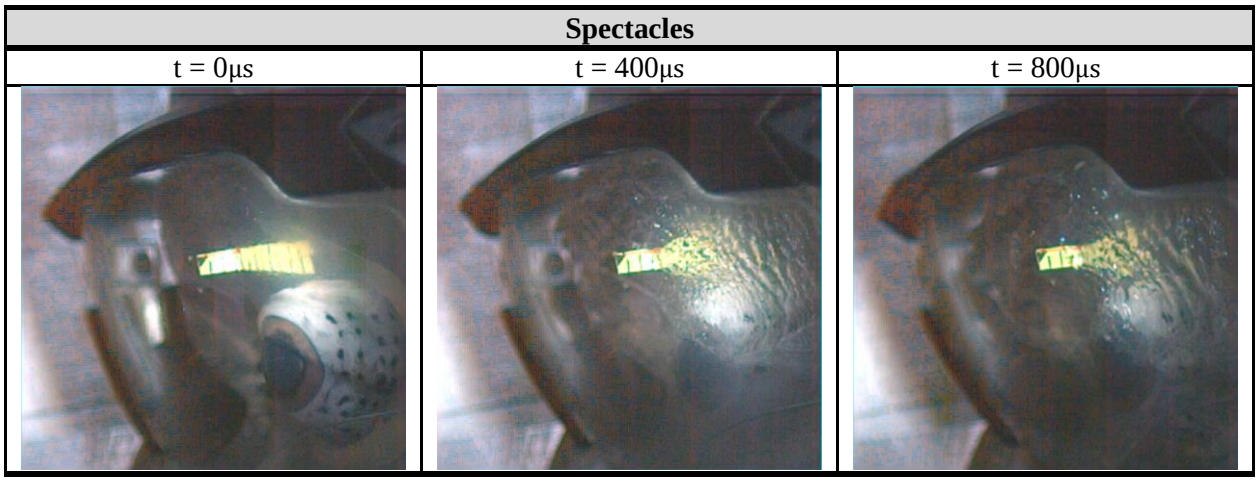

Figure 46. Still images from high-speed video of 30 psi blast with spectacle.

Goggles		
t = 0μs	t = 400μs	t = 800μs
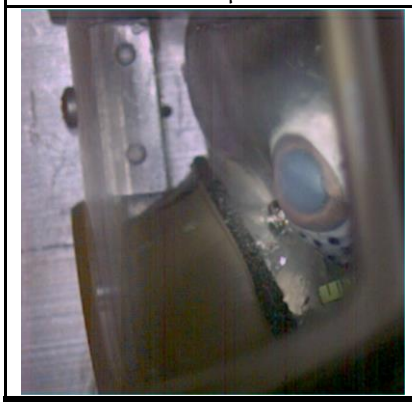		

Figure 47. Still images from high-speed video of 30 psi blast with goggles.

Discussion

Results from this study indicate that both the spectacles and goggles tested were generally able to reduce the magnitude of the pressure exposed to the eye during primary blast overpressure exposure as compared to the unprotected eye. Interestingly, the addition of the spectacles consistently increased peak IOP only at the 10 psi level. This resulted in an average of 28% increase in peak IOP as compared to an unprotected eye at the 10 psi level, but a 27% and a 23% reduction in peak IOP as compared to an unprotected eye at the 20 psi, and 30 psi levels, respectively. The goggles showed a 35%, 34%, and a 24% reduction in peak IOP as compared to the unprotected eye at the 10 psi, 20 psi, and 30 psi levels, respectively. Based on these results, it appears that the spectacles and goggles have similar protective abilities at the 30 psi level.

The greater reduction in peak IOP for the goggles as compared to the spectacles at the 10 psi and 20 psi test levels can be partially attributed to the physical differences in geometry of the lenses. The goggle has a larger lens area as well as padding that contacts the forehead and cheek. A thin mesh connects the lens to this padding, providing a surface around the goggle that prevents large fragmentation from entering the ocular space. It is likely that this small open area and added mesh minimizes the amount of pressure that can enter the space between the goggles and the eye, resulting in reduced peak IOPs. Conversely, the spectacles, which during normal wear only contacts the face along the bridge of the nose and at the ear, do not provide any protection from pressure entering the space between the lens and the front of the eye. The fact that padding of the goggles contacts the face might cause distributed loading and partial energy absorption when exposed to a shock wave. However, this further complicates the boundary condition around the

eye, because if the goggles compress due to the shock wave, it is possible that pressure in the space between the lens and the eye can increase. While the spectacle may also experience this phenomenon of increased pressure in this space, it would likely be to a lesser extent due to the open nature of the spectacles in comparison to the goggles. Furthermore, both the spectacle and goggle appear to absorb and/or reflect some of the energy of the shock wave and may redistribute the initial loading to other regions of the face such as the nasal bone, forehead, and cheek that may have various susceptibilities to injury.

The addition of the spectacles and goggles resulted oscillations within the eye that were not observed in the unprotected eye. This was illustrated in **Figure 39** and **Figure 40**. It is possible that these oscillations could correspond to expansion and contraction of the eye, potentially straining structures within the eye. Presumably, this could damage interfaces between tissues and fluids in the eye, such as the ciliary body, zonules, and vitreous humor. While no gross damage to these structures were observed to be caused by primary blast overpressure exposure in the current study, it remains possible that damage could occur at the microscopic level. Further examination of these structures using an animal model will elucidate a better understanding of the physiological response of the eye and its structures at the cellular and molecular levels.

The general shape of the pressure profile changed with the addition of eye protection as compared to the unprotected eye (**Figure 38**, **Figure 39**, and **Figure 40**). The rise time of the initial peak (not necessarily the peak overpressure) increased with the addition of eye protection. Examining the 30 psi condition where peak IOP was similar for spectacles and goggles, the time at the peak is different for these conditions. The spectacles shows an initial peak at the beginning of the shock wave, similar to what was observed for the unprotected eye. However, the goggles shows an approximately 1 ms delay in peak overpressure. This delayed rise time may be caused by the increased time needed for the pressure wave to pass around the lens. The goggles with padding that contacts the face further delays the rise time in comparison to the spectacles. Furthermore, lens shape can affect wave propagation to the eye and around the face. Both the spectacles and goggles are curved in the transverse plane to match the curvature of the human head. However, in the sagittal plane the lens of the spectacles is curved while the lens of the goggles is flat. Side-view photographs of the spectacles and goggles mounted on the 3D orbit in **Figure 48** shows this lens curvature. The curvature in the spectacle results in

asymmetrical loading on the surface of the lens which results in uneven pressure profiles around the lens, similar to an airfoil. The characteristic loading pattern could potentially affect the overall response of the eye during exposure.

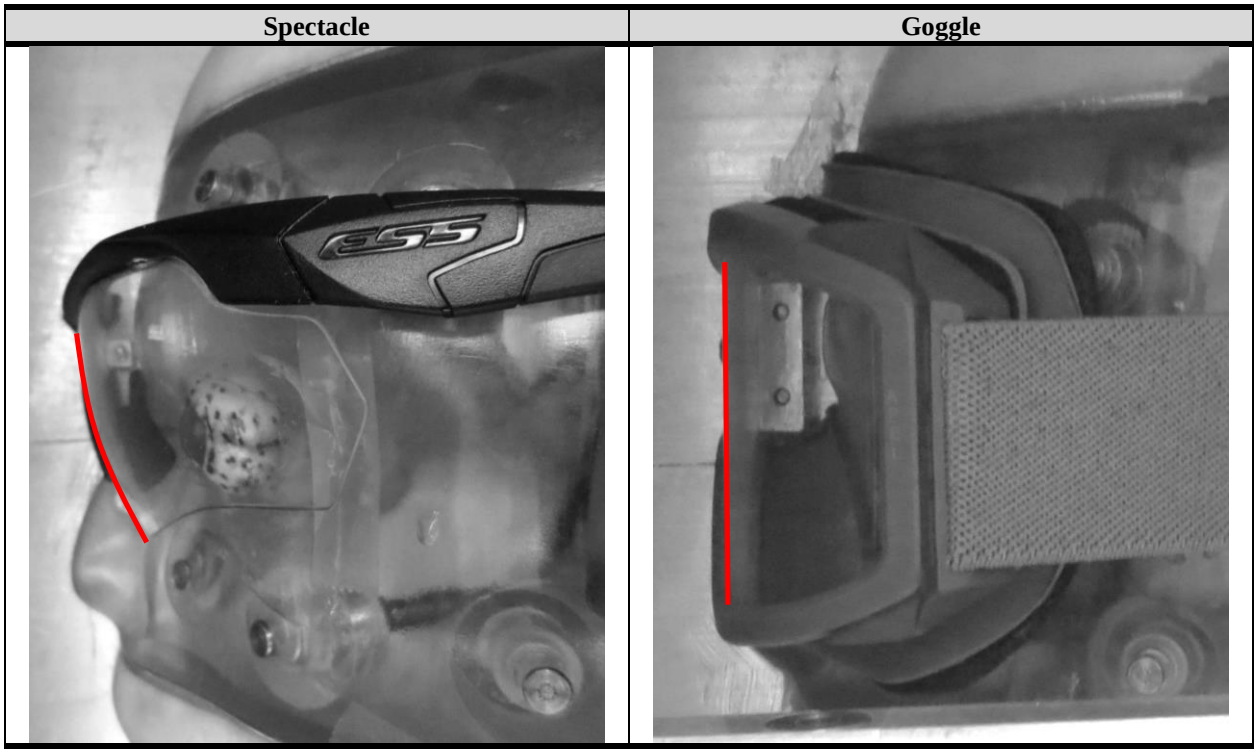

Figure 48. Lens shape for spectacles and goggles.

The results of the current study are similar to those predicted by a previously published computational models of the eye with and without spectacles and goggles [64]. The published study developed a 3D fluid-structure interaction computational model of the face and goggles and validated the response using experimental blast tests conducted on an unprotected and protected FOCUS headform [64, 66]. The computational model was validated using experimental data from a test series that exposed two FOCUS headforms to blast overpressure from a free hanging cylindrical charge. The charge was suspended in air at the 5’7” eyelevel height. Each headform was mounted such that the eye was 5’7” above ground level. One FOCUS headform was tested with goggles and spectacles from the Military Combat Eye Protection (MCEP) systems, while the other was tested with no eye protection. Varying stand-off distances were used to create multiple peak overpressure levels. The computational model showed that pressure measured with virtual probes around the face was highest near the nose and decreased temporally around the face for the unprotected face. A similar decrease in peak

pressure was observed for the protected face tests. The spectacles and/or goggles caused a decreased peak overpressure measured at the eye.

Although injury risk for the unprotected eye was previously shown in Chapter 3 to be less than 5% for the pressure levels tested in this study, it was important to understand whether the addition of eye protection could affect peak IOP and therefore, alter injury risk for primary blast overpressure exposure. This study showed that the addition of the spectacles increased peak IOP at the 10 psi level, which resulted in an increased risk of eye injury as compared to the unprotected eye. Peak IOP for the remaining test levels for the spectacles and all test levels for the goggles decreased peak IOP, which resulted in a decreased risk of eye injury as compared to the unprotected eye. It remains important that protective eyewear be used during combat scenarios where blast exposure is a threat. While the injury risk from primary blast overpressure was shown to be low, overpressure exposure is only one potential injury mechanism. Other threats associated with blasts, such as impact from debris, can be mitigated with the use of protective eyewear. Further, the experimental methods described in this study can be used for future work evaluating new forms of eyewear or eventually for developing blast testing standards such as those that currently exist for ballistic loading.

Limitations

A limitation of the current test setup is that the lens of the spectacles and goggles were rigidly held in place in front of the eye where they would be located *in situ*. It is possible that the lens may deflect, translate, or become dislodged during normal use. Tests conducted with the FOCUS headform only reported one test where eyewear came off the headform during blast exposure [66]. However, a human wearing spectacles or goggles has more friction due to eyewear contact with skin and hair than the FOCUS headform. Similarly, a soldier wearing spectacles or goggles is also probably wearing a helmet, which could also prevent the PPE from coming off during normal wear. This further complicates the blast phenomena around the eye and face. The effects of both eyewear and a helmet provide an area for future research. While a helmet may reflect some of the energy of the blast, depending on the direction of the shock wave propagation, the addition of the helmet could create alternate complex loading patterns for the blast wave around the eye, face, and orbit.

A porcine model was chosen for the current study due to its anatomical and geometrical similarities to the human eye. The most important difference between the porcine and human eye models is perhaps their structural properties at various loading regimes. It was previously established that the porcine eye is significantly stronger (nearly twice) than the human eye, which is likely due to the greater scleral thickness of the porcine eye in comparison to that of the human eye [41]. The tests conducted to quantify this difference involved statically and dynamically pressurizing human and porcine eyes and measuring the pressure at rupture. As such, it is possible that a human eye would experience greater deflection than a porcine eye exposed to the same blast test pressure level. Therefore, results in this study potentially underestimate the risk of human eye injury.

The tests in this study were designed to simulate an eye-level, forward-facing blast event. This only accounts for one loading direction, and does not take into account the effect of oblique loading or ground charges, both of which are possible scenarios during combat.

Conclusions

This study quantified peak intraocular pressure for porcine eyes protected by spectacles and/or goggles to assess the ability of military protective eyewear to minimize eye injury risk from primary blast overpressure. The addition of the spectacles increased IOP at the 10 psi level, but decreased IOP at the 20 psi and 30 psi test levels. However, these changes were only significantly different for the 10 psi level. The addition of the goggles decreased IOP at all test levels. The reduction of peak IOP measured in this study correlates to a lower risk of eye injuries from primary blast overpressure for scenarios where eye protection is used. This further supports the need to increase military personnel compliance with properly using protective eyewear during combat. Interestingly, the spectacles and goggles produced similar reduction in peak IOP at the 30 psi condition. It is possible that the 30 psi test level represents the threshold between spectacles and goggles where lens shape and/or contact with the face does not affect the resulting propagation of pressure toward the eye. Future work with higher pressure levels will elucidate further trends in the ability of spectacle and goggles to protect the eye from primary blast overpressure. Further, the combined effects of protective eyewear and helmets will increase the fidelity of the results for comparison to combat scenarios.

Chapter 5

Pressure Propagation within the Orbit and around the Face of Unprotected and Protected Eyes during Primary Blast Overpressure Exposure

Introduction

Although, a number of computational and finite element models of the eye currently exist, none have been rigorously validated for blast loading conditions [52, 53, 55]. One computational model of a head wearing spectacles and goggles was validated against experimental data collected for matched tests using the FOCUS headform during live-fire blast testing [64, 66]. Results from this computational model and the experimental tests used to validate it were similar to those reported in experimental tests conducted in Chapter 3, as discussed in Chapter 4 of this dissertation. However, the overall paucity of experimental data for blast loading to the eye and face necessitates quantifying the pressure response at various locations around the face and orbit. Therefore, the purpose of this study is to measure pressure within the orbit and around the face during blast loading to the unprotected and protected human eye in order to develop response corridors that can be used to validate computational and finite element models of the eye specifically for blast loading.

Methods

The full experimental methods for this study are described in detail in Chapter 3 and Chapter 4 of this dissertation. Briefly, enucleated porcine eyes were placed in an orbit and exposed to a single blast overpressure event at 10 psi, 20 psi, or 30 psi (static overpressure) using an Advanced Blast Simulator. Two orbit geometries were tested with unprotected eyes to examine the effect of orbital geometry. The first orbit had a first-order approximation of the human orbital geometry ("Synthetic Orbit"). The second orbit was a 3D printed orbit that was based on the Global Human Body Models Consortium (GHBMC) facial and orbital geometry ("3D Orbit"). Using the 3D printed orbit, additional tests were conducted with the addition of military spectacles or goggles. All test conditions occluded less than 20% of the cross-sectional area of the tube. A minimum of three tests were conducted for each condition at each test level.

Pressure was measured at ten novel locations around the eye for the current study: intraorbital pressure was measured at four locations within the orbit and facial pressure was measured at seven locations[3] around the face. Intraorbital pressure was measured with miniature pressure sensors (Model 060, 100 psi, Precision Measurement Company, Ann Arbor, MI) mounted along the intraorbital bones. Intraorbital pressure sensors were mounted ½" inside the orbit, along the intraorbital surfaces that simulate the maxilla, lacrimal, and frontal bones. Two sensors were placed on the frontal bone, with the second sensor ½" posterior to the first sensor. These sensors were secured in place using a small piece of tape placed on the sensor wire just behind the sensing element. No glue was used to adhere either the sensing element or the wire to the orbit surface. **Figure 49** illustrates the intraorbital sensor locations for both the synthetic and 3D orbits. All pressure data were recorded at 301.887 kHz (TDAS PRO, Diversified Technical Systems, Inc., Seal Beach, CA). High speed video was recorded at 10 kHz.

[3]Pressure data from the top middle facial sensor were previously discussed in comparison to the peak static and peak IOP in Chapter 3 for the unprotected porcine eye tests. These data are included herein for comparison with the six other facial pressure sensors.

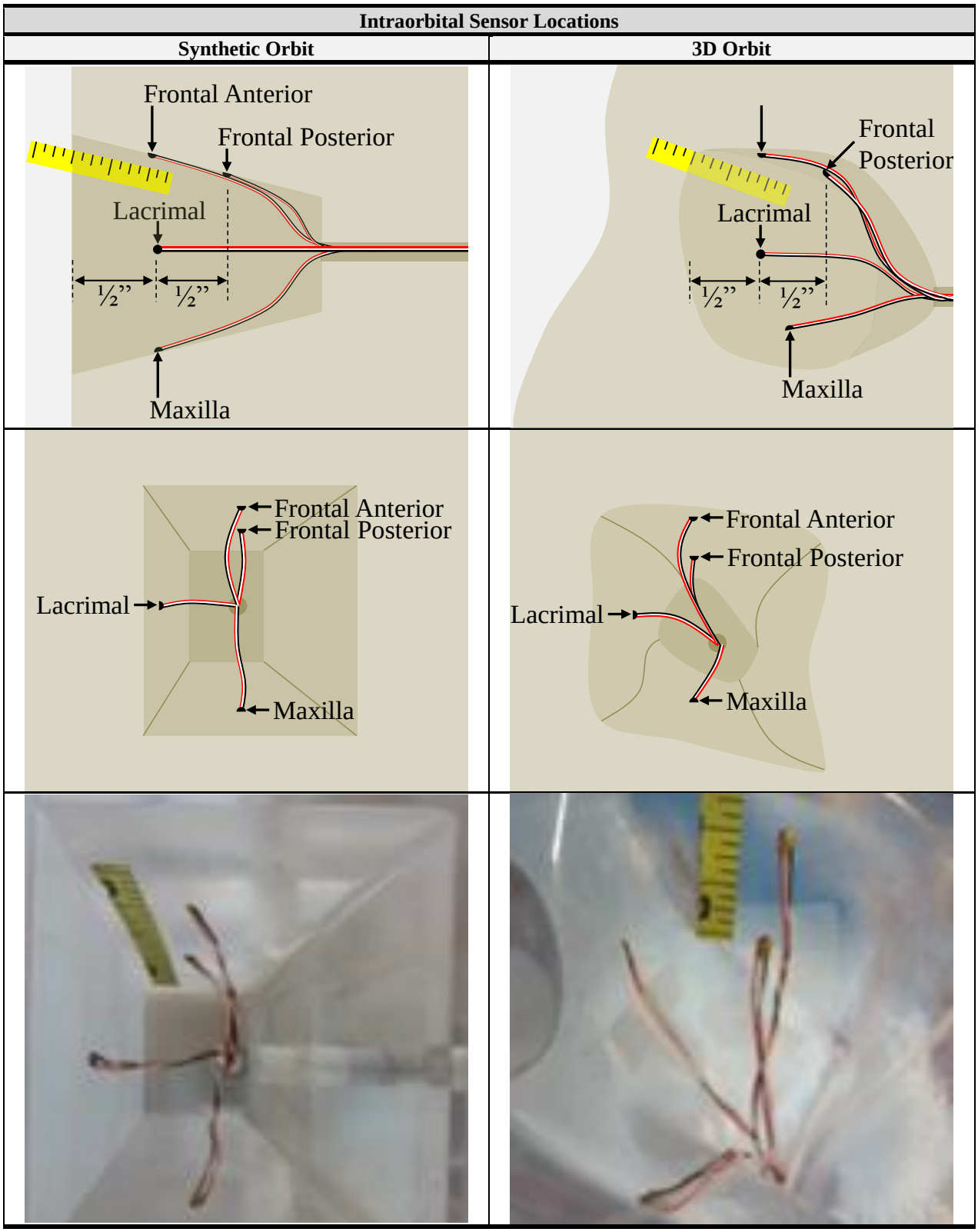

Figure 49. Intraorbital pressure sensor locations for synthetic and 3D orbits.
(Eye not illustrated for simplicity.)

Facial pressure was measured with sensors specifically designed for measuring blast loading (Model 113B21, 200 psi, PCB Piezotronics, Depew, NY). Facial pressure sensors were mounted inside the 3D printed orbit, with the sensing element oriented normal to the external facial geometry at each location. It should be noted that for the tests involving the goggles mounted on the 3D orbit, several of the facial sensors were covered by the goggles: Top Medial, Top Middle, and Bottom Middle. The sensing surface of these sensors was in direct contact with the goggle padding, and was therefore subject to loading by this surface. Error! Reference source not found. in Chapter 4 illustrated the facial sensor locations for the 3D orbit.

A custom MATLAB® (version 7.11.0.584 (R2010b), The MathWorks, Inc., Natick, MA) script was used to quantify the shock wave characteristics at each pressure sensor location (time of arrival, peak overpressure, positive duration, positive impulse). Pressure-time histories for each test were plotted at matched locations. Response corridors for each location were created using the average response of the sensor and ±1 standard deviation from the average.

Results

Example corridor plots are shown in **Figure 50**. Example pressure-time histories for the intraorbital sensors and facial sensors at all three pressure levels are shown in **Figure 51** and **Figure 52**, respectfully. Individual pressure traces as well as corridors based on the average response ±1 standard deviation for all pressure sensor locations can be found in **Appendix A**. Static overpressure pressure-time histories for empty tube tests conducted at each pressure level can also be found in **Appendix A** for comparison.

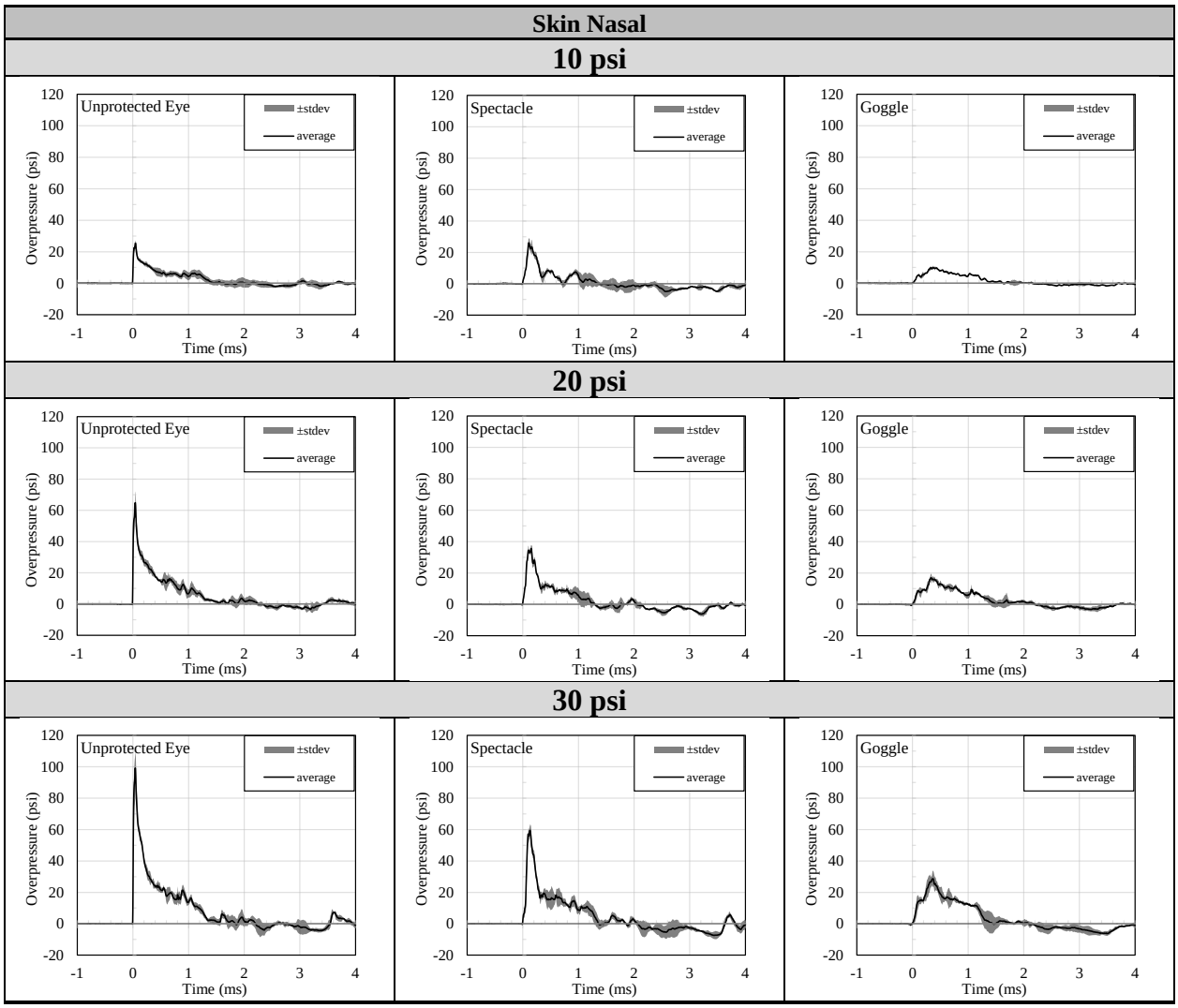

Figure 50. Corridor plots for the nasal sensor.

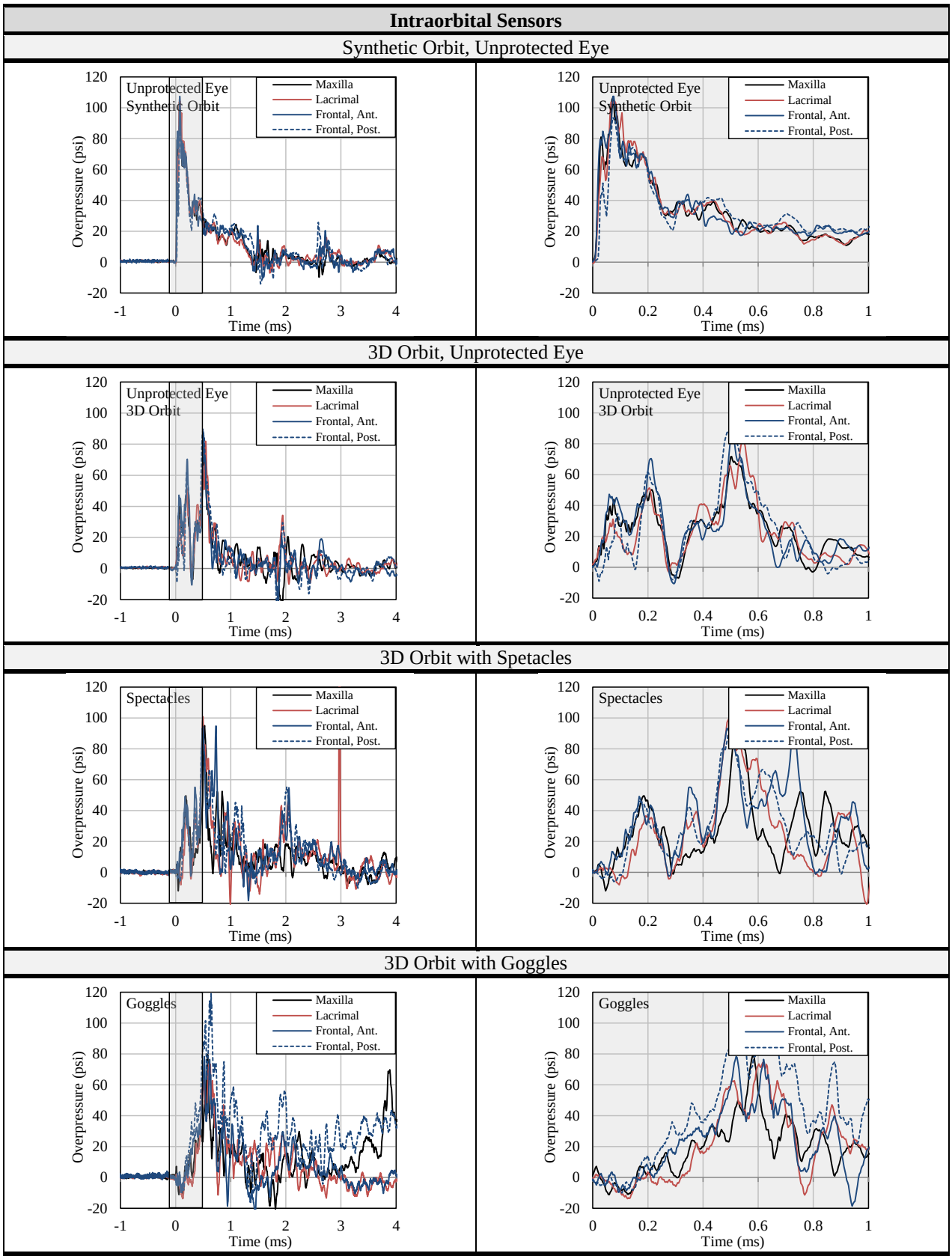

Figure 51. Pressure traces for intraorbital sensors at the 30 psi test level.

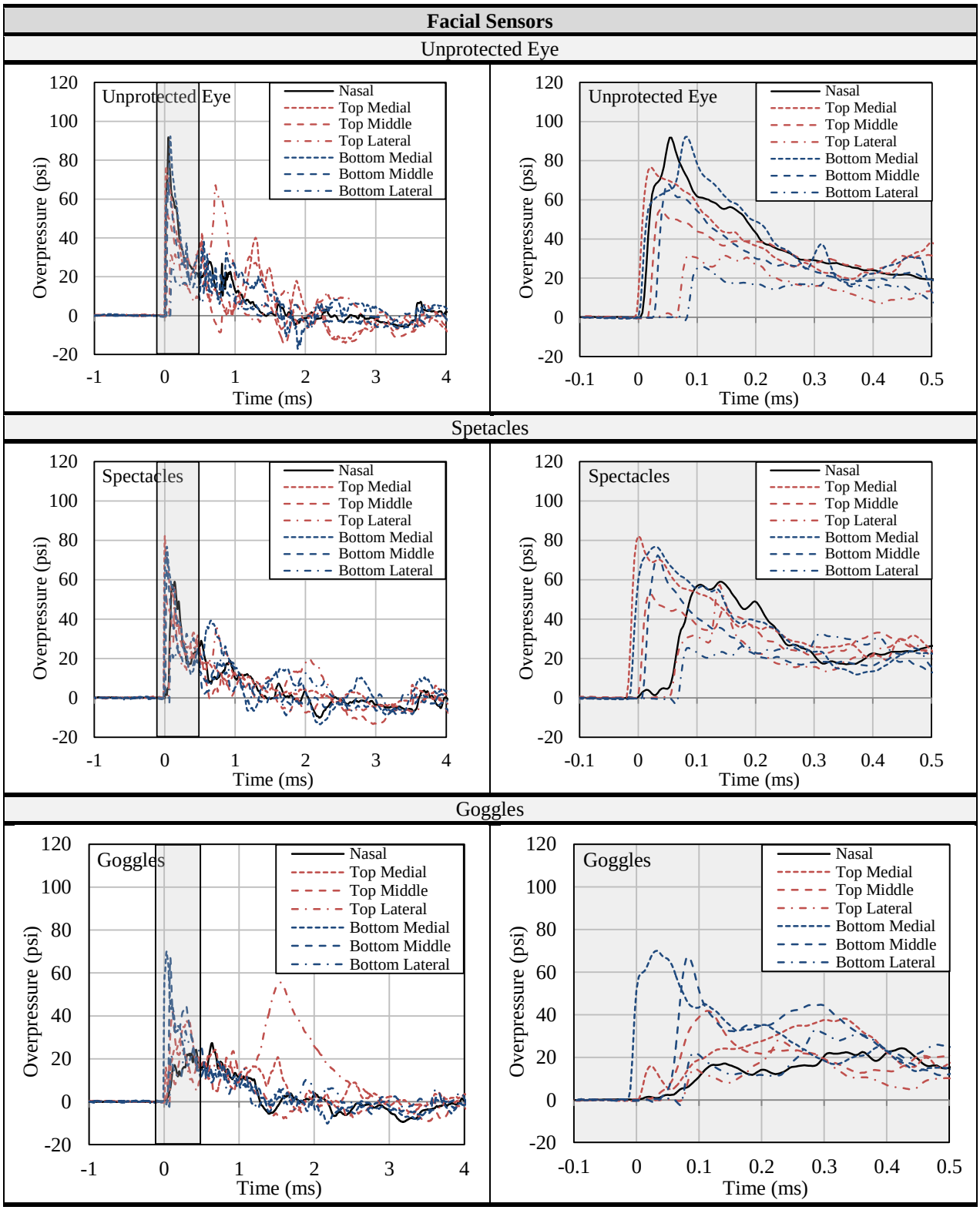

Figure 52. Facial sensor response at the 30 psi test level.

Average shock wave parameters for the intraorbital sensors in the synthetic orbit are listed in **Table 16.** Average shock wave parameters for the intraorbital sensors in the 3D orbit with no eye protection, with spectacles, and with goggles are listed in

Table 17, **Table 18**, and **Table 19**, respectively. Average shock wave parameters for the facial sensors in the 3D orbit with no eye protection, with spectacles, and with goggles are listed in **Table 20**, **Table 21**, and **Table 22**, respectively. Average shock wave parameters for the static overpressure measured at the remaining pressure sensor locations for the tests described in Chapter 3 and Chapter 4 are tabulated in **Appendix B.**

Table 16. Average shock wave parameters for intraorbital sensors - synthetic orbit.

Pressure	Test Condition	10 psi	20 psi	30 psi
Peak Overpressure (psi)				
Orbital	Synthetic – Maxilla	24.63 ± 2.95	74.34 ± 13.77	96.08 ± 8.98
	Synthetic – Lacrimal	23.08 ± 3.37	73.38 ± 15.39	99.45 ± 10.28
	Synthetic – Frontal A.	23.28 ± 1.62	72.89 ± 18.48	103.40 ± 20.93
	Synthetic – Frontal P.	27.73 ± 3.21	79.90 ± 16.46	96.97 ± 7.65
Time of Arrival (ms)				
Orbital	Synthetic – Maxilla	3.61 ± 0.09	2.56 ± 0.13	2.39 ± 0.06
	Synthetic – Lacrimal	3.61 ± 0.08	2.55 ± 0.13	2.39 ± 0.06
	Synthetic – Frontal A.	3.61 ± 0.08	2.55 ± 0.13	2.38 ± 0.06
	Synthetic – Frontal P.	3.63 ± 0.09	2.56 ± 0.14	2.39 ± 0.06
Positive Duration (ms)				
Orbital	Synthetic – Maxilla	1.30 ± 0.17	1.56 ± 0.39	1.73 ± 0.39
	Synthetic – Lacrimal	1.32 ± 0.17	1.33 ± 0.19	1.56 ± 0.41
	Synthetic – Frontal A.	1.30 ± 0.23	1.37 ± 0.27	1.22 ± 0.31
	Synthetic – Frontal P.	1.37 ± 0.02	1.33 ± 0.26	1.38 ± 0.56
Positive Impulse (psi*ms)				
Orbital	Synthetic – Maxilla	9.30 ± 1.46	28.05 ± 4.76	38.20 ± 2.42
	Synthetic – Lacrimal	9.20 ± 1.32	26.58 ± 4.60	35.88 ± 2.43
	Synthetic – Frontal A.	9.49 ± 1.35	27.13 ± 6.65	35.24 ± 5.80
	Synthetic – Frontal P.	10.35 ± 1.04	26.78 ± 5.67	34.83 ± 6.72

Table 17. Average shock wave parameters for intraorbital sensors - unprotected 3D orbit.

Pressure	Test Condition	10 psi	20 psi	30 psi
Peak Overpressure (Avg ± Stdev)				
Orbital	3D – Maxilla	16.17 ± 2.38	43.66 ± 4.13	79.10 ± 13.07
	3D – Lacrimal	17.33 ± 1.85	39.54 ± 6.39	85.76 ± 10.67
	3D – Frontal A.	16.62 ± 2.75	41.03 ± 4.96	80.36 ± 13.89
	3D – Frontal Post.	20.09 ± 3.62	46.77 ± 3.70	95.12 ± 12.68
Time of Arrival (ms)				
Orbital	3D – Maxilla	3.63 ± 0.05	2.70 ± 0.09	2.42 ± 0.03
	3D – Lacrimal	3.67 ± 0.09	2.70 ± 0.08	2.42 ± 0.04
	3D – Frontal A.	3.65 ± 0.07	2.70 ± 0.09	2.42 ± 0.03
	3D – Frontal Post.	3.66 ± 0.07	2.71 ± 0.09	2.43 ± 0.04
Positive Duration (ms)				
Orbital	3D – Maxilla	1.33 ± 0.30	0.43 ± 0.24	0.72 ± 0.29
	3D – Lacrimal	0.96 ± 0.54	0.87 ± 0.44	0.60 ± 0.32
	3D – Frontal A.	1.15 ± 0.52	0.69 ± 0.45	0.70 ± 0.43
	3D – Frontal Post.	1.04 ± 0.41	0.81 ± 0.21	0.62 ± 0.39
Positive Impulse (psi*ms)				
Orbital	3D – Maxilla	8.87 ± 1.04	8.10 ± 4.30	21.79 ± 7.19
	3D – Lacrimal	6.24 ± 3.83	15.19 ± 6.60	19.25 ± 10.55
	3D – Frontal A.	8.44 ± 3.36	13.08 ± 8.15	21.71 ± 10.60
	3D – Frontal Post.	8.23 ± 3.59	16.35 ± 4.03	19.56 ± 13.11

Table 18. Average shock wave parameters for intraorbital sensors - 3D orbit with spectacles.

Pressure	Test Condition	10 psi	20 psi	30 psi
Peak Overpressure (Avg ± Stdev)				
Orbital	3D – Maxilla	29.52 ± 11.57	41.80 ± 5.62	88.20 ± 9.06
	3D – Lacrimal	19.43 ± 3.29*	44.77 ± 5.34	82.65 ± 28.17
	3D – Frontal A.	29.60 ± 4.78	43.08 ± 5.51*	82.26 ± 11.77
	3D – Frontal Post.	35.00 ± 4.03	73.45 ± 19.52	106.34 ± 12.66
Time of Arrival (ms)				
Orbital	3D – Maxilla	3.33 ± 0.11	2.84 ± 0.02	2.51 ± 0.03
	3D – Lacrimal	3.49 ± 0.06*	2.87 ± 0.03	2.55 ± 0.03
	3D – Frontal A.	3.32 ± 0.10	2.82 ± 0.03	2.49 ± 0.04
	3D – Frontal Post.	3.37 ± 0.12	2.85 ± 0.06	2.54 ± 0.04
Positive Duration (ms)				
Orbital	3D – Maxilla	0.38 ± 0.25	0.66 ± 0.16	0.49 ± 0.40
	3D – Lacrimal	0.69 ± 0.45*	0.56 ± 0.32	0.54 ± 0.39
	3D – Frontal A.	0.71 ± 0.23	0.83 ± 0.06	0.62 ± 0.37
	3D – Frontal Post.	1.11 ± 0.45	0.88 ± 0.00*	2.22 ± 1.86
Positive Impulse (psi*ms)				
Orbital	3D – Maxilla	3.92 ± 2.21	10.40 ± 2.84	11.09 ± 10.69
	3D – Lacrimal	6.32 ± 5.10*	10.68 ± 7.55	17.60 ± 15.34
	3D – Frontal A.	8.58 ± 1.27	14.66 ± 0.52*	18.09 ± 12.69
	3D – Frontal Post.	16.56 ± 3.57	25.46 ± 8.71	63.71 ± 37.35

Table 19. Average shock wave parameters for intraorbital sensors - 3D orbit with goggles.

Pressure	Test Condition	10 psi	20 psi	30 psi
Peak Overpressure (Avg ± Stdev)				
Orbital	3D – Maxilla	17.74 ± 4.62	35.28 ± 11.61	66.80 ± 19.57*
	3D – Lacrimal	25.76 ± 12.64	63.72 ± 18.03	70.39 ± 14.38
	3D – Frontal A.	17.49 ± 0.92	38.73 ± 2.79	75.91 ± 22.10
	3D – Frontal Post.	22.84 ± 2.97	54.44 ± 16.03	101.41 ± 19.05
Time of Arrival (ms)				
Orbital	3D – Maxilla	3.81 ± 0.33	3.47 ± 0.33	3.64 ± 0.31*
	3D – Lacrimal	3.86 ± 0.02	3.18 ± 0.17	2.74 ± 0.10
	3D – Frontal A.	3.68 ± 0.06	3.04 ± 0.13	2.66 ± 0.07
	3D – Frontal Post.	3.75 ± 0.07	1.87 ± 2.08	2.66 ± 0.09
Positive Duration (ms)				
Orbital	3D – Maxilla	0.90 ± 0.18	0.91 ± 0.11	1.06 ± 0.39*
	3D – Lacrimal	0.72 ± 0.19	0.58 ± 0.54	0.70 ± 0.31
	3D – Frontal A.	0.71 ± 0.38	0.88 ± 0.16	0.67 ± 0.08
	3D – Frontal Post.	1.48 ± 0.91	1.35 ± 0.08	2.32 ± 1.88
Positive Impulse (psi*ms)				
Orbital	3D – Maxilla	7.17 ± 0.26	13.24 ± 1.55	25.27 ± 14.19*
	3D – Lacrimal	8.11 ± 2.74	13.27 ± 5.73	19.96 ± 6.79
	3D – Frontal A.	5.29 ± 3.44	13.11 ± 2.24	19.29 ± 3.73
	3D – Frontal Post.	11.45 ± 6.36	31.21 ± 12.40	63.52 ± 33.62

*Only three tests because insufficient DAS available for two tests.

Table 20. Average shock wave parameters for facial sensors - unprotected 3D orbit.

Pressure	Test Condition	10 psi	20 psi	30 psi
Peak Overpressure (psi)				
Facial	3D – Nasal	25.73 ± 1.65	68.47 ± 3.33	101.16 ± 12.34
	3D – Top Medial	19.40 ± 1.30	48.10 ± 4.12	76.08 ± 7.66
	3D – Top Middle	15.17 ± 0.93	36.47 ± 4.92	56.49 ± 6.91
	3D – Top Lateral	13.33 ± 1.50	29.06 ± 5.31	51.84 ± 11.02
	3D – Bot. Medial	20.41 ± 0.83	49.33 ± 5.81	81.94 ± 7.47
	3D – Bot. Middle	17.35 ± 1.18	44.85 ± 3.06	66.99 ± 3.73
	3D – Bot. Lateral	12.02 ± 1.71	22.17 ± 3.60	30.36 ± 3.53
Time of Arrival (ms)				
Facial	3D – Nasal	3.61 ± 0.06	2.68 ± 0.09	2.38 ± 0.04
	3D – Top Medial	3.60 ± 0.06	2.67 ± 0.08	2.37 ± 0.04
	3D – Top Middle	3.63 ± 0.06	2.69 ± 0.09	2.39 ± 0.04
	3D – Top Lateral	3.69 ± 0.06	2.74 ± 0.09	1.85 ± 1.41
	3D – Bot. Medial	3.60 ± 0.06	2.67 ± 0.09	2.38 ± 0.04
	3D – Bot. Middle	3.63 ± 0.06	2.70 ± 0.09	2.40 ± 0.04
	3D – Bot. Lateral	3.71 ± 0.06	2.76 ± 0.09	2.46 ± 0.04
Positive Duration (ms)				
Facial	3D – Nasal	1.52 ± 0.19	1.82 ± 0.31	1.60 ± 0.30
	3D – Top Medial	1.15 ± 0.52	1.18 ± 0.36	1.20 ± 0.30
	3D – Top Middle	1.25 ± 0.22	1.04 ± 0.25	1.02 ± 0.36
	3D – Top Lateral	0.92 ± 0.28	1.22 ± 0.24	1.54 ± 0.33
	3D – Bot. Medial	1.52 ± 0.56	1.29 ± 0.20	1.59 ± 0.29
	3D – Bot. Middle	1.33 ± 0.07	1.39 ± 0.18	1.32 ± 0.04
	3D – Bot. Lateral	1.37 ± 0.40	1.16 ± 0.44	1.86 ± 0.49
Positive Impulse (psi*ms)				
Facial	3D – Nasal	10.89 ± 1.73	23.61 ± 2.33	34.73 ± 3.12
	3D – Top Medial	8.42 ± 2.85	18.69 ± 3.66	29.35 ± 5.74
	3D – Top Middle	7.90 ± 1.20	15.29 ± 2.42	22.98 ± 4.93
	3D – Top Lateral	6.45 ± 1.42	15.59 ± 2.60	32.59 ± 5.14
	3D – Bot. Medial	10.40 ± 2.80	19.10 ± 1.48	35.42 ± 4.34
	3D – Bot. Middle	7.09 ± 0.43	14.99 ± 1.09	21.92 ± 1.36
	3D – Bot. Lateral	6.89 ± 1.23	10.88 ± 1.59	19.51 ± 4.85

Table 21. Average shock wave parameters for facial sensors - 3D orbit with spectacles.

Pressure	Test Condition	10 psi	20 psi	30 psi
Peak Overpressure (psi)				
Facial	3D – Nasal	26.37 ± 2.70	37.50 ± 0.78	62.22 ± 2.14
	3D – Top Medial	27.16 ± 2.41	45.67 ± 2.57	79.18 ± 2.28
	3D – Top Middle	20.52 ± 1.31	32.26 ± 1.11	52.77 ± 1.36
	3D – Top Lateral	24.87 ± 1.50	40.13 ± 3.50	67.72 ± 25.25§
	3D – Bot. Medial	29.22 ± 2.42	42.82 ± 2.45	73.96 ± 2.39
	3D – Bot. Middle	27.32 ± 2.96	45.19 ± 1.29	73.65 ± 3.54
	3D – Bot. Lateral	15.93 ± 0.74	23.31 ± 2.05	42.64 ± 8.75*
Time of Arrival (ms)				
Facial	3D – Nasal	3.27 ± 0.11	2.77 ± 0.01	2.46 ± 0.05
	3D – Top Medial	3.19 ± 0.12	2.78 ± †	1.72 ± 1.52
	3D – Top Middle	3.19 ± 0.05	2.77 ± 0.02	2.45 ± 0.04
	3D – Top Lateral	3.27 ± 0.24	2.80 ± 0.05	2.47 ± 0.09
	3D – Bot. Medial	3.12 ± 0.01	2.69 ± 0.13	2.40 ± 0.10
	3D – Bot. Middle	3.21 ± 0.14	2.78 ± 0.02	2.46 ± 0.04
	3D – Bot. Lateral	3.35 ± 0.11	2.85 ± 0.01	2.54 ± 0.04*
Positive Duration (ms)				
Facial	3D – Nasal	1.09 ± 1.00	1.20 ± 0.14	1.48 ± 0.34
	3D – Top Medial	1.46 ± 0.89	1.17 ± †	1.83 ± 0.43‡
	3D – Top Middle	1.48 ± 0.44	1.07 ± 0.44	1.38 ± 0.47
	3D – Top Lateral	0.90 ± 0.44	1.53 ± 0.54	1.57 ± 0.29‡
	3D – Bot. Medial	1.07 ± 0.48¦	1.45 ± 0.07	1.46 ± 0.27
	3D – Bot. Middle	1.29 ± 0.16‡	1.29 ± 0.03	1.41 ± 0.20
	3D – Bot. Lateral	0.93 ± 0.08	1.39 ± 0.47	1.30 ± 0.39*
Positive Impulse (psi*ms)				
Facial	3D – Nasal	7.83 ± 3.90	14.02 ± 2.16	24.09 ± 2.59
	3D – Top Medial	16.10 ± 9.57	16.74 ± †	35.58 ± 5.21
	3D – Top Middle	11.47 ± 3.04	13.10 ± 2.52	24.22 ± 3.95
	3D – Top Lateral	8.66 ± 4.16	25.41 ± 16.05	25.10 ± 1.49‡
	3D – Bot. Medial	11.09 ± 3.76¦	21.99 ± 2.78	35.21 ± 2.39
	3D – Bot. Middle	9.36 ± 0.69‡	14.48 ± 1.27	22.19 ± 2.05
	3D – Bot. Lateral	7.50 ± 0.80	16.50 ± 5.70	22.15 ± 5.85*

*Only three tests at this level because two tests do not return to zero after initial peak.
†Only one test at this level because two tests do not return to zero after initial peak.
‡Only four tests at this level because one test did not return to zero after initial peak.
§Only four tests at this level because one test did not return to zero after initial peak.
¦Only two tests at this test level because one test recorded an uncharacteristic response after initial peak.

Table 22. Average shock wave parameters for facial sensors - 3D orbit with goggles.

Pressure	Test Condition	10 psi	20 psi	30 psi
Peak Overpressure (psi)				
Facial	3D – Nasal	10.30 ± 0.84	18.63 ± 4.02	30.90 ± 2.69
	3D – Top Medial	13.97 ± 3.70	28.77 ± 6.05	35.28 ± 4.06
	3D – Top Middle	11.06 ± 0.65	22.74 ± 1.86	39.24 ± 1.50
	3D – Top Lateral	14.91 ± 0.34	24.87 ± 3.91	63.33 ± 22.67
	3D – Bot. Medial	18.83 ± 3.63	37.47 ± 10.35	105.33 ± 61.19
	3D – Bot. Middle	10.72 ± 0.23	29.96 ± 10.47	68.54 ± 6.21
	3D – Bot. Lateral	14.62 ± 1.49	23.78 ± 0.93	50.01 ± 12.36*
Time of Arrival (ms)				
Facial	3D – Nasal	3.49 ± 0.03	2.88 ± 0.08	2.45 ± 0.07
	3D – Top Medial	3.39 ± 0.11	2.82 ± 0.09	2.40 ± 0.10
	3D – Top Middle	3.33 ± 0.15	2.76 ± 0.18	2.43 ± 0.07
	3D – Top Lateral	3.50 ± 0.12	2.82 ± 0.03	2.51 ± 0.05
	3D – Bot. Medial	3.48 ± 0.02	2.56 ± 0.38	2.39 ± 0.11
	3D – Bot. Middle	3.50 ± 0.03	2.97 ± 0.09	2.47 ± 0.04
	3D – Bot. Lateral	3.55 ± 0.03	2.91 ± 0.09	2.50 ± 0.05*
Positive Duration (ms)				
Facial	3D – Nasal	1.65 ± 0.07	2.07 ± 0.08	1.53 ± 0.39
	3D – Top Medial	1.12 ± 0.46	1.12 ± 0.98	1.54 ± 0.18
	3D – Top Middle	0.77 ± 0.19	0.98 ± 0.57	1.32 ± 0.12
	3D – Top Lateral	0.81 ± 0.19	1.37 ± 0.59	2.18 ± 1.07
	3D – Bot. Medial	1.52 ± 1.59†	1.49 ± 0.12	1.51 ± 0.99
	3D – Bot. Middle	2.43 ± 0.09	1.63 ± 0.58	1.38 ± 0.14
	3D – Bot. Lateral	1.35 ± 0.55	2.43 ± 0.42	2.02 ± 1.32*
Positive Impulse (psi*ms)				
Facial	3D – Nasal	7.99 ± 0.28	14.61 ± 2.00	20.59 ± 2.60
	3D – Top Medial	6.84 ± 1.25	11.19 ± 3.86	22.52 ± 3.83
	3D – Top Middle	4.89 ± 0.63	9.25 ± 4.38	19.34 ± 1.13
	3D – Top Lateral	5.91 ± 1.04	12.54 ± 3.03	52.04 ± 34.65
	3D – Bot. Medial	8.71 ± 8.04†	23.89 ± 2.85	33.65 ± 17.95
	3D – Bot. Middle	12.42 ± 1.77	14.88 ± 3.24	24.18 ± 1.15
	3D – Bot. Lateral	7.28 ± 1.37	17.70 ± 6.18	26.26 ± 13.91*

*Only two tests at this level because one test did not return to zero after initial peak.

Discussion

Intraorbital Pressure Sensors

This study showed that the shock wave propagated through and within the intraorbital space. This yields credibility to one theory that shock waves may enter the skull through small openings in the bones of the skull (e.g., orbital foramen). However, it remains unclear whether the shock wave could propagate through small openings such as the optic canal *in vivo* due to the fact that other structures, such as the optic nerve, occupy this space. The optic nerve itself may be susceptible to damage from shock waves that propagate through the eye and orbital cavity.

Various experimental models using rodents have previously reported retinal and optic nerve damage following blast exposure. One study placed mice in a side-on configuration and reported chronic damage to both eyes [67]. Another study previously examined the optic nerve and retina for acute changes in these tissues following blast overpressure exposure up to approximately 17.5 psi in a rat model [68]. This study showed that both the optic nerve and retina experienced apoptosis following blast exposure. Recently, it was shown that both single and repeated exposure to blast overpressure caused retinal damage and optic nerve inflammation in rats [47]. Though there are differences in the methods of producing the blast overpressure for these studies, and the inherent limitation that a rodent model may not accurately translate to human injury, these preliminary studies all indicate the possibility of physiologic injury due to the propagation of a shock wave into the ocular space.

The synthetic and 3D orbits showed characteristically different shapes for the response of the intraorbital sensors. That is to say, the time to peak overpressure in the 3D orbit was delayed by approximately 0.5 ms. Conversely, the synthetic orbit shows a response much more similar to the idealized Friedlander waveform with peak overpressure closely following the ToA of the wave at the sensor location. The flat surfaces of the synthetic orbit provide a simplified response of intraorbital pressure propagation. The resulting pressure pulses for the synthetic orbit were more similar to the theoretical response to primary blast overpressure exposure than the 3D orbit pressure pulses. The complex surfaces of the 3D orbit provide a realistic geometry and the results of this boundary condition are very different from that of the synthetic orbit. The posterior sensor located on the frontal bone in both the synthetic and 3D orbit tests tended to record a higher overpressure than the three sensors located anterior to this one. This indicates that the pressure wave may be reflecting off the intraorbital surfaces and compounding the response; i.e, the waves may be interacting to effectively increase the peak magnitude of the wave beyond that was originally transmitted into the orbital cavity.

The addition of the spectacles and goggles on the 3D orbit did not have a considerable effect on the IOP response. However, the goggles attenuated the oscillating response of the intraorbital sensors that was observed in the unprotected eye and spectacle tests. This is likely caused by a reduction in the magnitude of the waves that propagated within the gelatin when the goggles were used. Photographs of the gelatin waves were shown in Chapter 4.

Facial Pressure Sensors

The general trends in facial pressure response were that the ToA was delayed and peak overpressure decreased as the pressure sensor location moved medially-laterally across the face. This was due to the expected reduction in pressure as the wave propagated to locations further away from the bursting membrane as well wave propagation around the curved surface of the face. As the pressure sensor location moved medially-laterally across the face, the sensing elements became less normal to the direction of shock wave propagation. As such, these sensors measured decreasing amounts of dynamic pressure, thereby decreasing the overall peak pressure at these locations. Furthermore, energy was effectively lost as the wave traveled down the tube and around the face. These trends are consistent with the physics of blast wave propagation as well as the type of pressure measured by sensors.

Experiments with the goggles recorded an oscillating response on the temporal sensor. This was attributed to the "slapping" of the goggles on the sensing surface of this sensor. Consequently, the addition of protective equipment may make the body susceptible to relatively minor secondary blast injuries such as contusions or lacerations that could be caused by the spectacles or goggles themselves. That is to say, without protective equipment, the secondary effects of impacting the face with the spectacles or goggles would not exist. Potential injuries such as bruising of the forehead and cheek caused by loading the spectacles or goggles will likely be minor in comparison to their protective effects from other secondary blast injuries. However, the magnitude of force applied to the face by the "slapping" of the goggles was likely small and well below the injury threshold for serious injury. Additionally, it was shown in Chapter 4 that the use of spectacles or goggles reduced the pressure transmitted into the orbital space, and absorbs and dissipates loading of the pressure wave.

Response Corridors

The development of response corridors remains debated within the field of injury biomechanics. Two published studies notably describe techniques to develop response corridors for biological specimens that have been used since their original publication in 2004 [69, 70]. These exemplify techniques using postmortem human surrogate data from blunt thoracic impacts to develop response corridors for the chest. The first describes a technique for time-based responses that

uses discreet points chosen along the general path of the response to define a corridor [69]. This technique remains subjective, as the discreet points chosen to develop corridors are only loosely defined. The second describes a rigorous, repeatable technique that removes the subjectivity of the corridors [70]. This normalization technique uses a characteristic average response with ellipse corridors based on horizontal and vertical standard deviations to preserve the overall shape of the individual data traces. Arguably, this works well for structural response corridors (force-deflection corridors) but does not work well for time-based responses. Therefore, the current study is dissimilar from both of these techniques.

Conclusions

This study provides novel experimental data for wave propagation within the human orbit and around the face that can be used to validate computational and physical models of the eye and face. Pressure response corridors for pressure measurement locations within the orbit and around the face were quantified for three scenarios: unprotected eye, eye with spectacles, and eye with goggles. The shape of the bony human orbit produced a complex response that indicated the wave was reflecting and interacting within this space. The delayed time of arrival and decreased magnitude of the pressure measured as sensor location varied medial-temporally across the face showed that the pressure wave propagated around the face as anticipated. Average shock wave parameters (time of arrival, peak overpressure, positive duration, and positive impulse) were quantified for each location. The benefit of these data beyond their theoretical calculations is that these experiments account for the effects of a biofidelic geometry. Computational models of the eye and face can use these specific pressure measurement locations to match the response of individual geometries and models. It is possible that select computational models might account for the additional structures within the eye as well as the skin and underlying bones of the face, thereby providing additional biofidelity of the response of the model system.

Chapter 6

Evaluating the FOCUS Headform Eye for Exposure to Primary Blast Overpressure

Introduction

Anthropomorphic test devices (ATDs), which are colloquially referred to as 'crash test dummies', are frequently used to assess trauma in lieu of experimental tests using human cadavers. However, for an ATD to simulate a realistic response, it must first be validated for the loading regime at which testing will occur. Historically, ATDs were developed for automotive safety, with crash pulses on the order of 100 ms in duration. The increase in blast-related injuries in recent military conflicts necessitates an understanding of specific injury mechanisms associated with blast loading conditions. Blast events are an order of magnitude shorter than a typical car crash pulse, often between 2-5 ms in duration. Given the near-instantaneous increase in pressure associated with a blast, a blast pressure pulse varies not only in duration but also in pulse shape when compared to automotive crash pulses. Therefore, ATDs that were originally designed and validated for assessing injury at automotive collision loading rates may not provide an accurate assessment of injury risk during blast loading events.

The Facial and Ocular CountermeasUre Safety (FOCUS) headform is an advanced ATD headform originally designed and validated for blunt impacts to the eye and face (Humanetics Innovative Solutions, Plymouth, MI, USA) (**Figure 7**). ATD headforms are often instrumented with triaxial accelerometer arrays and angular rate sensors to quantify head acceleration and angular velocity during impacts. The FOCUS headform is unique in that in addition to a triaxial accelerometer array, it has eight facial bone segments and two eyes instrumented with load cells (**Figure 7**). Injury risk curves were previously developed using peak load and validated for blunt loading with experimental data from matched tests using cadavers [62]. Additionally, the size and geometry of the FOCUS headform was developed to be representative of a 50th percentile male soldier and has a more realistic geometry than other headforms. Therefore, the FOCUS headform is the best option for a headform that can potentially assess injury risk during blast loading events that mimic *in theatre* military scenarios. However, data from various

experimental cadaveric models of blast loading to the eye and face is needed to validate the response of the FOCUS headform during these events.

Previously, low-level blast tests were conducted on isolated human eyes using fireworks and homemade charges [40]. This study measured pressure in and around the eye to quantify the response of the eye and predict injury risk associated with explosions that mimicked low-level blast loading. The purpose of the current study is to expose the FOCUS headform to a similar test matrix, compare the response of the isolated human eye and the FOCUS eye, and to evaluate the ability of the FOCUS headform eye to predict eye injury risk for blast loading rates.

Methods

A total of nine tests were conducted on the FOCUS headform that was instrumented with the left eye load cell (Model 8065J, Humanetics Innovative Solutions, Plymouth, MI, USA). The experimental test setup was described in detail previously for the isolated human eye tests, and modified for the current test series [40]. Briefly, the FOCUS headform was rigidly attached to a custom metal frame using the standard Hybrid III neck and lower neck bracket. The headform was mounted such that it was oriented face-down at a distance of approximately 3 ft from the ground (**Figure 53**). Custom 10 g charges of Pyrex® gunpowder were exploded at 8.66” (22 cm), 4.7” (12 cm), or 2.75” (7 cm) from the cornea of the eye. As many commercial fireworks were found to explode inconsistently, the charges were designed to repeatedly simulate the severity of commercial fireworks. These pressure levels are referred to herein as ‘low’, ‘medium’, or ‘high’. The charge was offset from the eye by 0.79” (2 cm) in the superior direction (i.e., toward the forehead) in order to minimize the amount of debris projected directly at the eye.

FOCUS Headform Blast Testing

Figure 53. FOCUS headform blast test setup.
(**Note:** The side frame sensor is out of the image.)

A total of six pressure sensors (Model 113B21, PCB Piezotronics, Depew, NY, USA) were mounted around the eye and to the frame (**Figure 54**). The sensor array consisted of a total pressure sensor ('total') and a static pressure sensors ('static') adjacent to the eye, two static pressure sensors ('static 1', 'static 2') mounted 1.18" apart in a polycarbonate airfoil-shaped block, one total pressure sensor ('top') mounted on top of the metal frame, and one static pressure sensor ('side') mounted to the side of the metal frame. The two pressure sensors mounted to the metal frame were used to measure the blast wave at minimally-reflecting surfaces surrounding the eye. As the test setup was designed to measure primary blasts in an open field, pressures measured from the frame-mounted sensors ensured that possible reflected waves would cause insignificant pressure change or damage to the eye. While both eyes were placed in the FOCUS headform, load was measured only using the left FOCUS eye load cell.

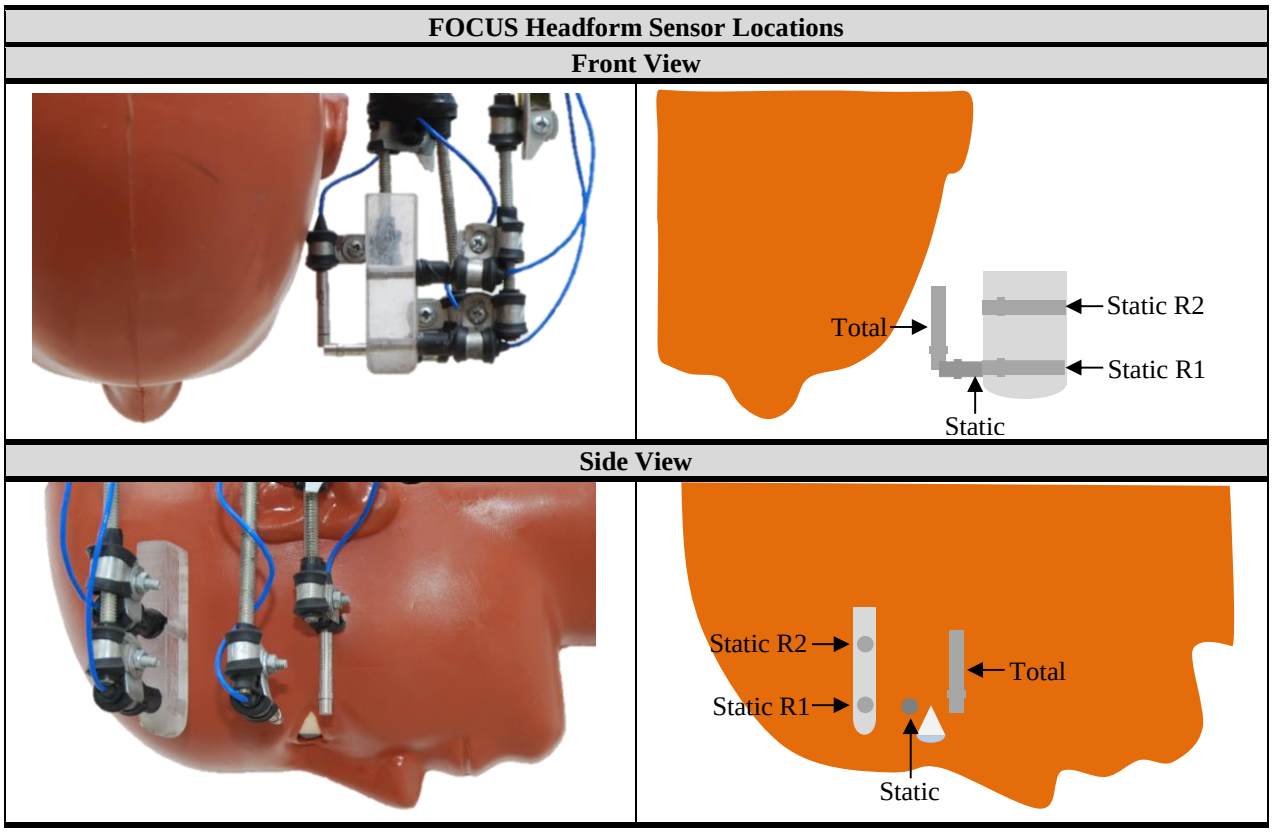

Figure 54. FOCUS headform sensor locations.

All pressure and load cell data were collected at 301.887 kHz (TDAS PRO, Diversified Technical Systems, Inc., Seal beach, CA, USA). The standard TDAS PRO anti-aliasing filter (4,300 Hz) was bypassed for this test series since the frequency content of the overpressure event exceeds 4,300 Hz. However, the TDAS PRO sensor input modules (SIM) have a bandwidth of 0-25 kHz, which acts as a low-pass filter with a frequency cutoff of 25 kHz. A Phantom v9.1 camera (Vision Research, Wayne, NJ, USA) was used to capture high speed video at 20k frames per second with a resolution of 256x192 pixels. A custom MATLAB® script (version 7.11.0.584 (R2010b), The MathWorks, Inc., Natick, MA) was used to quantify peak pressure or load for each sensor location. The time of arrival (ToA) of the pressure wave at the two static pressure sensors mounted in the airfoil was used to quantify wave velocity. One-way ANOVA was used to determine statistical significance (α=0.05) between the current FOCUS eye tests and the previously published human eye tests for matched locations.

Eye injury risk for the FOCUS eye tests was quantified using previously published injury risk curves for peak load [62]. These injury risk curves were developed using projectile impacts, and the final curves are specific to impactor size (3.2 mm, 4.5 mm, 6.4 mm, 9.5 mm, 12.7 mm, 15.9

mm, and 17.5 mm). Injury risk was calculated using each impactor size for comparison of injury risk prediction. It should be noted that the largest impactor size (17.4 mm diameter) most closely matched the area of the unprotected eye.

Results

Figure 55 shows the relationship between FOCUS eye load and human eye intraocular pressure during matched overpressure events. The relationship shows that while the FOCUS eye load cells were not originally validated for blast events, the response of the FOCUS eye is almost linearly proportional to the pressure response of human eyes exposed to matched overpressure levels. Shock wave velocity for all tests is plotted in **Figure 56**. Although increasing standoff distance decreased the shock wave velocity, all FOCUS tests were conducted above the speed of sound in air, or Mach 1. Two of the human eye tests were conducted just under Mach 1.

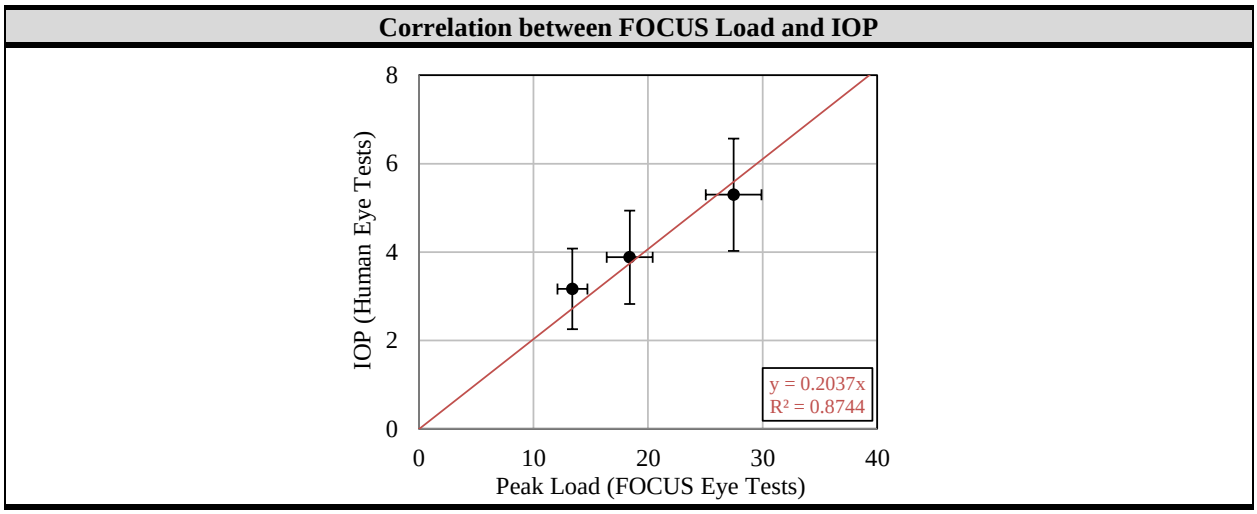

Figure 55. Correlation between average FOCUS eye load and average human IOP.

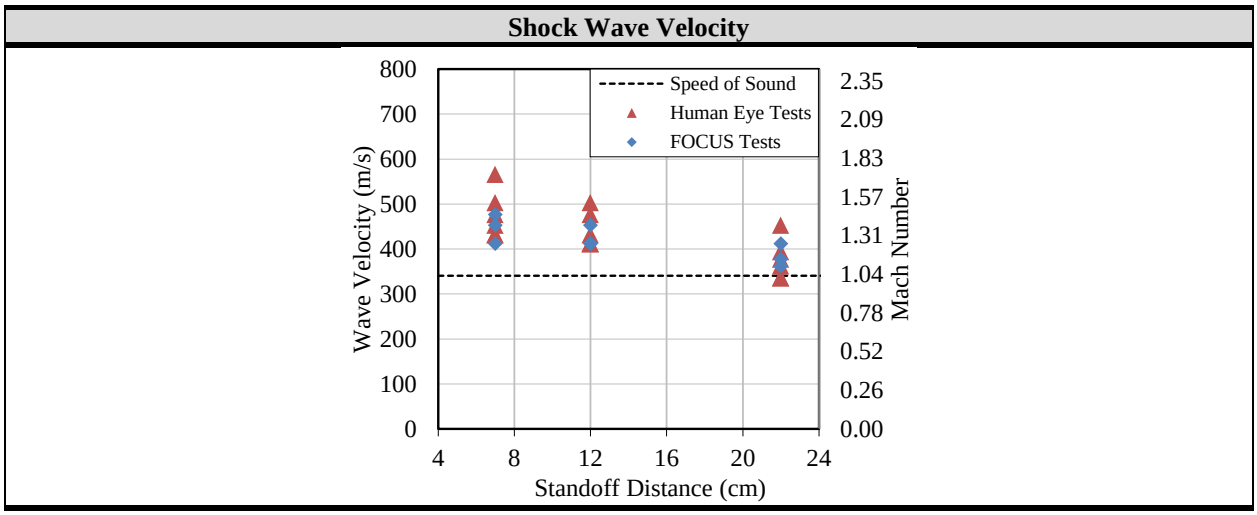

Figure 56. Shock wave velocity based on standoff distance.

Response of the load cell to each test is shown in **Figure 57**. Injury risk for hyphema, lens damage, retinal damage, and globe rupture was calculated based on peak load, using the correlations for all seven projectile sizes. The eye injury risk function developed for a 17.4 mm projectile, which is comparable to the area of the unprotected eye affected by blast loading, predicted negligible eye injury risk. Specifically, all tests resulted predicted injury risk <1% for these injuries. Comparatively, injury risk was still <1% for these injuries even using the most conservative eye injury risk functions developed for the 3.2 mm projectile. This is consistent with the experimental results and calculated injury risk for isolated human eyes exposed to the same overpressure loading conditions published previously [40]. **Figure 58** compares injury risk for hyphema, lens damage, retinal damage, and globe rupture using all seven projectile sizes.

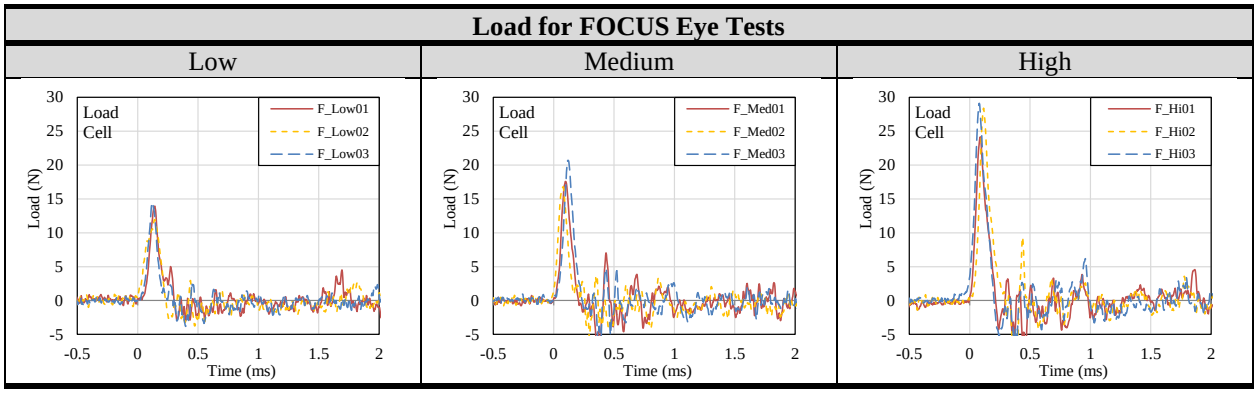

Figure 57. Load cell traces for FOCUS eye tests.

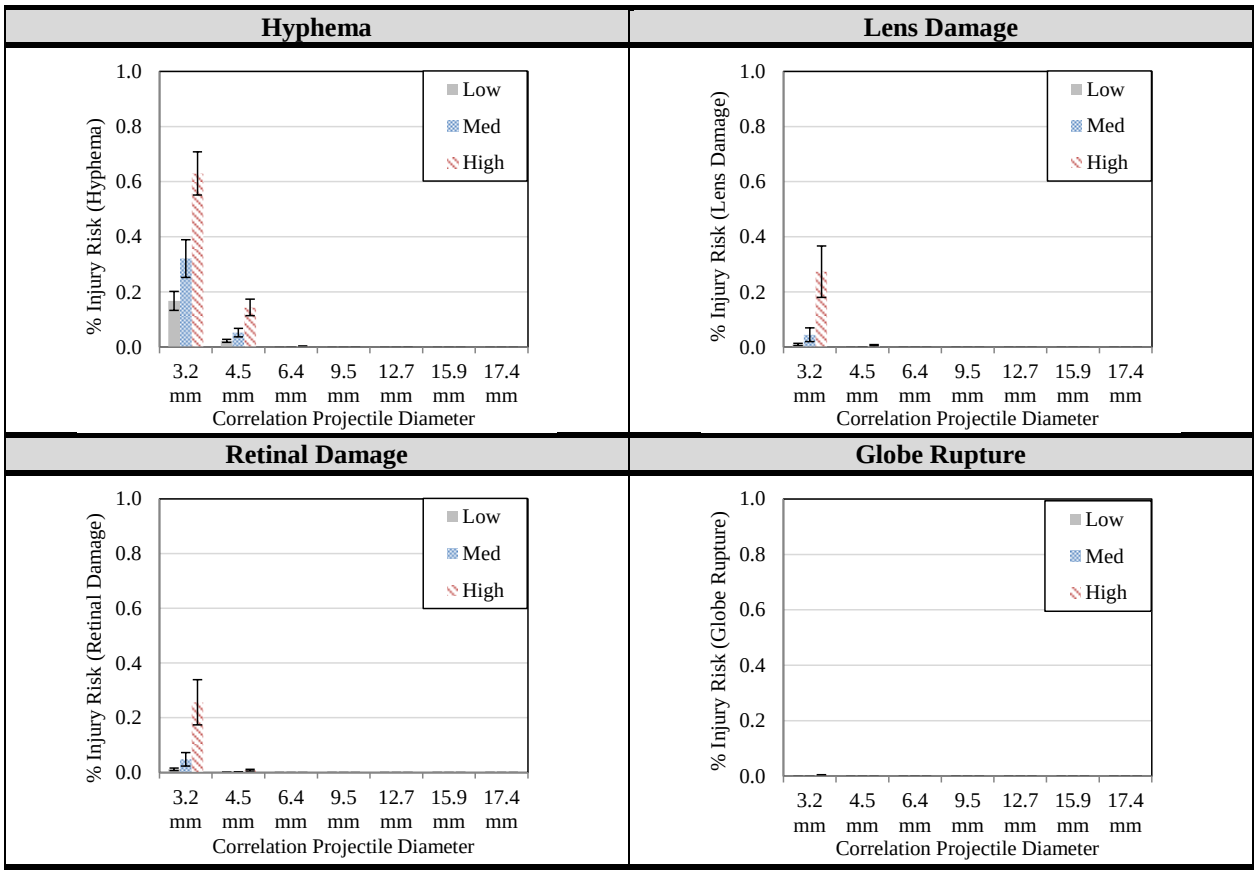

Figure 58. Eye injury risk for FOCUS eye tests predicted using peak load.

Peak overpressure decreased with decreasing distance between the charge and eye for all sensor locations. Peak overpressure was significantly higher for the FOCUS eye tests than the human eye tests at the high test level for the total and static block 2 sensors locations (**Figure 59**). Peak overpressure was significantly higher for the human eye tests than the FOCUS eye tests at all test levels for the top frame location and at the low test level for the side frame level (**Figure 59**).

The time histories of the total and static overpressure for the FOCUS tests were plotted along with human tests by standoff distance for comparison in **Figure 60** and **Figure 61**. The pressure pulses measured during FOCUS eye testing were extremely similar to the pressure pulses measured during the human eye testing, and were therefore considered matched tests.

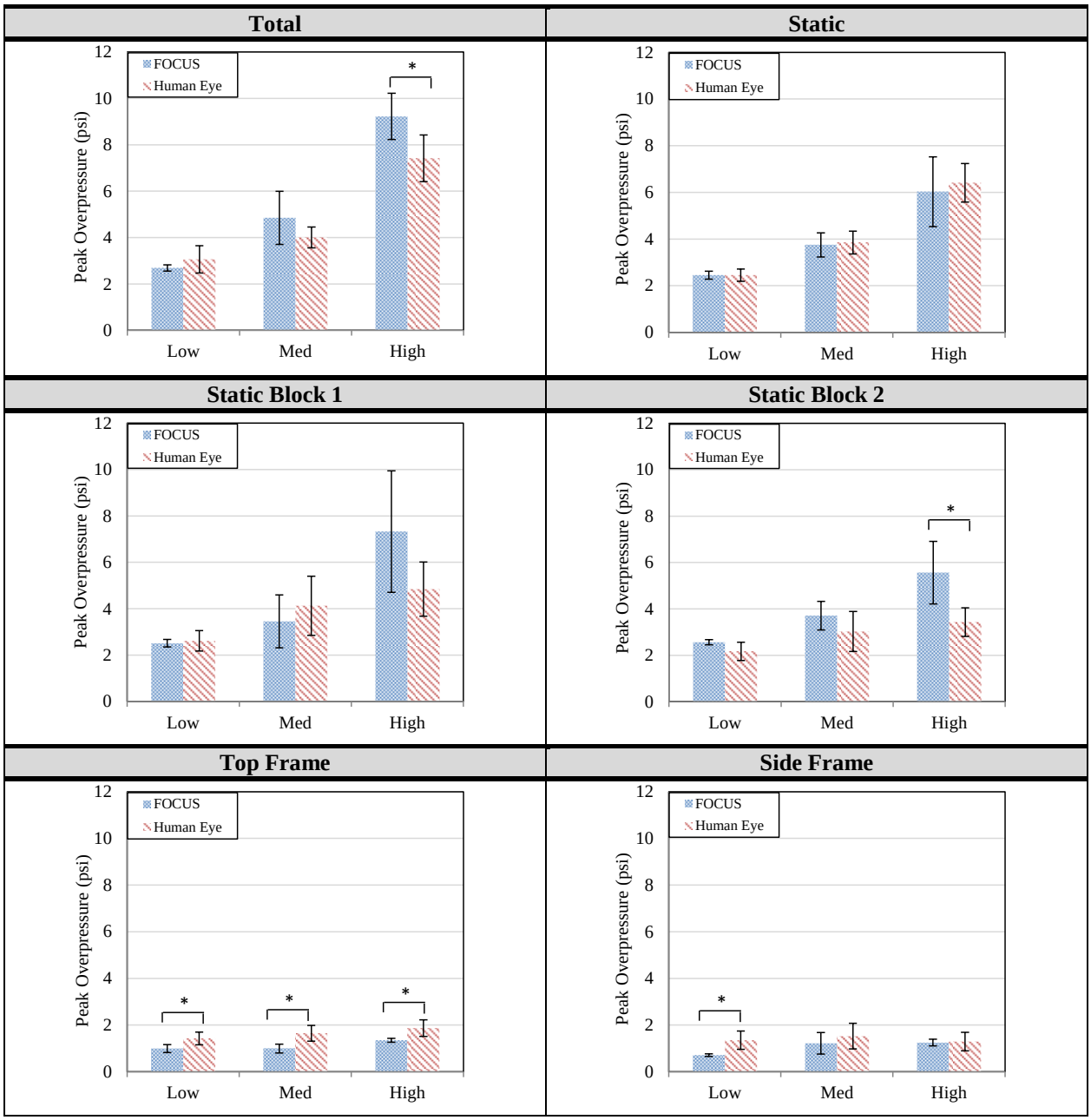

Figure 59. Peak overpressure around the eye for FOCUS and human eye tests.

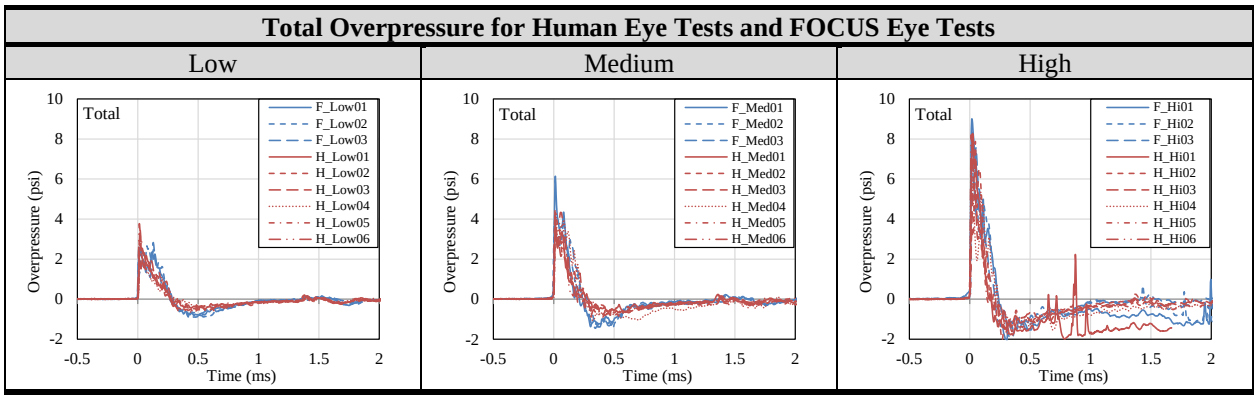

Figure 60. Total overpressure traces for human and FOCUS eye tests.

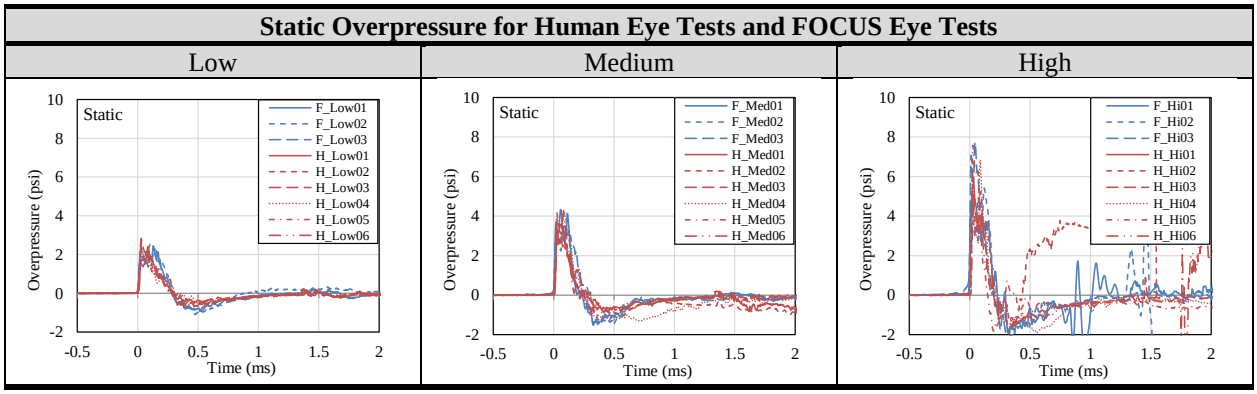

Figure 61. Static overpressure traces for human and FOCUS eye tests.

Despite the offset in charge location with respect to the front of FOCUS headform, unspent gunpowder was projected onto the FOCUS headform face during testing. Increasing the standoff distance (decreasing severity) produced less projected material. As standoff distance decreased (increasing severity), the pattern of gunpowder concentrated around the forehead and orbit. Analysis of the high speed video confirms the increase in the amount of gunpowder that impacted the face with decreasing standoff distance. Post-test photographs for a single test at each test level are shown in **Figure 62**. The human eye testing reported similar results.

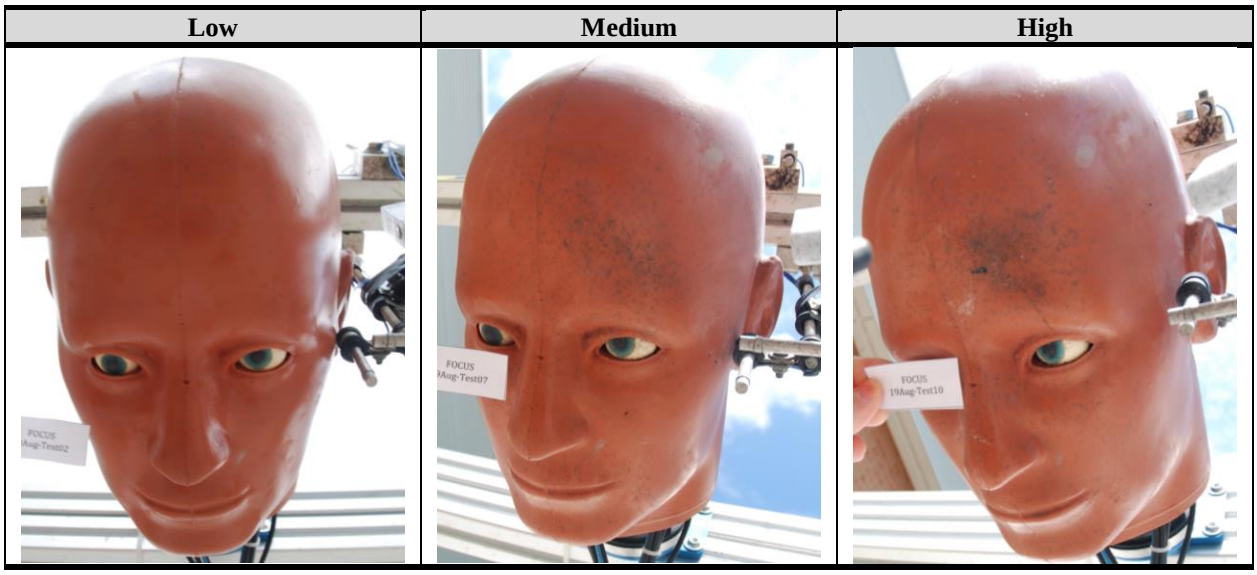

Figure 62. Projected unspent gunpowder on FOUCS headform after blast testing.

Discussion

The low calculated injury risk determined via the FOCUS eye load cell is consistent with the human eye experimental findings and associated injury risk. The correlation between FOCUS eye force and intraocular pressure as well as the agreement of injury risk between FOCUS and human eye tests indicate that the current FOCUS eye and orbit assembly could be used for evaluating injury risk using peak load measured during overpressure events similar to those evaluated in the current study. Despite obvious differences in boundary conditions surrounding the eye for the FOCUS eye and human eye tests, the similarities in the test setup and pressure measurement allows for the comparison between injury risk calculated from the load cell in the FOCUS eye tests and injury risk calculated from peak intraocular overpressure in the human eye tests. However, it must be noted that the load cell recorded a pulse that was more similar in shape to blunt loading than to typical blast loading. This could affect the overall response of the system to primary blast overpressure loading.

Peak overpressure measured at the top of the frame was statistically higher for the human eye tests than for the FOCUS eye tests. This is likely due to the addition of the FOCUS headform, which was located between the charge and the top sensor. This caused the pressure wave to reflect off the headform, thereby decreasing the peak pressure observed above the head compared to the isolated eye tests.

Limitations

The current study has a number of limitations. This study examines test pressure levels that are very low. Although the FOCUS eye load cell predicted injury risk similar to the injury risk predicted using IOP from human eyes exposed to the same loading conditions, it is unclear if the load cell would continue to produce matched responses at higher, more lethal blast levels. Despite the fact that care was taken to minimize the effects of projected material, the FOCUS headform was still subjected to debris from the charge. Other methods for simulating primary blast, such as a shock tube, could be used for future studies to eliminate debris. While the FOCUS test results are compared to human eye tests conducted with a similar test setup, the FOCUS accounts for the entire geometry of the face while the human eye tests were conducted in isolation. The additional structures around the eye (e.g., the forehead, nose, and chin) can affect the overall response of the system due to the reflection of the pressure wave off of these. Furthermore, the area-specific injury risk curves used to predict eye injuries can affect the overall accuracy of the FOCUS headform as a system. These injury risk curves were originally developed for blunt loading, and may not be a direct correlate to injury induced during blast loading. Future work in this field could produce blast-specific injury risk curves, thereby improving upon the selection of the correlation for predicted eye injury risk.

Conclusions

This study illustrated that the FOCUS headform could be used to predict eye injury risk using peak load for low-level overpressure loading event. The matched injury risk prediction between previously published human eye tests and the current FOCUS eye tests serves as a proof of concept that the FOCUS could be able to predict injuries similar to those predicted using peak intraocular pressure in human cadaver eyes. Therefore, the FOCUS headform and eye load cell was validated for predicting eye injury risk for low-level primary blast overpressure (<10 psi static overpressure). Future work examining other methods for injury risk prediction should be evaluated. Furthermore, the FOCUS headform should be tested and evaluated at higher pressure levels that could lead to more severe injuries.

Chapter 7

An Area-Sensitive Synthetic Eye that Differentiates between Blunt and Blast Loading

Introduction

The Facial and Ocular CountermeasUre Safety (FOCUS) headform is an advanced anthropometric test device (ATD) specifically designed to quantify and assess injury risk due to facial and ocular loading. It has eight segments that represent facial bones (two frontal, two zygoma, two maxilla, one mandible, one nasal) and two eyes (**Figure 7**). Each bone segment and eye is instrumented with a load cell, allowing the FOCUS to quantify the load applied to each region during loading.

A three-part study provided data to develop and validate the FOCUS eye for blunt loading injury risk assessment. First, human cadaver eyes and synthetic eyes were tested in isolation to quantify the force-deflection response of the eye [71]. Next, human cadaver eyes were tested *in situ* with and without ocular muscles intact, and synthetic eyes were tested in a simulated orbit. It was determined that the effect of extraocular muscles was negligible in considering the response of the eye [72]. Lastly, the synthetic eye was placed in the FOCUS headform and exposed to 82 impacts from BBs to quantify injury risk. Nearly 400 blunt impact tests were conducted beyond this initial study using six spherical projectiles varying in size from 3.2 mm to 17.5 mm in diameter [62]. Using the peak load reported by the FOCUS eye load cell for each of the impacts reported in this study, injury risk functions for hyphema, lens damage, retinal damage, and globe rupture were developed for each projectile. It was determined from this work that the eye load cell response was proportional and highly correlated to the normalized energy of the projectile, which requires the projected area of the impactor to be known. However, in contrast to earlier efforts to develop eye injury functions with logistic regression, the final risk functions presented were determined using survival analysis, which is more robust. The final recommended risk functions employ survival analysis using a maximum likelihood method and a Weibull distribution to estimate parameters. Using this methodology, final eye injury risk functions and 5%-95% confidence intervals were presented for hyphema, lens damage, retinal damage, as well as globe rupture based on peak load measured with the eye load cell.

The limitation of current the method for assessing eye injury risk is that contact or "affected" area of the eye must be known. However, the size and shape of the insulting object are rarely known in most cases of blunt eye trauma. Additionally, blast loading presents a unique loading scenario in which there is no physical "impactor" comparable to blunt loading. While a conservative estimate of projectile size can be used to evaluate injury risk when the insulting object is unknown (i.e. calculating injury risk using correlations for the smallest projectile), this could lead to an overestimation of injury risk. When projectile characteristics are unknown or there is no known projectile impact, as is the case with blast overpressure exposure, it becomes necessary to develop another method of quantifying the affected area of the eye. Therefore, the purpose this study is to develop an area-sensitive FOCUS eye and evaluate its ability to both distinguish between various impactor sizes in blunt trauma as well as distinguish between blunt loading and blast loading.

Methods

The current FOCUS eye was modified to create an area-sensitive eye (**Figure 63**). This was done by bisecting the eye at 40% of the anterior-posterior depth of the eye. An array of nine miniature pressure sensors (Model 060, 100 psi, Precision Measurement Company, Ann Arbor, MI) was placed along the posterior half of the cut surface. This array was designed to distinguish between small (6.5 mm dia.), medium (12.7 mm dia.), and large (17.5 mm dia.) impactor sizes during direct corneal impacts. A thin layer of silicon adhesive was used to secure the anterior half of the cut surface to the posterior half.

FOCUS Eye	Bisected Eye	Pressure Sensor Array	Silicon Adhesive
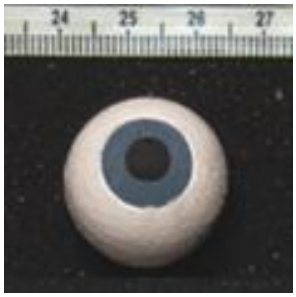	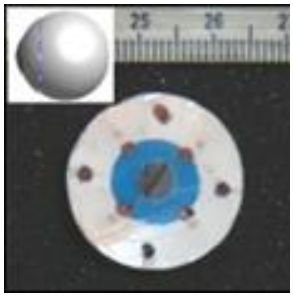	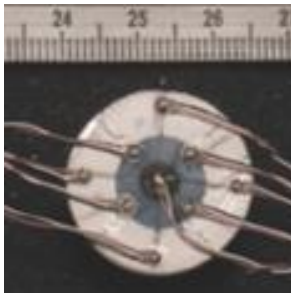	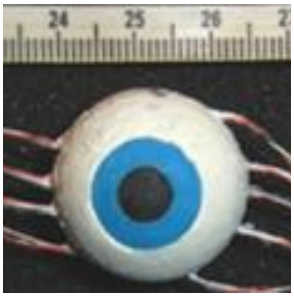

Figure 63. Area-sensitive FOCUS eye development.

The area-sensitive eye was tested in blunt and blast loading conditions in an isolated eye test setup. The area-sensitive eye was placed in a similar test setup as the one used for the

experimental isolated porcine eye blast loading test described previously in Chapter 3 (**Figure 64**, right). This consisted of a rigid concave cup that minimized boundary conditions around the eye. The eye was secured in place within this rigid concave cup using a small amount of silicon adhesive. The FOCUS eye load cell was attached to the back side of the rigid concave cup for both blunt and blast tests.

Blunt impact tests were conducted with a drop tower system using three different impactor tips: 6.4 mm, 12.7 mm, and 17.5 mm (**Figure 64**, left). Tests were conducted in triplicate at two drop heights (12 in. and 24 in.) to simulate multiple impacting energies. Mass of the impactor (175 g) was consistent for all tests. Blunt tests were designed for a direct corneal impact for this test series. Blast tests were conducted in triplicate at 10 psi, 20 psi, and 30 psi to simulate survivable pressure levels using the VT ABS (**Figure 4**). Pressure was measured at a number of locations around the eye for these tests. Static overpressure in the fluid flow was measured using a "pencil" sensor mounted 2 inches from the temporal side of the orbit (Model 137A24, PCB Piezotronics, Depew, NY, USA). The sensing element of the pencil sensor was aligned with the front of the cornea. Total overpressure was measured for the isolated eye condition using a sensor mounted above the eye (Model 113B21, PCB Piezotronics, Depew, NY, USA). Static overpressure was also measured along the wall for comparison with other tests (Model 102B16, PCB Piezotronics, Depew, NY, USA).

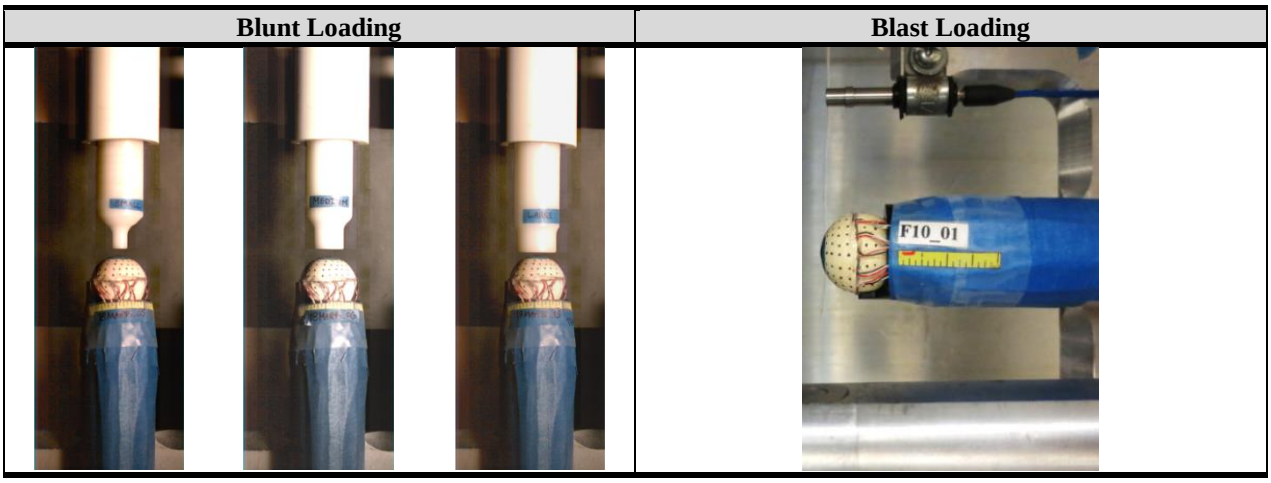

Figure 64. Experimental test setups for the area-sensitive eye for blunt and blast loading.

All data were collected at 38 kHz for blunt tests and at 301.887 kHz for blast tests (TDAS PRO, Diversified Technical Systems, Inc., Seal Beach, CA). The standard TDAS PRO anti-aliasing filter was bypassed for the blast tests because the frequency content of the blast overpressure exceeded the 4,300 Hz cutoff frequency. However, the TDAS PRO sensor input modules (SIMs) bandwidth of 0-25 kHz acts as a low-pass filter with a frequency cutoff of 25 kHz. All pressure and load data were zeroed prior to the event. A custom MATLAB® script (version 7.11.0.584 (R2010b), The MathWorks, Inc., Natick, MA) was used to quantify pulse parameters (peak pressure, positive duration, and positive impulse) for each sensor for all tests. High speed video of each test was captured at 1000 fps for blunt tests and 10 kfps for blast tests (v9.1, Vision Research, Wayne, NJ).

The array of pressure sensors was analyzed as a system; the simultaneous response of all nine pressure sensors was assessed for both peak pressure and positive duration in order to create characteristic response profiles for each loading condition. Positive impulse, which takes into account both the peak pressure and the positive duration of the pulse, did not provide additional sensitivity to distinguish between loading types and was therefore excluded from the current analysis to prevent redundancy. Normalized peak pressure was quantified by dividing the peak pressure from each channel by the maximum peak pressure value of all nine pressure sensors in the eye. Thresholds for positive duration and normalized peak pressure were quantified at values that were chosen to distinguish between blunt loading and blast loading. Where possible, thresholds to further distinguish between blunt loading impactor sizes and blast test levels were

also quantified. Furthermore, peak pressure for the area-sensitive eye blast tests was compared to the peak pressure for the unprotected isolated porcine eye tests conducted in Chapter 3.

The maximum force recorded by the eye load cell during each test was used to quantify injury risk using the current FOCUS headform injury risk curves. As this calculation requires choosing an appropriate size-specific correlation, the correlation was chosen *a priori* based on the test type. That is to say, for the blunt tests, the size-specific correlation matched the test impactor diameter closely. The largest impactor size was chosen for the blast tests because its size best matches the area of an unprotected eye.

Results

Figure 65 and **Figure 66** show representative pressure traces for the pressure sensor array during blunt and blast loading, respectively. These figures show characteristically different responses for blunt and blast loading. The notable differences in peak pressure and positive duration of the pulses indicate that these parameters can be used to distinguish between blunt and blast loading. Pulse parameters (peak pressure, positive duration, and positive impulse) for all sensor locations are summarized in **Figure 67**. Normalized peak pressure for all tests is shown in **Figure 68**. Thresholds for normalized peak overpressure are given in **Table 23**. Positive duration for all tests is shown in **Figure 69**. Thresholds for positive duration are given in **Table 24.** Channel 7 of the nine-sensor array was excluded from the analyses presented herein, because it consistently responded differently from the three other sensors in the outer "ring". It is possible that this sensor was damaged during preparation of the area-sensitive eye. The area-sensitive FOCUS eye recorded peak pressures in the sensor array that were similar to those recorded for the isolated porcine eye blast tests conducted in Chapter 3 (**Figure 70**).

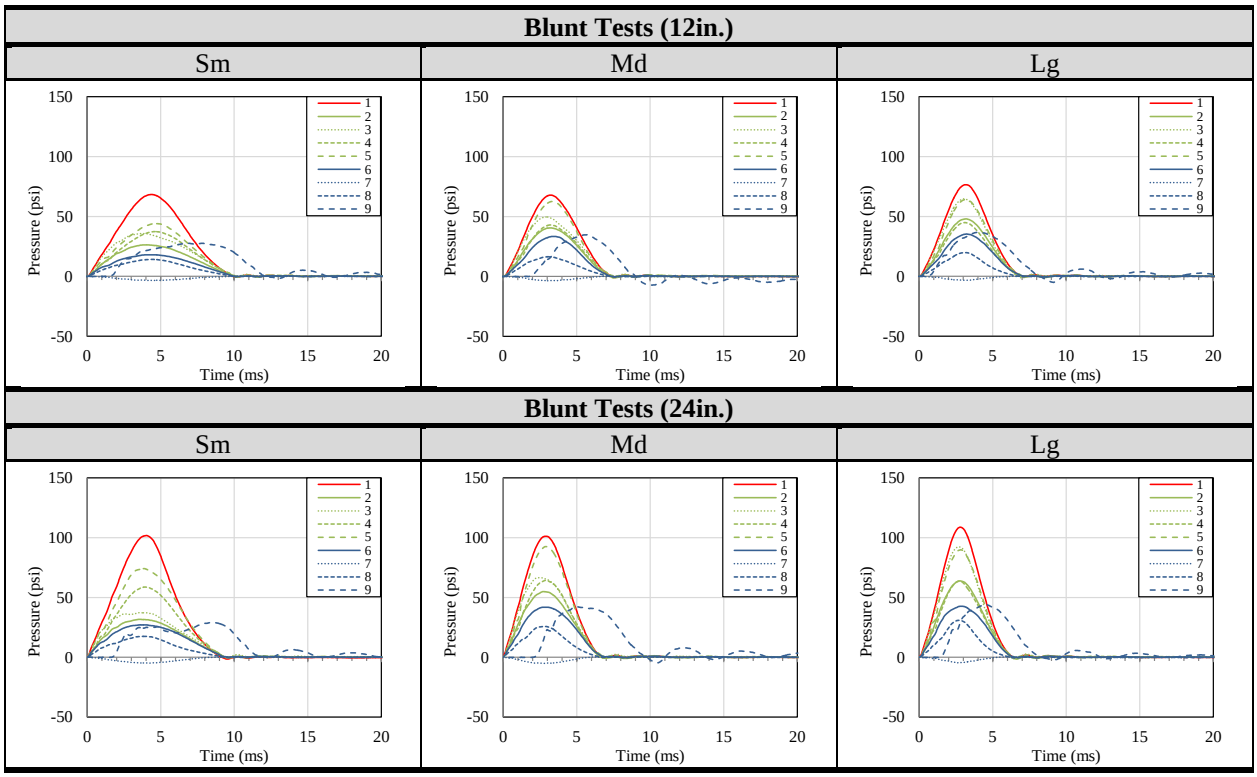

Figure 65. Characteristic responses of area-sensitive FOCUS eye to blunt loading.

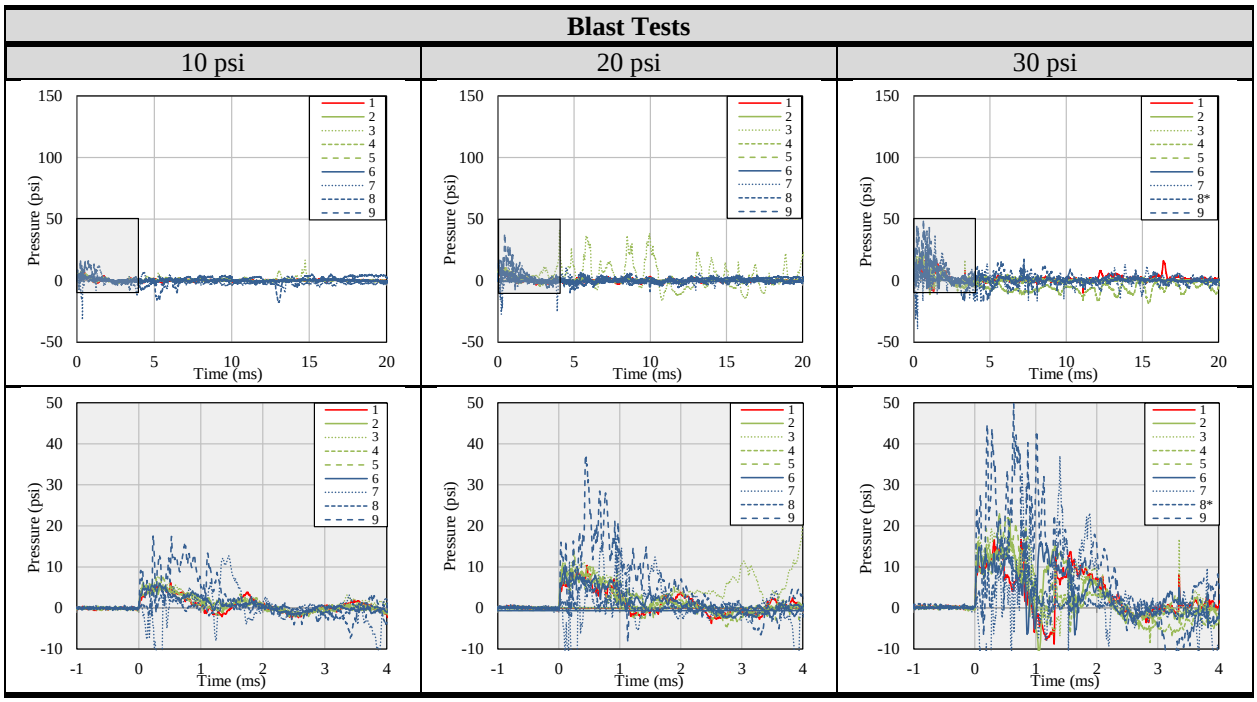

Figure 66. Characteristic responses of area-sensitive FOCUS eye to blast loading.
Note: bottom graphs are zoomed in views of the blast event.

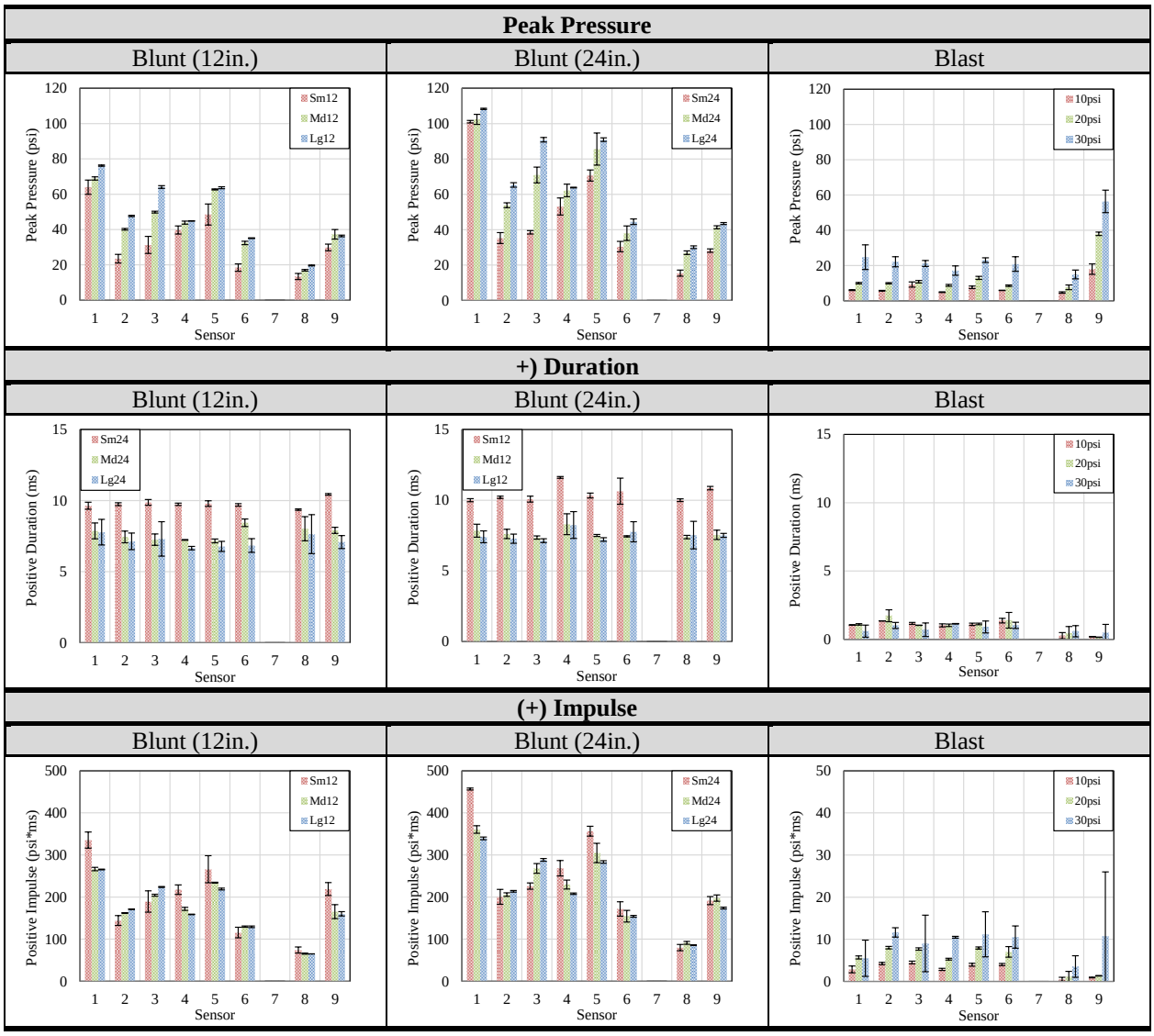

Figure 67. Pulse parameters for sensor array in area-sensitive FOCUS eye.

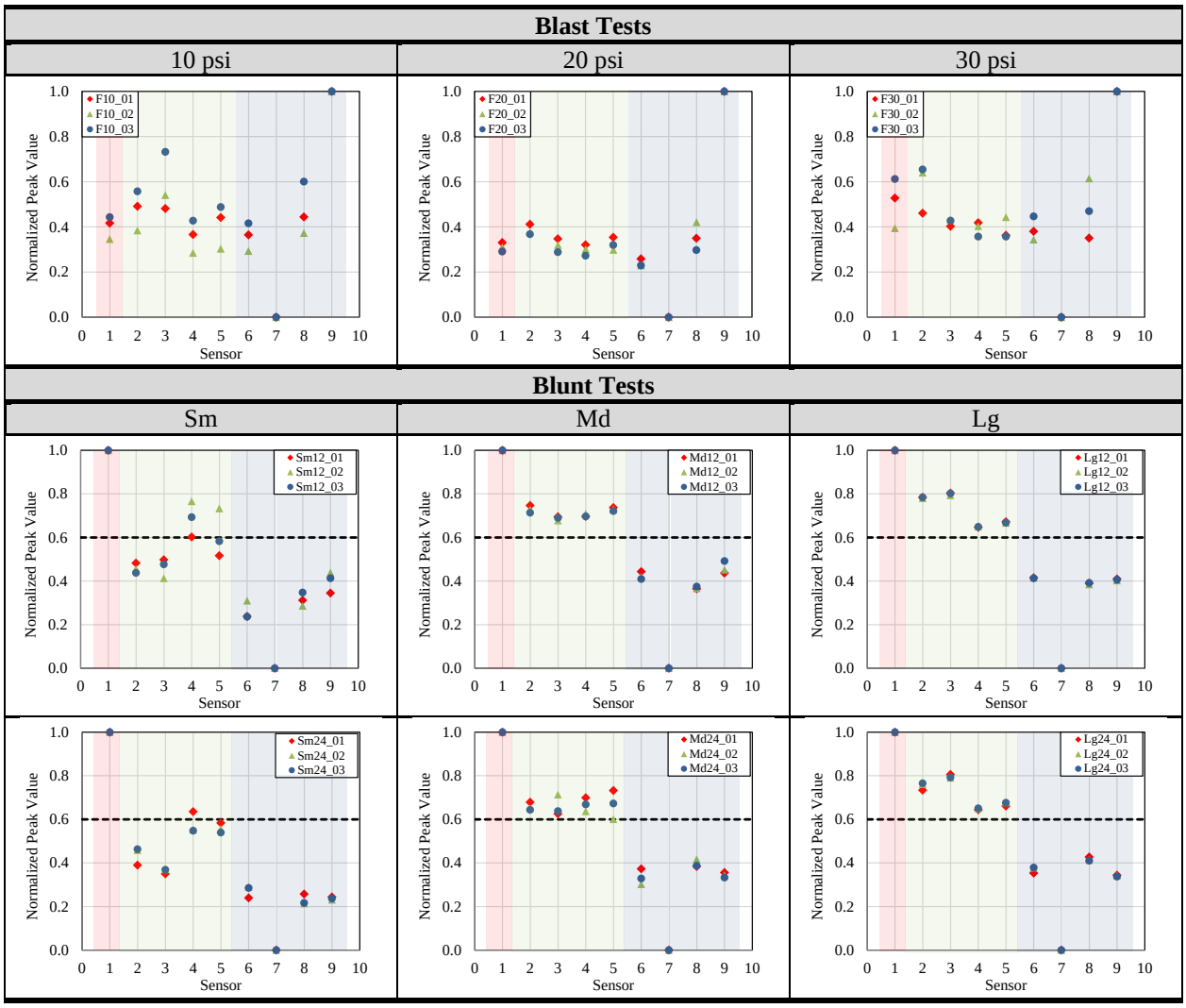

Figure 68. Normalized peak pressure area-sensitive FOCUS eye tests.

Table 23. Normalized peak pressure thresholds for area-sensitive FOCUS eye.

Blunt v. Blast Loading	
Blunt Loading	"Bullseye" loading with highest magnitude at center sensor.
Blast Loading	All sensors approximately same magnitude at same time.
Blunt Loading	
Small Projectile	Not all middle sensors above 60% maximum. All outer sensors below 60% maximum.
Medium Projectile	All middle sensors above 60% maximum. All outer sensors below 60% maximum.
Large Projectile	
Blast Loading	
10 psi	Cannot distinguish between chosen pressure levels.
20 psi	
30 psi	

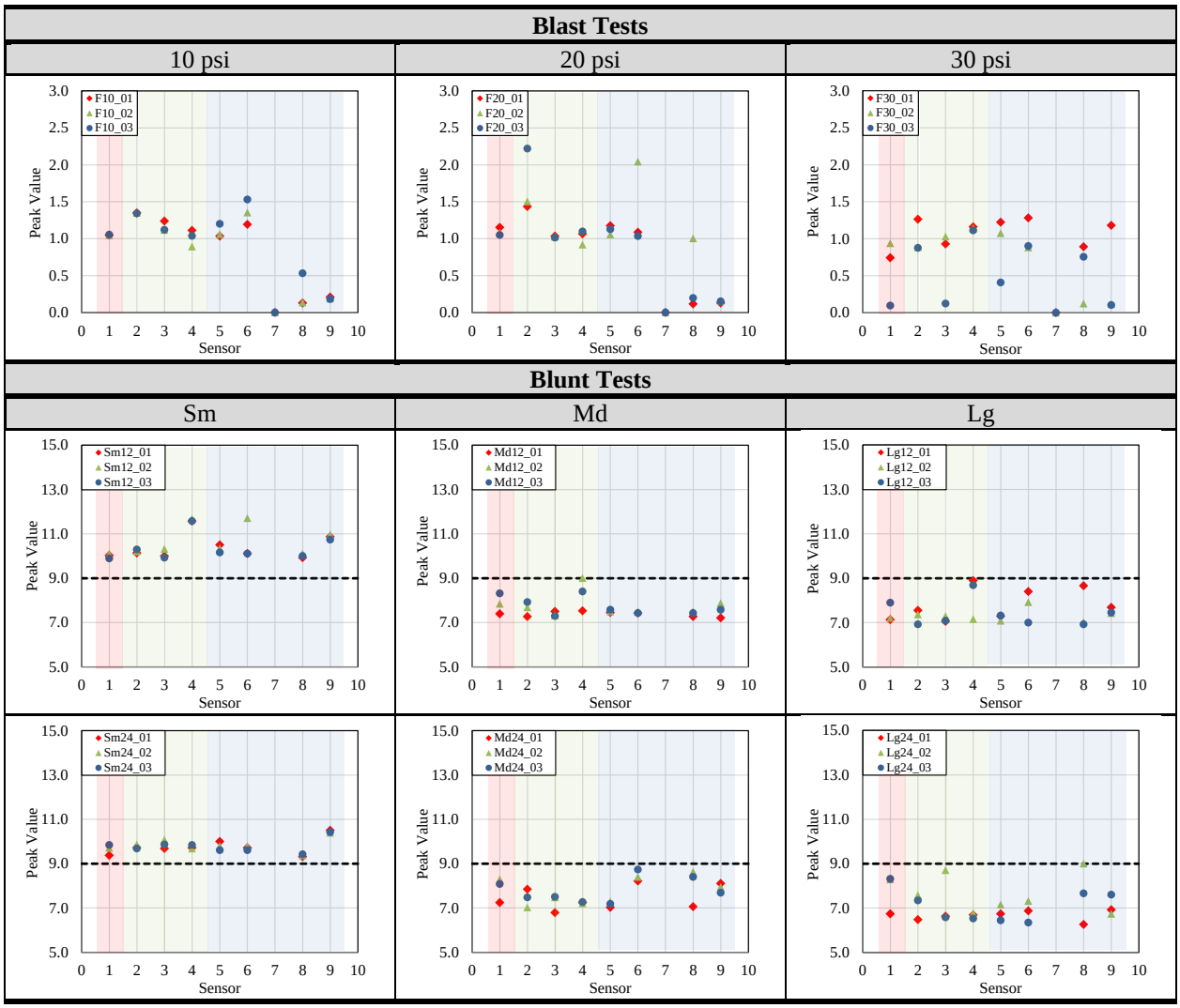

Figure 69. Positive duration for area-sensitive FOCUS eye tests.

Table 24. Positive duration thresholds for area-sensitive FOCUS eye.

Blunt v. Blast Loading	
Blunt Loading	Duration >3 ms.
Blast Loading	Duration <3 ms.
Blunt Loading	
Small Projectile	Duration >9ms.
Medium Projectile	Duration <9ms.
Large Projectile	
Blast Loading	
10 psi	Cannot distinguish between chosen pressure levels.
20 psi	
30 psi	

Injury risk was predicted using peak load (**Table 25**). Normalized energy was calculated using the correlation from the projectile size that most closely matched the impactor size which was determined *a priori*. Note that results from this work will be used to determine which correlation should be used without *a priori* knowledge of the injury mechanism.

Table 25. Predicted percent injury risk for area-sensitive eye using peak load.

		Peak Load (N)	Hyphema	Lens Damage	Retinal Damage	Globe Rupture
Blunt						
Sm. 12”	*	128.78 ± 1.68	44.13 ± 1.45	9.61 ± 0.86	9.74 ± 0.81	0.07 ± 0.01
Sm. 24”	*	194.59 ± 0.90	90.93 ± 0.35	85.36 ± 0.93	79.08 ± 1.00	4.32 ± 0.20
Md. 12”	†	191.44 ± 1.49	10.58 ± 0.20	0.32 ± 0.01	0.43 ± 0.02	0.00 ± 0.00
Md. 24”	†	277.97 ± 7.77	24.81 ± 1.49	2.27 ± 0.32	2.56 ± 0.33	0.01 ± 0.00
Lg. 12”	‡	224.01 ± 2.04	4.69 ± 0.13	0.06 ± 0.00	0.08 ± 0.00	0.00 ± 0.00
Lg, 24”	‡	337.09 ± 3.11	15.26 ± 0.39	0.73 ± 0.04	0.90 ± 0.05	0.00 ± 0.00
Blast						
10 psi	‡	121.40 ± 3.88	0.75 ± 0.07	0.00 ± 0.00	0.00 ± 0.00	0.00 ± 0.00
20 psi	‡	225.45 ± 6.47	4.79 ± 0.40	0.06 ± 0.01	0.09 ± 0.01	0.00 ± 0.00
30 psi	‡	349.89 ± 1.26	16.92 ± 0.17	0.93 ± 0.02	1.12 ± 0.02	0.00 ± 0.00

* Normalized energy calculated using the correlation for a 6.4 mm diameter projectile.
† Normalized energy calculated using the correlation for a 12.7 mm diameter projectile.
‡ Normalized energy calculated using the correlation for a 17.4 mm diameter projectile.

Comparison between Area-Sensitive FOCUS Eye and Isolated Porcine Eye Blast Tests

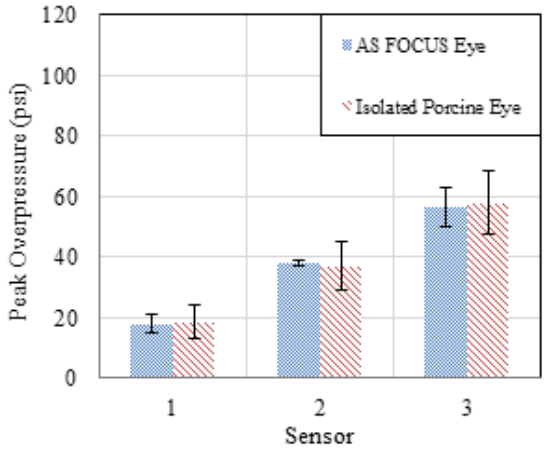

Figure 70. Comparison between area-sensitive FOCUS eye and isolated porcine eye tests.

Discussion

The blunt and blast tests conducted on the area-sensitive eye elicited characteristically different responses from the pressure sensor array. Notably, pulse parameter magnitudes were strikingly different between blunt and blast loading. Blunt tests resulted in a “bullseye” response, where the center pressure sensor recorded the highest pressure, and lower pressures were measured as

the location of the sensor moved outward radially. Pressure sensors located the same distance from the center produced similar pressure magnitudes. The blunt impact test in this study represented focal loading; i.e., loading occurred directly on the center of the eye. As such, the center sensor records the highest peak pressure, and peak pressure decreases radially outward. This response is consistent with Hertzian mechanics for a flat surface (impactor) impacting a sphere (eyeball). Blast tests resulted in a more consistent response across all nine sensors, where no sensor showed a prominent peak pressure greater than the other sensors. The duration of blast tests were an order of magnitude shorter than the duration of blunt tests. These differences noted can be attributed to the nature of loading and contact mechanics which varies between these two loading scenarios. The blast test represented distributed loading; i.e., loading occurred simultaneously over the entire front surface of the eye. As the blast wave propagation was perpendicular to the surface upon which the pressure sensors were mounted, it was expected that the array would pick up approximately the same magnitude of pressure at the same time for all pressure sensor locations.

Based on the characteristic loading patterns of the pressure sensors in the area-sensitive eye, it is possible to visually distinguish between blunt and blast loading. However, thresholds for these parameters were determined to provide a quantitative method to distinguish between impact size and between blunt and blast loading, i.e., the loading area and loading type. Normalizing peak pressure allowed for the comparison between the various magnitudes of the key loading parameters recorded during blunt and blast loading. The magnitude of positive duration provided a dichotomous response for blunt and blast trauma and therefore was not normalized as was peak pressure. It should be noted that these thresholds are specific to the energies tested in this study. That is to say, it is possible that varying mass of the impactor or drop height for the blunt tests, or test pressure level for the blast tests could produce peak pressures and durations different from what was reported for the current test series. Future work could assess varying test energies in order to assess if this affects the thresholds quantified herein.

Small differences in the responses of the four outer sensors can be attributed to the preparation of the nine-sensor array. The seemingly high and low responses of the contralateral sides of the array (sensors 6 and 8) can be attributed to a minor incline in the cut surface or inconsistent application of silicon adhesive. If the front half of the eye does not sit flush with the back half, it

is possible that minor loading differences will be observed by the sensor array. Though care was taken to properly strain relieve all sensors, the outer sensors were more susceptible to noise than the inner or central sensors during testing. The tiny lead wires, each only 0.005 in. in diameter, were not as well supported as the other sensors due to their close proximity to the edge of the synthetic eye.

Given the sensitivity of the nine-sensor array, the area-sensitive eye is currently able to distinguish between two impactor sizes: small and medium or large. A conservative approach should be taken when using this system in the case where a projectile is determined to be medium or large; that is, the smaller projectile size should be assumed, as this predicts a higher injury risk. Future work can examine if additional sensors can increase the sensitivity of the eye to be able to distinguish between the medium and larger impactor sizes. One possible solution would be that instead of using individual sensors, it would be possible to use a small-scale 3D pressure mapping system if a similar or higher resolution (>9 sensors/in.^{2}) could be obtained.

While the rigid concave cup loosely simulated the FOCUS orbit and muscle insert, the area-sensitive eye was tested in isolation from the face for these tests. The current study evaluates the area-sensitive eye in an isolated condition and focuses on a direct corneal impact for blunt tests and a forward-facing orientation for blast tests. It is unclear from these tests alone how the system would respond to oblique loading. Similarly, placing the area-sensitive eye within the FOCUS headform could potentially change the response of the system, even for a direct corneal blunt impact or forward-facing blast loading. Notably, the eyelid of the FOCUS headform may limit the contact area of the eye, and may change the loading pattern response of the current system. The specific response of the eye in the FOCUS headform should be quantified before the data collected herein be used to predict injury.

It must be noted that the peak pressure measured in the area-sensitive FOCUS eye is not a direct correlate to IOP measured in a cadaveric porcine eye model. However, similarities in the experimental setups provided for one comparison. Differences in the responses of these models are likely due to the fact that the area-sensitive eye is a solid material and the porcine eye is fluid-filled. Developing a synthetic fluid-filled eye that is both biofidelic in force-deflection

response and instrumented with a miniature pressure sensor, with area-sensing capabilities could further provide a better tool for predicting injury risk to the eye.

Conclusions

The area-sensitive eye designed and assessed in this study serves as a proof of concept that a biofidelic eyeball for an advanced anthropomorphic test device can distinguish between blunt and blast loading as well as between various impactor sizes for blunt impacts. This is an improvement beyond the abilities of the current FOCUS eye, which relies solely on load measured during loading to predict injury risk. Based on blunt testing with direct impacts to the cornea and blast testing with a forward-facing orientation to the shock wave, the current area-sensitive eye can distinguish between blunt and blast loading based on the characteristic response of the nine pressure sensor array. Normalized peak pressure and positive duration of the nine sensor array can be used to further distinguish between impactor sizes less than and greater than 12.70 mm in diameter. It is possible that additional sensors may provide increased sensitivity to distinguish between additional projectile sizes. Furthermore, testing the area-sensitive eye within the FOCUS headform will provide a more realistic response of the eye to various loading, and should be done in future work.

Conclusions

Research Summary

The research in this dissertation focused on the response of the eye, orbit, and face to primary blast overpressure exposure. Relying heavily on experimental work, these studies added to current work in the field of blast injury biomechanics and serve as the seminal work for future research in this area, including the development and validation of computational and physical models of the eye. The studies in this dissertation were designed to sequentially expand upon the preceding work, with the ultimate goal of gaining a better understanding of the potentially injurious effects of primary blast overpressure exposure to the eye. Chapters 1 and 2 focused on developing experimental methods of accurately simulating a primary blast overpressure event using an ABS. Results of these two studies can be applied to designing future studies using shock tubes to simulate primary blast overpressure. Chapters 3, 4, and 5 focused on quantifying the response of the eye from primary blast overpressure for unprotected and protected enucleated porcine eyes. The pressure levels tested resulted in low levels of physical injury to the eye, both from the low predicted injury risk and lack of severe injuries upon dissection. Eyewear effectively reduced the peak overpressure exposed to the eye, and were proven to have protective ability for primary blast. Chapters 6 and 7 focused on assessing the FOCUS headform eye and developing an area-sensitive synthetic eye that can distinguish between blunt and blast loading. These studies provided a framework for developing a more robust ATD headform eye. Overall, the experimental techniques used for all of these studies can be applied to other body regions for future work that quantifies and assesses injuries from primary blast overpressure exposure.

Limitations

There are a number of limitations in the studies presented in this dissertation. All eye tests were conducted on enucleated porcine eyes. The injuries directly assessed from these eyes were limited to gross injury to the tissues and structures of the eye. It is of the utmost importance that physiologic and psychologic injuries and responses be assessed in future work. Furthermore, although porcine eyes are similar in anatomy and structure to human eyes, the structural properties of porcine eyes differ slightly from those of human eyes. As such, it is critical that structural properties of the human eye be quantified at the high loading rates related to blast. An

inherent limitation of this work is the pressure levels assessed. Test pressure levels of 10 psi, 20 psi, and 30 psi (static overpressure) were chosen to provide information for increasing severity. While 30 psi test level approaches the threshold for human lung injury in both magnitude and duration and serves as a preliminary indicator of survivable blast levels, it remains unknown how higher pressure levels, longer pulse durations, or greater blast energies can affect the eye. The forward-facing nature of the test setups that simulated various boundary conditions around the eye simulated a direct explosion at eyelevel. Future work should be conducted to quantify the response to various blast locations, including various oblique and ground-level charges. These limitations lead into ongoing and future work in the field which will provide answers to these critical questions.

A main focus of this dissertation was the measurement of IOP for the quantification of injury risk for injuries that could not be assessed otherwise. It is possible that other shock wave parameters (positive/negative duration and impulse) or combinations thereof may affect the overall response of the eye to blast overpressure exposure. A more comprehensive understanding of injuries could provide additional information about the roles these parameters have in causing injury risk from primary blast overpressure.

Ongoing Work

The experimental studies described in this thesis provided a foundation for future work within the field of blast injury biomechanics for experimentation, computational modeling, and the development of blast-specific ATDs. The test methods described for the use of an ABS can be translated to various labs that use ABSs and shock tubes to simulate blast overpressure loading. Further, the methods used to systematically assess the ocular response to blast overpressure can be replicated for other body regions. The experimental data and CAD geometries can supplied for validation of computational models of the eye, orbit, and face. Following this, the specific CAD geometries and pressure corridors were supplied to an external contractor that specialized in computational fluid dynamic models for blast loading rates. Results from the computational fluid dynamic work will provide data necessary to validate finite element models of the eye specifically for blast. Working in conjunction with collaborators at Wake Forest University, the VT-WFU Eye Model will be validated using this data. Once validated, these computational models can be used to quickly assess the response of the eye and face to various blast locations,

and will in turn dictate future experimental work. Accounting for the limitations mentioned with the area-sensitive FOCUS eye testing, there is an ongoing effort to examine the effects of placing the area-sensitive FOCUS eye within the FOCUS headform. Testing the area-sensitive eye within the FOCUS headform for both blunt and blast loading takes into account the effect of the eyelid which possibly changes the loading distribution for both loading regimes, and adds biofidelity to the test setup by using the previously developed muscle and orbit simulant. These tests will provide a better assessment of the area-sensitive eye.

Future Work

One research topic directly related to the current work could compare the blast overpressure response of enucleated porcine and human cadaver eyes to determine how well the porcine eye simulates the response of a human cadaver eye. Due to the nature of blast-related research, this would require specific "potentially destructive" verbiage in human body donor paperwork to obtain human cadaver eyes for this use. Another pertinent research question related to the eye and visual system is how these regions respond physiologically to primary blast overpressure. An anesthetized animal model could provide critical information on specific biomarkers, cellular responses, and organ function that cannot be assessed with cadaveric or physical models.

The work described in this dissertation represents only a small portion of the overall research related to primary blast overpressure exposure. Findings of the studies presented herein provide critical data that lay the groundwork for the development of future experimental studies as well as the validation of physical and computational models for primary blast overpressure. As the research described herein reported low injury risk, a main focus for future research can be to examine higher magnitude blasts. Quantifying a threshold for human eye injury to primary blast trauma requires assessing more severe test levels, both physical and physiologic models, and better reporting of trauma at combat sites. Expanding upon the head as a body region, future work can focus on more fully examining the response of the brain to primary blast overpressure exposure. Collecting primary blast overpressure exposure data from currently deployed soldiers could provide invaluable information on the magnitude, frequency, and directionality of commonly observed blast events. The development and validation of sensors that can accurately detect and record shock waves and simultaneously be integrated into personal protective equipment and power systems is critical to this overall mission. Once established, human injury

tolerances and thresholds could be used develop a device that can detect a soldier's exposure to potentially injurious events, akin to a radiological dosimeter.

The value of clinical injuries reported and treated by doctors *in-theatre* and when a solider returns from duty cannot be overlooked. A full understanding of physical and physiological injuries caused by primary blast overpressure will provide doctors with information to more accurately detect and treat these injuries. Updating metrics to assess visual dysfunction that reflect injuries caused by primary blast overpressure would be beneficial for quantifying the incidence of these injuries as well as provide critical data for treatment. There also lies a potential for physiological and psychological assessments to be administered to soldiers prior to deployment and upon return home to further quantify "invisible" injuries caused by both emotional and physical trauma, similar to the ImPACT© program that uses a pre- and post-injury test given to assess an individual concussions [73].

Dissemination of Knowledge

A number of publications are anticipated upon completion of the currently proposed research. **Table 26** lists the journals and conferences to which each the topic has been or will be submitted.

Table 26. Anticipated publication and conference topics from the proposed research.

Dissertation Chapter	Title	Journal (*Conference*)
Chapter 1*	Membrane characteristics for biological blast overpressure testing using blast simulators	Biomedical Sciences Instrumentation (*Rocky Mountain Bioengineering Symposium*)
Chapter 2*	Effects of filtering on experimental blast overpressure measurements	Biomedical Sciences Instrumentation (*Rocky Mountain Bioengineering Symposium*)
Chapter 3	Injury risk from primary blast overpressure to the unprotected porcine eye	Journal of Biomechanics (*Biomedical Engineering Society)*
Chapter 4	Effects of spectacles and goggles on eye injury risk from primary blast overpressure exposure	Archives of Ophthalmology
Chapter 5	Intraorbital and facial response corridors for primary blast overpressure exposure	Biomechanics and Modeling in Mechanobiology
Chapter 6	Evaluating the FOCUS headform for exposure to primary blast overpressure	Biomedical Sciences Instrumentation (*Rocky Mountain Bioengineering Symposium*)
Chapter 7	An area-sensitive synthetic eye that differentiates between blunt and blast loading	Journal of Trauma

* Published at time of electronic dissertation submission.

Acknowledgements

I would like to thank the United States Army Medical Research and Materiel Command (MRMC) as well as the United States Army Aeromedical Research Laboratory (USAARL) for financially supporting the research and development studies presented in this dissertation.

References

[1] G. McGwin, A. Xie, and C. Owsley, "Rate of eye injury in the United States," *Archives of ophthalmology,* vol. 123, pp. 970-976, 2005.

[2] U. S. E. I. Registry, "Eye trauma: epidemiology and prevention " <http://www.useironline.org/Prevention.htm>, vol. Accesssed 11 Mar 2009.

[3] K. D. Frick, E. W. Gower, J. H. Kempen, and J. L. Wolff, "Economic impact of visual impairment and blindness in the United States," *Archives of ophthalmology,* vol. 125, pp. 544-550, 2007.

[4] D. B. Rein, P. Zhang, K. E. Wirth, P. P. Lee, T. J. Hoerger, N. McCall, *et al.*, "The economic burden of major adult visual disorders in the United States," *Archives of ophthalmology,* vol. 124, pp. 1754-1760, 2006.

[5] J. S. Heier, R. W. Enzenauer, S. F. Wintermeyer, M. Delaney, and F. P. LaPiana, "Ocular injuries and diseases at a combat support hospital in support of Operations Desert Shield and Desert Storm," *Archives of ophthalmology,* vol. 111, pp. 795-798, 1993.

[6] P. Belmont, A. J. Schoenfeld, and G. Goodman, "Epidemiology of combat wounds in Operation Iraqi Freedom and Operation Enduring Freedom: orthopaedic burden of disease," *J Surg Orthop Adv,* vol. 19, pp. 2-7, 2010.

[7] F. H. *U.S. military casualty statistics: Operation New Dawn, Operation Iraqi Freedom, and Operation Enduring Freedom.* . Available: <www.fas.org/sgp/crs/natsec/RS22452.pdf>

[8] A. B. Thach, A. J. Johnson, R. B. Carroll, A. Huchun, D. J. Ainbinder, R. D. Stutzman, *et al.*, "Severe eye injuries in the war in Iraq, 2003–2005," *Ophthalmology,* vol. 115, pp. 377-382, 2008.

[9] J. B. Holcomb, L. G. Stansbury, H. R. Champion, C. Wade, and R. F. Bellamy, "Understanding combat casualty care statistics," *Journal of Trauma and Acute Care Surgery,* vol. 60, pp. 397-401, 2006.

[10] R. Thomas, J. G. McManus, A. Johnson, P. Mayer, C. Wade, and J. B. Holcomb, "Ocular injury reduction from ocular protection use in current combat operations," *Journal of Trauma and Acute Care Surgery,* vol. 66, pp. S99-S103, 2009.

[11] T. H. Mader, R. D. Carroll, C. S. Slade, R. K. George, J. P. Ritchey, and S. P. Neville, "Ocular war injuries of the Iraqi insurgency, January–September 2004," *Ophthalmology,* vol. 113, pp. 97-104, 2006.

[12] E. D. Weichel and M. H. Colyer, "Combat ocular trauma and systemic injury," *Current opinion in ophthalmology,* vol. 19, pp. 519-525, 2008.

[13] Y. Yonekawa, H. D. Hacker, R. E. Lehman, C. J. Beal, P. B. Veldman, N. M. Vyas, *et al.*, "Ocular blast injuries in mass-casualty incidents: the Marathon bombing in Boston, Massachusetts, and the fertilizer plant explosion in West, Texas," *Ophthalmology,* vol. 121, pp. 1670-1676. e1, 2014.

[14] G. H, *Anatomy of the human body*. Philadelphia: Lea & Febiger, 1918.

[15] J. H. Stuhmiller, Phillips III YY, Richmond DR, "The physics and mechanisms of primary blast injury," in *Conventional Warfare: Ballistic, Blast, and Burn Injuries*, R. F. Bellamy, Zajtchuk R, Ed., ed Washington, DC: Office of the Surgeon General at TMM Publications, 1990, pp. 241-270.

[16] R. G. DePalma, D. G. Burris, H. R. Champion, and M. J. Hodgson, "Blast injuries," *New England journal of medicine,* vol. 352, pp. 1335-1342, 2005.

[17] A. E. Ritenour and T. W. Baskin, "Primary blast injury: update on diagnosis and treatment," *Critical care medicine,* vol. 36, pp. S311-S317, 2008.
[18] R. Abbotts, S. Harrison, and G. Cooper, "Primary blast injuries to the eye: a review of the evidence," *Journal of the Royal Army Medical Corps,* vol. 153, pp. 119-123, 2007.
[19] (10 Aug 2013). *Spalling*. Available: unterm.un.org.
[20] A. Nakagawa, G. T. Manley, A. D. Gean, K. Ohtani, R. Armonda, A. Tsukamoto*, et al.*, "Mechanisms of primary blast-induced traumatic brain injury: insights from shock-wave research," *Journal of neurotrauma,* vol. 28, pp. 1101-1119, 2011.
[21] E. Herbert, S. Balibar, and F. Caupin, "Cavitation pressure in water," *Physical Review E,* vol. 74, p. 041603, 2006.
[22] I. R. Webb, S. J. Payne, and C.-C. Coussios, "The effect of temperature and viscoelasticity on cavitation dynamics during ultrasonic ablation," *The Journal of the Acoustical Society of America,* vol. 130, pp. 3458-3466, 2011.
[23] M. B. Panzer, B. S. Myers, B. P. Capehart, and C. R. Bass, "Development of a finite element model for blast brain injury and the effects of CSF cavitation," *Annals of biomedical engineering,* vol. 40, pp. 1530-1544, 2012.
[24] C. D. Harrison, V. S. Bebarta, and G. A. Grant, "Tympanic membrane perforation after combat blast exposure in Iraq: a poor biomarker of primary blast injury," *Journal of Trauma and Acute Care Surgery,* vol. 67, pp. 210-211, 2009.
[25] M. A. Mayorga, "The pathology of primary blast overpressure injury," *Toxicology,* vol. 121, pp. 17-28, 1997.
[26] H. L. Brode, "Blast wave from a spherical charge," *Physics of Fluids (1958-1988),* vol. 2, pp. 217-229, 1959.
[27] D. Ritzel, "Title," unpublished|.
[28] D. T. WEIDENTHAL, "Experimental ocular contusion," *Archives of ophthalmology,* vol. 71, pp. 77-81, 1964.
[29] D. T. Weidenthal and C. L. Schepens, "Peripheral fundus changes associated with ocular contusion," *American journal of ophthalmology,* vol. 62, pp. 465-477, 1966.
[30] F. Delori, O. Pomerantzeff, and M. Cox, "Deformation of the globe under high-speed impact: it relation to contusion injuries," *Investigative ophthalmology,* vol. 8, p. 290, 1969.
[31] S. McKnight, J. Fitz, and J. Giangiacomo, "Corneal rupture following radial keratotomy in cats subjected to BB gun injury," *Ophthalmic surgery,* vol. 19, pp. 165-167, 1988.
[32] R. P. Green Jr, D. R. Peters, J. W. Shore, J. W. Fanton, and H. Davis, "Force necessary to fracture the orbital floor," *Ophthalmic Plastic & Reconstructive Surgery,* vol. 6, pp. 211-217, 1990.
[33] S. M. Duma and J. R. Crandall, "Eye injuries from airbags with seamless module covers," *Journal of Trauma and Acute Care Surgery,* vol. 48, pp. 786-789, 2000.
[34] W. R. M. Scott, W. C. Lloyd, J. V. Benedict, and R. Meredith, "Ocular injuries due to projectile impacts," in *Annual Proceedings/Association for the Advancement of Automotive Medicine*, 2000, p. 205.
[35] E. A. Kennedy, T. P. Ng, C. McNally, J. D. Stitzel, and S. M. Duma, "Risk functions for human and porcine eye rupture based on projectile characteristics of blunt objects," *Stapp car crash journal,* vol. 50, p. 651, 2006.

[36] S. M. Duma, J. A. Bisplinghoff, D. M. Senge, C. McNally, and V. D. Alphonse, "Evaluating the risk of eye injuries: intraocular pressure during high speed projectile impacts," *Current eye research,* vol. 37, pp. 43-49, 2012.

[37] S. M. Duma, J. A. Bisplinghoff, D. M. Senge, C. McNally, and V. D. Alphonse, "Eye injury risk from water stream impact: biomechanically based design parameters for water toy and park design," *Current eye research,* vol. 37, pp. 279-285, 2012.

[38] P. F. Vinger, S. M. Duma, and J. Crandall, "Baseball hardness as a risk factor for eye injuries," *Archives of ophthalmology,* vol. 117, pp. 354-358, 1999.

[39] V. D. Alphonse, A. R. Kemper, S. Rowson, and S. M. Duma, "Eye injury risk associated with remote control toy helicopter blades," *Biomedical sciences instrumentation,* vol. 48, pp. 20-26, 2011.

[40] V. D. Alphonse, A. R. Kemper, B. T. Strom, S. M. Beeman, and S. M. Duma, "Mechanisms of eye injuries from fireworks," *JAMA,* vol. 308, pp. 33-34, 2012.

[41] E. A. Kennedy, K. D. Voorhies, I. P. Herring, A. L. Rath, and S. M. Duma, "Prediction of severe eye injuries in automobile accidents: static and dynamic rupture pressure of the eye," in *Annual Proceedings/Association for the Advancement of Automotive Medicine*, 2004, p. 165.

[42] J. Hines-Beard, J. Marchetta, S. Gordon, E. Chaum, E. E. Geisert, and T. S. Rex, "A mouse model of ocular blast injury that induces closed globe anterior and posterior pole damage," *Experimental eye research,* vol. 99, pp. 63-70, 2012.

[43] Y.-Y. Zou, E. M. Kan, J. Lu, K. C. Ng, M. H. Tan, L. Yao, *et al.*, "Primary blast injury-induced lesions in the retina of adult rats," *J Neuroinflammation,* vol. 10, p. 1186, 2013.

[44] C. Bricker-Anthony, J. Hines-Beard, L. D'Surney, and T. S. Rex, "Exacerbation of blast-induced ocular trauma by an immune response," *Journal of neuroinflammation,* vol. 11, pp. 1-15, 2014.

[45] C. Bricker-Anthony, J. Hines-Beard, and T. S. Rex, "Molecular changes and vision loss in a mouse model of closed-globe blast trauma," *Invest Ophthalmol Vis Sci,* vol. 55, pp. 4853-4862, 2014.

[46] D. Sherwood, W. E. Sponsel, B. J. Lund, W. Gray, R. Watson, S. L. Groth, *et al.*, "Anatomical Manifestations of Primary Blast Ocular Trauma Observed in a Postmortem Porcine ModelPrimary Blast Ocular Trauma," *Investigative ophthalmology & visual science,* vol. 55, pp. 1124-1132, 2014.

[47] J. H. Choi, W. A. Greene, A. J. Johnson, M. Chavko, J. M. Cleland, R. M. McCarron, *et al.*, "Pathophysiology of blast-induced ocular trauma in rats after repeated exposure to low-level blast overpressure," *Clinical & experimental ophthalmology,* vol. 43, pp. 239-246, 2015.

[48] E. Uchio, S. Ohno, J. Kudoh, K. Aoki, and L. T. Kisielewicz, "Simulation model of an eyeball based on finite element analysis on a supercomputer," *British Journal of Ophthalmology,* vol. 83, pp. 1106-1111, 1999.

[49] J. D. Stitzel, S. M. Duma, J. M. Cormier, and I. P. Herring, "A nonlinear finite element model of the eye with experimental validation for the prediction of globe rupture," in *SAE CONFERENCE PROCEEDINGS P*, 2002, pp. 81-102.

[50] A. A. Weaver, E. A. Kennedy, S. M. Duma, and J. D. Stitzel, "Evaluation of different projectiles in matched experimental eye impact simulations," *Journal of biomechanical engineering,* vol. 133, p. 031002, 2011.

[51] A. A. Weaver, K. L. Loftis, J. C. Tan, S. M. Duma, and J. D. Stitzel, "CT based three-dimensional measurement of orbit and eye anthropometry," *Investigative ophthalmology & visual science,* vol. 51, pp. 4892-4897, 2010.

[52] J. D. Stitzel and A. A. Weaver, "Computational simulations of ocular blast loading and prediction of eye injury risk," in *ASME 2012 Summer Bioengineering Conference*, 2012, pp. 425-426.

[53] L. Esposito, C. Clemente, N. Bonora, and T. Rossi, "Modelling human eye under blast loading," *Computer methods in biomechanics and biomedical engineering,* vol. 18, pp. 107-115, 2015.

[54] J. H. Stuhmiller, K. H.-H. Ho, M. J. Vander Vorst, K. T. Dodd, T. Fitzpatrick, and M. Mayorga, "A model of blast overpressure injury to the lung," *Journal of biomechanics,* vol. 29, pp. 227-234, 1996.

[55] R. Bhardwaj, K. Ziegler, J. H. Seo, K. Ramesh, and T. D. Nguyen, "A computational model of blast loading on the human eye," *Biomechanics and modeling in mechanobiology,* vol. 13, pp. 123-140, 2014.

[56] R. Watson, W. Gray, W. E. Sponsel, B. J. Lund, R. D. Glickman, S. L. Groth, *et al.*, "Simulations of Porcine Eye Exposure to Primary Blast Insult," *Translational vision science & technology,* vol. 4, 2015.

[57] I. I. Glass and J. G. Hall, "Handbook of Supersonic Aerodynamics. Section 18. Shock Tubes," DTIC Document1959.

[58] D. Ritzel, S. Parks, J. Roseveare, G. Rude, and T. Sawyer, "Experimental blast simulation for injury studies," in *Proc. HFM-207 NATO Symposium on a Survey of Blast Injury Across the Full Landscape of Military Science*, 2011.

[59] V. S. S. S. Sajja, M. Galloway, F. Ghoddoussi, A. Kepsel, and P. VandeVord, "Effects of blast-induced neurotrauma on the nucleus accumbens," *Journal of neuroscience research,* vol. 91, pp. 593-601, 2013.

[60] "Instrumentation for impact tests- part 1 - electronic instrumentation SAE Standard J211/1," 1995.

[61] http://www.ghbmc.com/news.html

[62] E. Kennedy, Duma, SM, "Eye injury risk functions for human and FOCUS eyes: hyphema, lens dislocation, and retinal damage," *Prepared for: US Army Medical Research and Materiel Command,* 2011.

[63] N. F. JOHNSON and I. GRIERSON, "POST-MORTEM CHANGES IN THE RABBIT RETINA," *Acta ophthalmologica,* vol. 54, pp. 529-541, 1976.

[64] S. Bailoor, R. Bhardwaj, and T. D. Nguyen, "Effectiveness of eye armor during blast loading," *Biomechanics and modeling in mechanobiology,* 2015.

[65] *Authorized Protective Eyewear List (APEL)*. Available: http://www.peosoldier.army.mil/equipment/eyewear/

[66] G. G. Bentz V, "Joint live fire (JLF) final report for assessment of ocular pressure as a result of blast for protected and unprotected eyes," *Report number JLF-TR-13-01, U.S. Army Aberdeen Test Center, Aberdeen Proving Ground, MD,* 2013.

[67] K. Mohan, H. Kecova, E. Hernandez-Merino, R. H. Kardon, and M. M. Harper, "Retinal Ganglion Cell Damage in an Experimental Rodent Model of Blast-Mediated Traumatic Brain InjuryBlast-Mediated Traumatic Optic Neuropathy," *Investigative ophthalmology & visual science,* vol. 54, pp. 3440-3450, 2013.

[68] H.-C. H. Wang, J.-H. Choi, W. A. Greene, M. L. Plamper, H. E. Cortez, M. Chavko, *et al.*, "Pathophysiology of blast-induced ocular trauma with apoptosis in the retina and optic nerve," *Military medicine,* vol. 179, pp. 34-40, 2014.

[69] C. Bir, D. Viano, and A. King, "Development of biomechanical response corridors of the thorax to blunt ballistic impacts," *Journal of biomechanics,* vol. 37, pp. 73-79, 2004.

[70] D. Lessley, J. Crandall, G. Shaw, R. Kent, and J. Funk, "A normalization technique for developing corridors from individual subject responses," SAE Technical paper 0148-7191, 2004.

[71] E. A. Kennedy, J. A. Inzana, C. McNally, S. M. Duma, P. J. Depinet, K. H. Sullenberger, *et al.*, "Development and validation of a synthetic eye and orbit for estimating the potential for globe rupture due to specific impact conditions," *Stapp car crash journal,* vol. 51, p. 381, 2007.

[72] E. Kennedy and S. Duma, "The effects of the extraocular muscles on eye impact force–deflection and globe rupture response," *Journal of biomechanics,* vol. 41, pp. 3297-3302, 2008.

[73] Available: https://www.impacttest.com/

Appendix A
Overpressure Profiles and Corridors for Porcine Eye Tests

Figure A1. Static 01 (along wall) Empty Tube. 147
Figure A2. Static 01 (along wall) Isolated Eye. 148
Figure A3. Static 01 (along wall) Synthetic Orbit. 149
Figure A4. Static 01 (along wall) 3D Orbit – Unprotected Eye. 150
Figure A5. Static 01 (along wall) 3D Orbit – Spectacles. 151
Figure A6. Static 01 (along wall) 3D Orbit – Goggles. 152
Figure A7. Static 02 (along wall) Empty Tube. 153
Figure A8. Static 02 (along wall) Isolated Eye. 154
Figure A9. Static 02 (along wall) Synthetic Orbit. 155
Figure A10. Static 02 (along wall) 3D Orbit – Unprotected Eye. 156
Figure A11. Static 02 (along wall) 3D Orbit – Spectacles. 157
Figure A12. Static 02 (along wall) 3D Orbit – Goggles. 158
Figure A13. Static 03 (along wall) Empty Tube. 159
Figure A14. Static 03 (along wall) Isolated Eye. 160
Figure A15. Static 03 (along wall) Synthetic Orbit. 161
Figure A16. Static 03 (along wall) 3D Orbit – Unprotected Eye. 162
Figure A17. Static 03 (along wall) 3D Orbit – Spectacles. 163
Figure A18. Static 03 (along wall) 3D Orbit – Goggles. 164
Figure A19. Static 04 (in flow) Isolated Eye. 165
Figure A20. Static 04 (in flow) Synthetic Orbit. 166
Figure A21. Static 04 (in flow) 3D Orbit – Unprotected Eye. 167
Figure A22. Static 04 (in flow) 3D Orbit – Spectacles. 168
Figure A23. Static 04 (in flow) 3D Orbit – Goggles. 169
Figure A24. Intraocular Pressure (IOP) Isolated Eye. 170
Figure A25. Intraocular Pressure (IOP) Synthetic Orbit. 171
Figure A26. Intraocular Pressure (IOP) 3D Orbit – Unprotected Eye. 172
Figure A27. Intraocular Pressure (IOP) 3D Orbit – Spectacles. 173
Figure A28. Intraocular Pressure (IOP) 3D Orbit – Goggles 174
Figure A29. Orbital Surface Maxilla Bone Synthetic Orbit. 175
Figure A30. Orbital Surface Maxilla Bone 3D Orbit – Unprotected Eye. 176
Figure A31. Orbital Surface Maxilla Bone 3D Orbit – Spectacles. 177
Figure A32. Orbital Surface Maxilla Bone 3D Orbit – Goggles. 178
Figure A33. Orbital Surface Lacrimal Bone Synthetic Orbit. 179
Figure A34. Orbital Surface Lacrimal Bone 3D Orbit – Unprotected Eye. 180
Figure A35. Orbital Surface Lacrimal Bone 3D Orbit – Spectacles. 181
Figure A36. Orbital Surface Lacrimal Bone 3D Orbit - Goggles. 182
Figure A37. Orbital Surface Frontal Bone (Anterior Sensor) Synthetic Orbit. 183

Figure A38. Orbital Surface Frontal Bone (Anterior Sensor) 3D Orbit – Unprotected Eye. 184
Figure A39. Orbital Surface Frontal Bone (Anterior Sensor) 3D Orbit – Spectacles. 185
Figure A40. Orbital Surface Frontal Bone (Anterior Sensor) 3D Orbit – Goggles..... 186
Figure A41. Orbital Surface Frontal Bone (Posterior Sensor) Synthetic Orbit. 187
Figure A42. Orbital Surface Frontal Bone (Posterior Sensor) 3D Orbit – Unprotected Eye. 188
Figure A43. Orbital Surface Frontal Bone (Posterior Sensor) 3D Orbit – Spectacles. 189
Figure A44. Orbital Surface Frontal Bone (Posterior Sensor) 3D Orbit – Goggles. 190
Figure A45. Total Isolated Eye. 191
Figure A46. Reflected Synthetic Orbit. 192
Figure A47. Skin Nasal 3D Orbit – Unprotected Eye. 193
Figure A48. Skin Nasal 3D Orbit – Spectacles. 194
Figure A49. Skin Nasal 3D Orbit – Goggles. 195
Figure A50. Skin Top Medial 3D Orbit – Unprotected Eye. 196
Figure A51. Skin Top Medial 3D Orbit – Spectacles. 197
Figure A52. Skin Top Medial 3D Orbit – Goggles. 198
Figure A53. Skin Top Middle 3D Orbit – Unprotected Eye. 199
Figure A54. Skin Top Middle 3D Orbit – Spectacles. 200
Figure A55. Skin Top Middle 3D Orbit – Goggles. 201
Figure A56. Skin Top Lateral 3D Orbit – Unprotected Eye. 202
Figure A57. Skin Top Lateral 3D Orbit – Spectacles. 203
Figure A58. Skin Top Lateral 3D Orbit – Goggles. 204
Figure A59. Skin Bottom Medial 3D Orbit – Unprotected Eye. 205
Figure A60. Skin Bottom Medial 3D Orbit – Spectacles. 206
Figure A61. Skin Bottom Medial 3D Orbit – Goggles. 207
Figure A62. Skin Bottom Middle 3D Orbit – Unprotected Eye. 208
Figure A63. Skin Bottom Middle 3D Orbit – Spectacles. 209
Figure A64. Skin Bottom Middle 3D Orbit – Goggles. 210
Figure A65. Skin Bottom Lateral 3D Orbit – Unprotected Eye. 211
Figure A66. Skin Bottom Lateral 3D Orbit – Spectacles. 212
Figure A67. Skin Bottom Lateral 3D Orbit – Goggles. 213

Footnote	Comment
†	Spike in trace replaced with quadratic interpolation. Peak overpressure, positive duration, and positive impulse reflect modified trace. Average trace and corridors reflect modified trace.
‡	Noise in trace removed. Peak overpressure, positive duration, and positive impulse reflect modified trace. Average trace and corridors reflect modified trace.
§	Signal does not return to zero after initial peak. Positive duration and positive impulse were not quantified for this test. Average trace and corridors do not include this test.

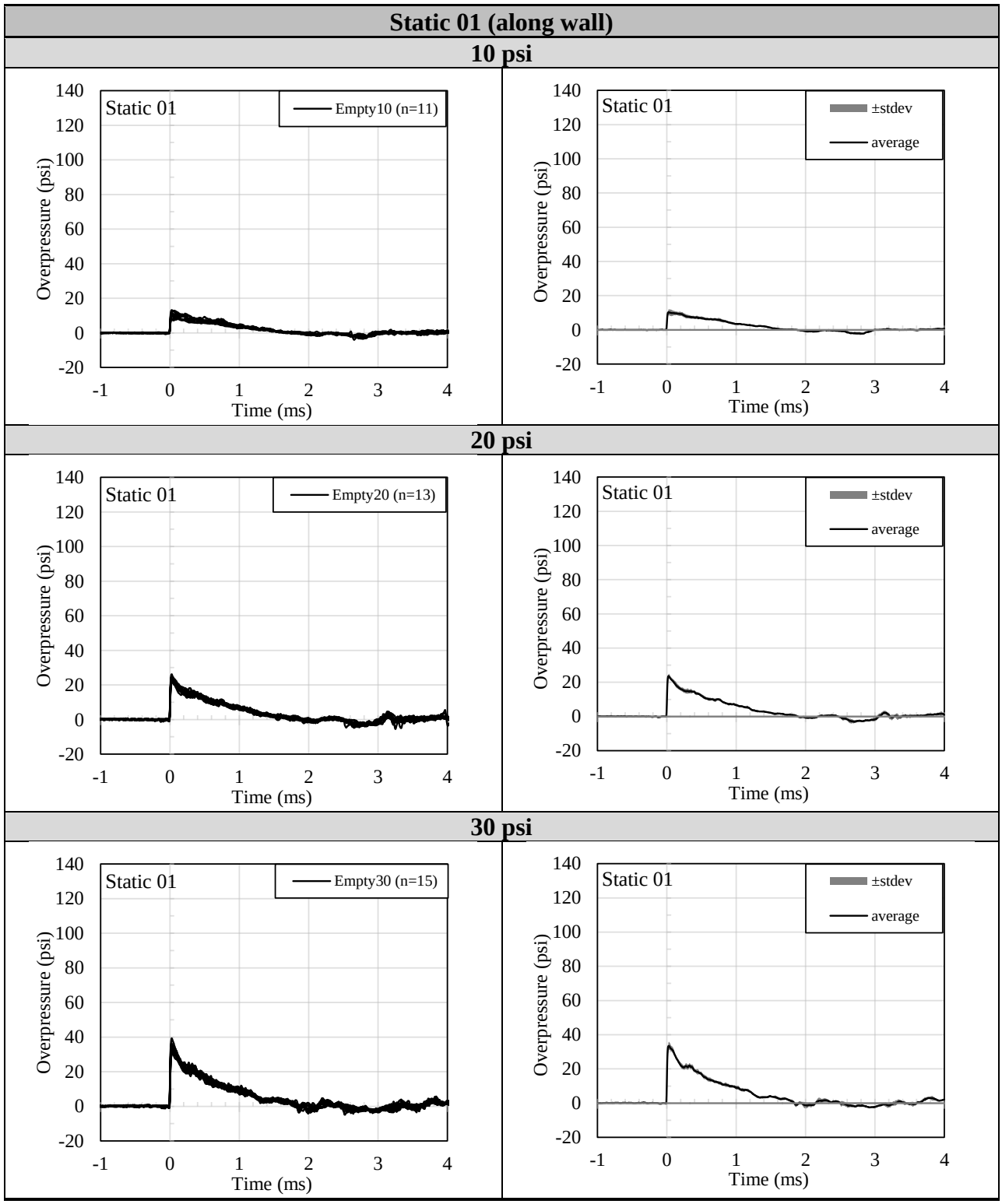

Figure A1. Static 01 (along wall) Empty Tube.

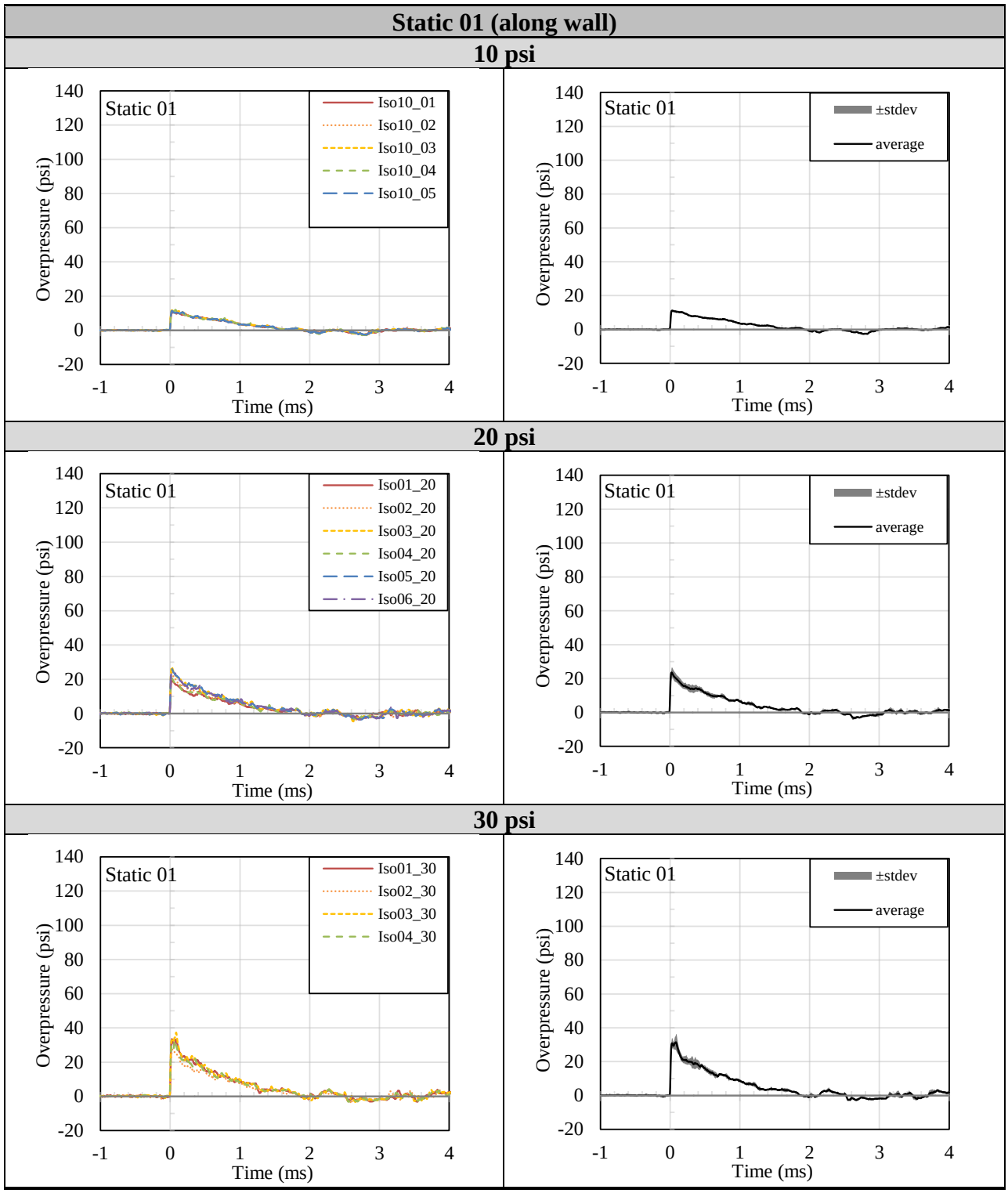

Figure A2. Static 01 (along wall) Isolated Eye.

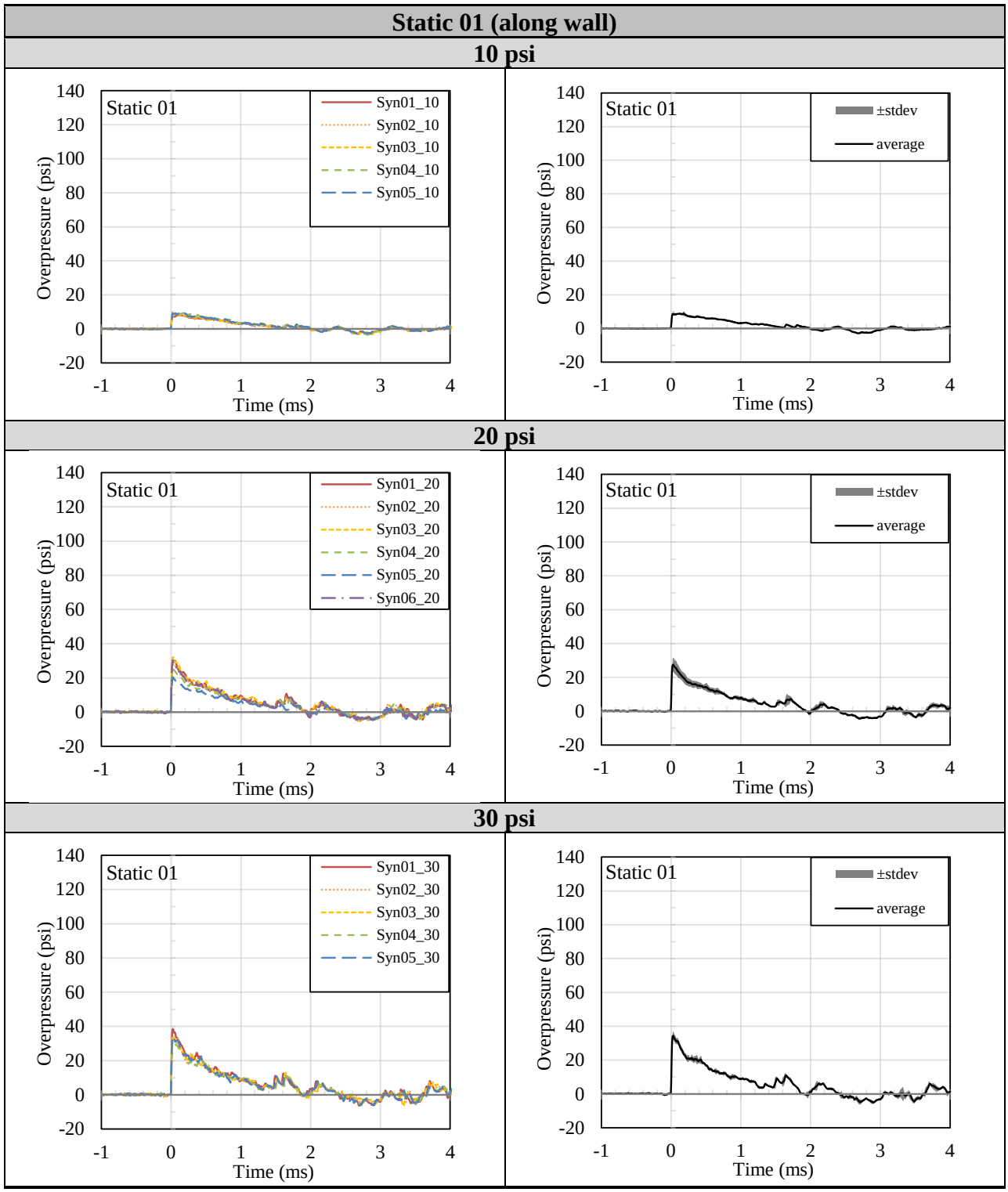

Figure A3. Static 01 (along wall) Synthetic Orbit.

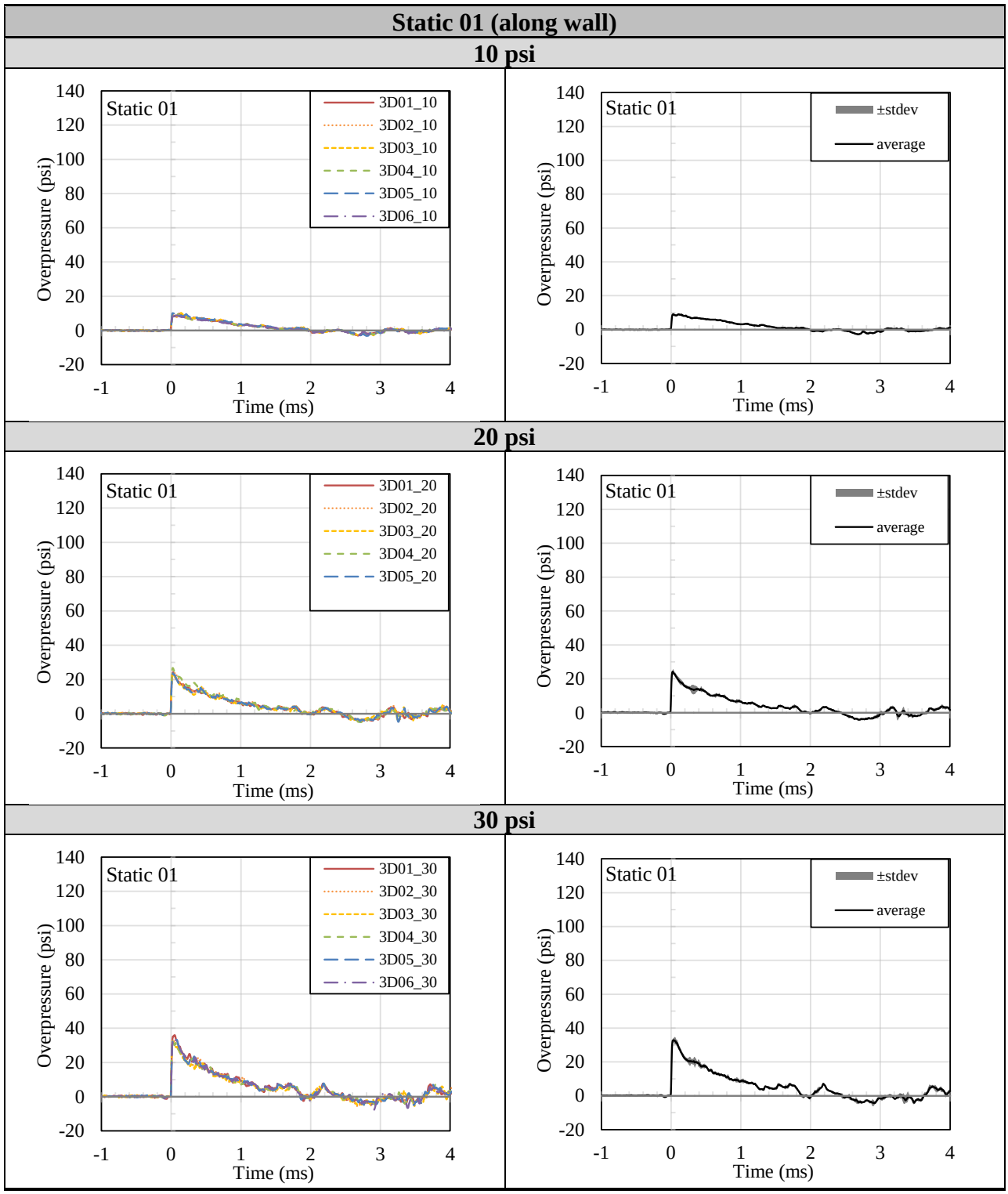

Figure A4. Static 01 (along wall) 3D Orbit – Unprotected Eye.

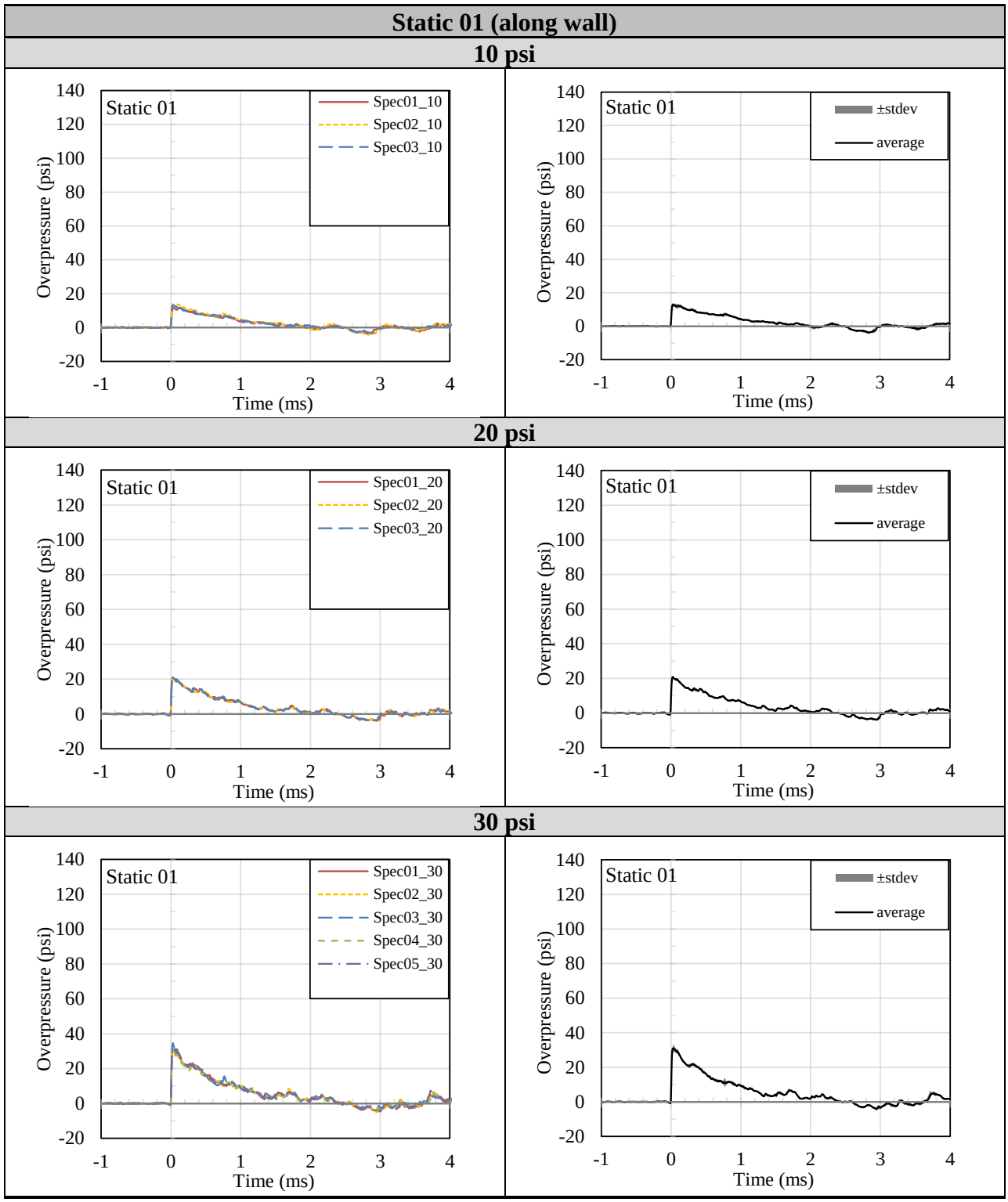

Figure A5. Static 01 (along wall) 3D Orbit – Spectacles.

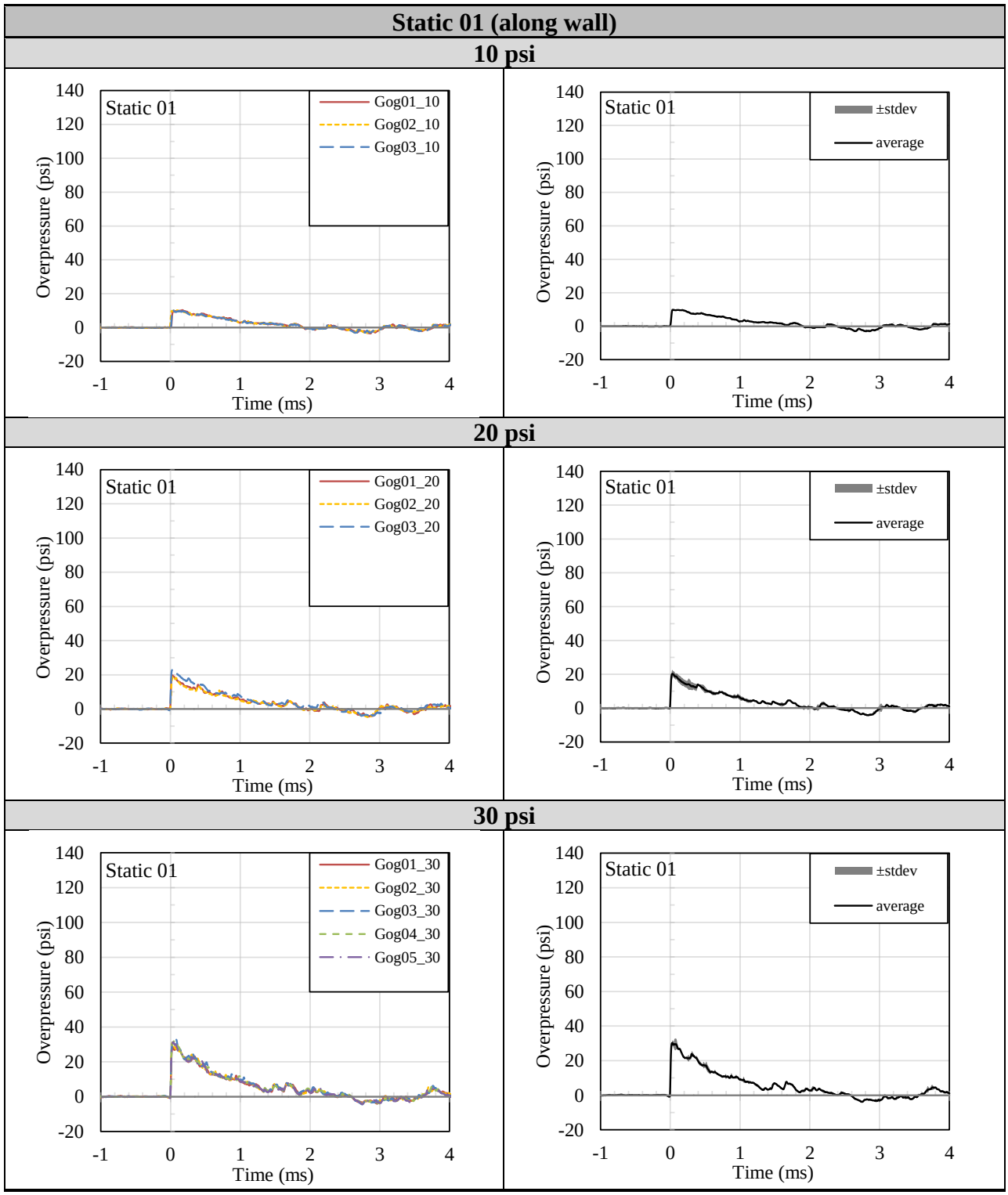

Figure A6. Static 01 (along wall) 3D Orbit – Goggles.

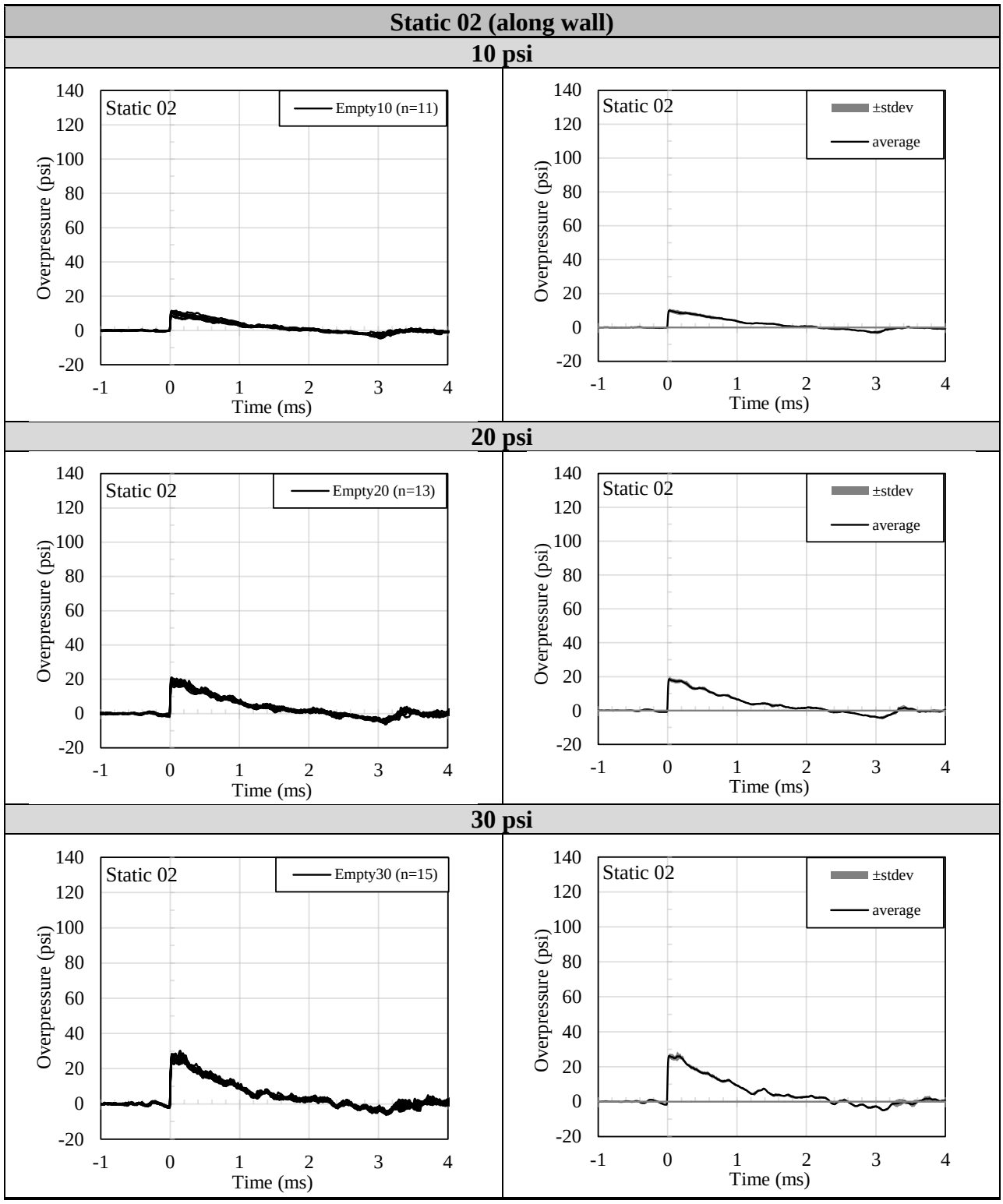

Figure A7. Static 02 (along wall) Empty Tube.

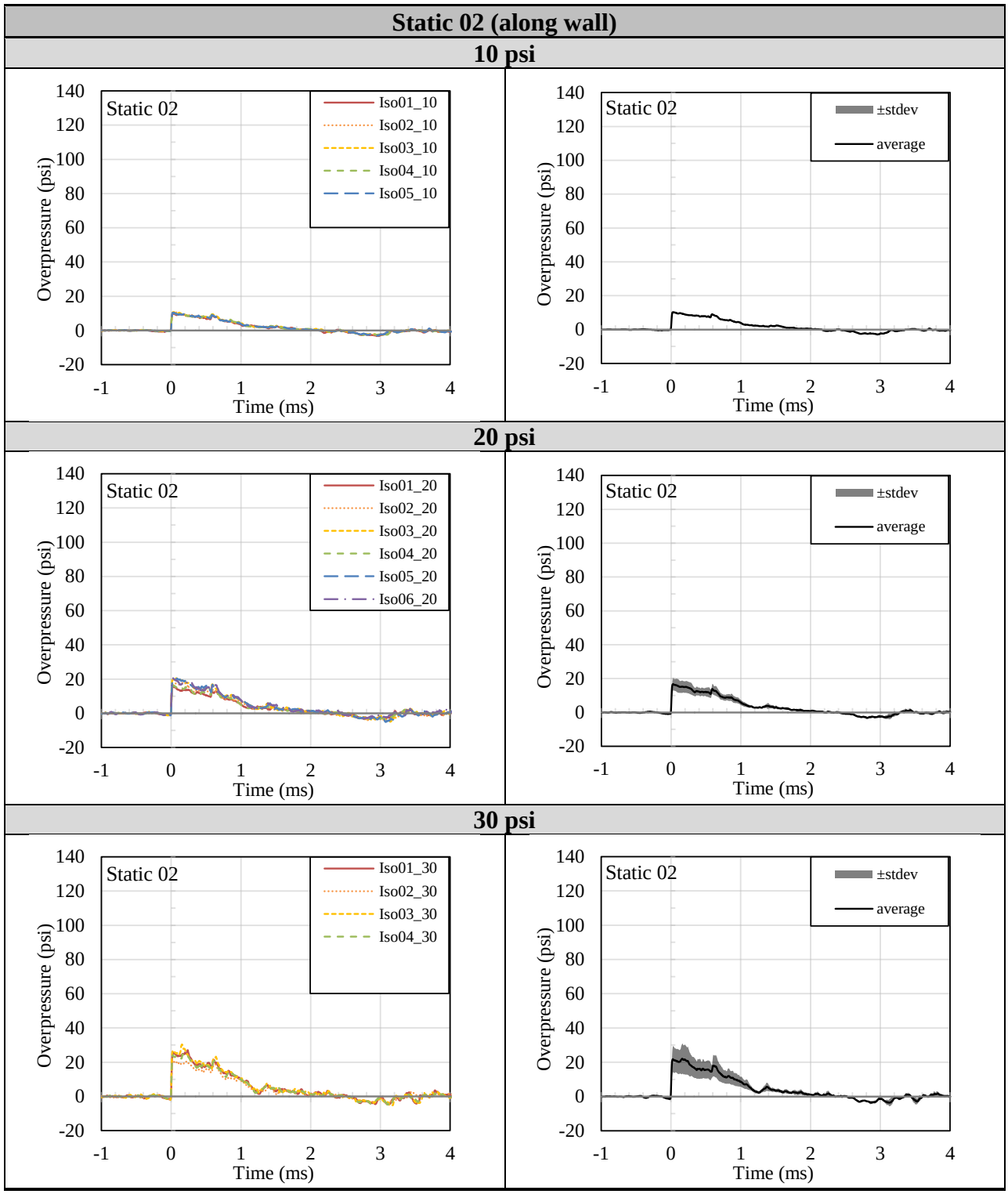

Figure A8. Static 02 (along wall) Isolated Eye.

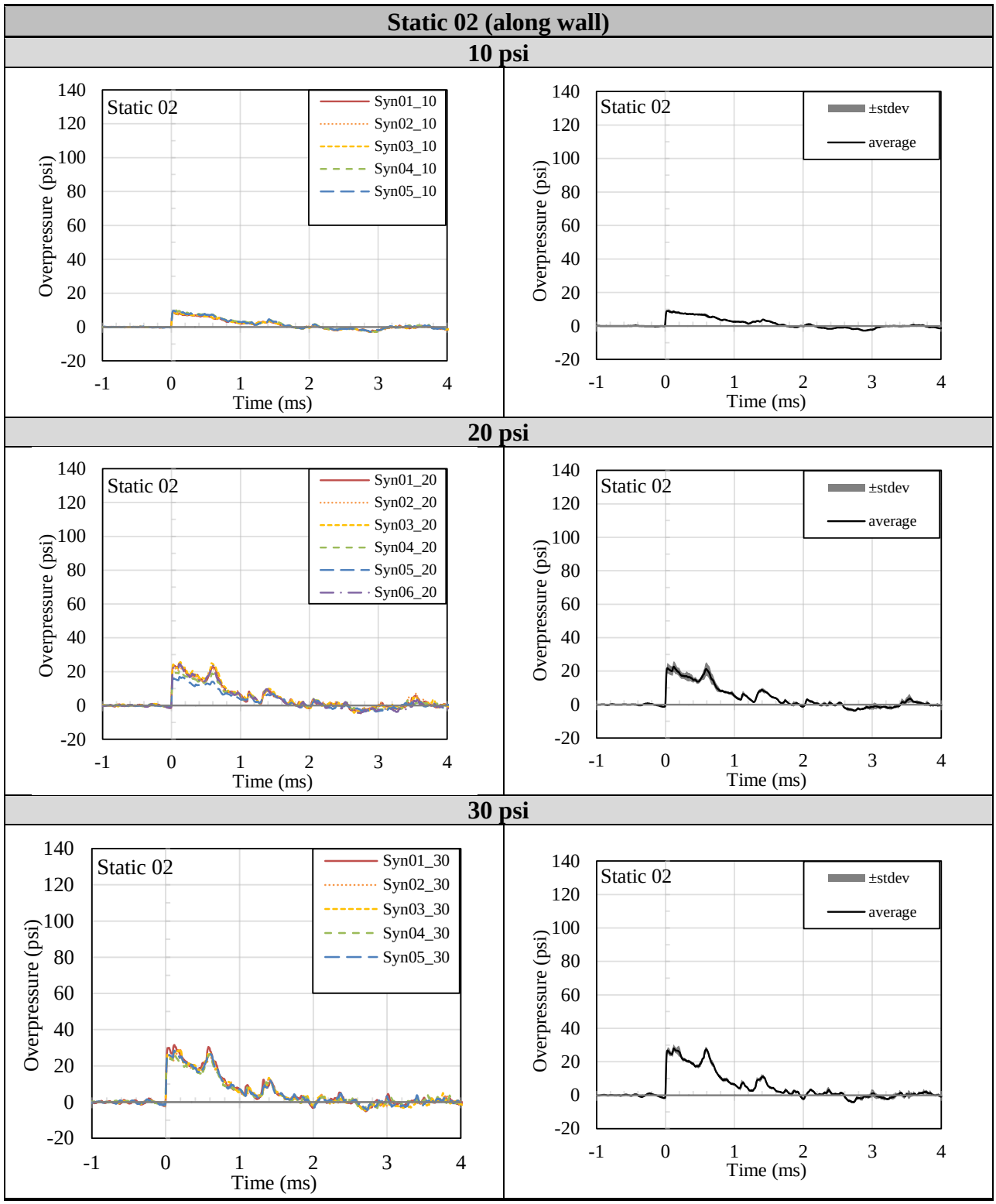

Figure A9. Static 02 (along wall) Synthetic Orbit.

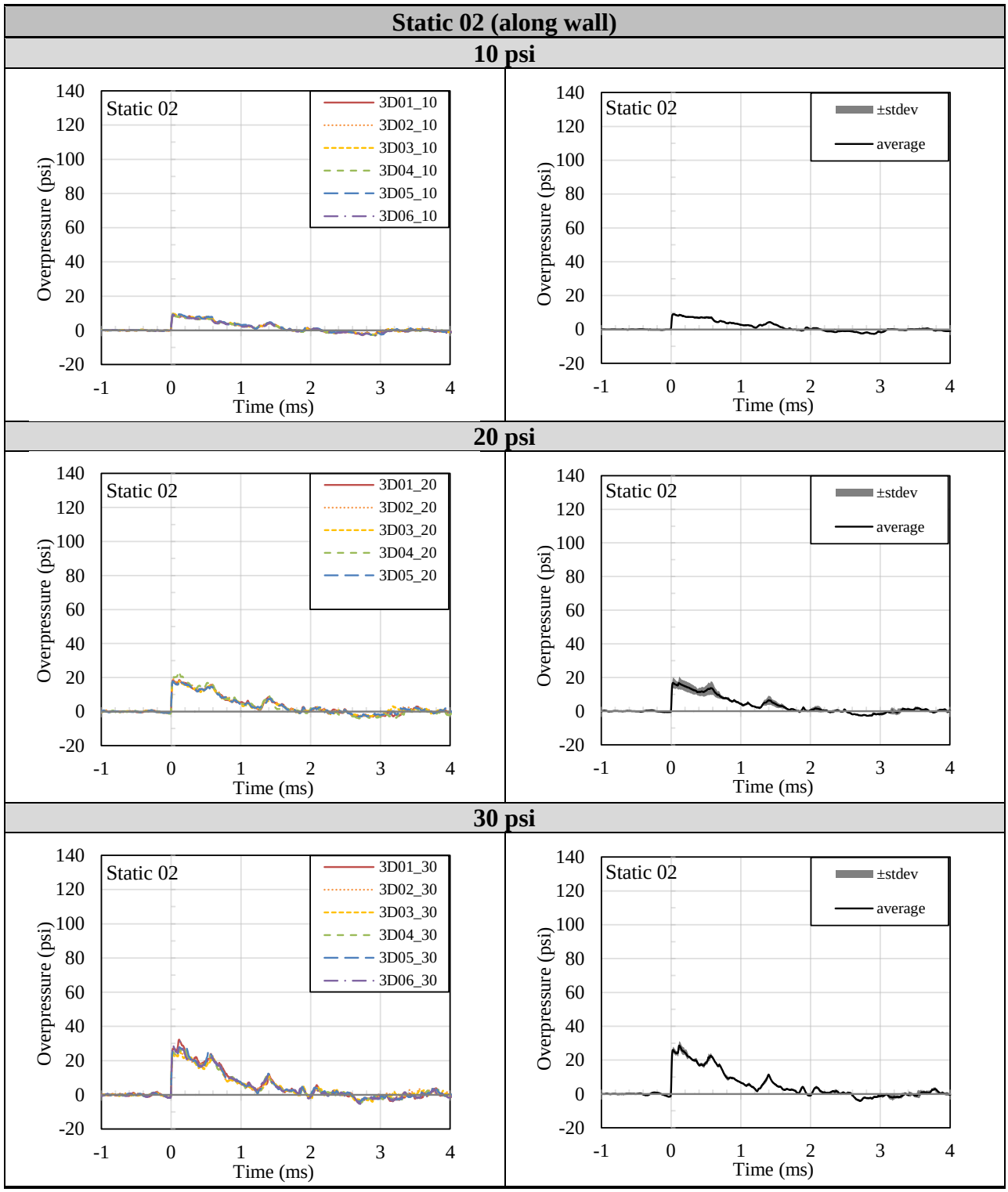

Figure A10. Static 02 (along wall) 3D Orbit – Unprotected Eye.

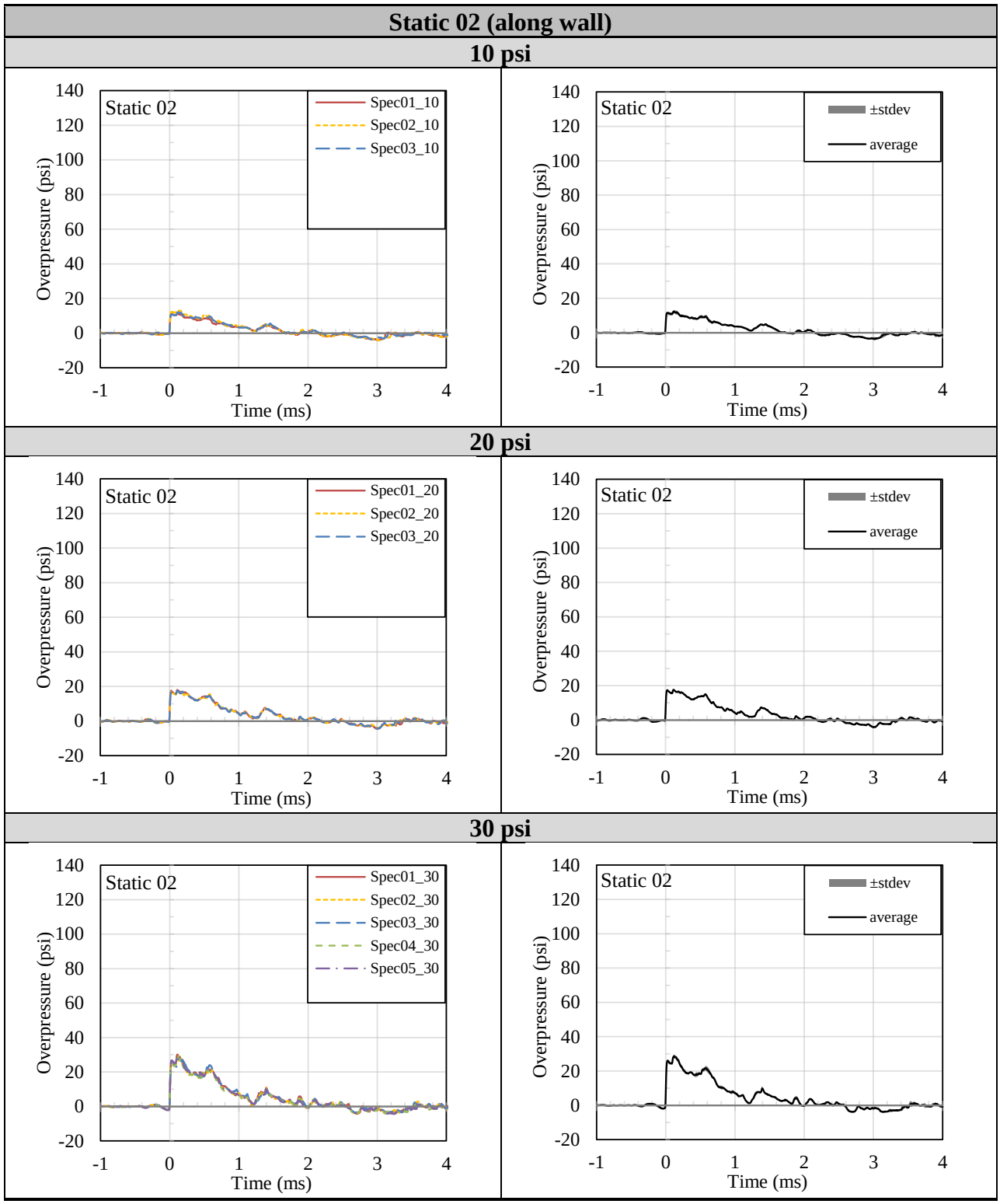

Figure A11. Static 02 (along wall) 3D Orbit – Spectacles.

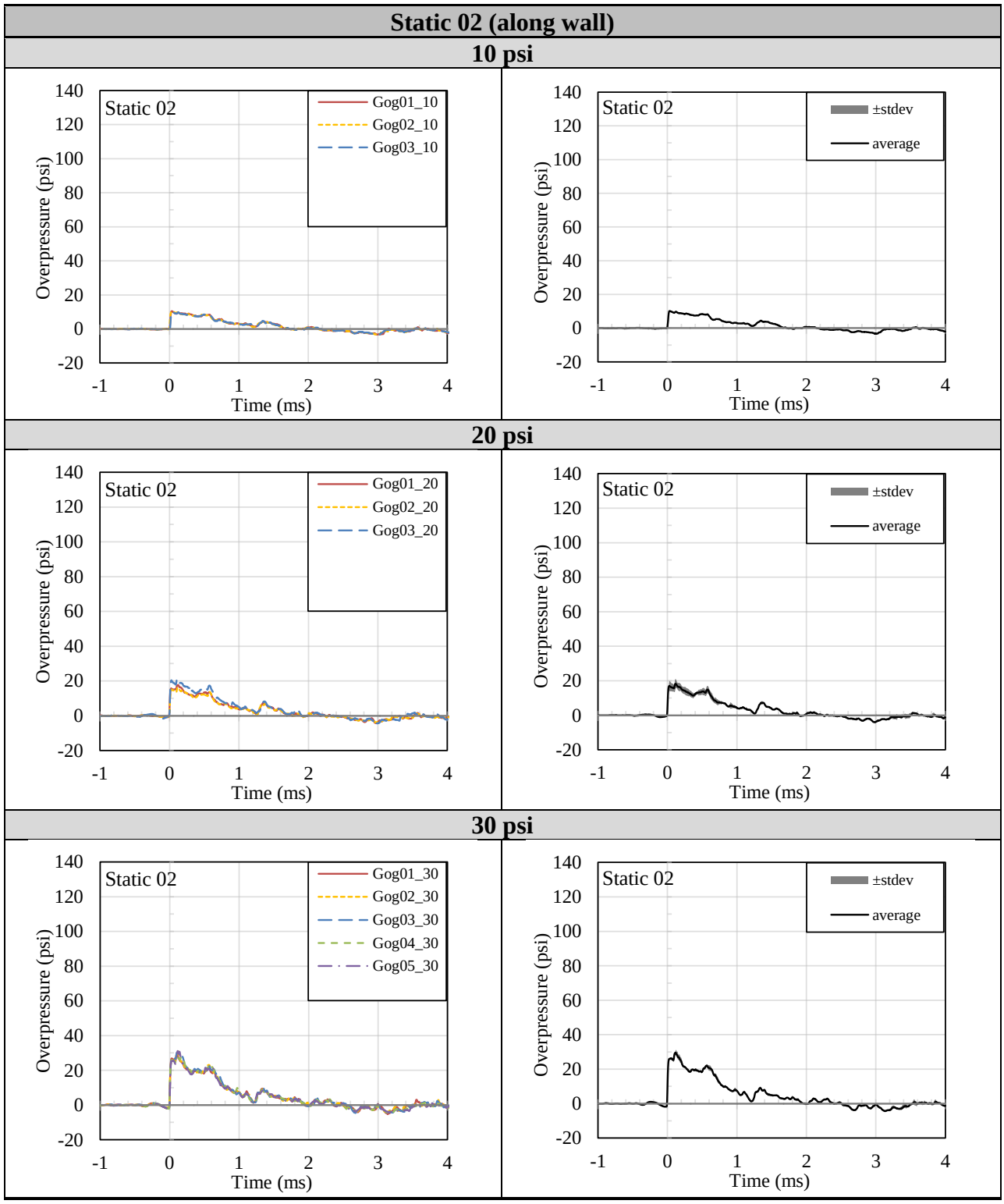

Figure A12. Static 02 (along wall) 3D Orbit – Goggles.

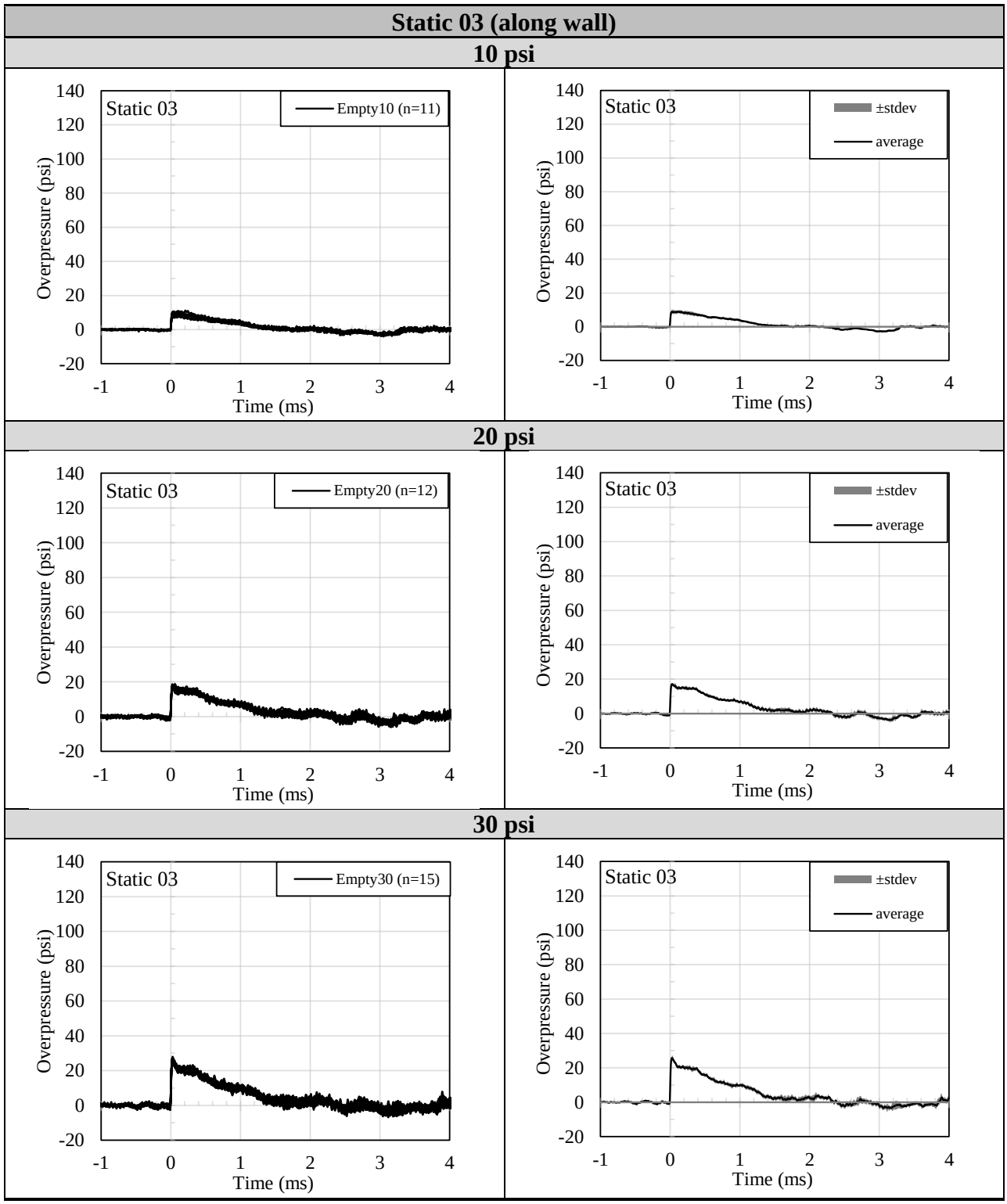

Figure A13. Static 03 (along wall) Empty Tube.

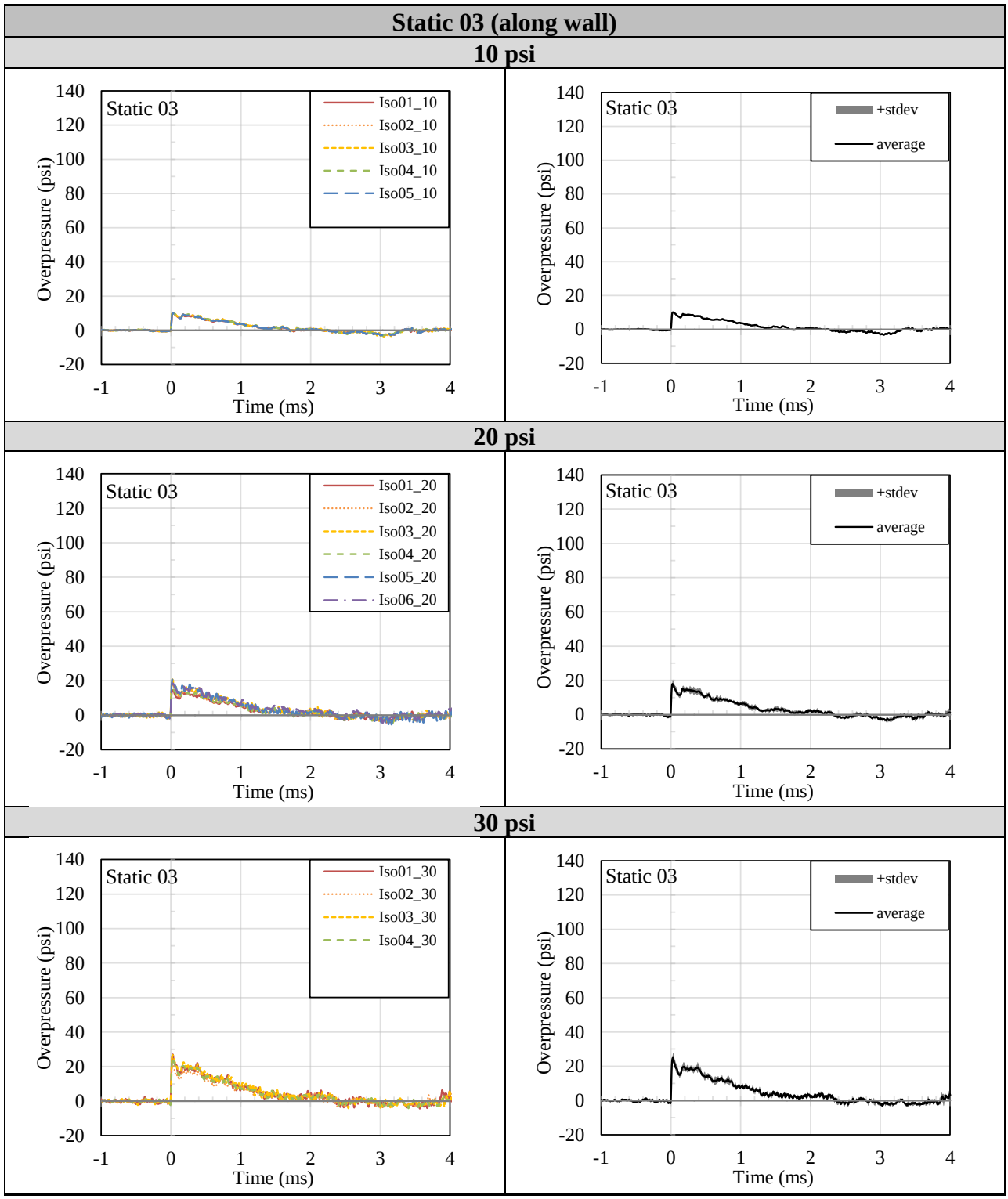

Figure A14. Static 03 (along wall) Isolated Eye.

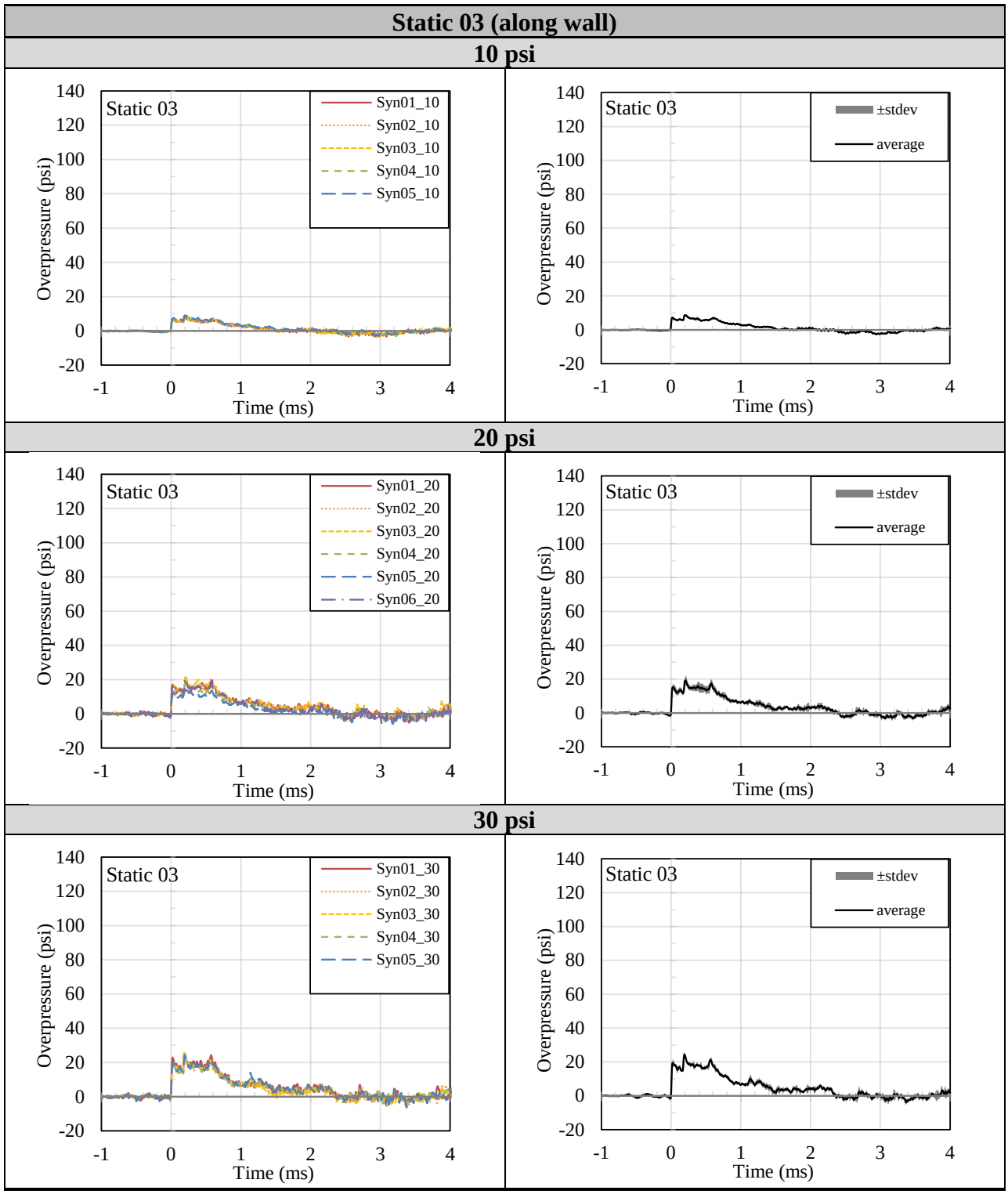

Figure A15. Static 03 (along wall) Synthetic Orbit.

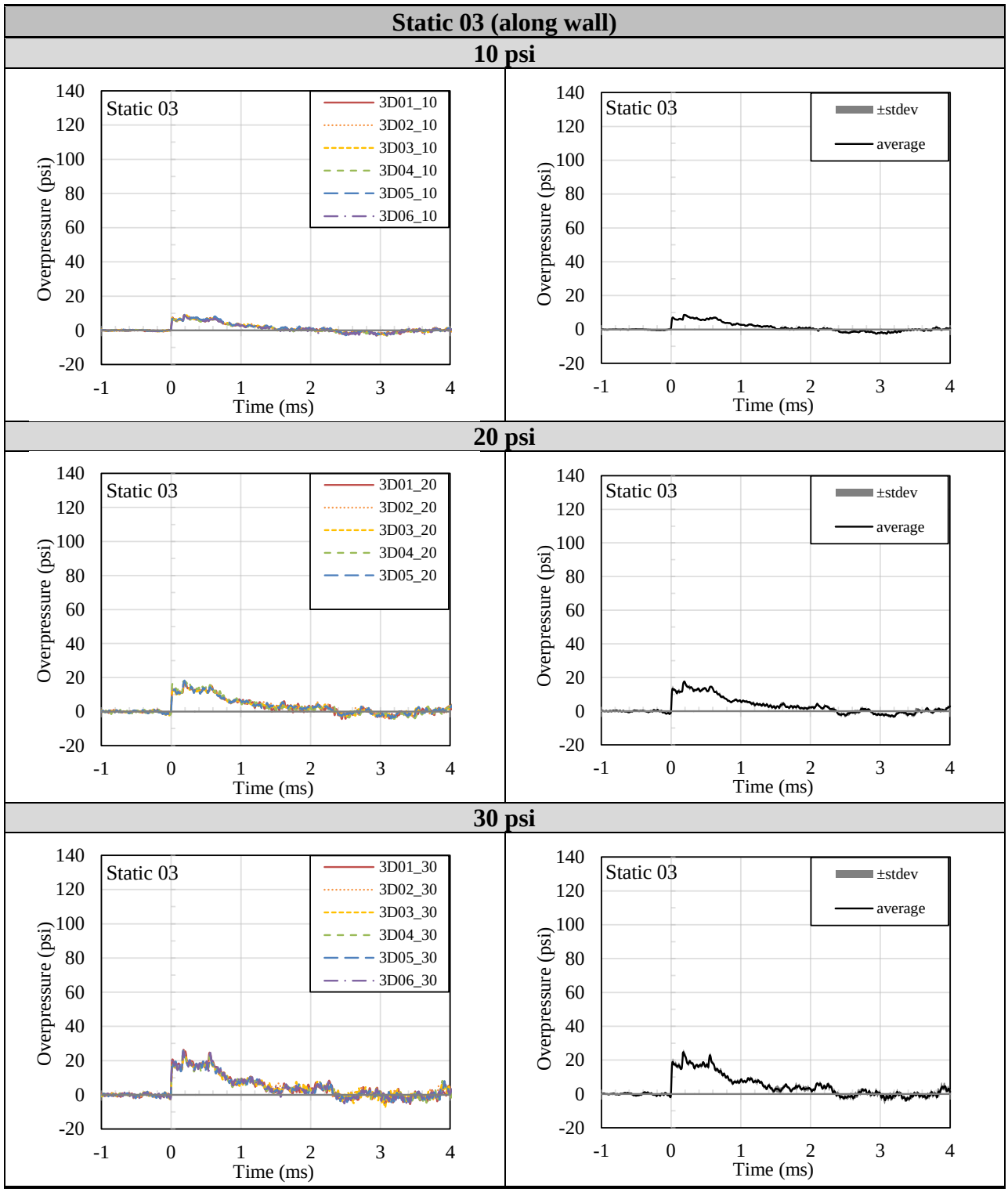

Figure A16. Static 03 (along wall) 3D Orbit – Unprotected Eye.

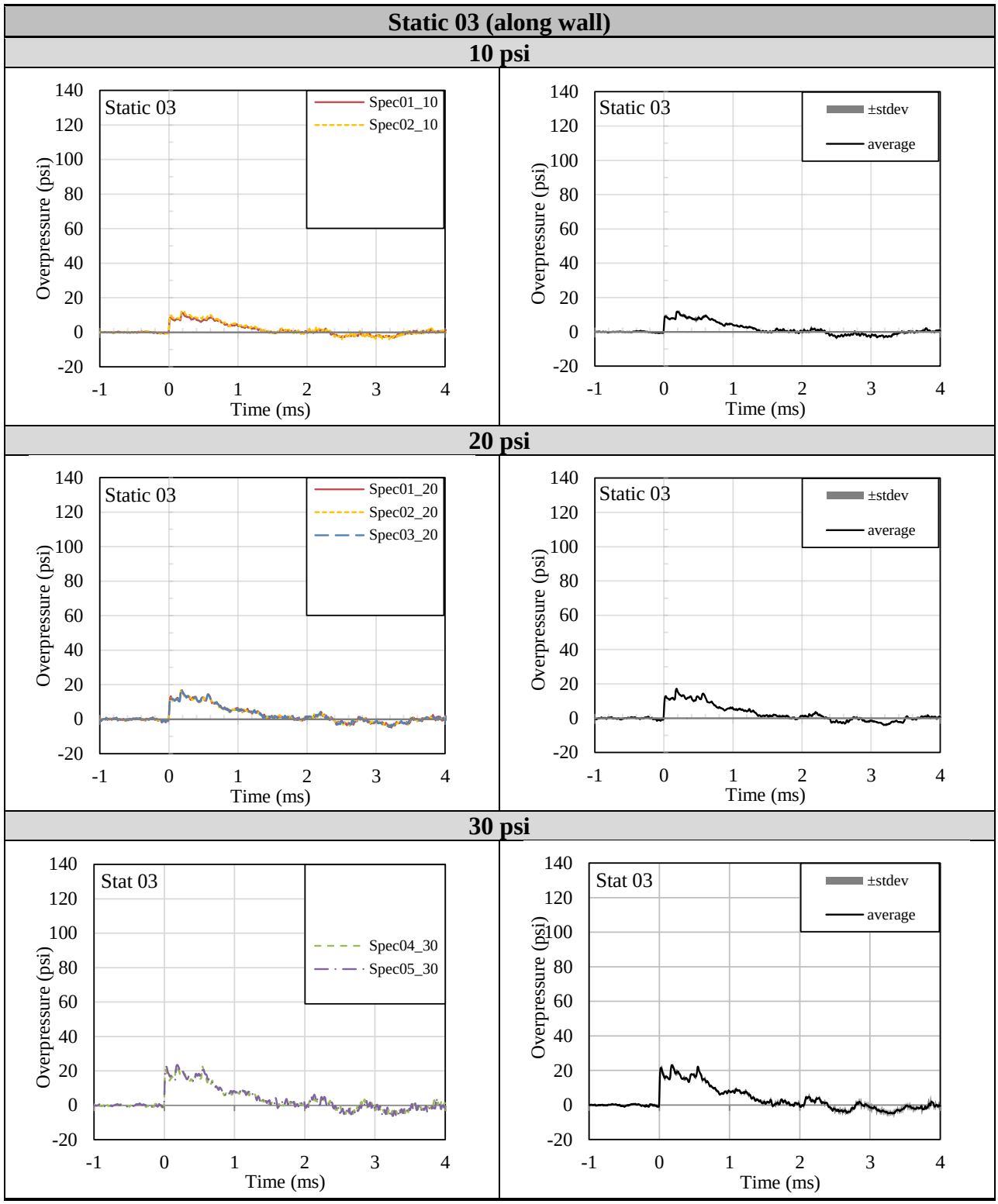

Figure A17. Static 03 (along wall) 3D Orbit – Spectacles.
Note: Only one test for the 10 psi test level and two tests for the 30 psi test level due to DAS availability.

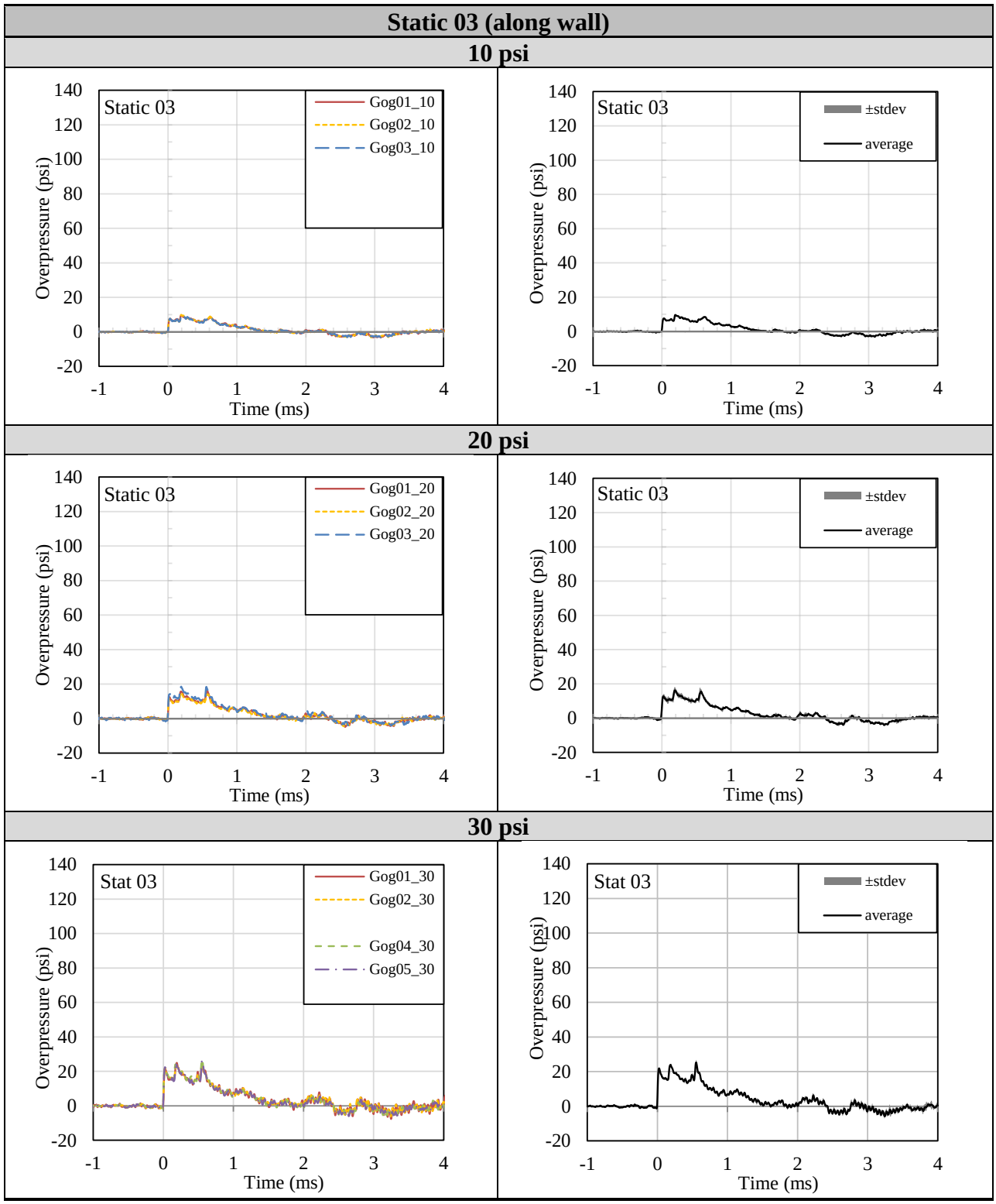

Figure A18. Static 03 (along wall) 3D Orbit – Goggles.
Note: Only four tests for the 30 psi test level due to DAS availability.

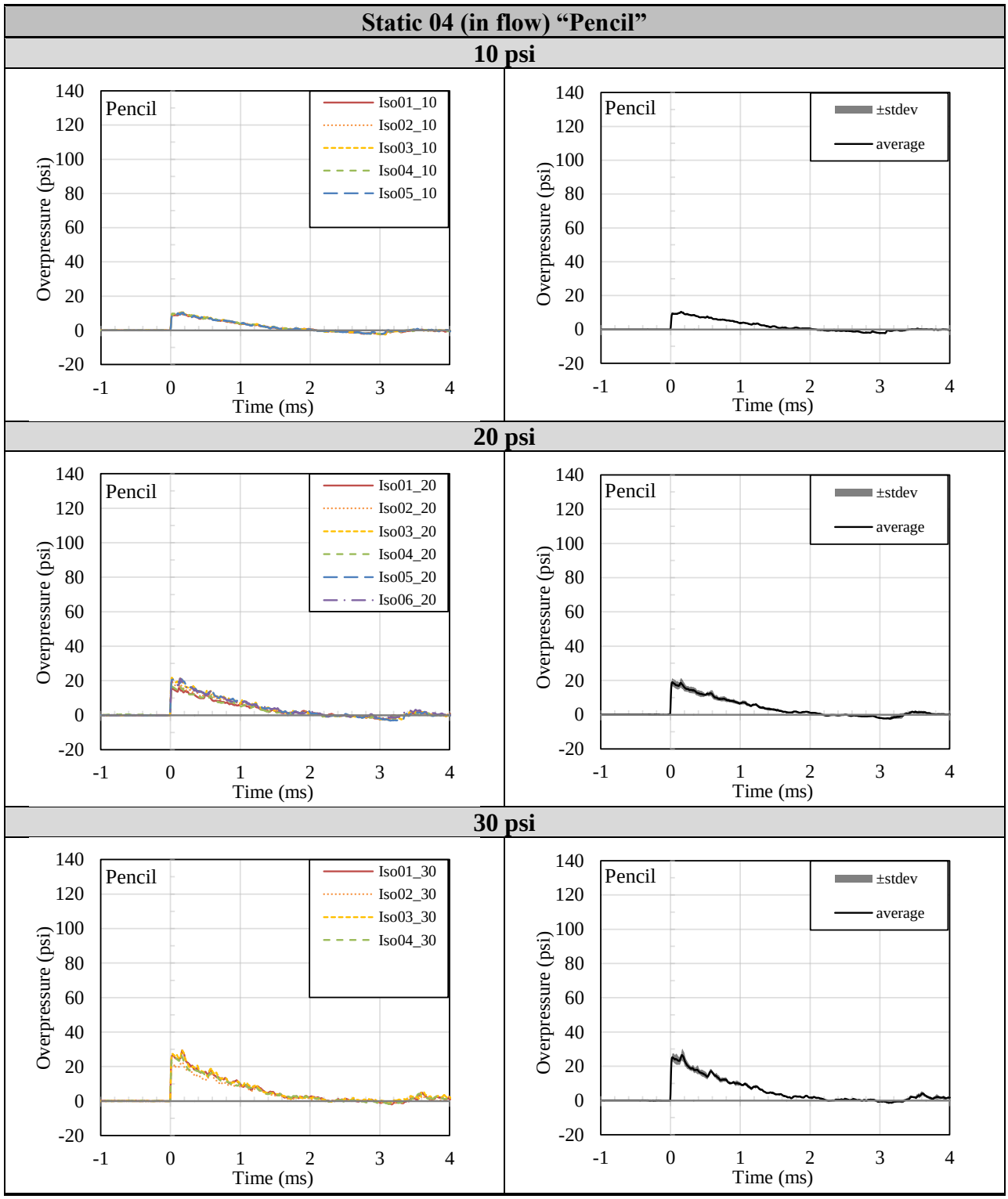

Figure A19. Static 04 (in flow) Isolated Eye.

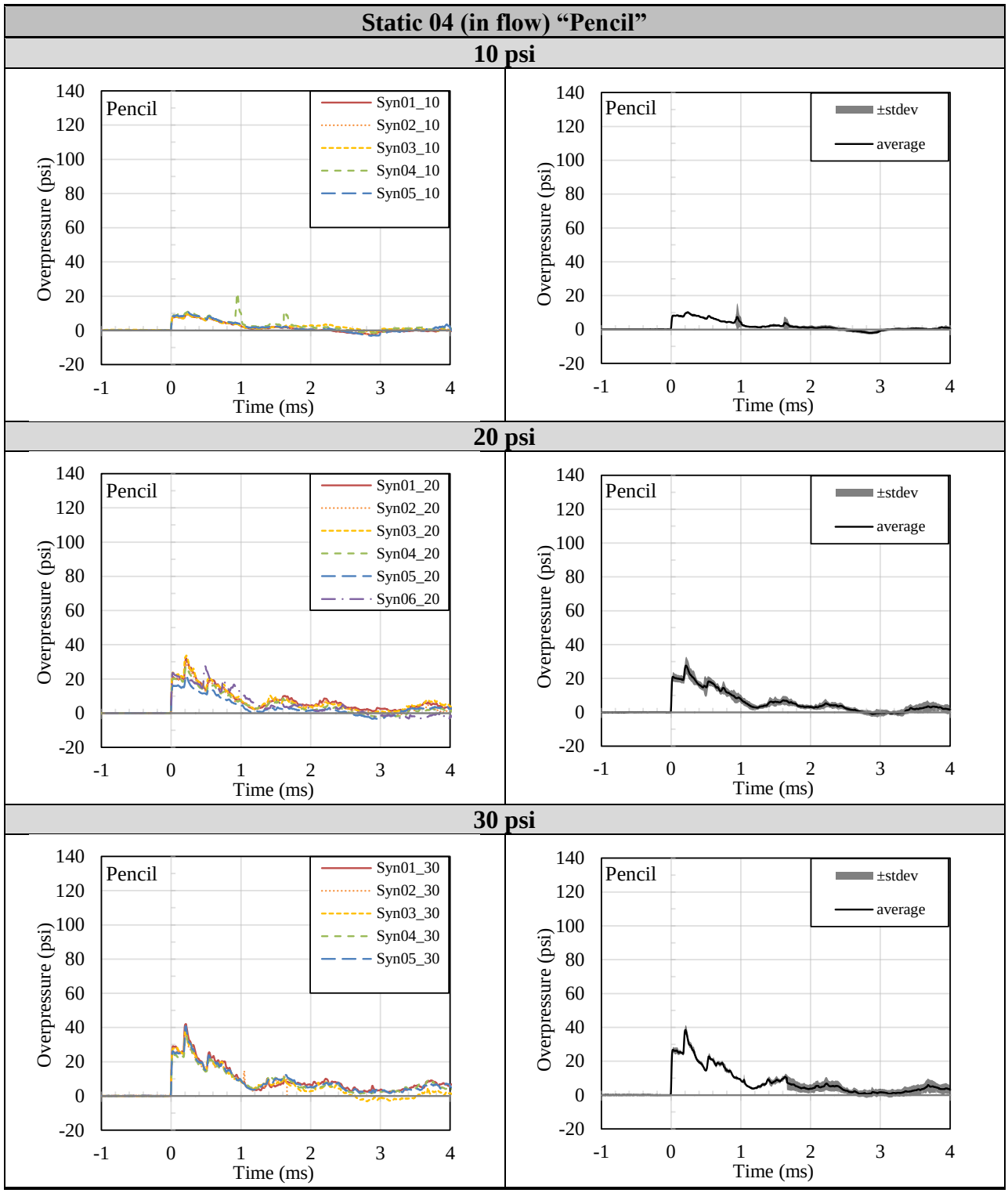

Figure A20. Static 04 (in flow) Synthetic Orbit.

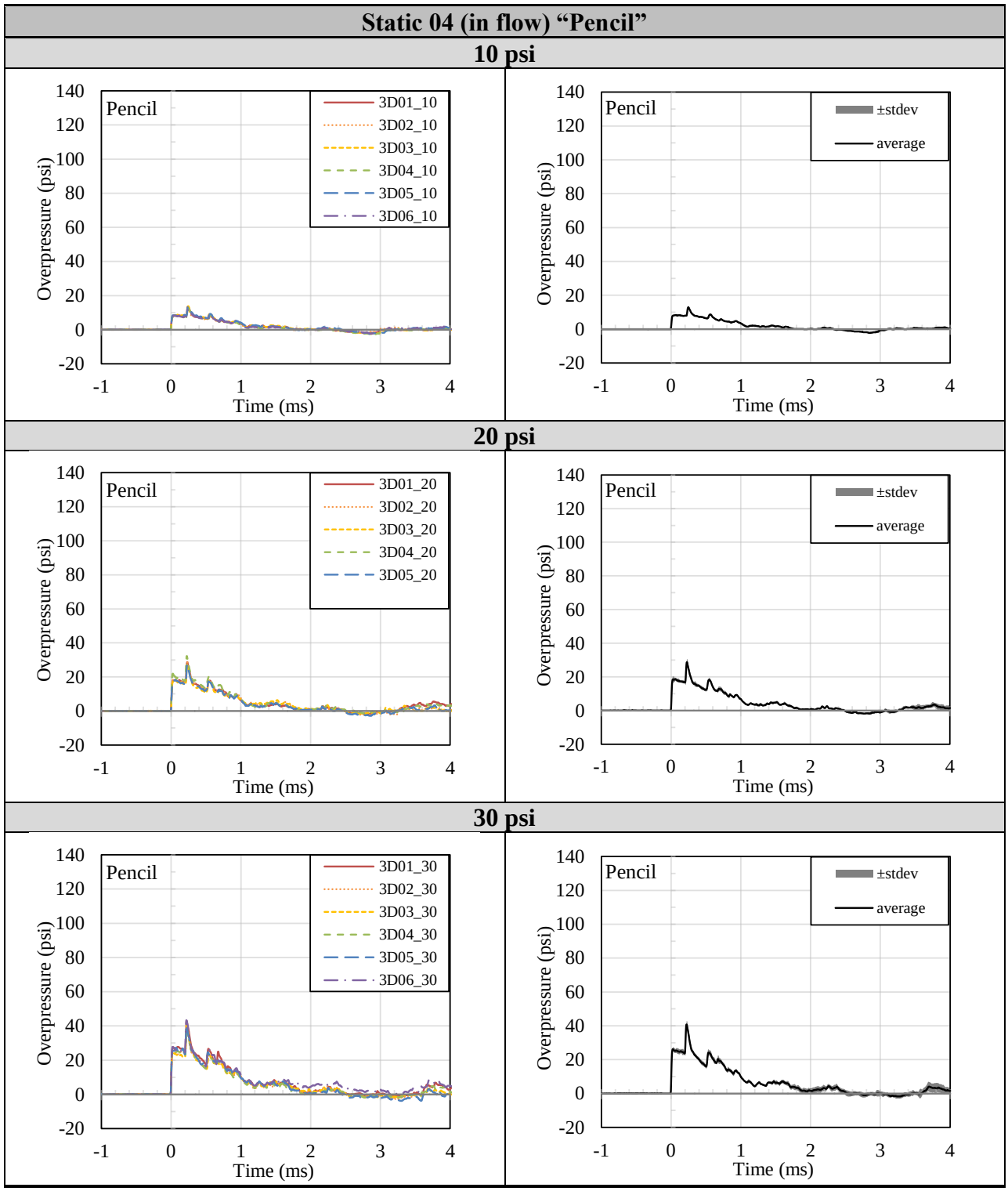

Figure A21. Static 04 (in flow) 3D Orbit – Unprotected Eye.

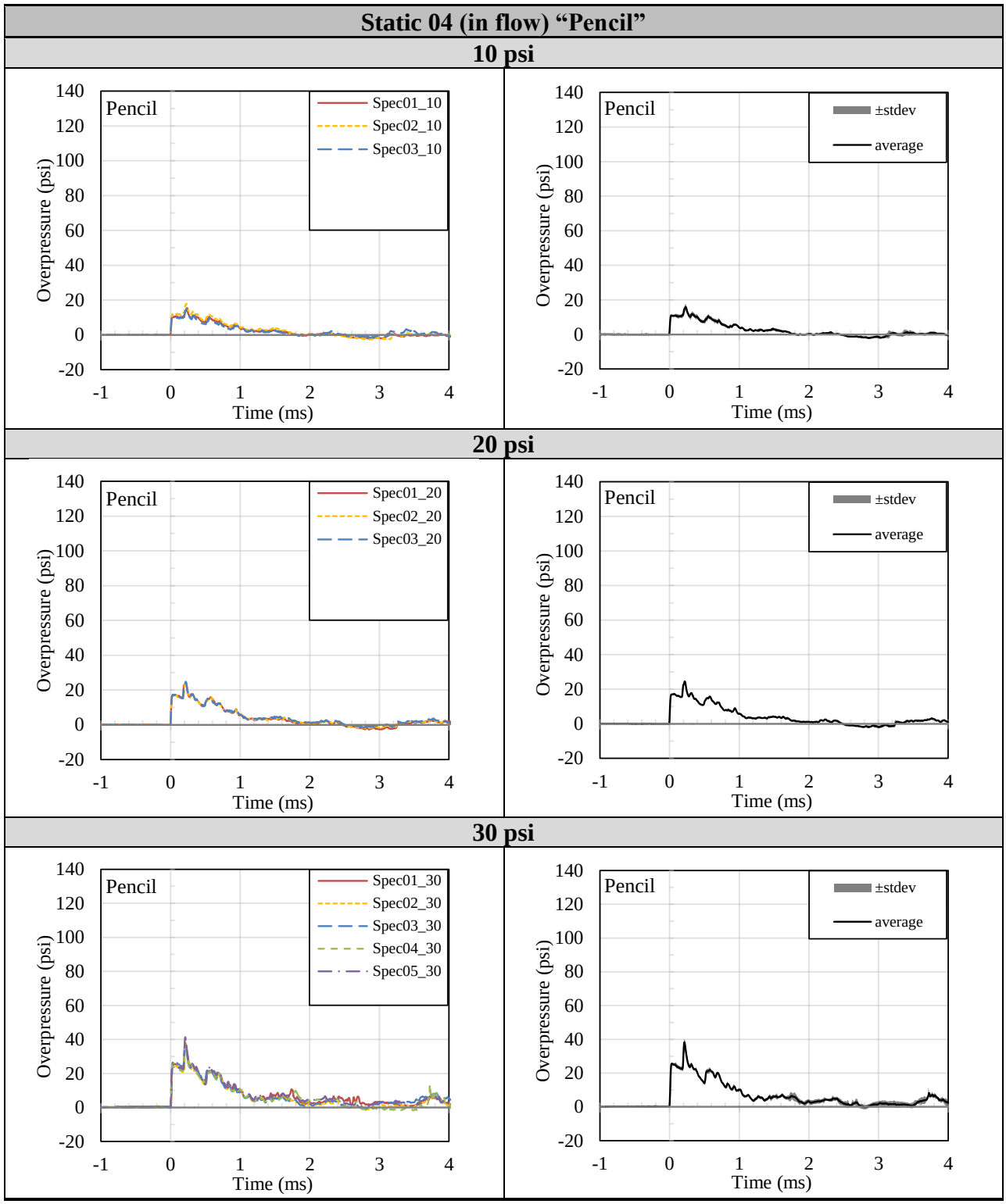

Figure A22. Static 04 (in flow) 3D Orbit – Spectacles.

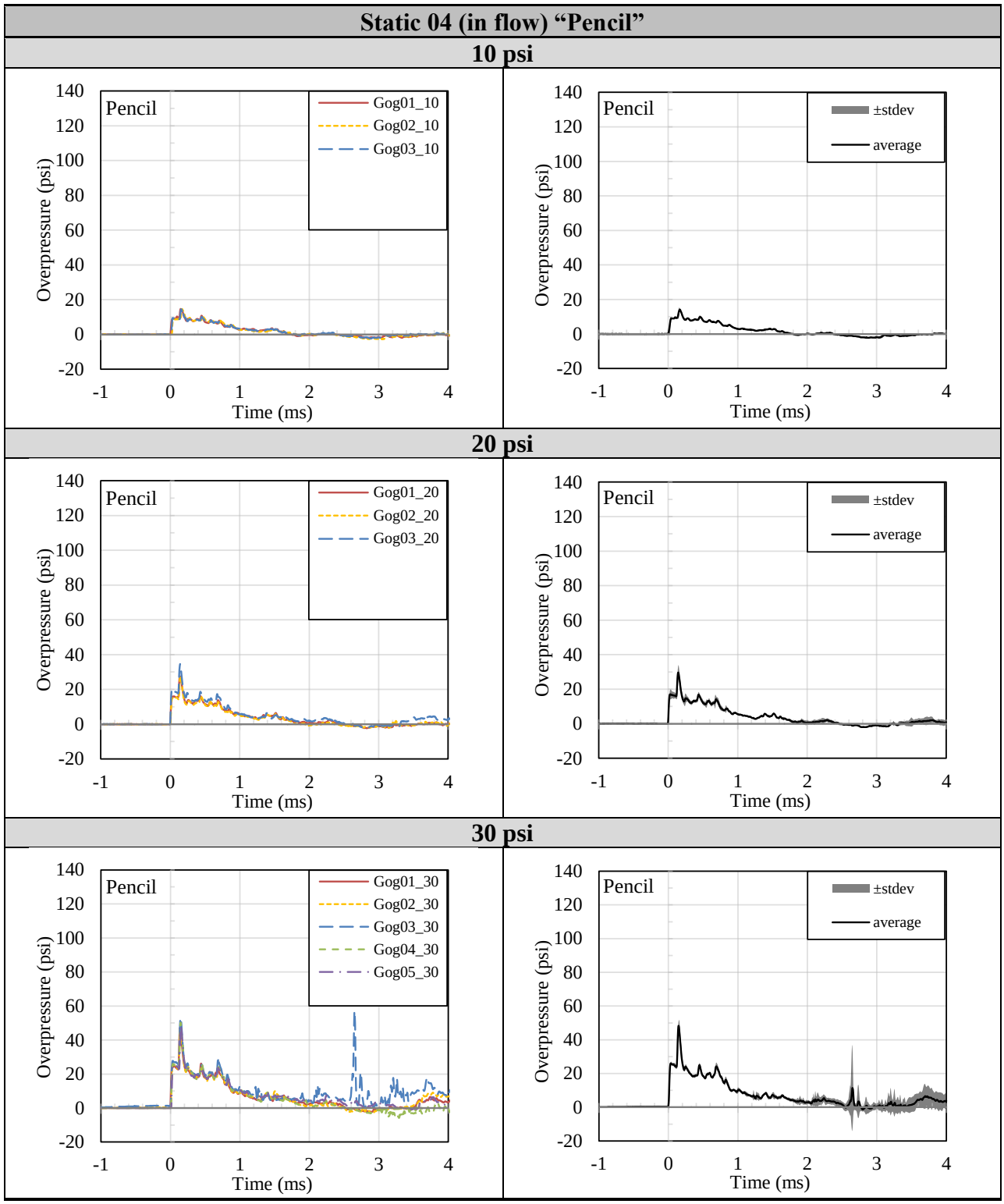

Figure A23. Static 04 (in flow) 3D Orbit – Goggles.

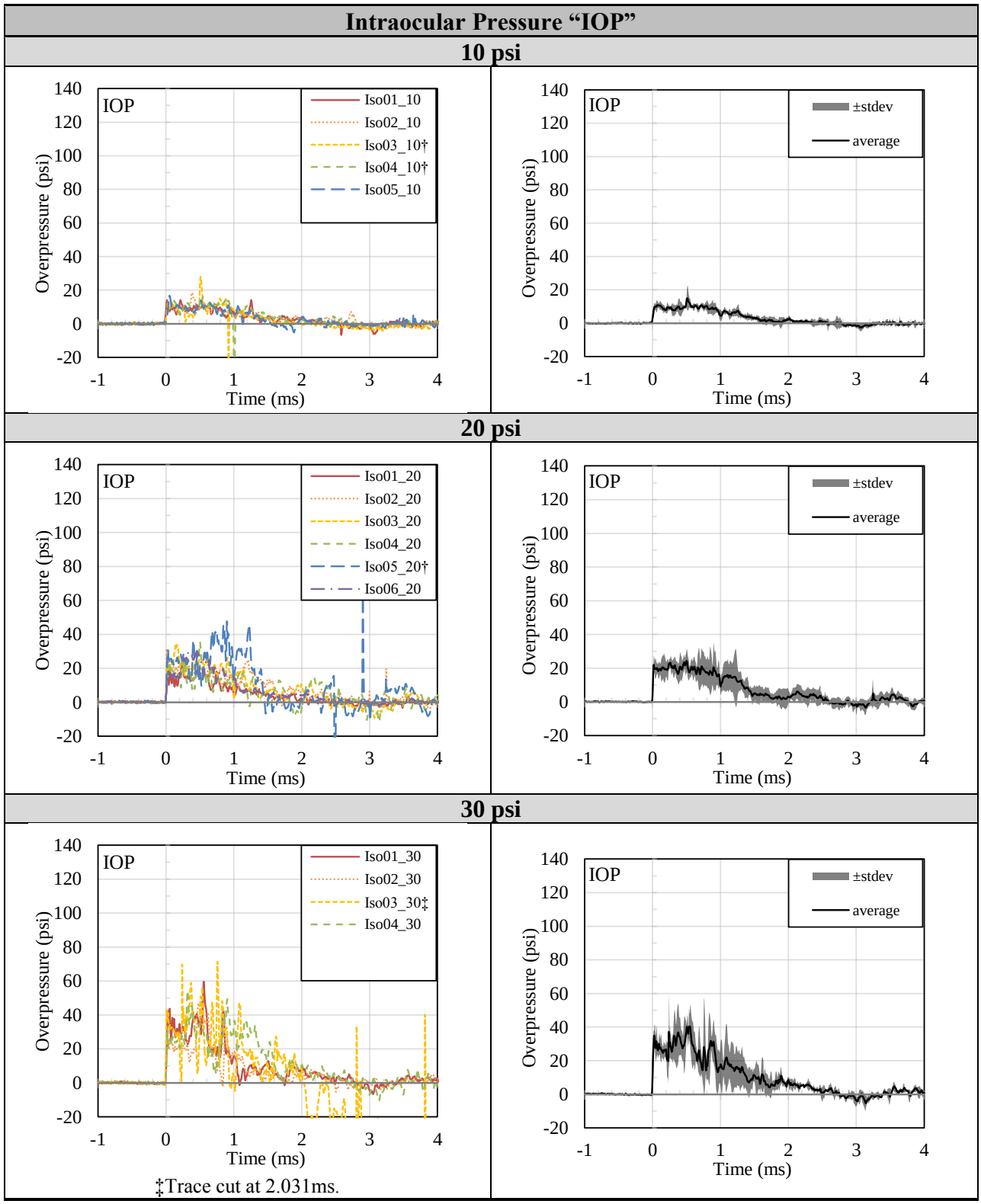

Figure A24. Intraocular Pressure (IOP) Isolated Eye.

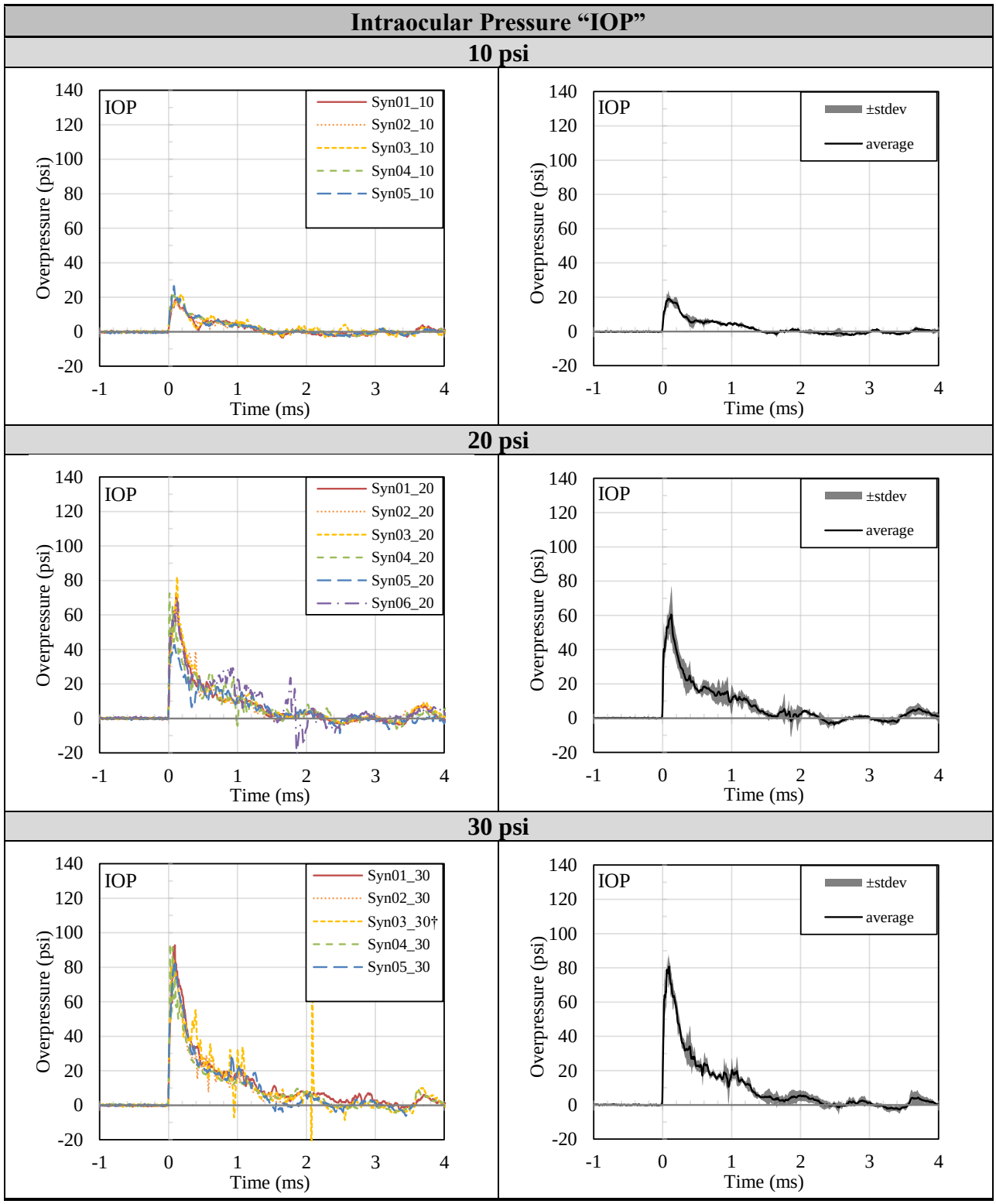

Figure A25. Intraocular Pressure (IOP) Synthetic Orbit.

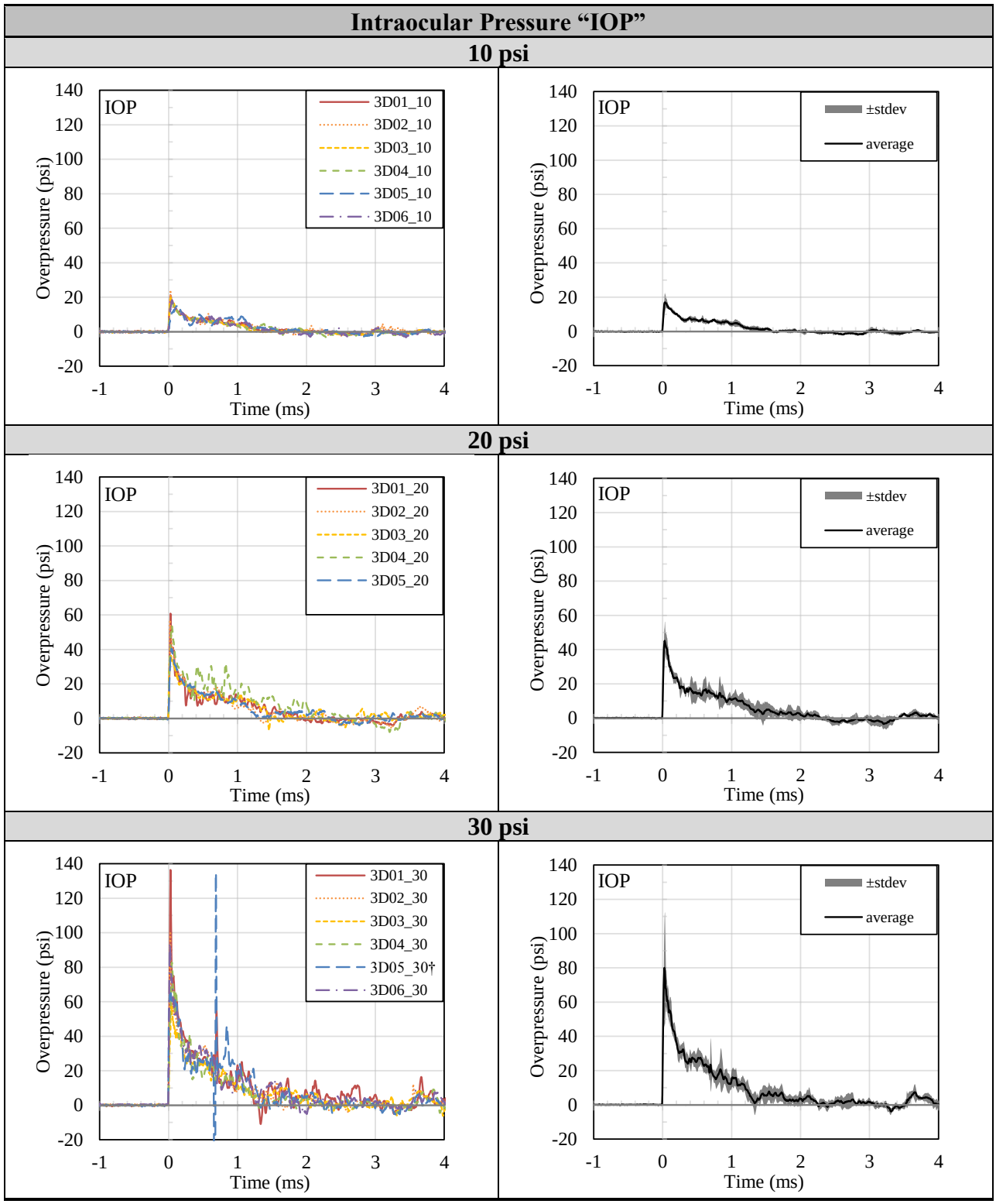

Figure A26. Intraocular Pressure (IOP) 3D Orbit – Unprotected Eye.

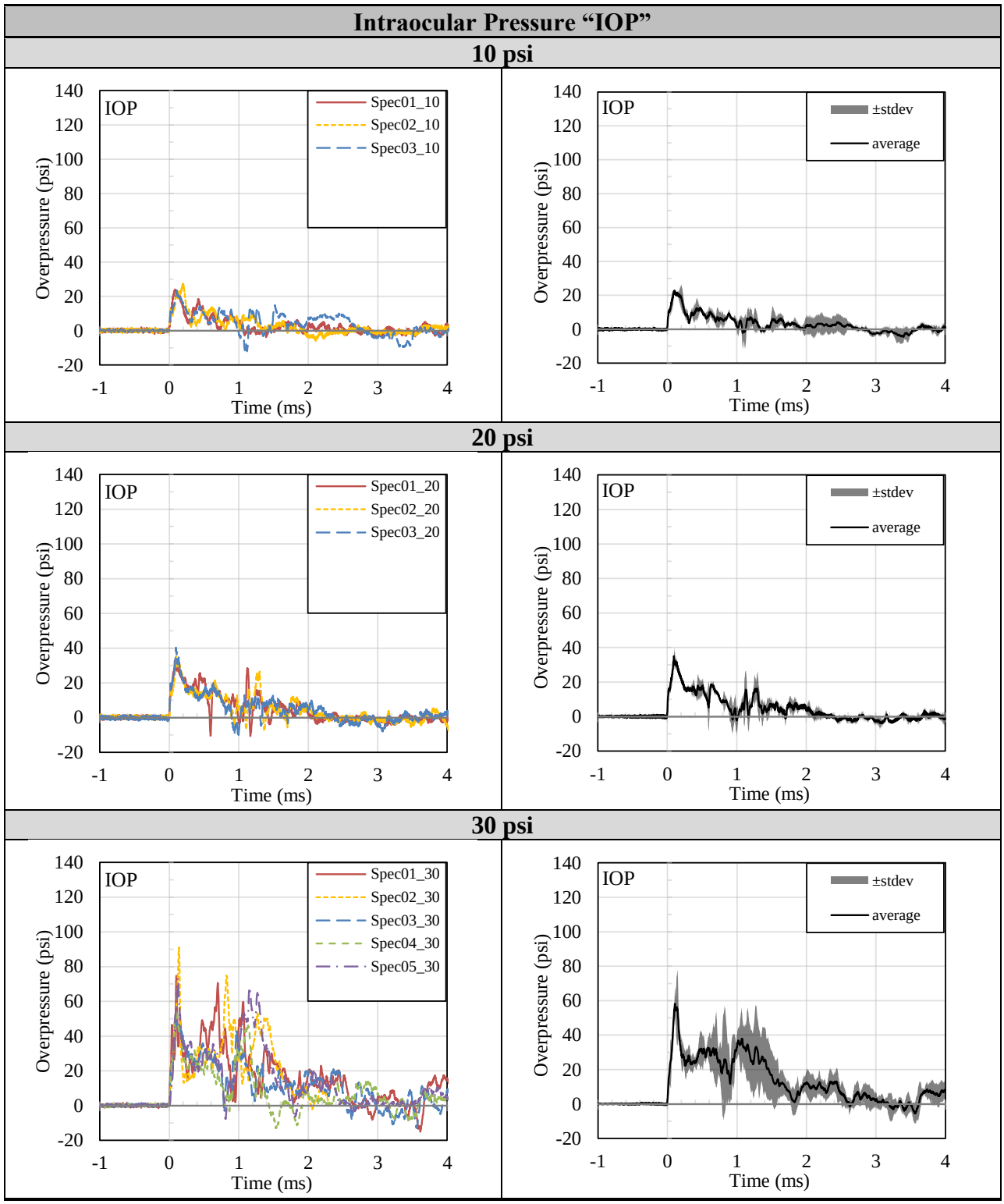

Figure A27. Intraocular Pressure (IOP) 3D Orbit – Spectacles.

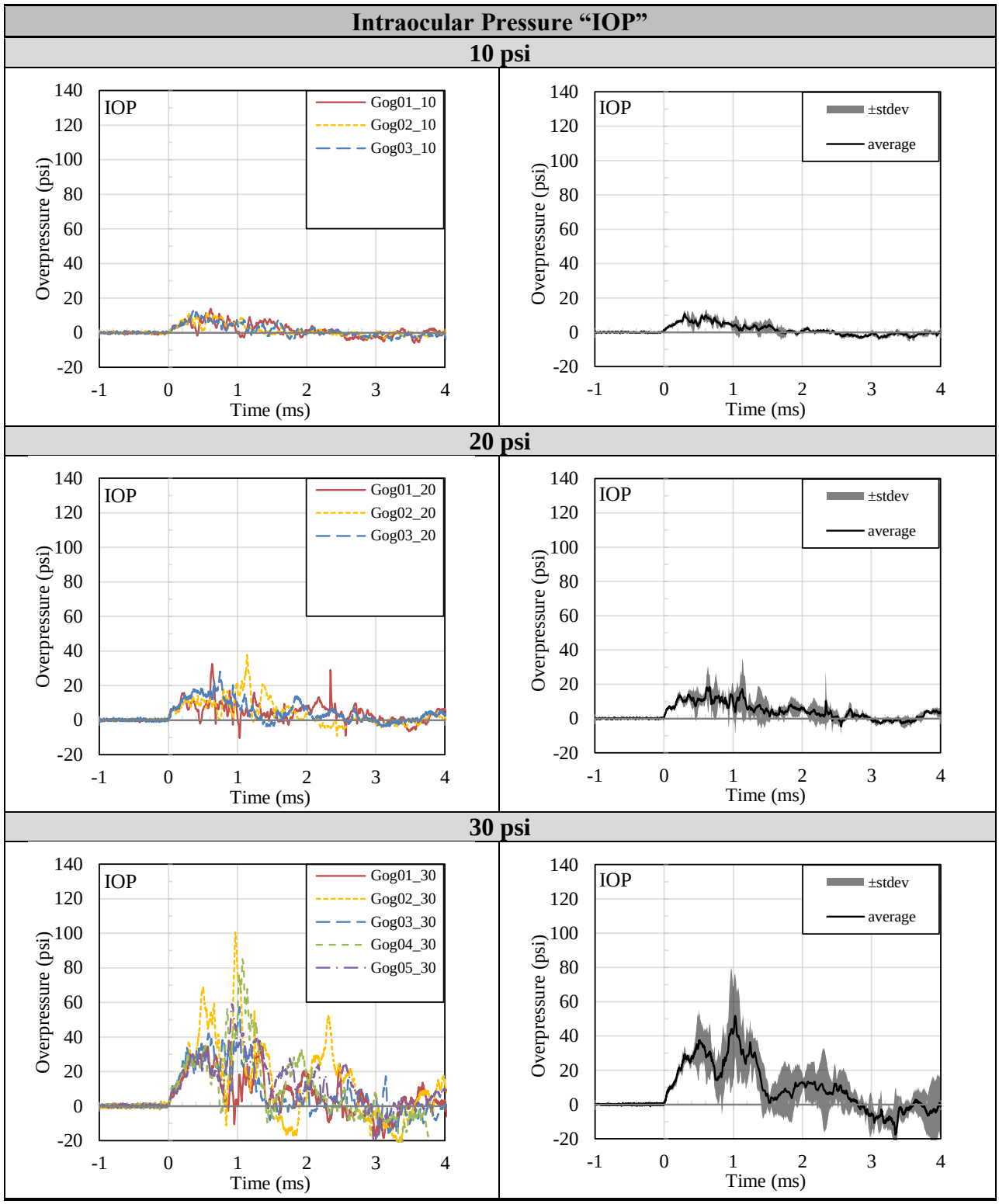

Figure A28. Intraocular Pressure (IOP) 3D Orbit – Goggles

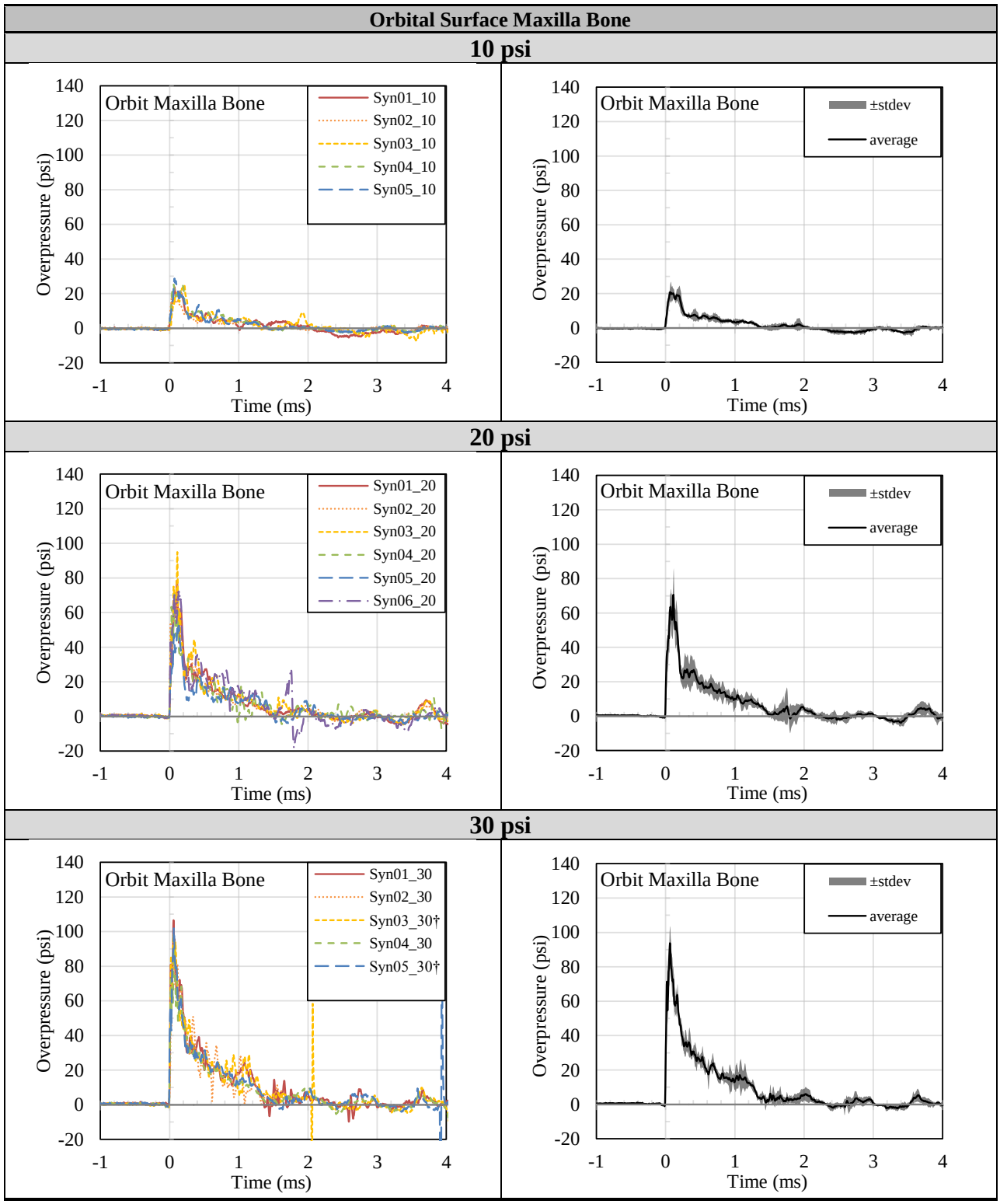

Figure A29. Orbital Surface Maxilla Bone Synthetic Orbit.

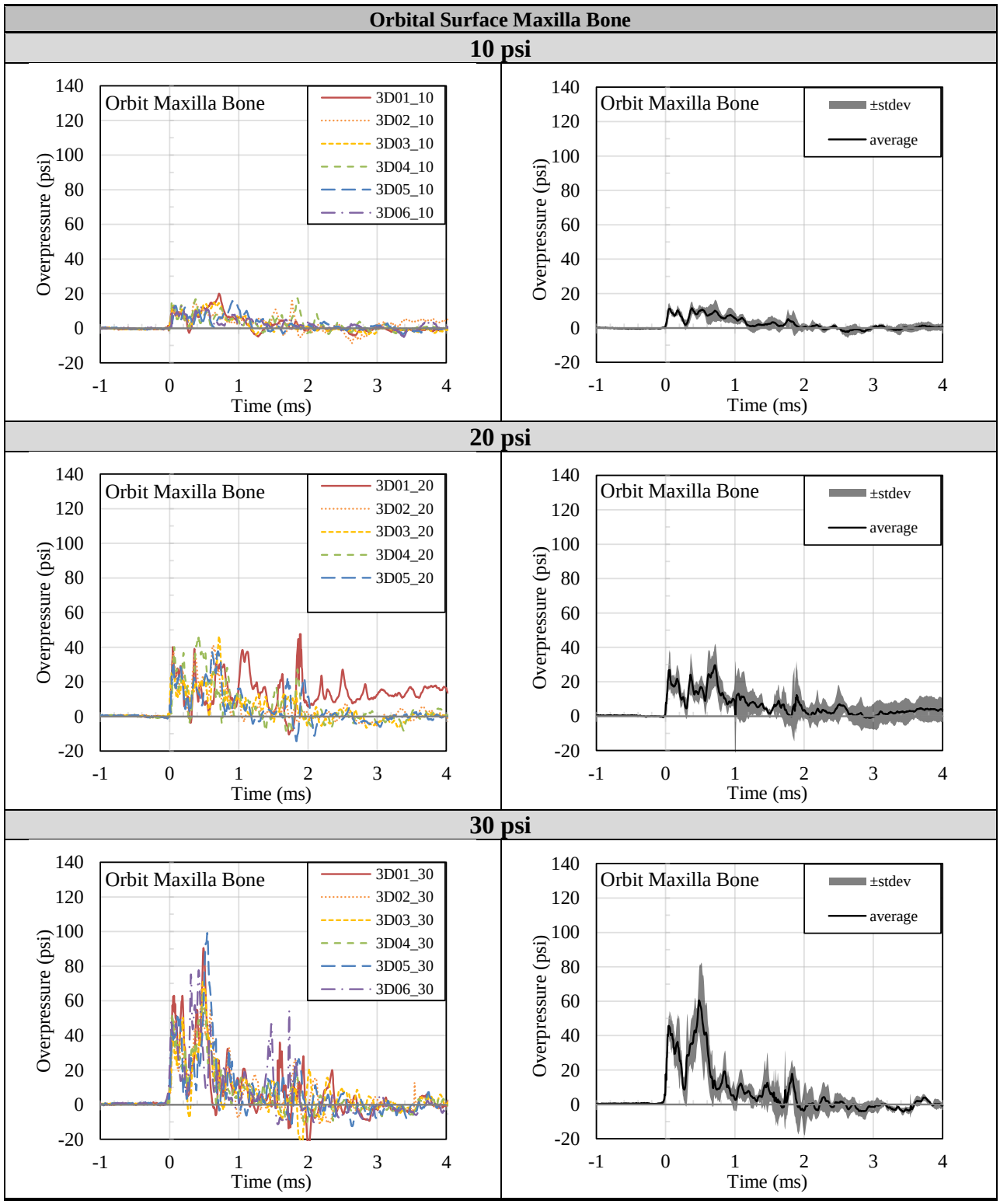

Figure A30. Orbital Surface Maxilla Bone 3D Orbit – Unprotected Eye.

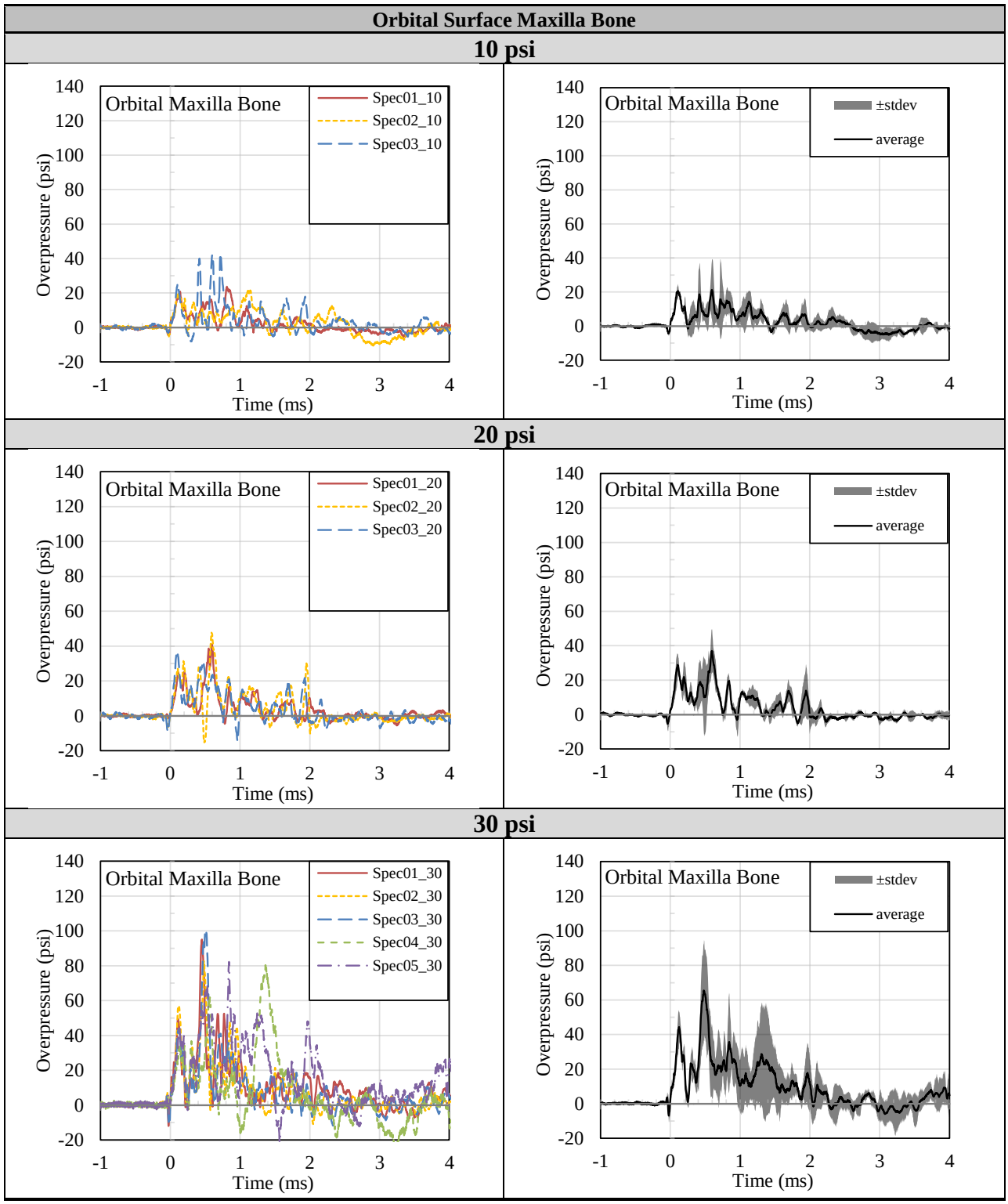

Figure A31. Orbital Surface Maxilla Bone 3D Orbit – Spectacles.

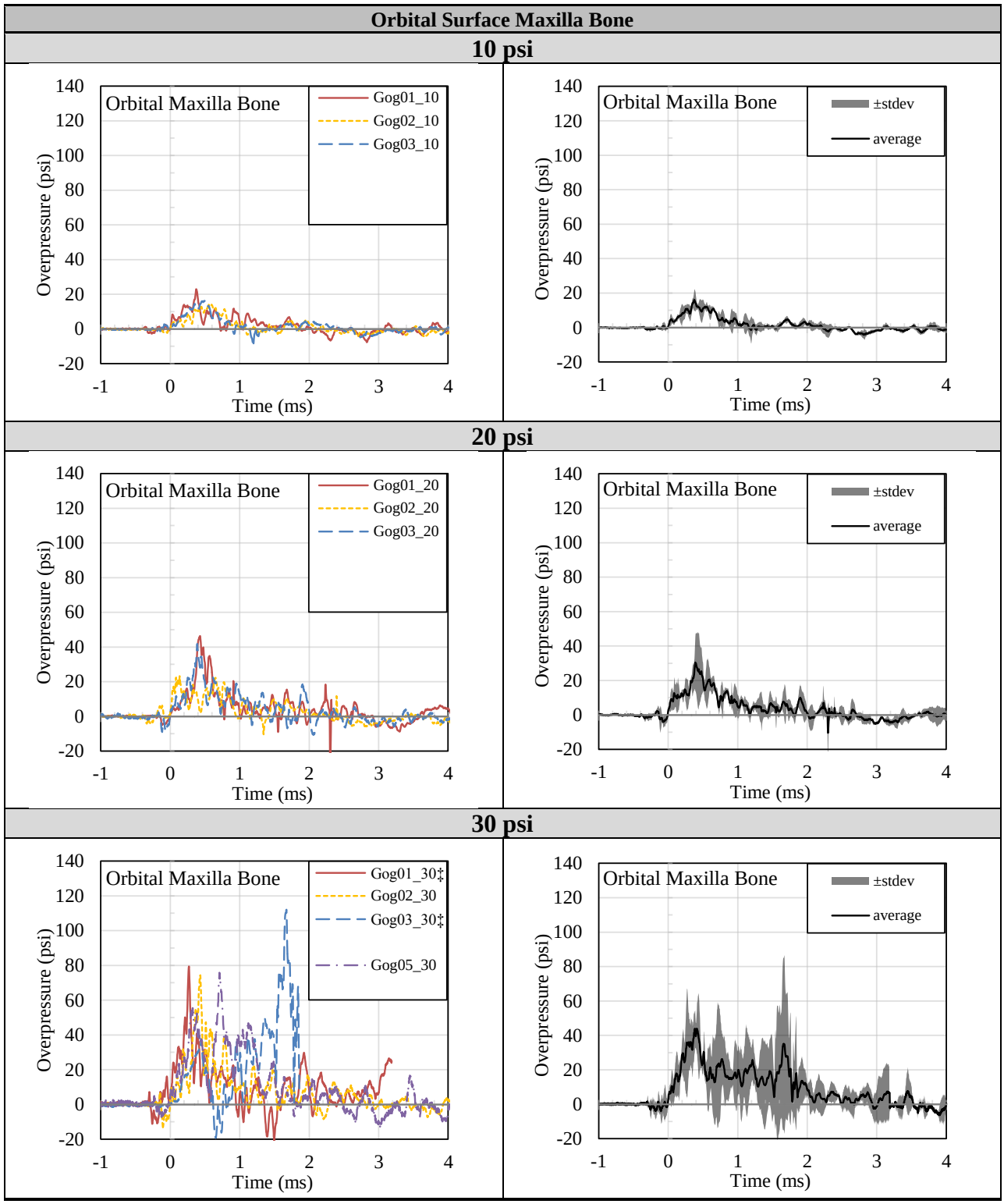

Figure A32. Orbital Surface Maxilla Bone 3D Orbit – Goggles.

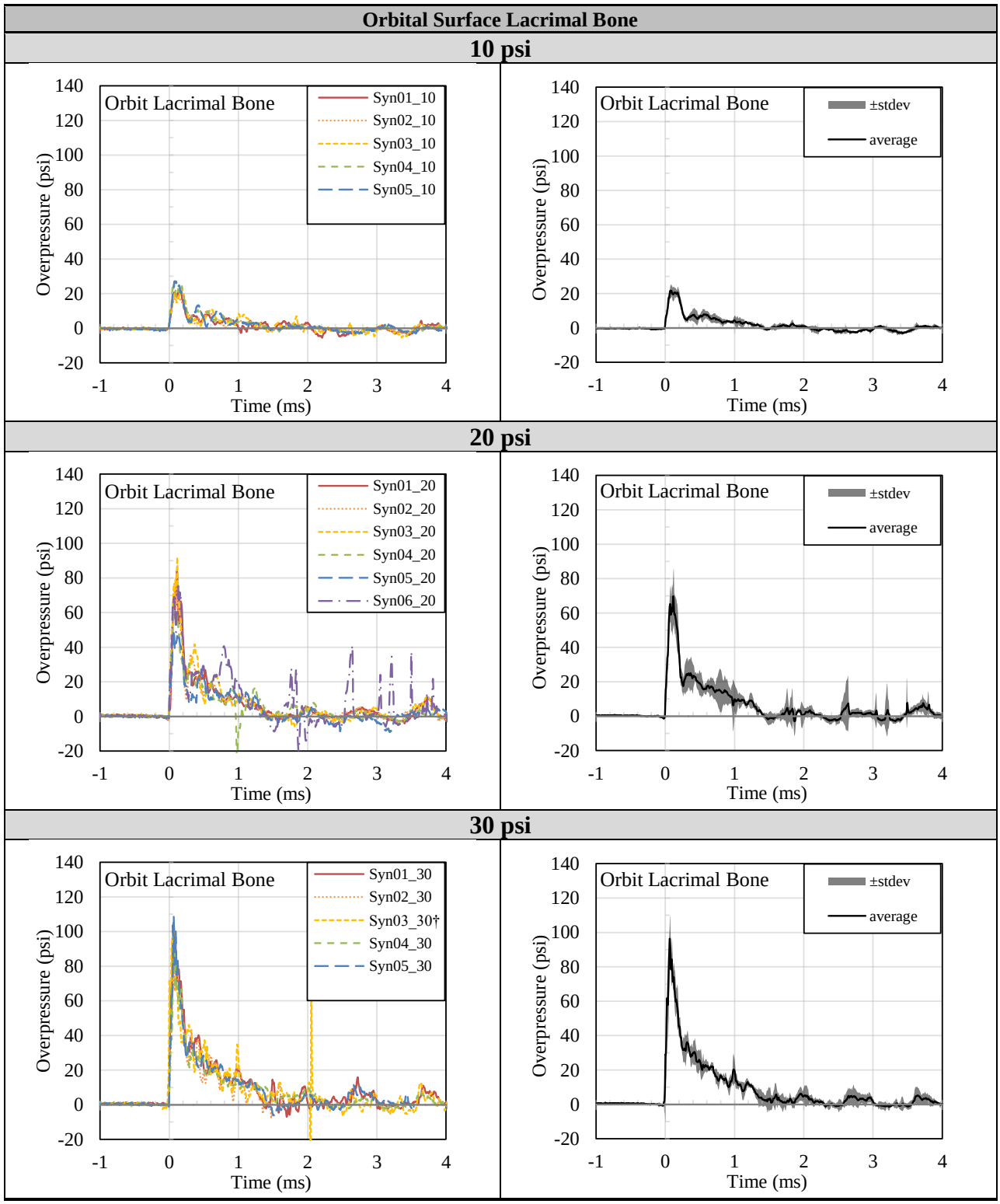

Figure A33. Orbital Surface Lacrimal Bone Synthetic Orbit.

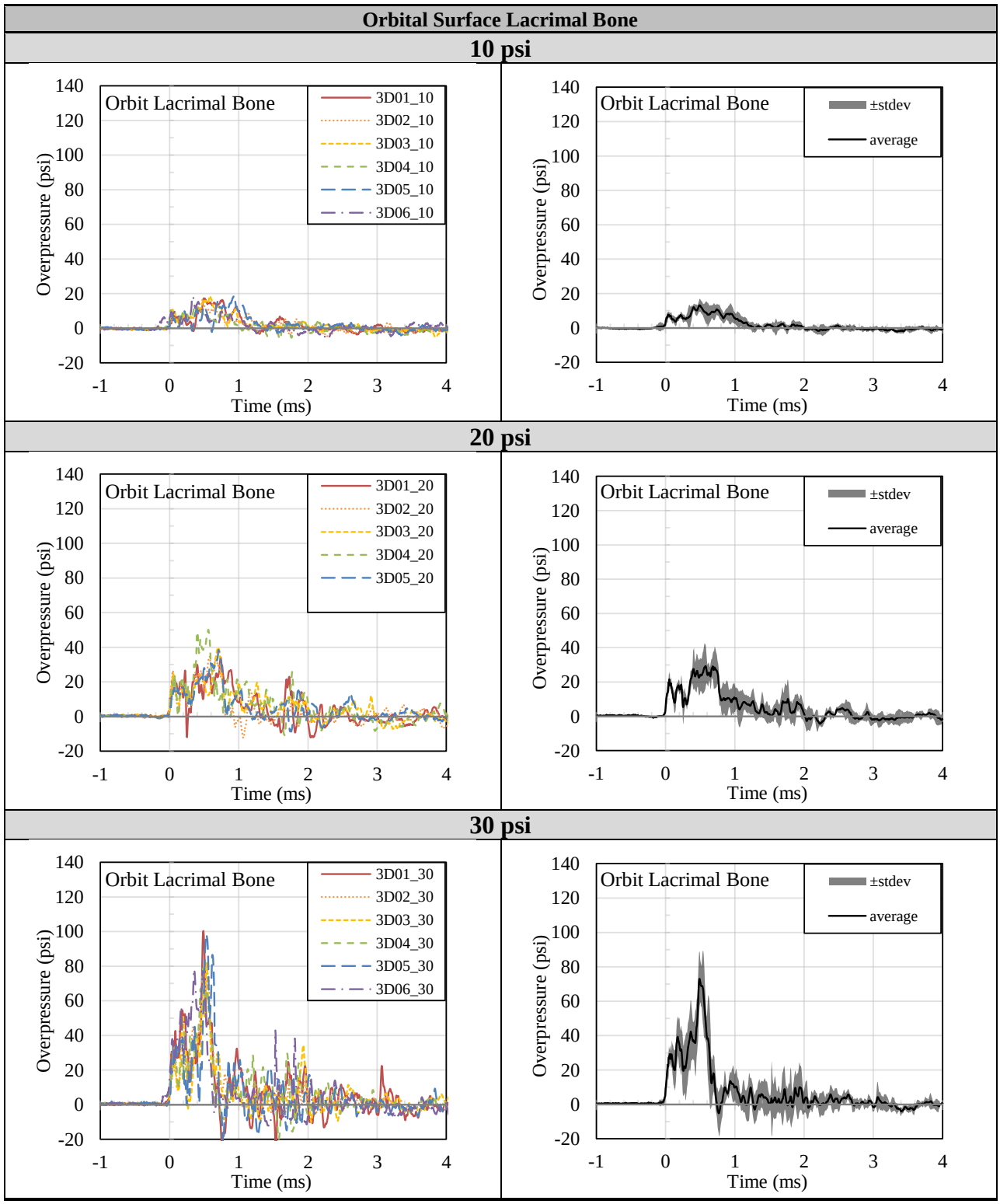

Figure A34. Orbital Surface Lacrimal Bone 3D Orbit – Unprotected Eye.

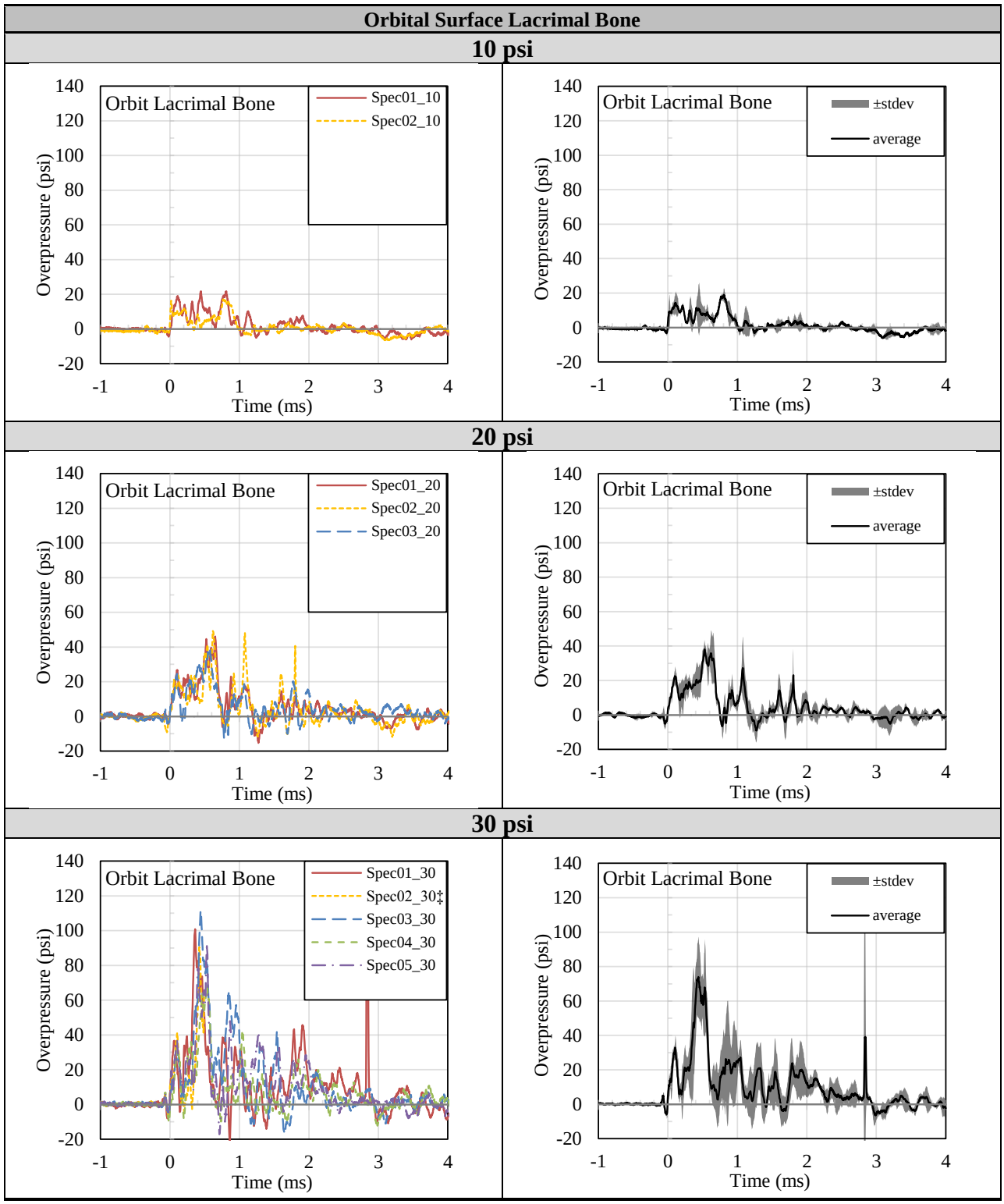

Figure A35. Orbital Surface Lacrimal Bone 3D Orbit – Spectacles.

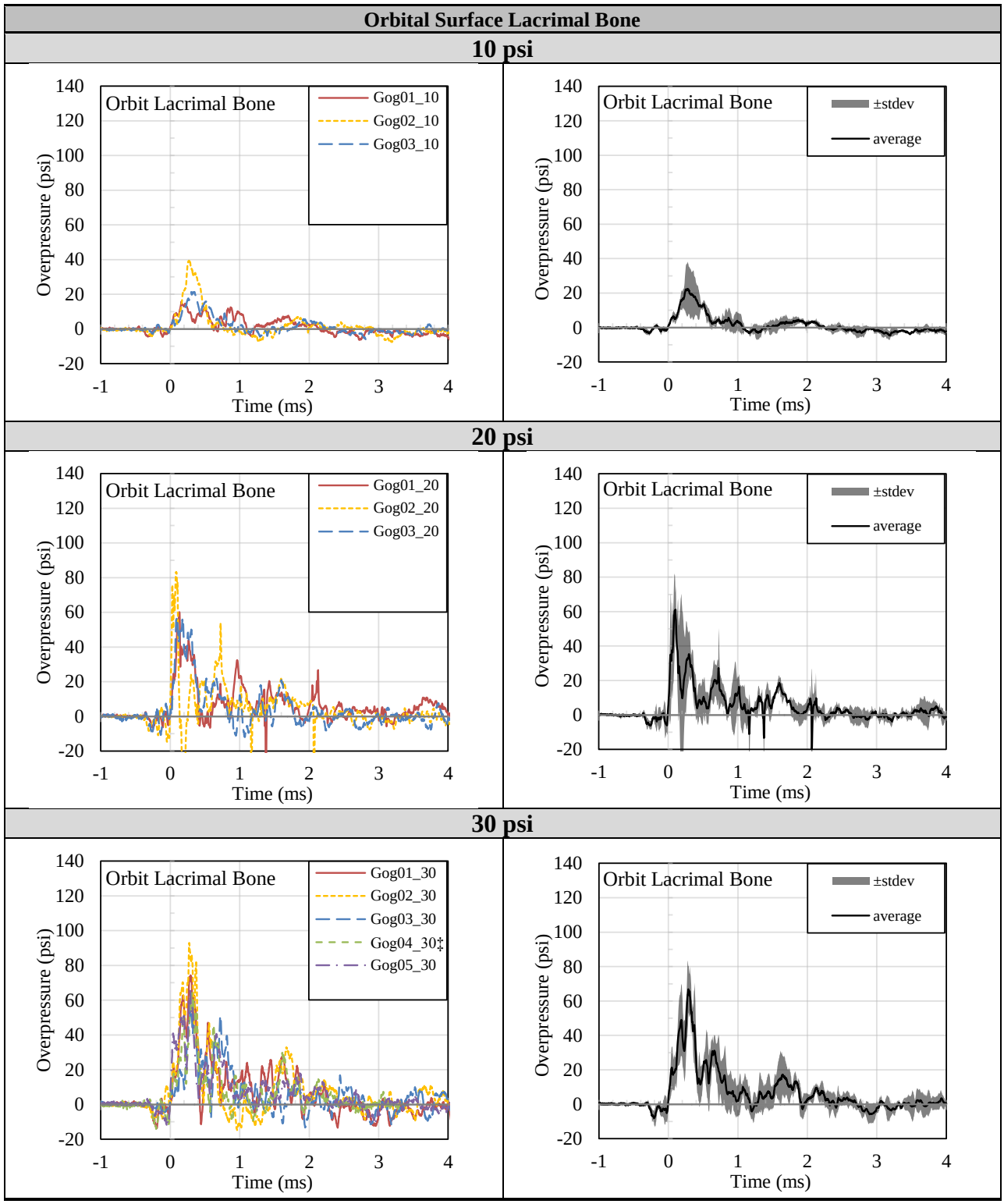

Figure A36. Orbital Surface Lacrimal Bone 3D Orbit - Goggles.

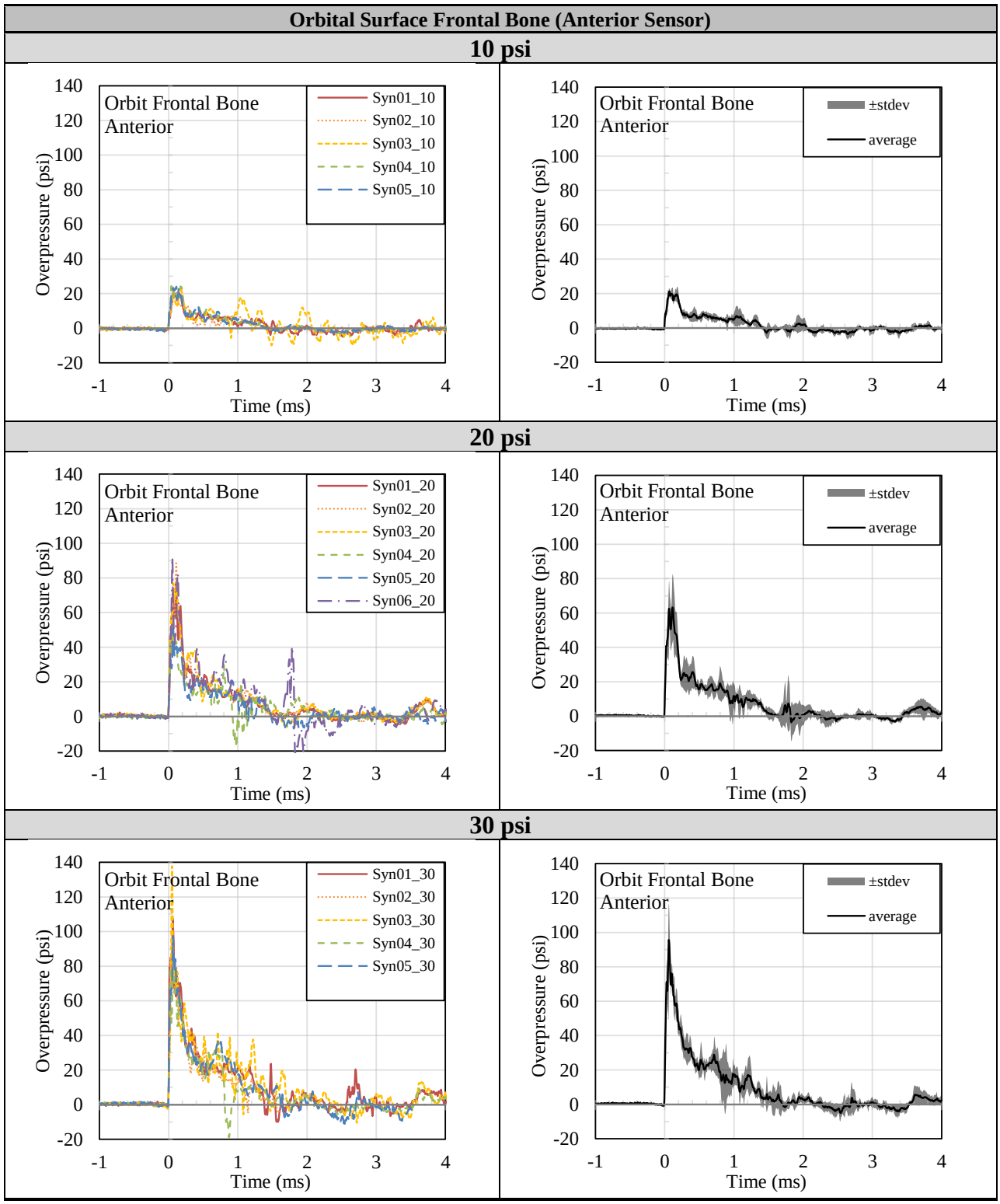

Figure A37. Orbital Surface Frontal Bone (Anterior Sensor) Synthetic Orbit.

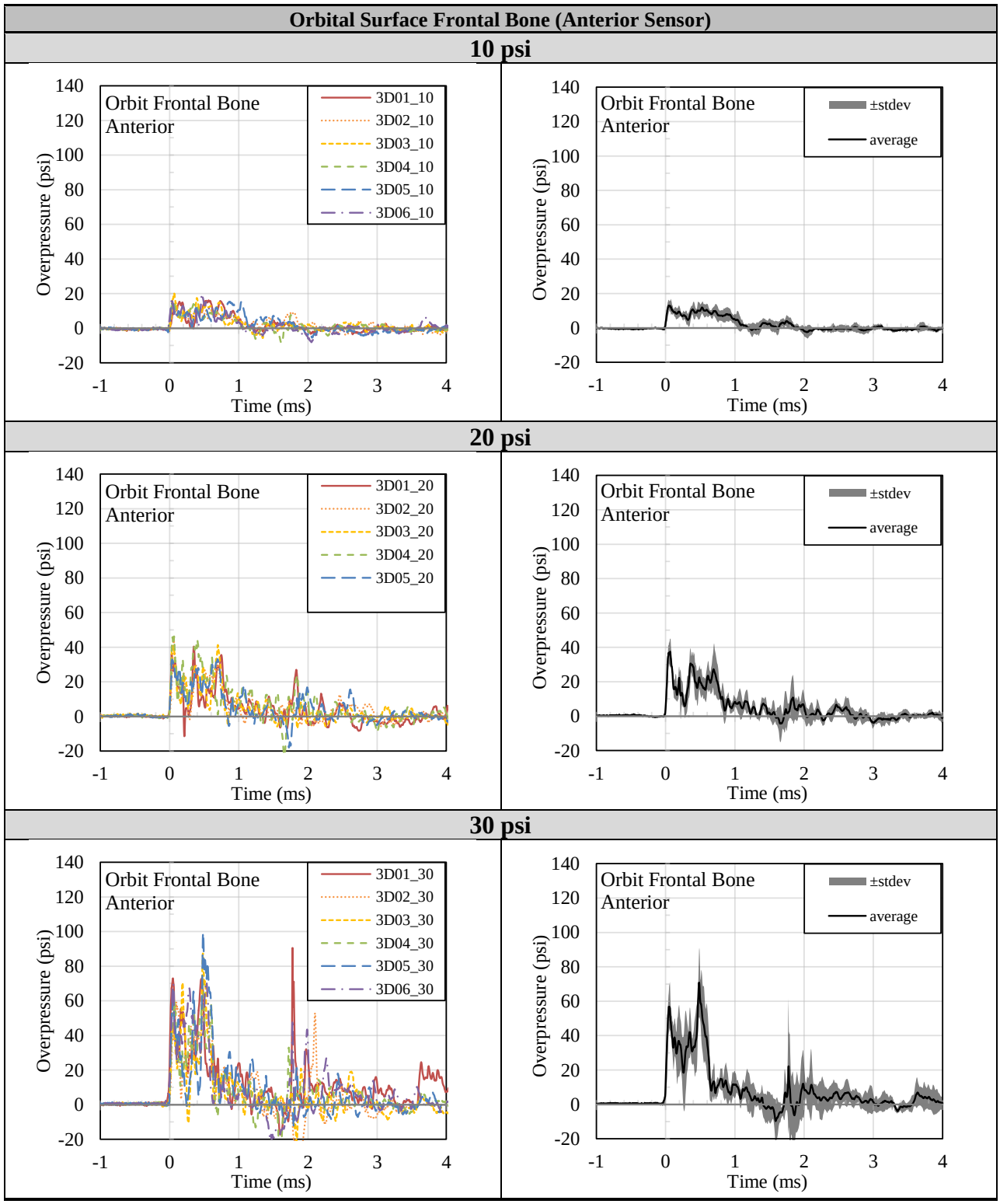

Figure A38. Orbital Surface Frontal Bone (Anterior Sensor) 3D Orbit – Unprotected Eye.

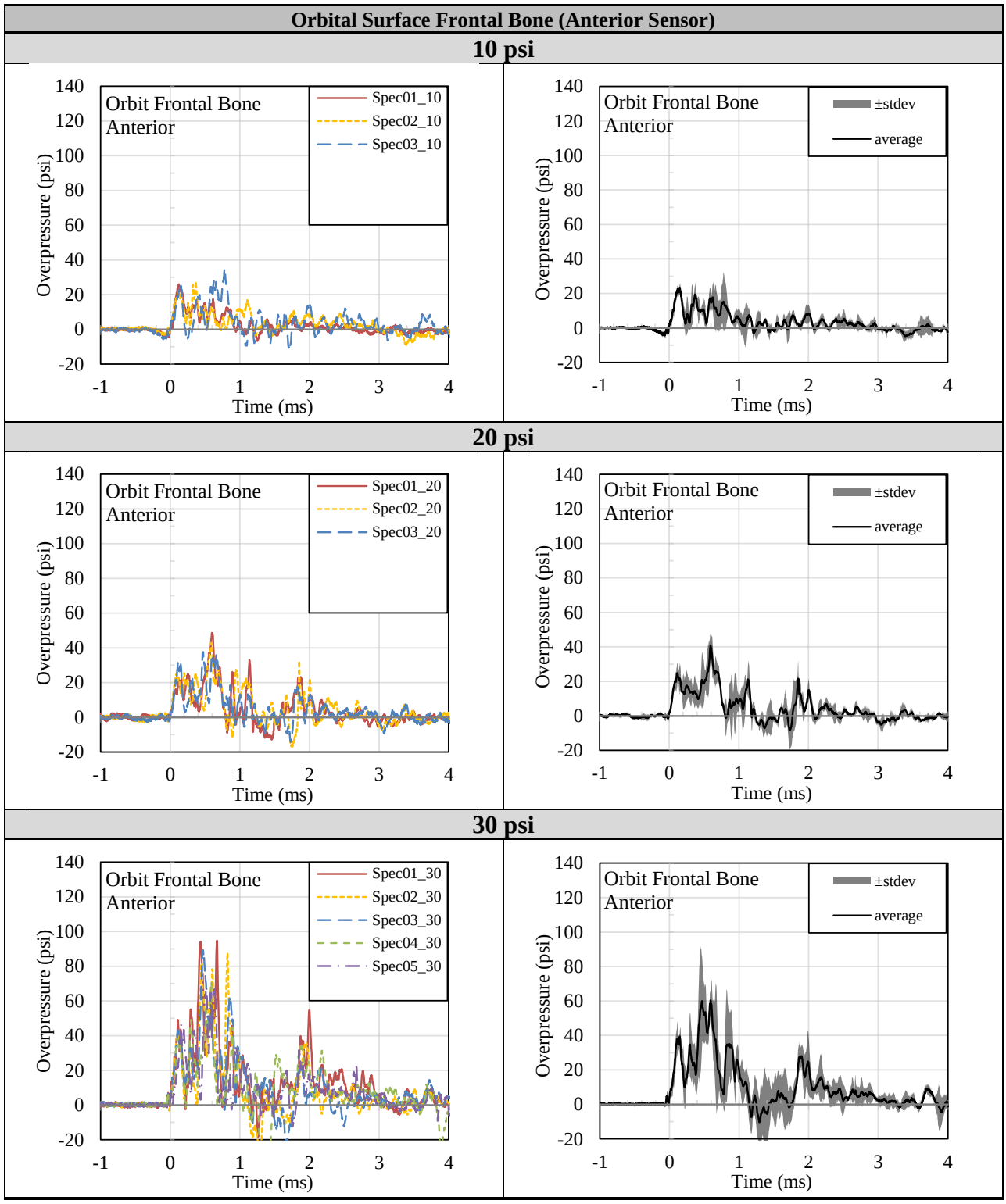

Figure A39. Orbital Surface Frontal Bone (Anterior Sensor) 3D Orbit – Spectacles.

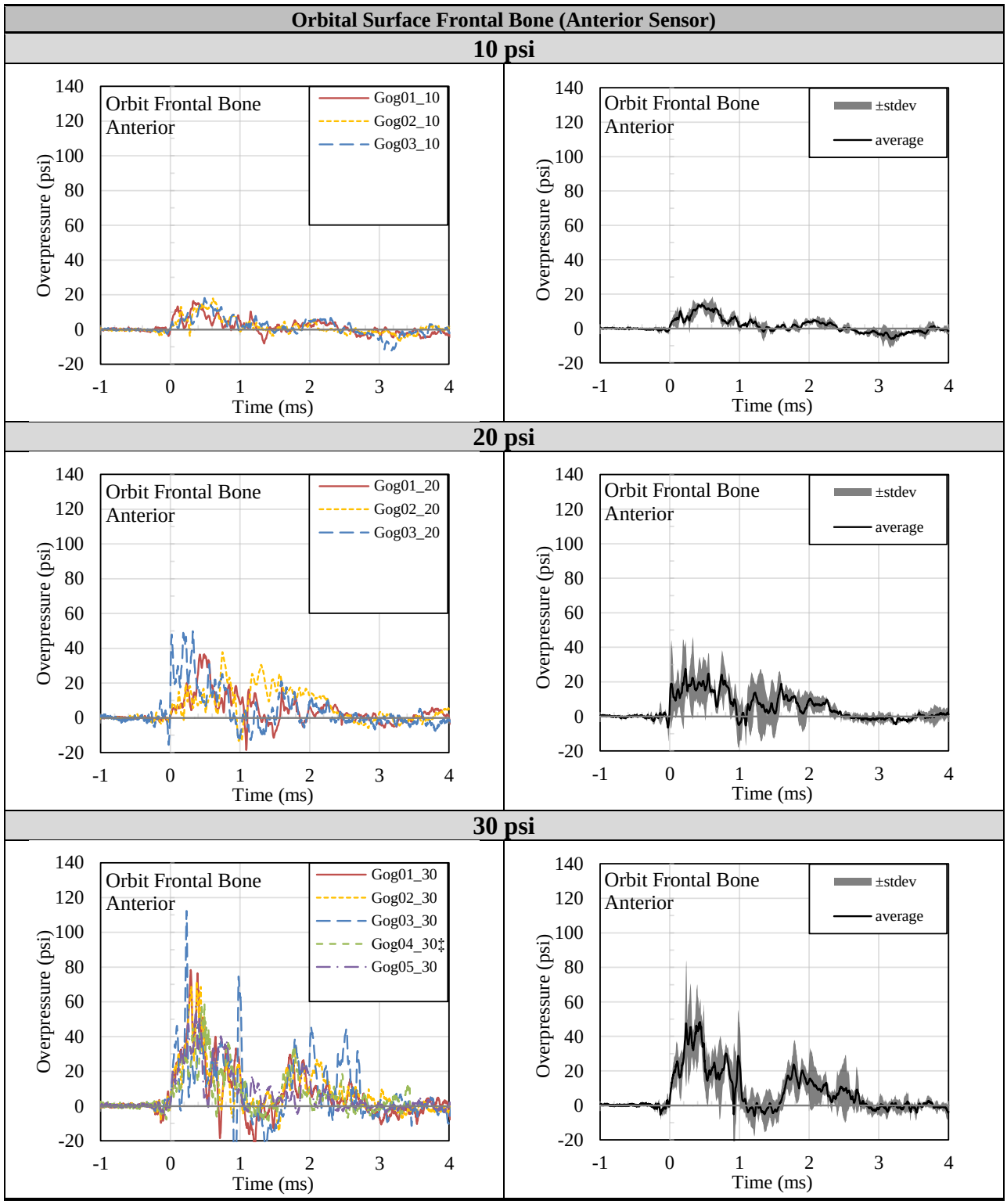

Figure A40. Orbital Surface Frontal Bone (Anterior Sensor) 3D Orbit – Goggles

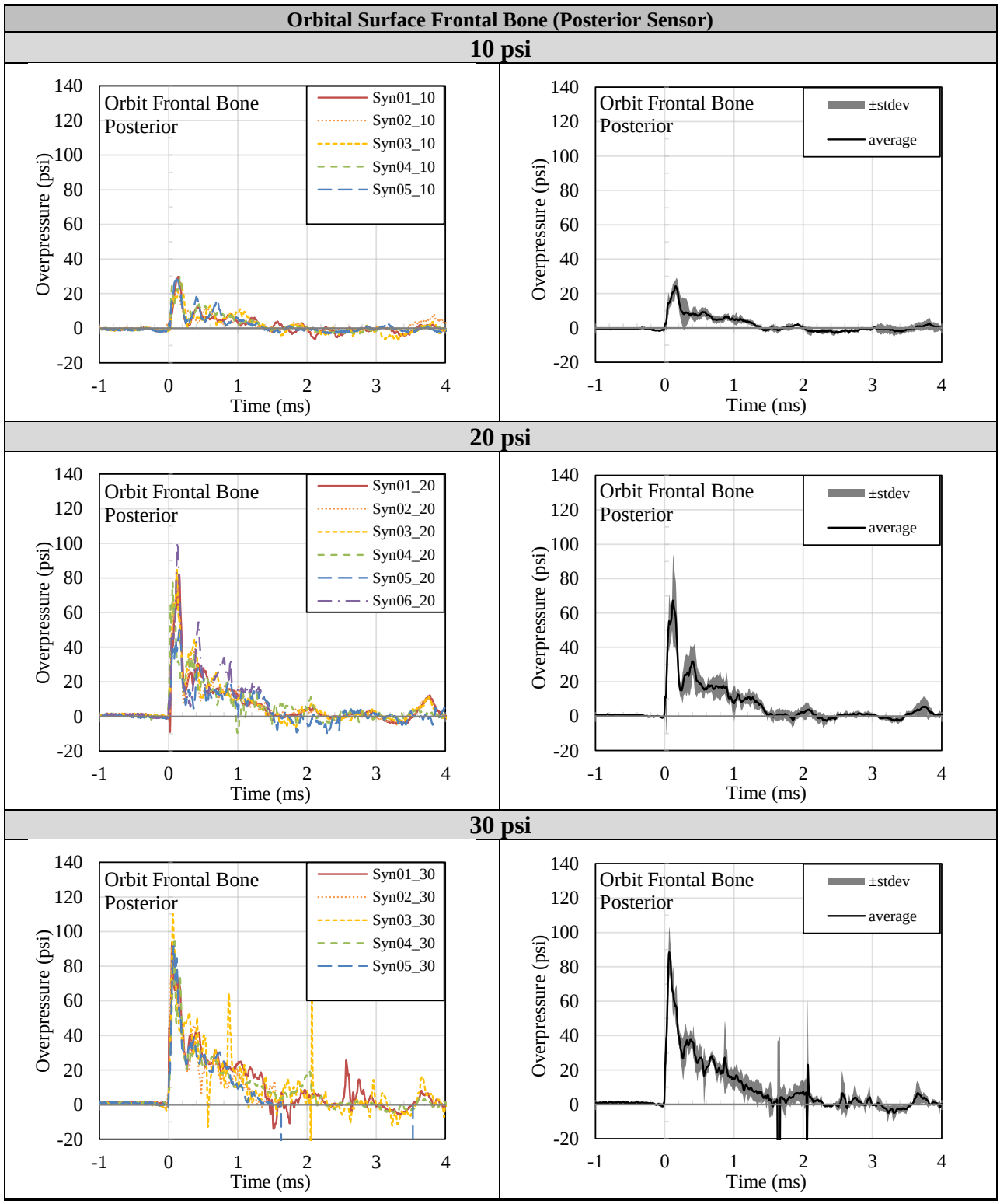

Figure A41. Orbital Surface Frontal Bone (Posterior Sensor) Synthetic Orbit.

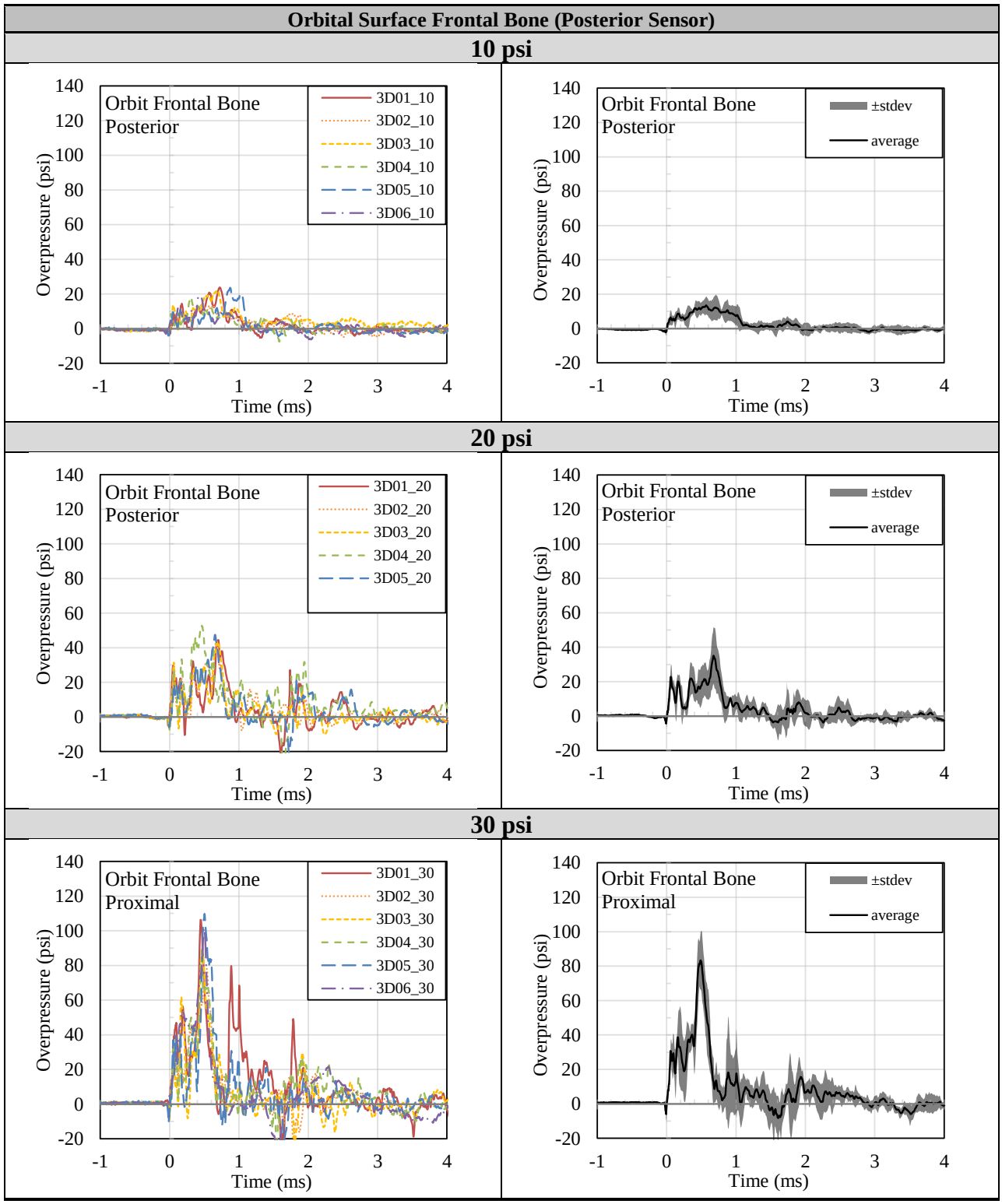

Figure A42. Orbital Surface Frontal Bone (Posterior Sensor) 3D Orbit – Unprotected Eye.

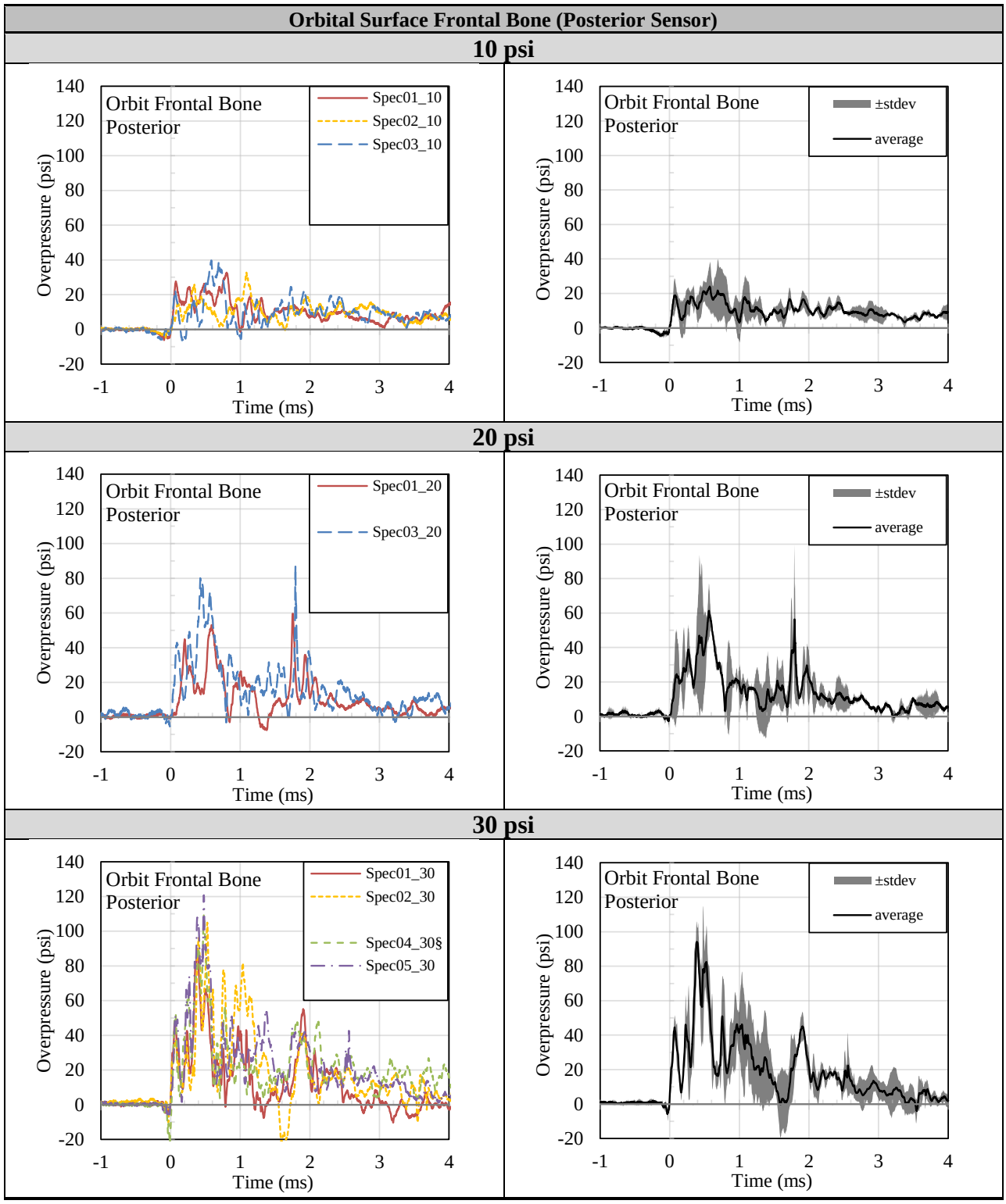

Figure A43. Orbital Surface Frontal Bone (Posterior Sensor) 3D Orbit – Spectacles.
Note: Only two tests for 20 psi test level because one test maxed out sensor.

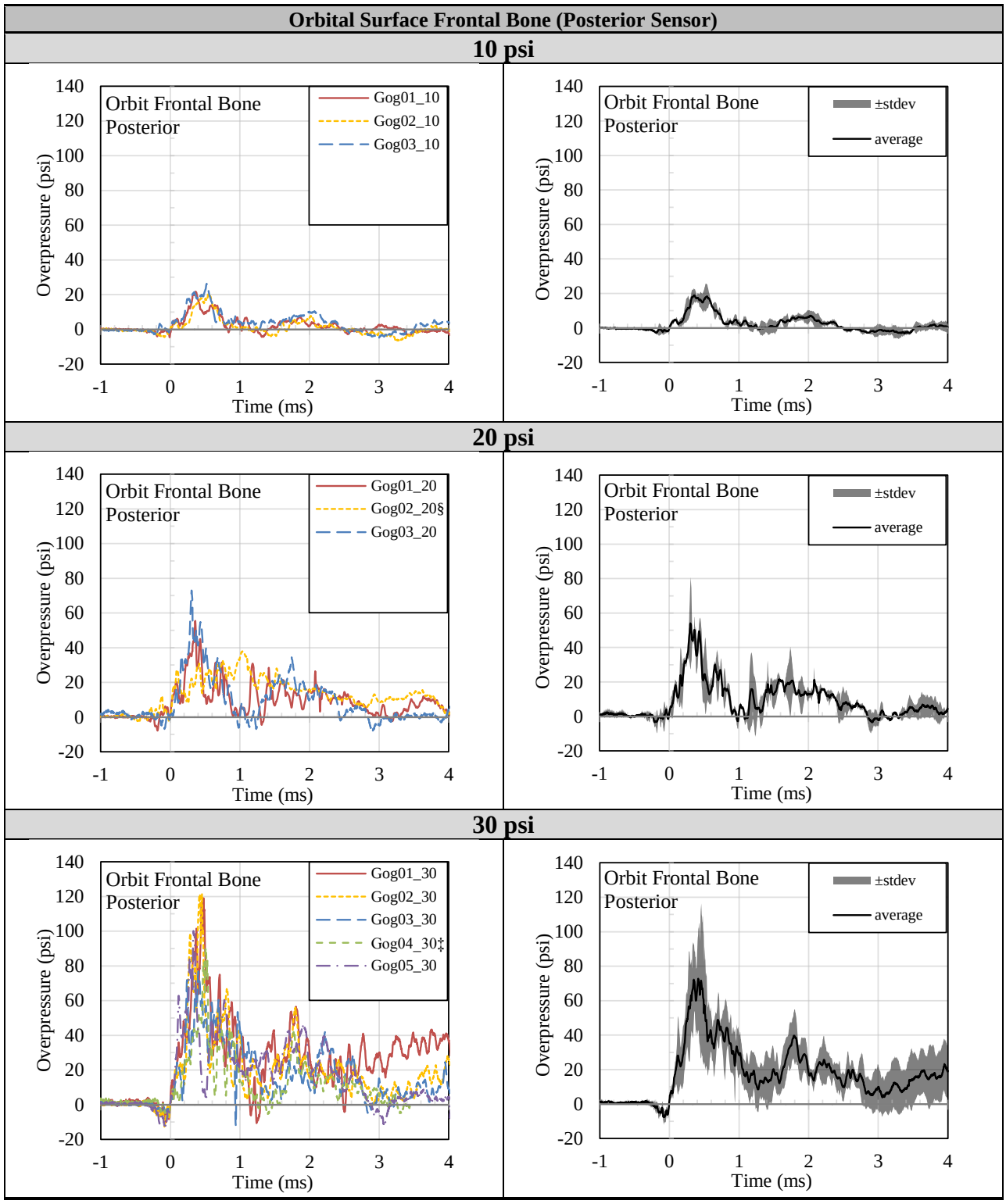

Figure A44. Orbital Surface Frontal Bone (Posterior Sensor) 3D Orbit – Goggles.

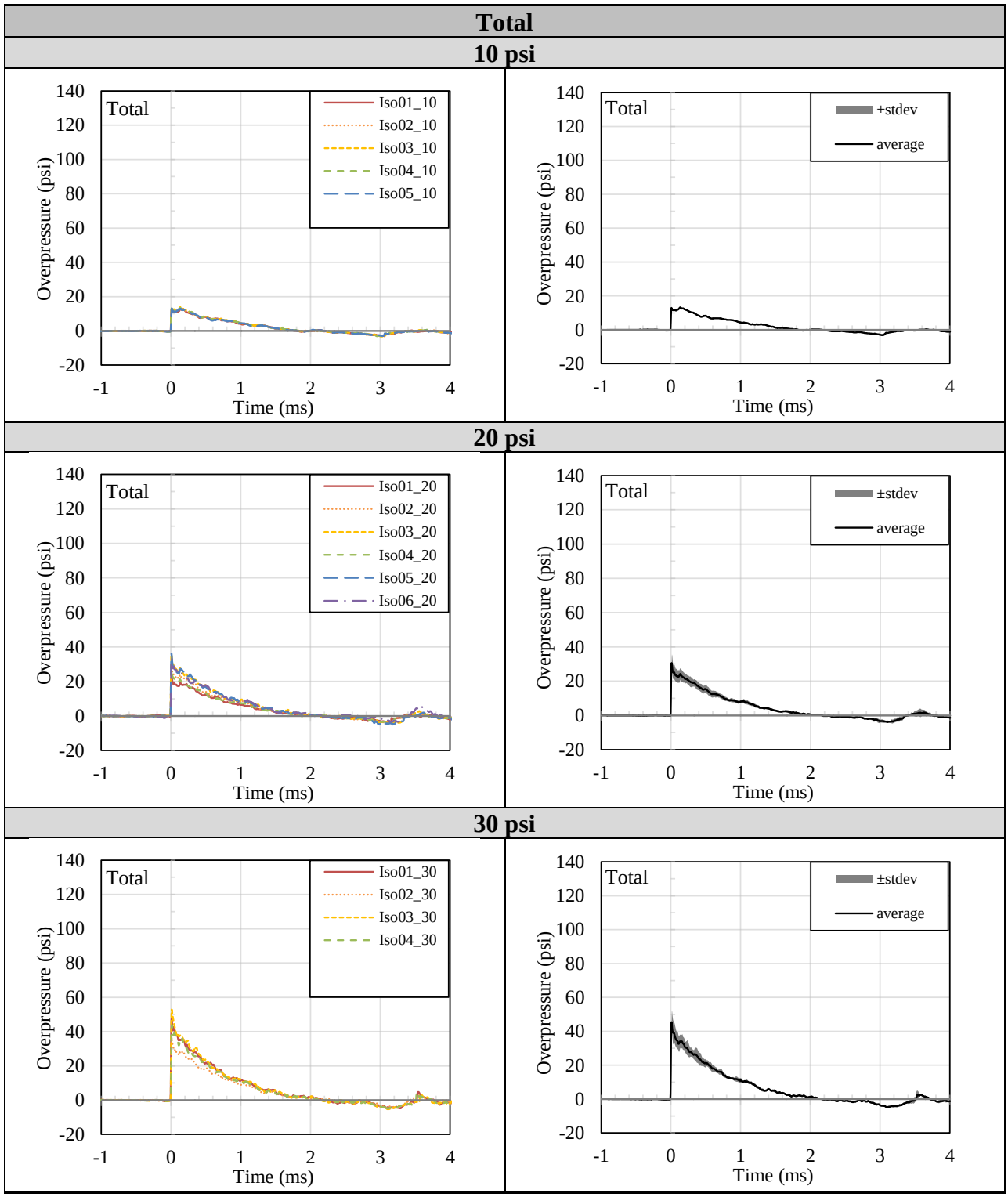

Figure A45. Total Isolated Eye.

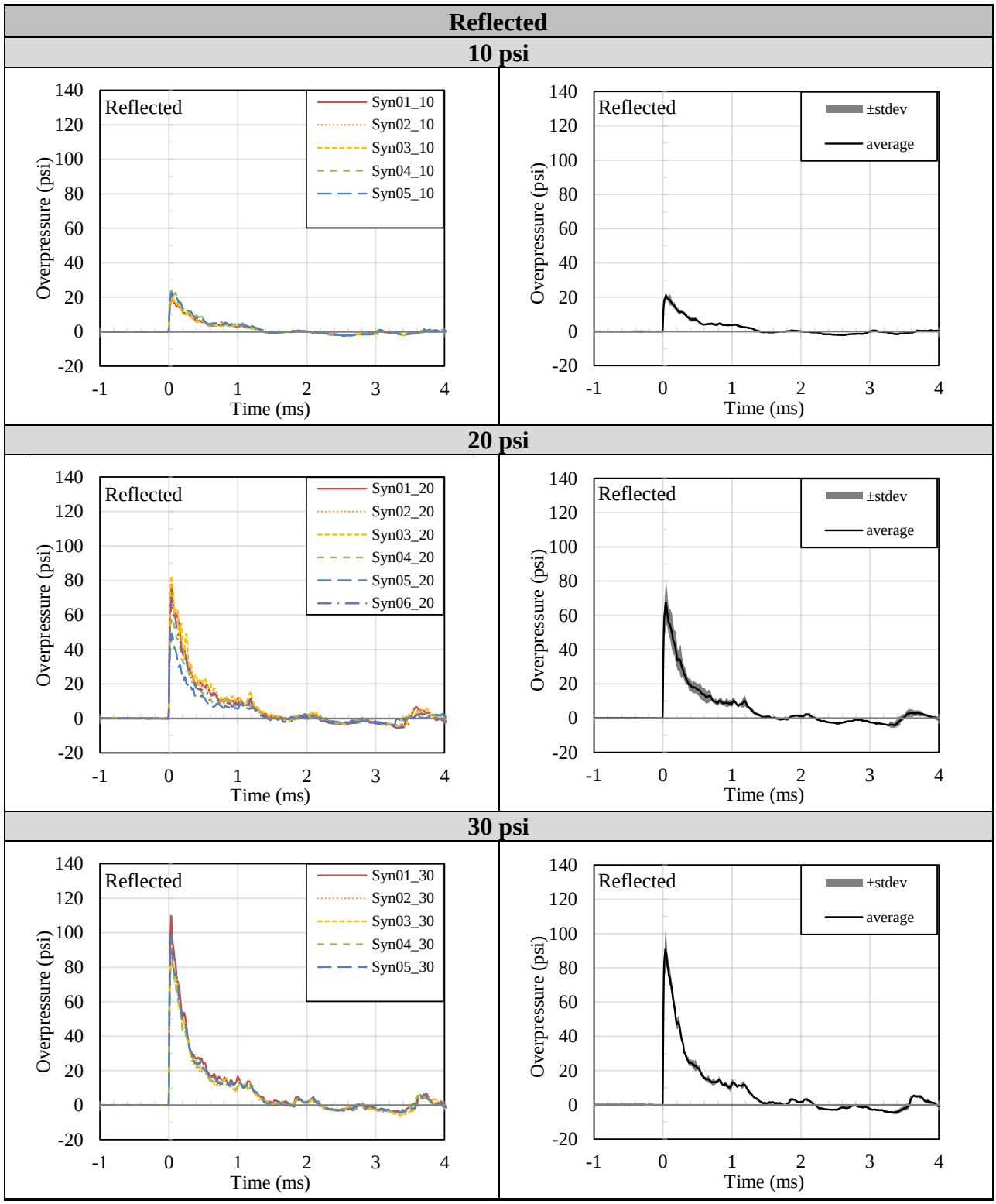

Figure A46. Reflected Synthetic Orbit.

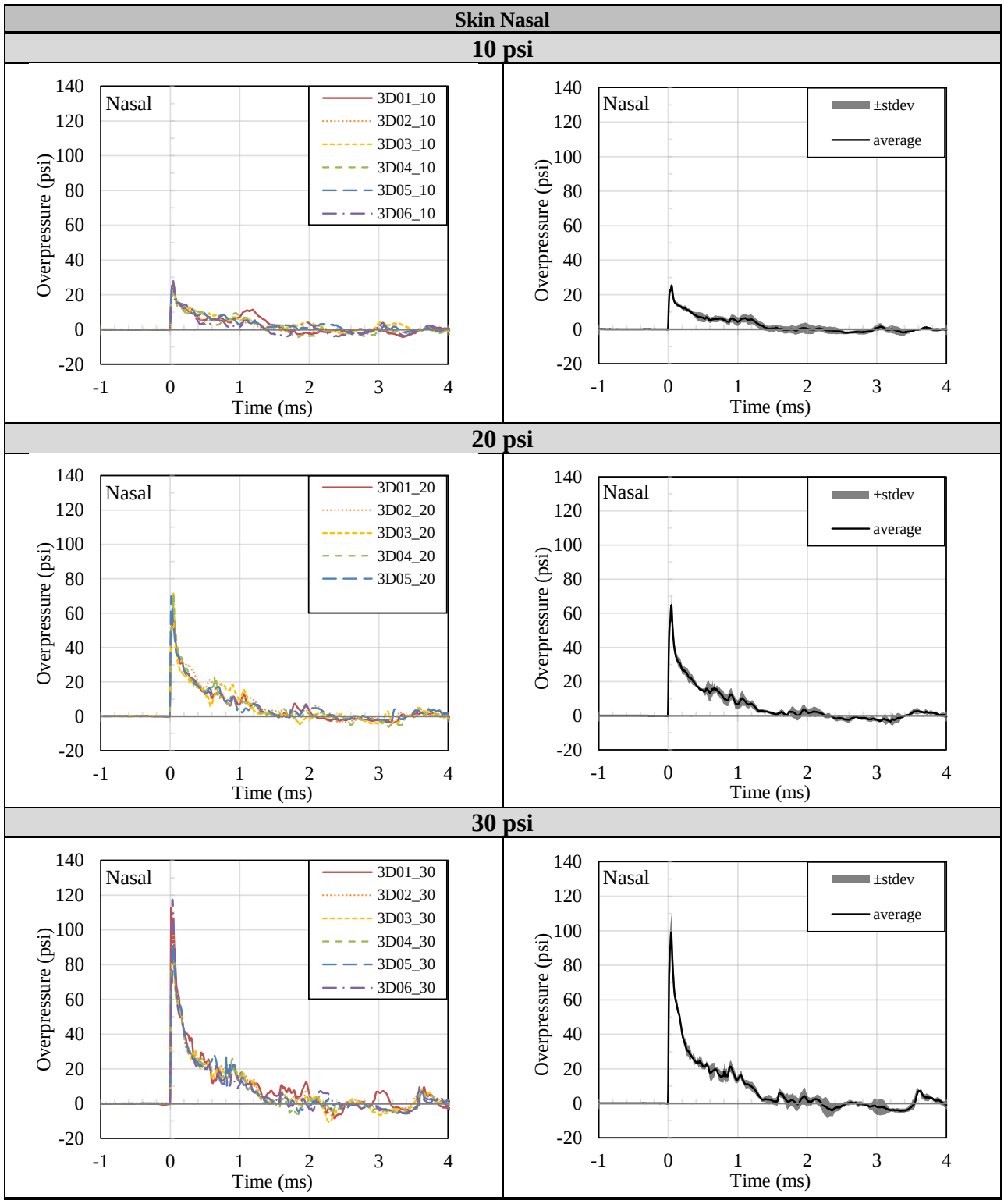

Figure A47. Skin Nasal 3D Orbit – Unprotected Eye.

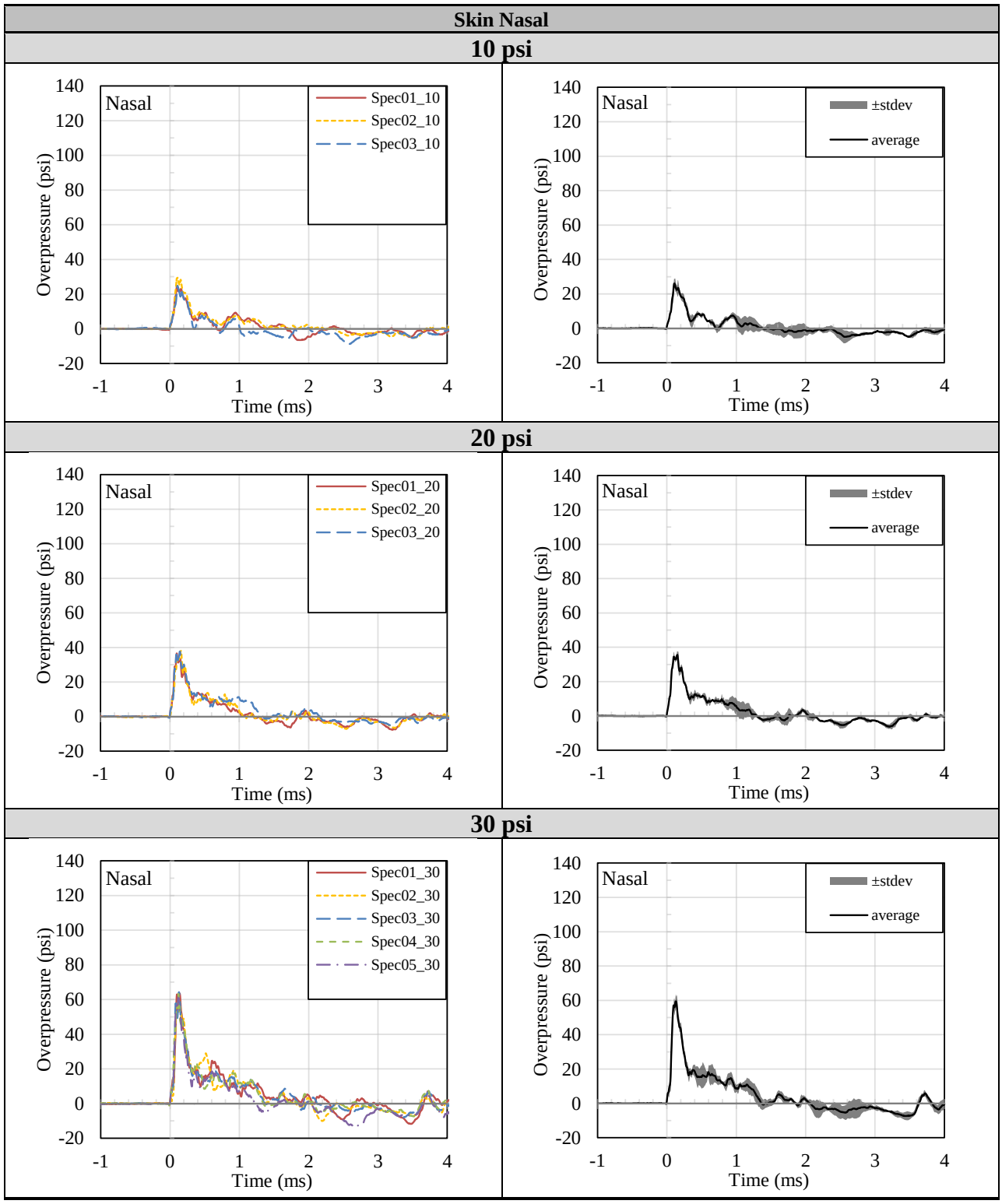

Figure A48. Skin Nasal 3D Orbit – Spectacles.

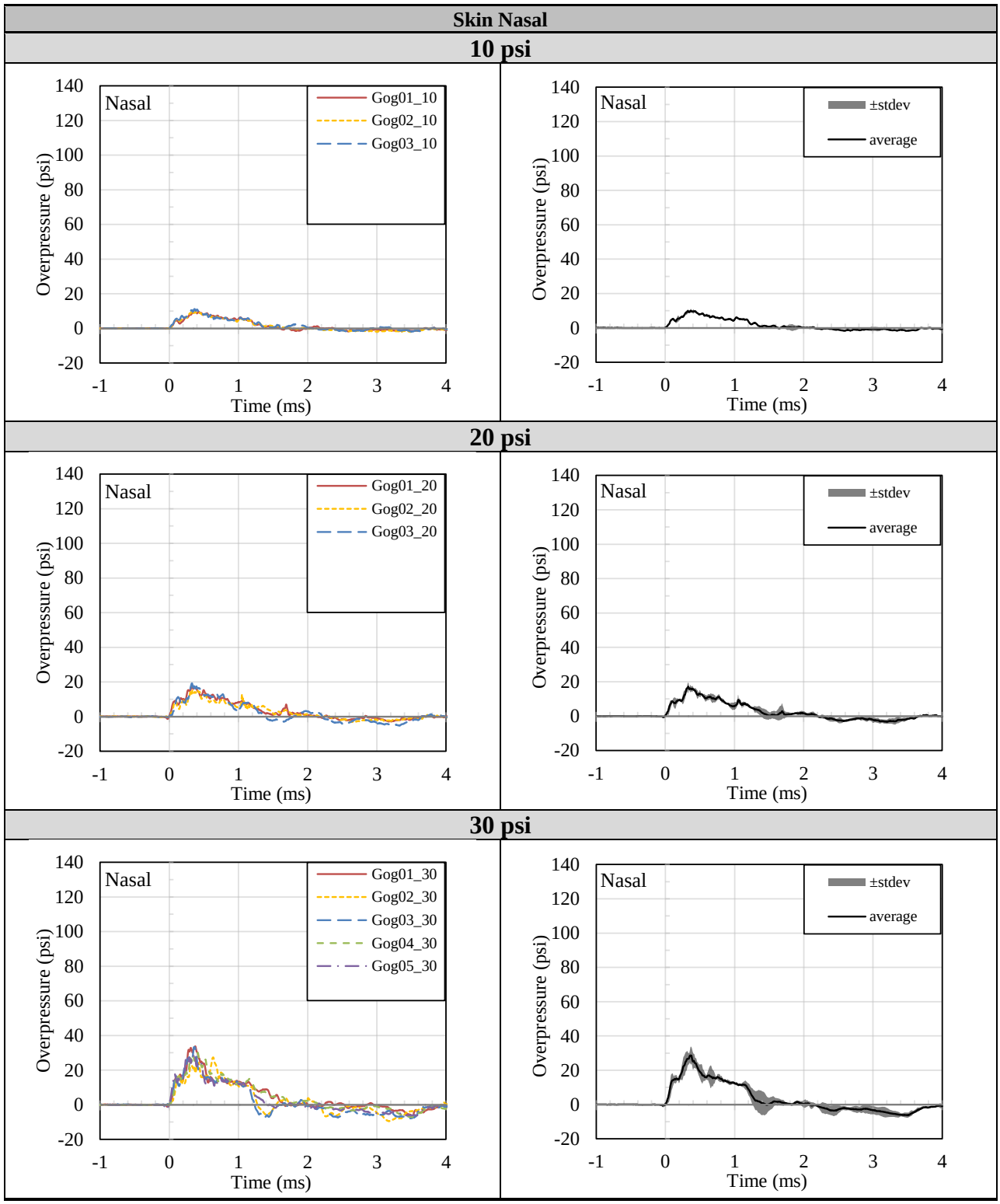

Figure A49. Skin Nasal 3D Orbit – Goggles.

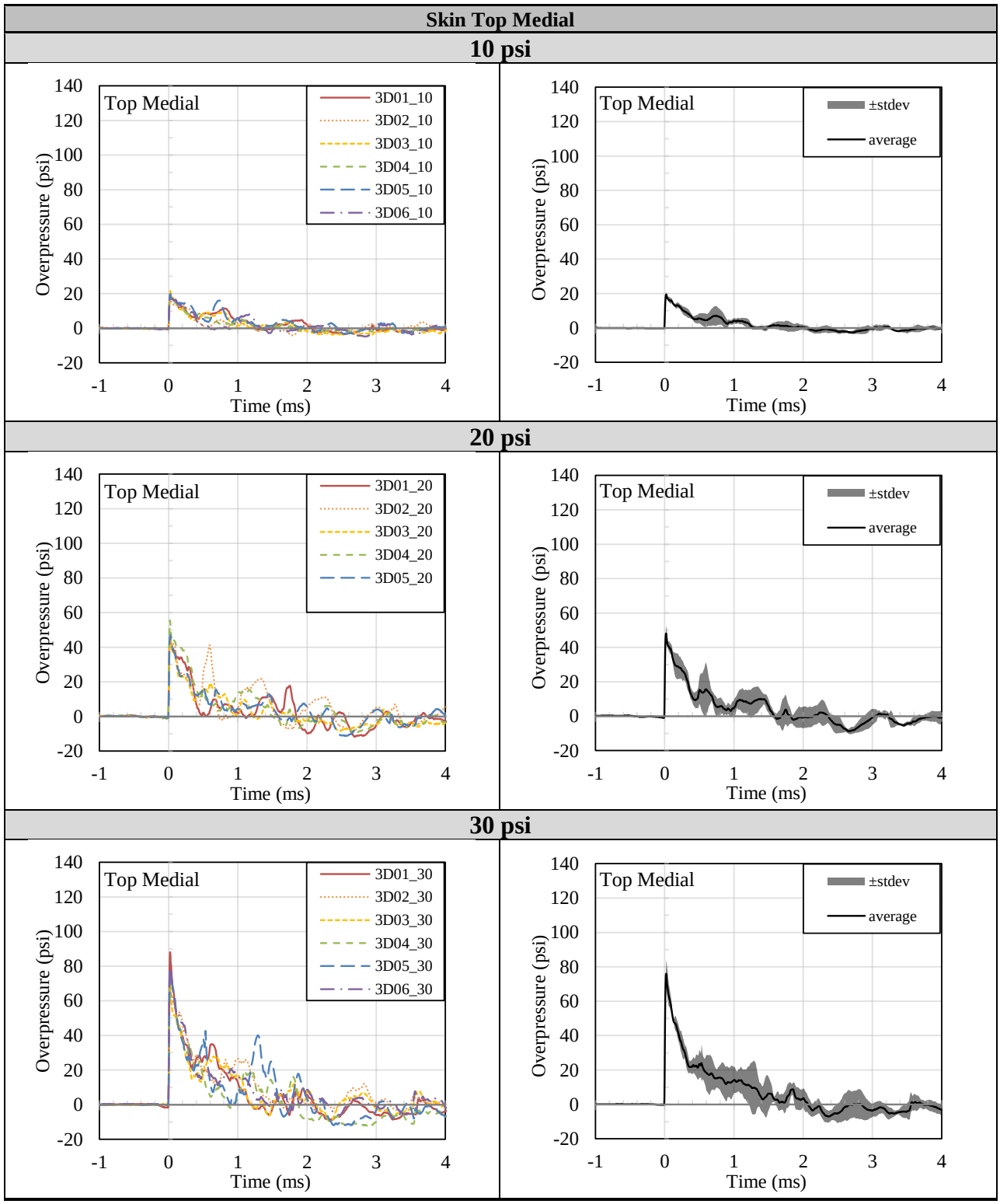

Figure A50. Skin Top Medial 3D Orbit – Unprotected Eye.

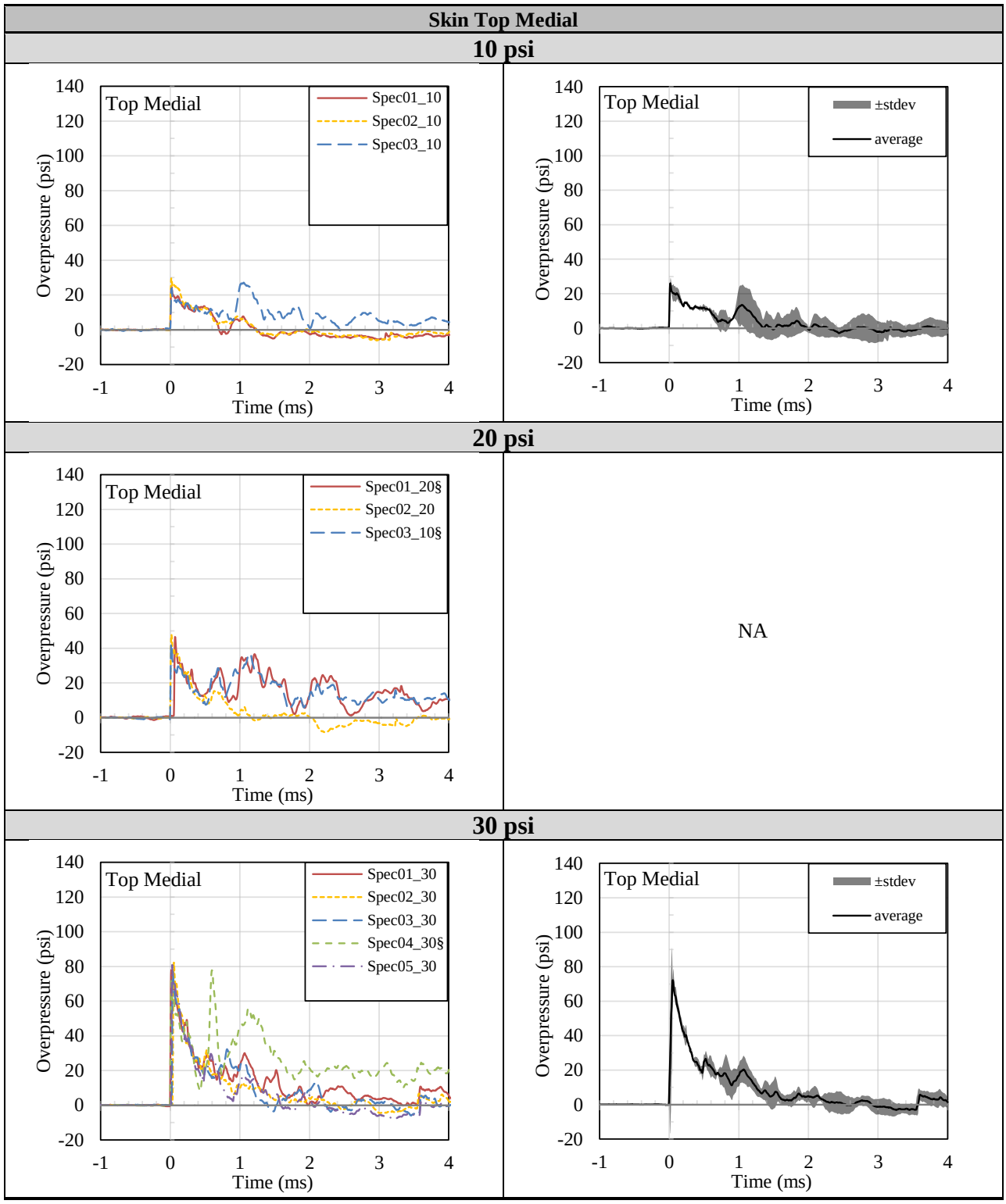

Figure A51. Skin Top Medial 3D Orbit – Spectacles.

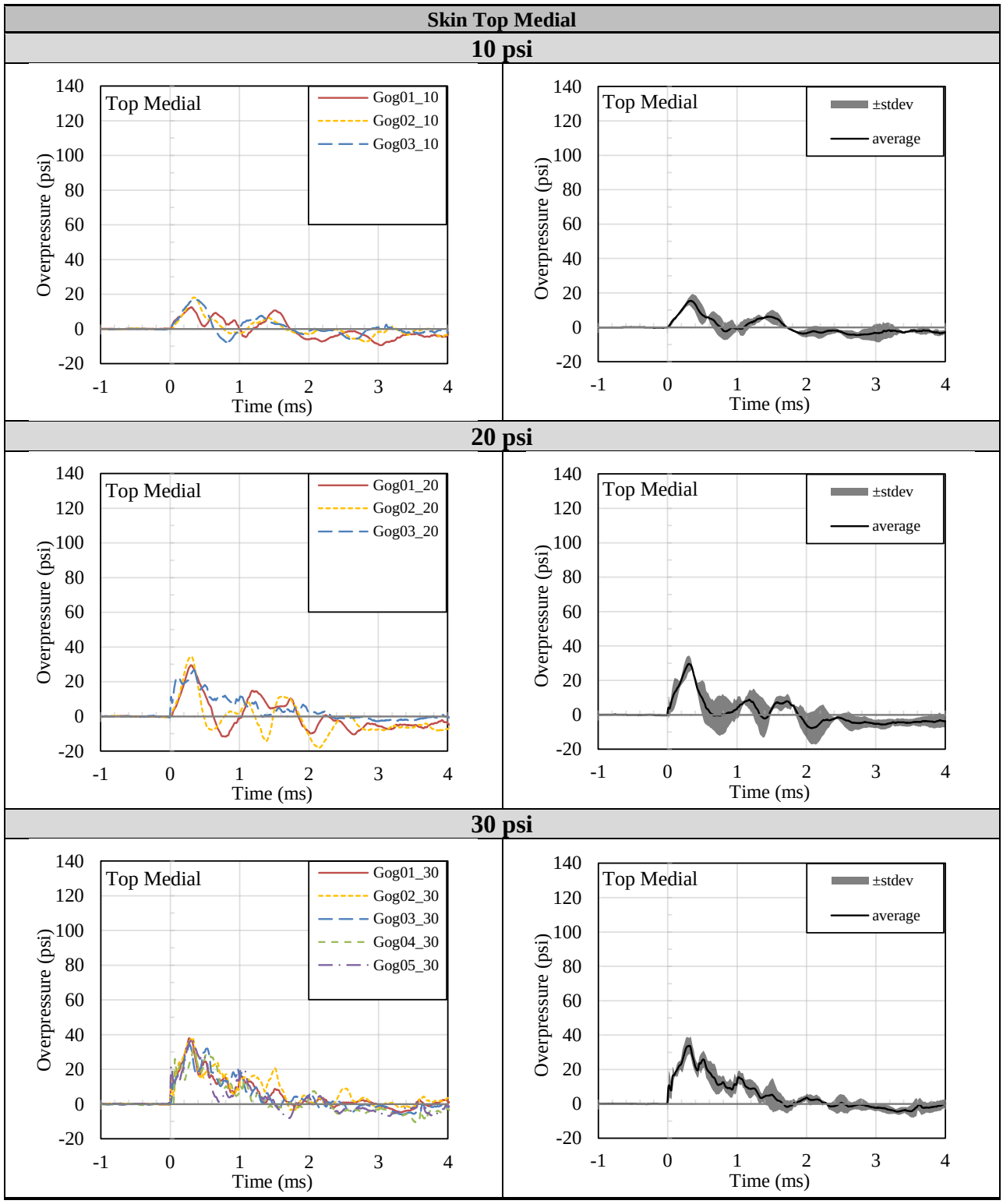

Figure A52. Skin Top Medial 3D Orbit – Goggles.
Note: Sensor covered by Goggles.

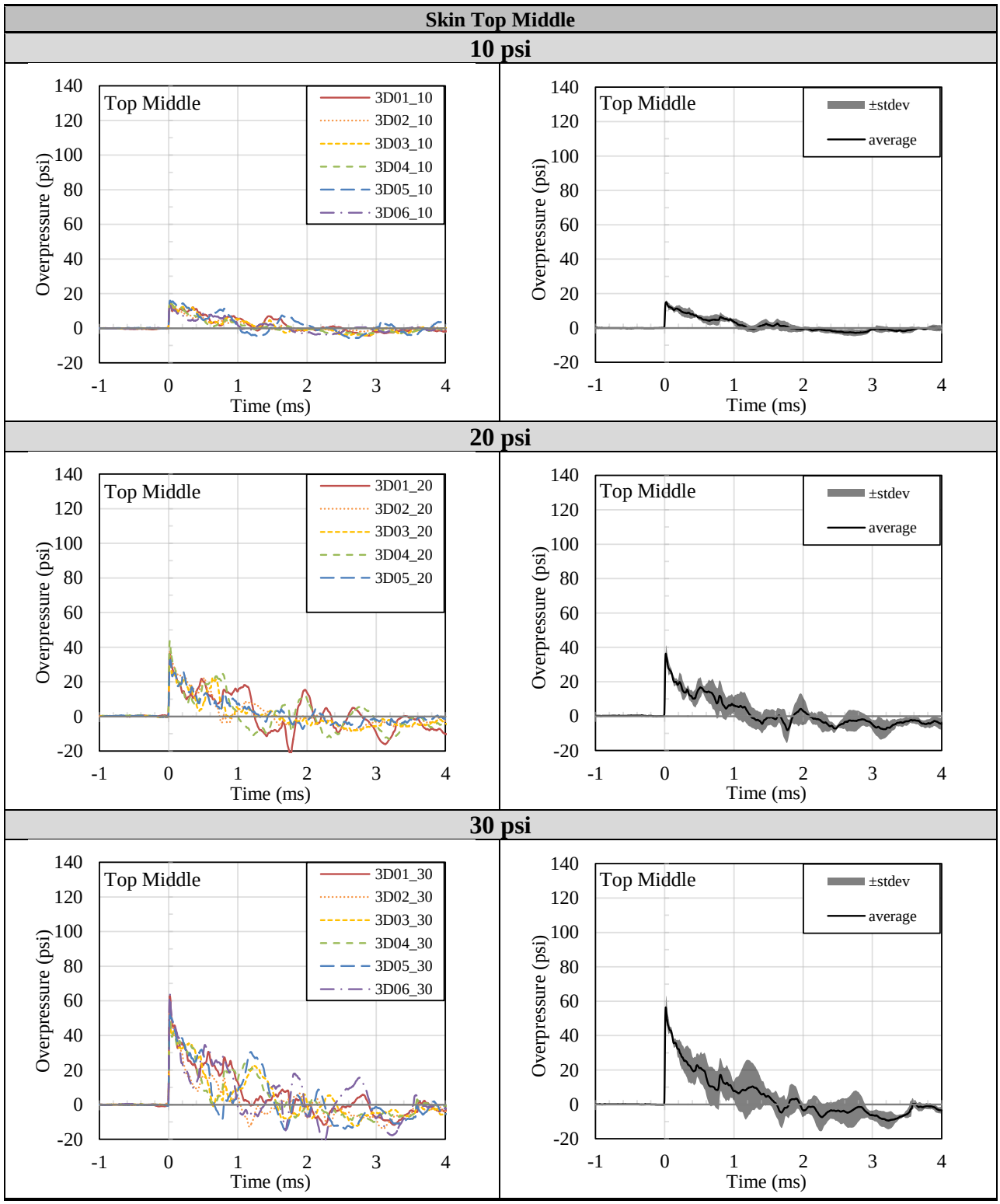

Figure A53. Skin Top Middle 3D Orbit – Unprotected Eye.

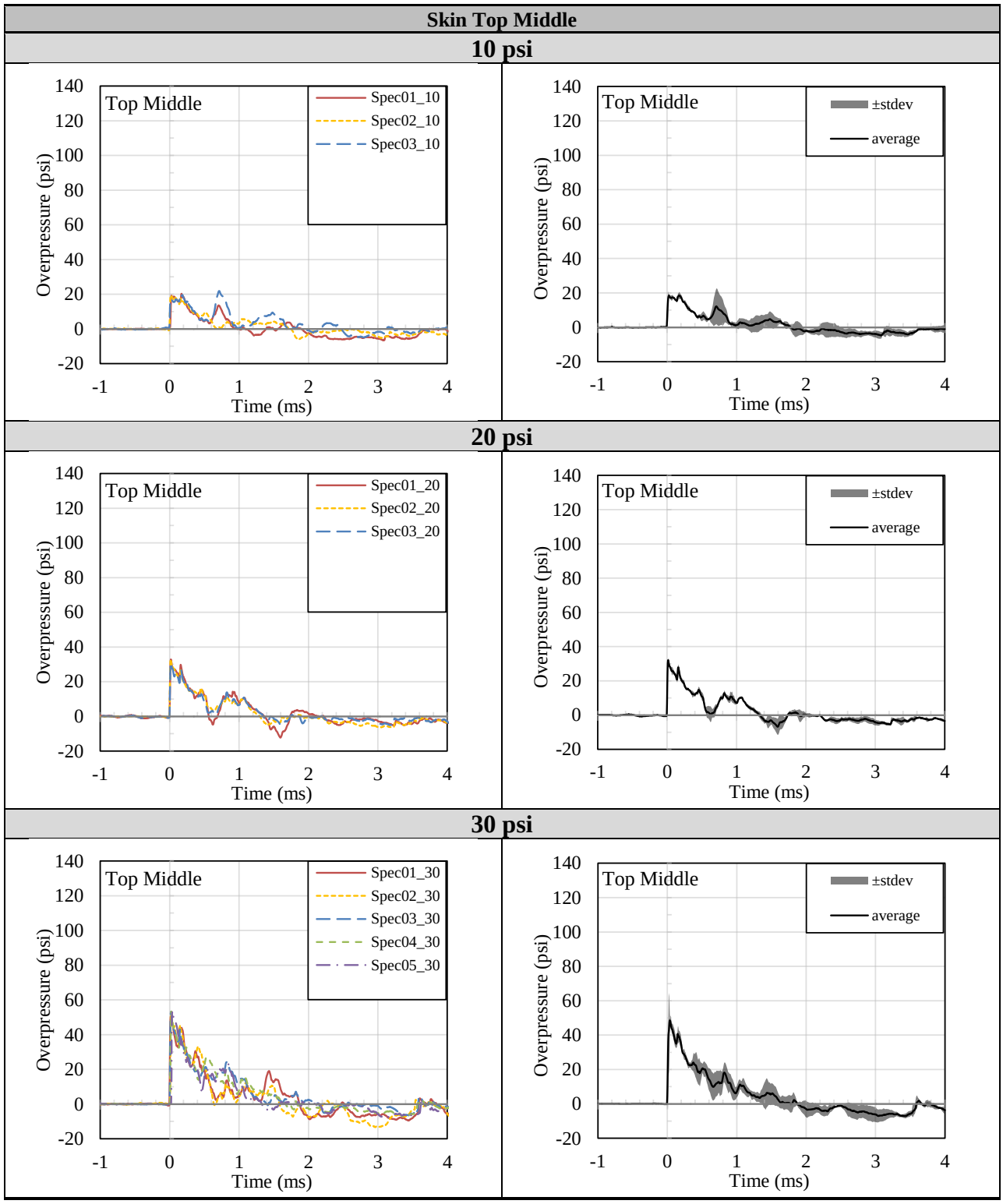

Figure A54. Skin Top Middle 3D Orbit – Spectacles.

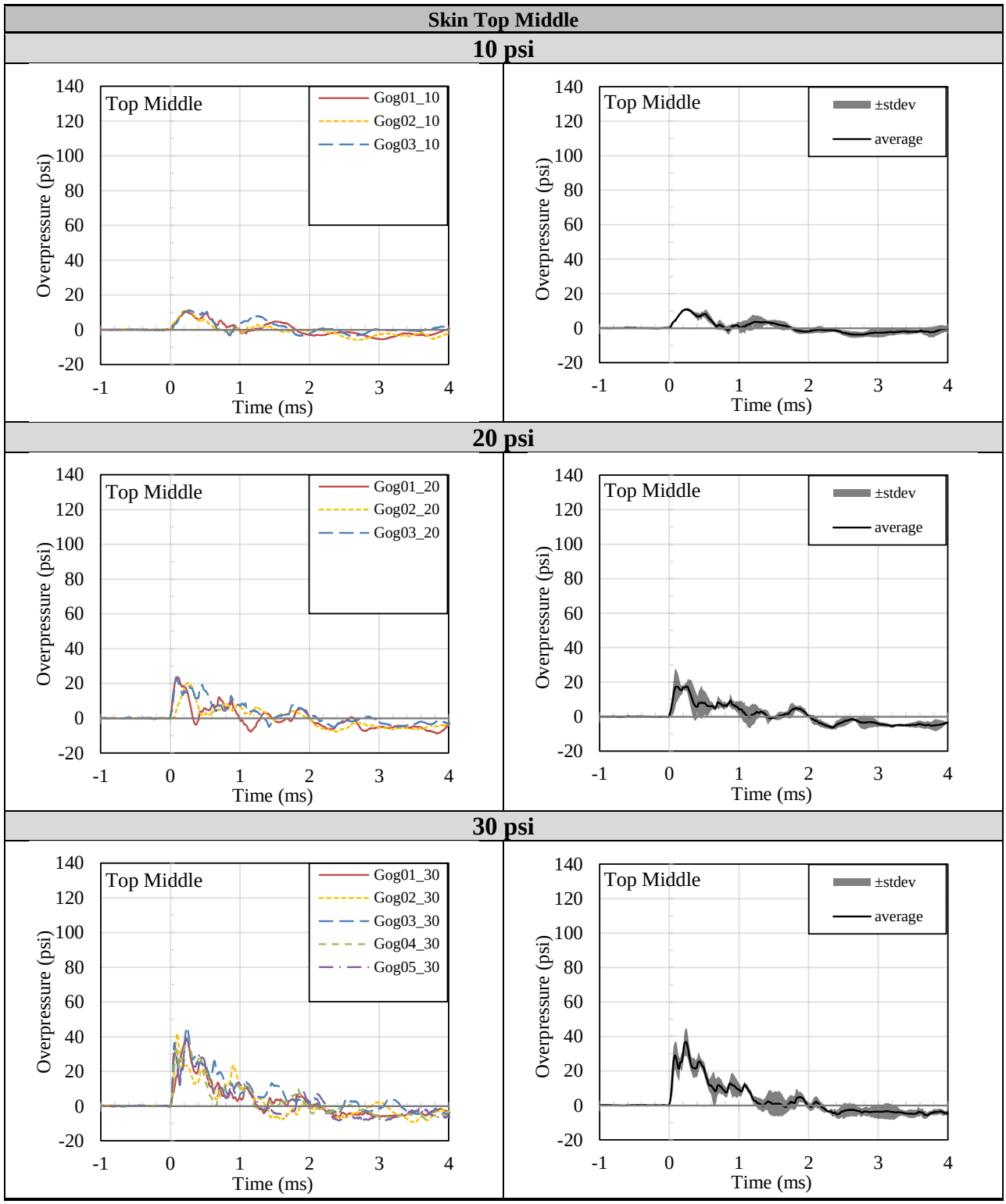

Figure A55. Skin Top Middle 3D Orbit – Goggles.
Note: Sensor covered by Goggles.

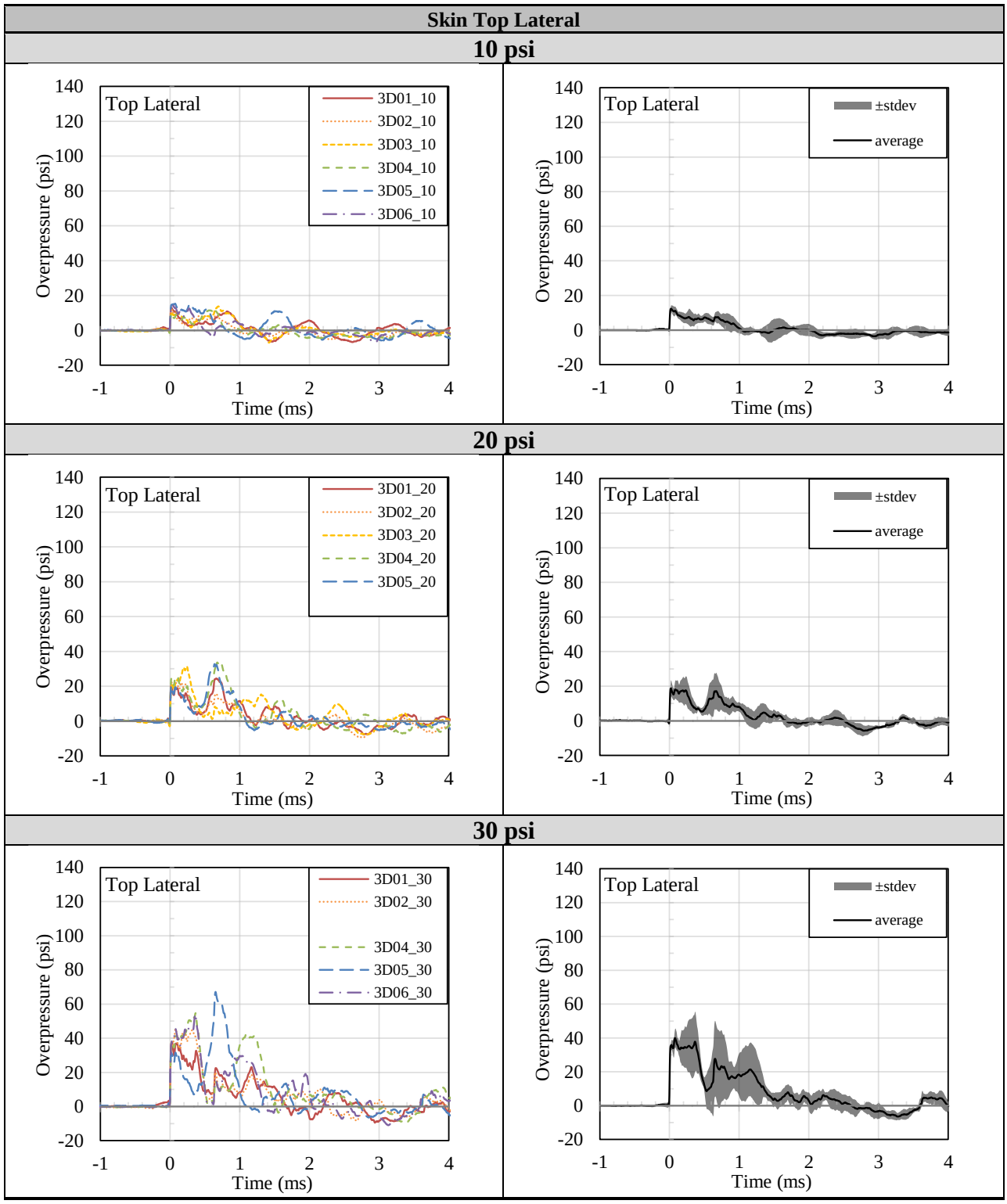

Figure A56. Skin Top Lateral 3D Orbit – Unprotected Eye.
Note: Only five tests for 30 psi test level because sensor did not work properly during test.

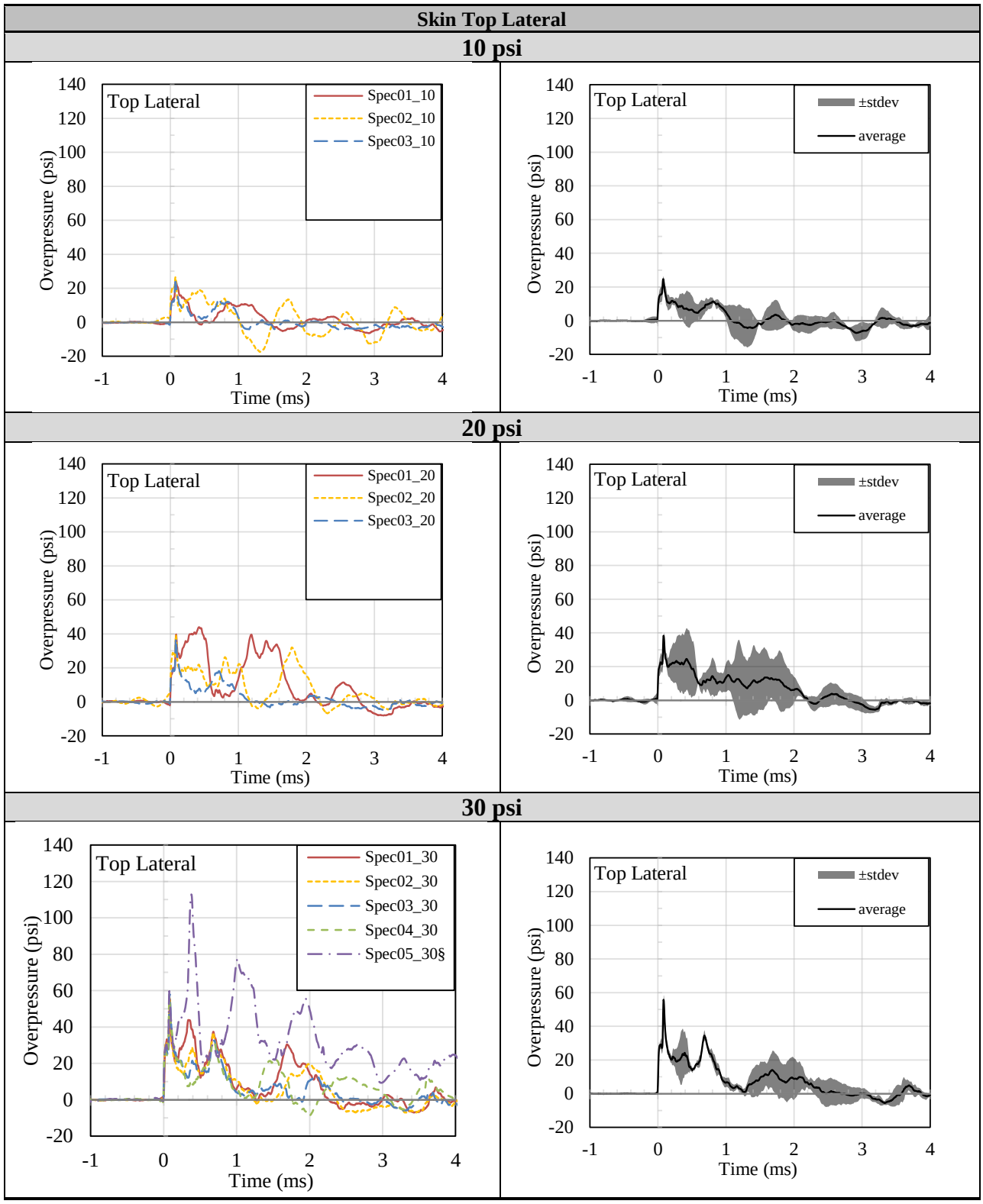

Figure A57. Skin Top Lateral 3D Orbit – Spectacles.

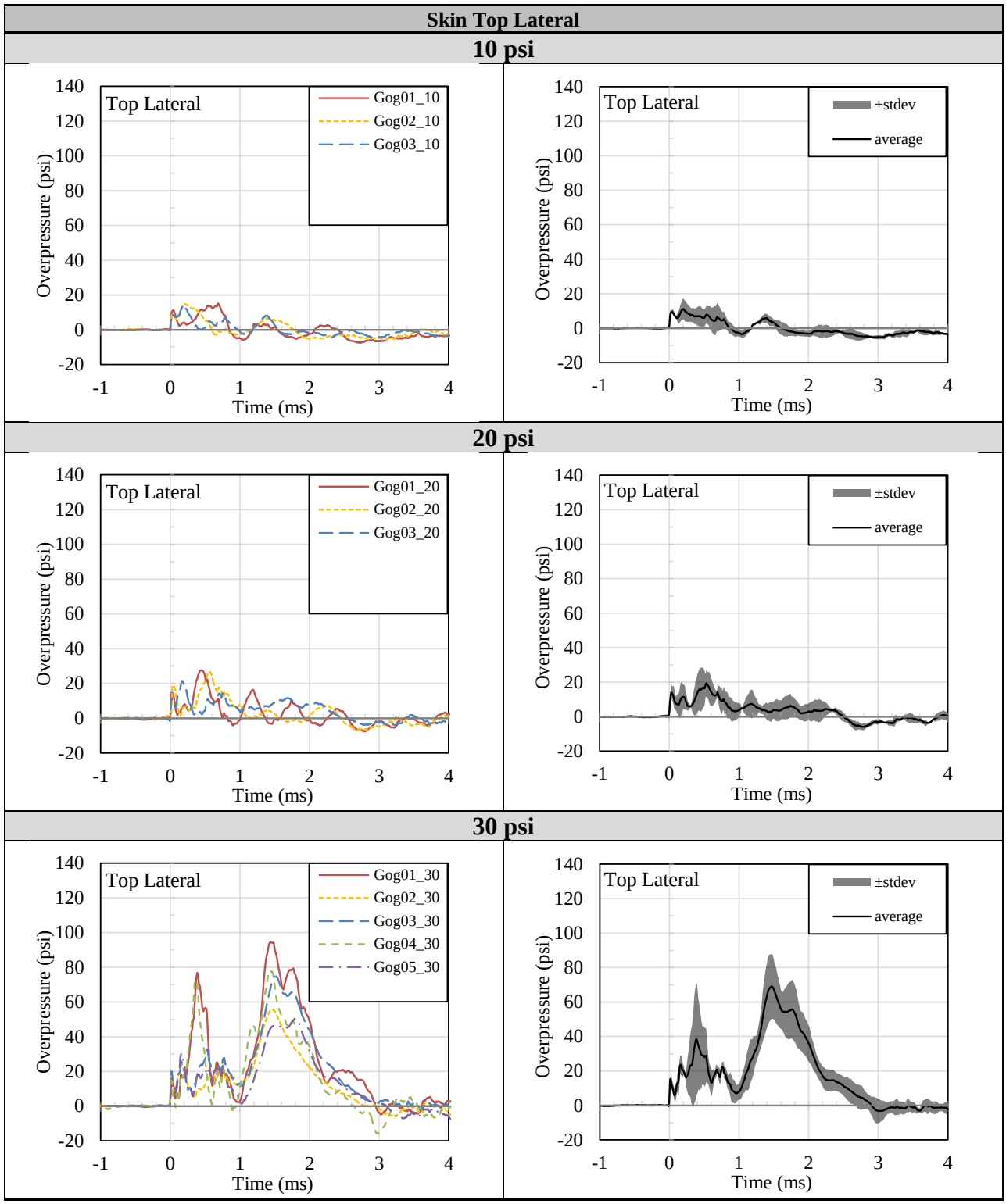

Figure A58. Skin Top Lateral 3D Orbit – Goggles.
Note: Sensor covered by Goggles.

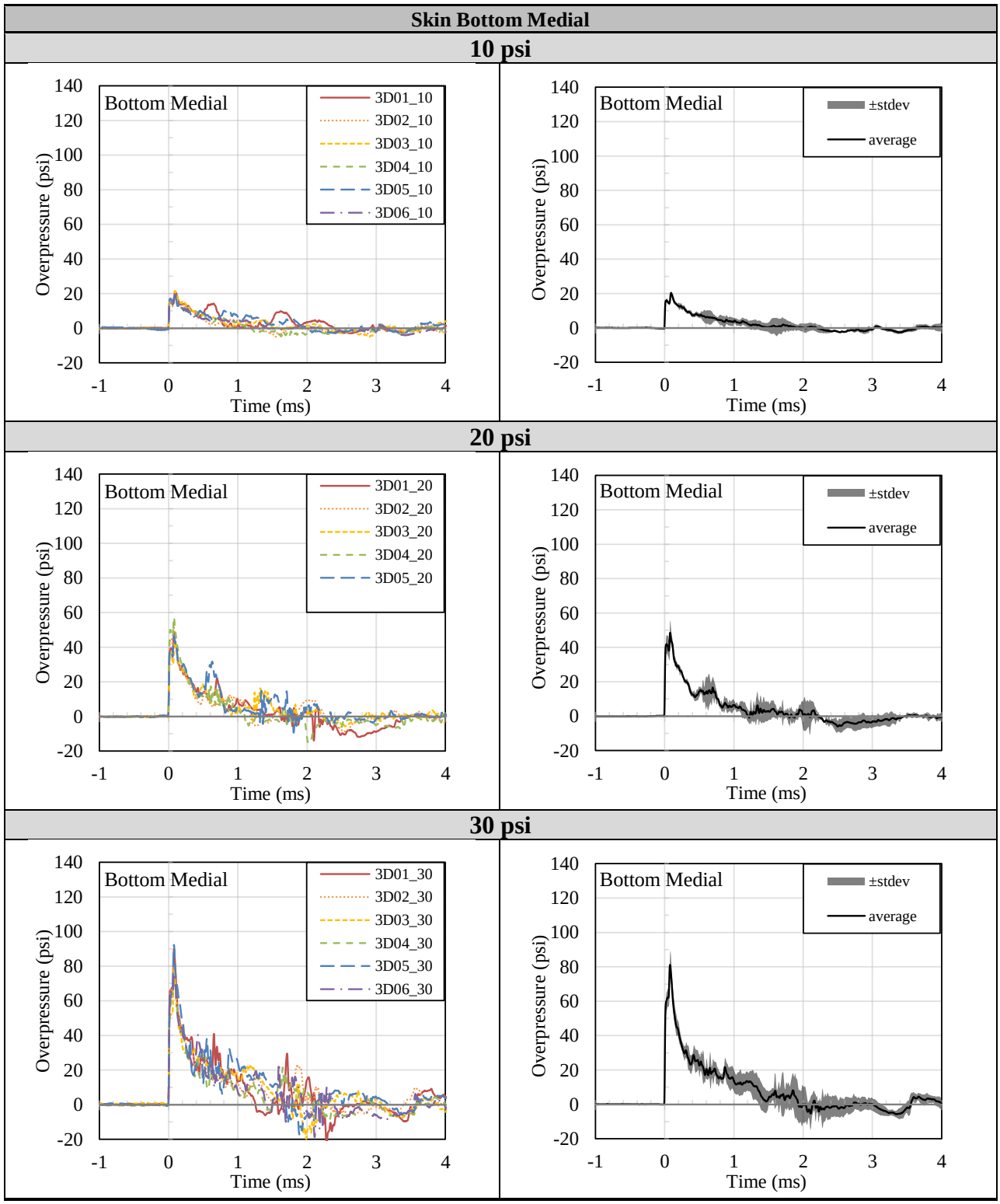

Figure A59. Skin Bottom Medial 3D Orbit – Unprotected Eye.

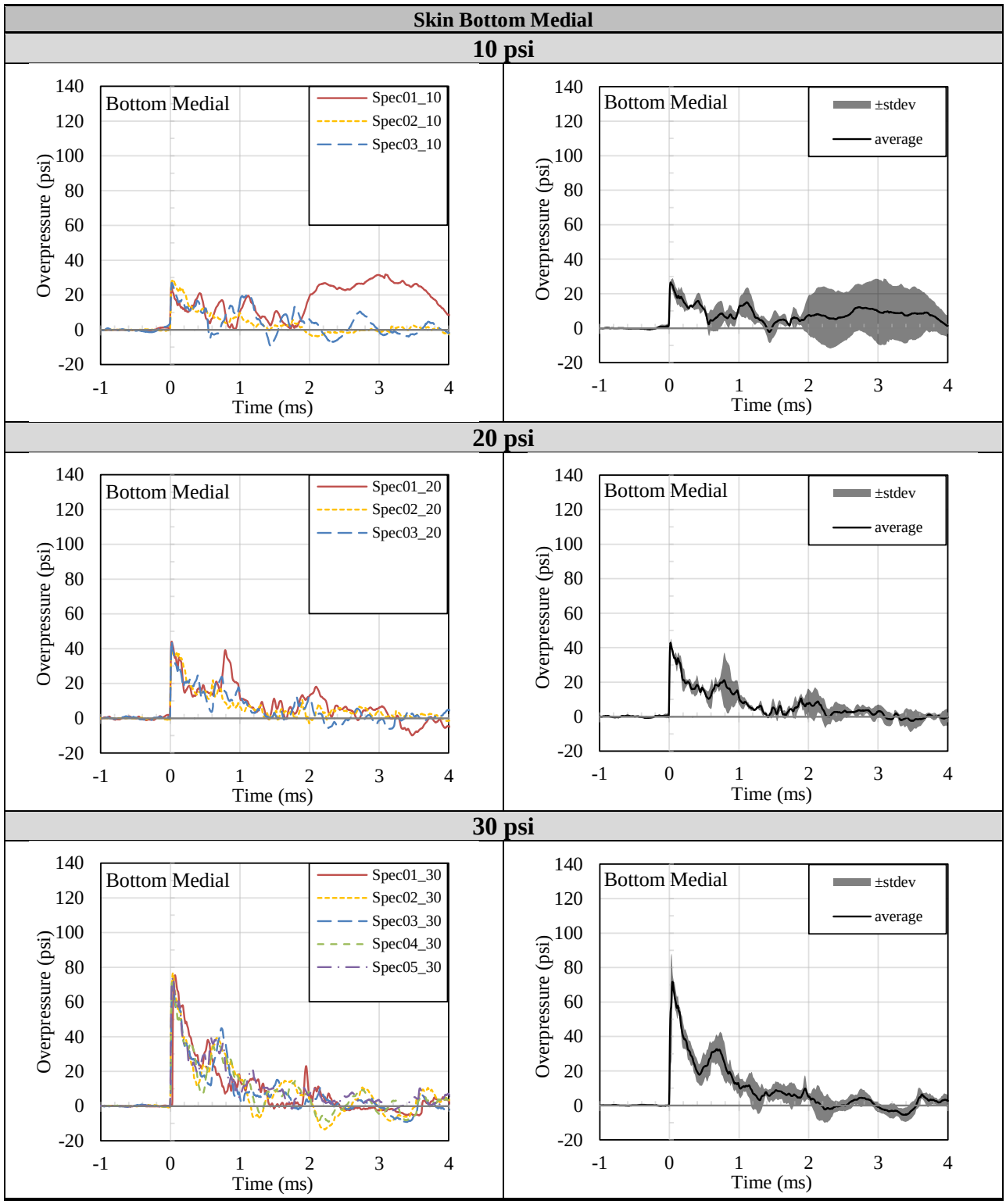

Figure A60. Skin Bottom Medial 3D Orbit – Spectacles.

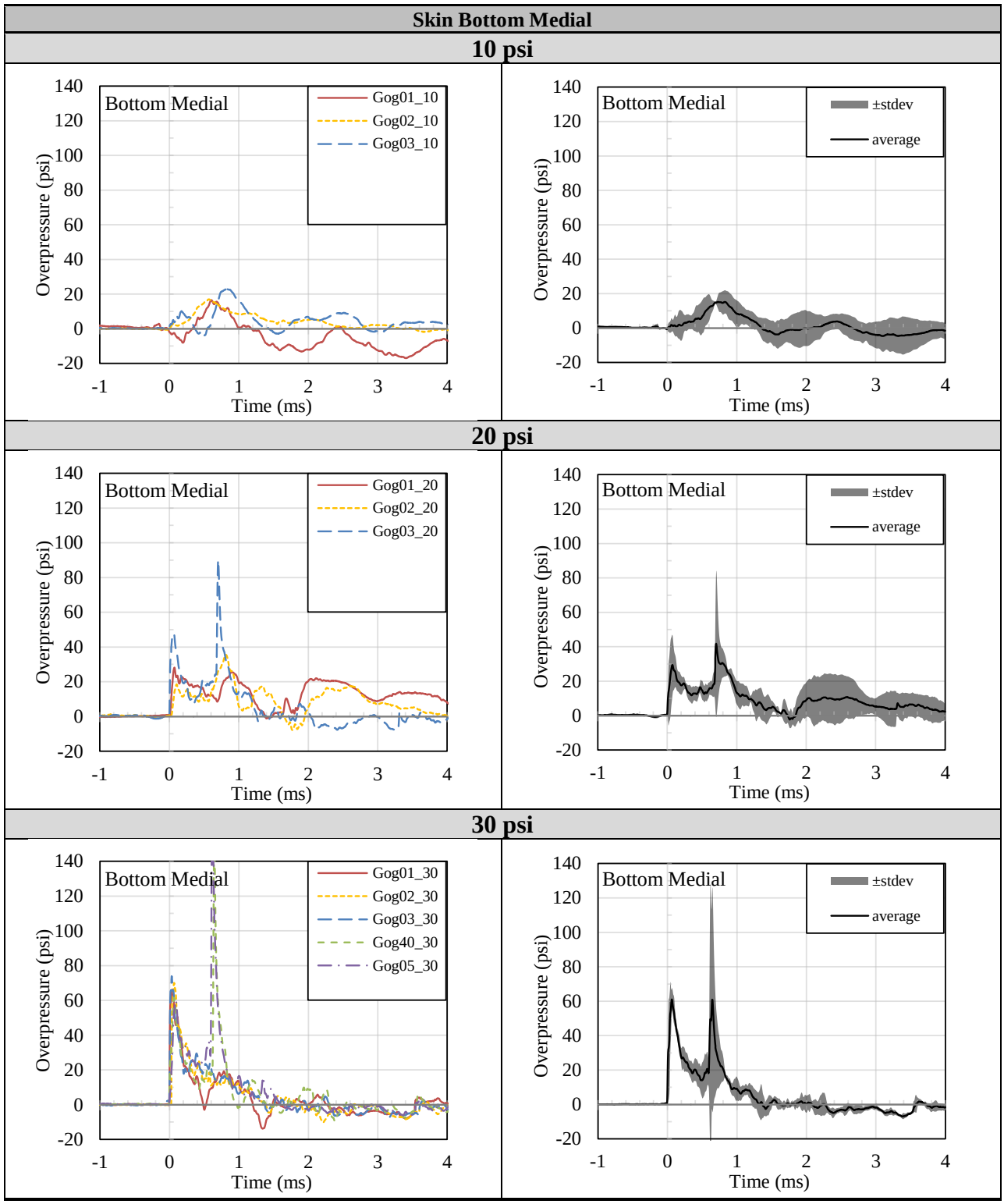

Figure A61. Skin Bottom Medial 3D Orbit – Goggles.

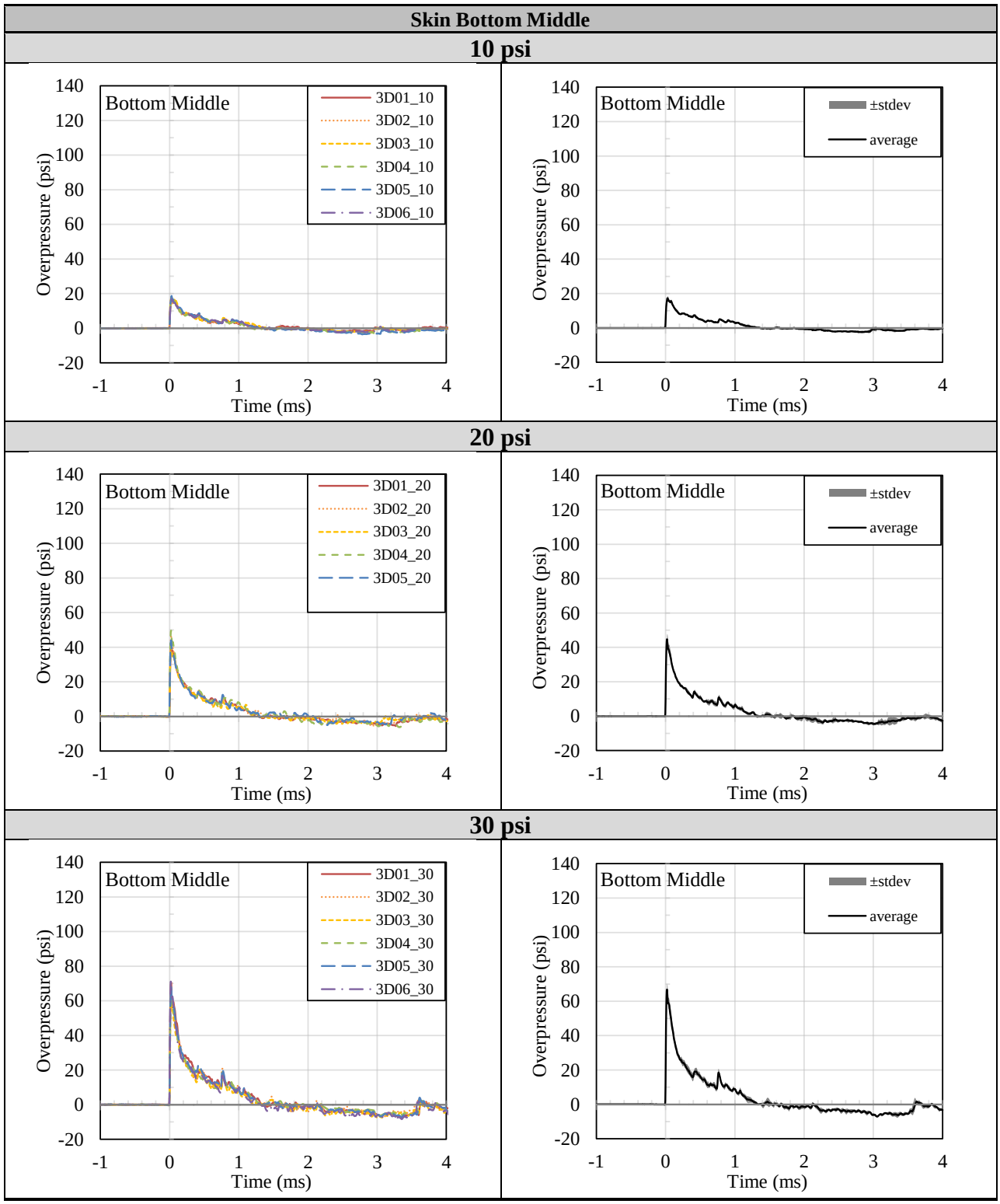

Figure A62. Skin Bottom Middle 3D Orbit – Unprotected Eye.

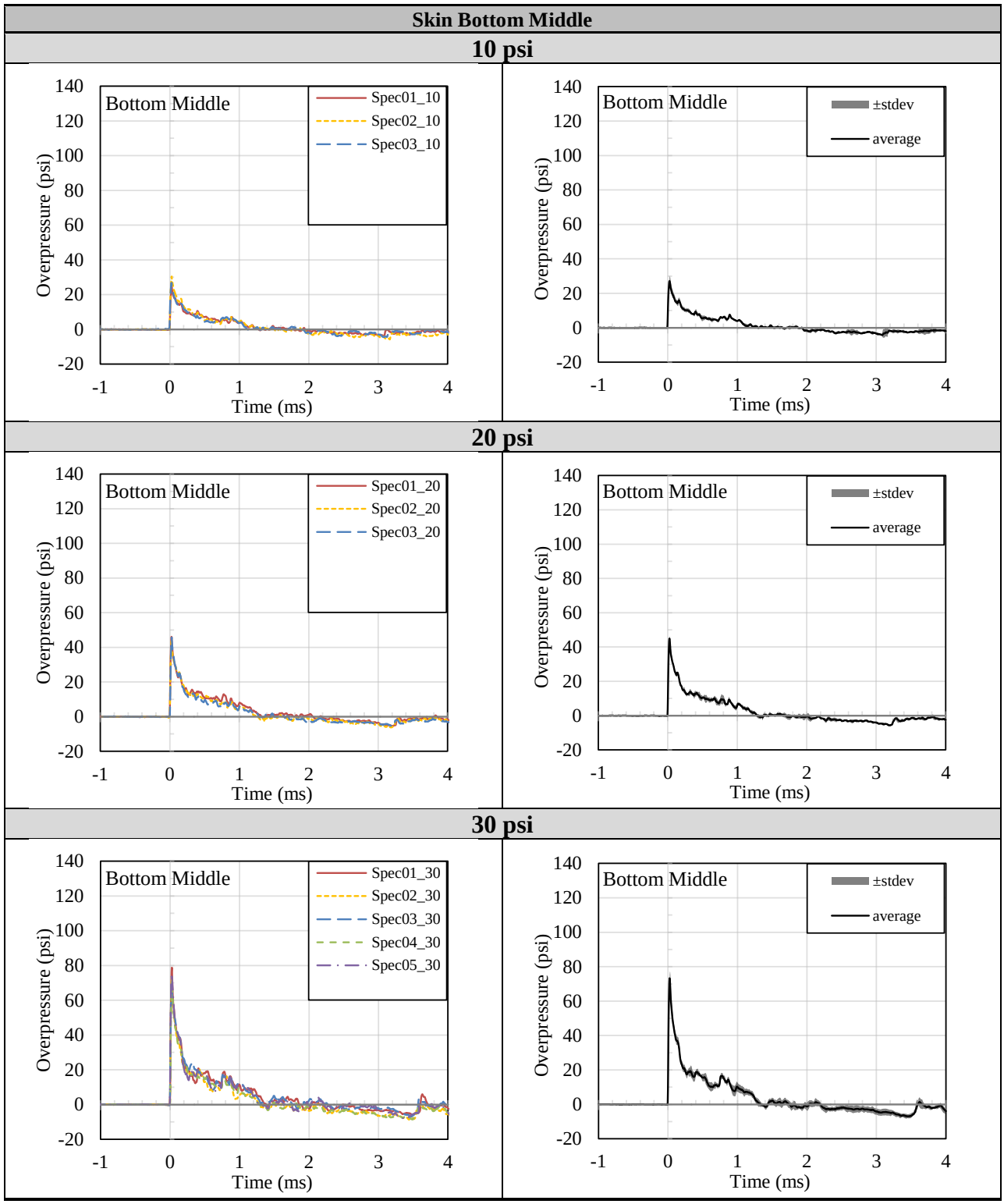

Figure A63. Skin Bottom Middle 3D Orbit – Spectacles.

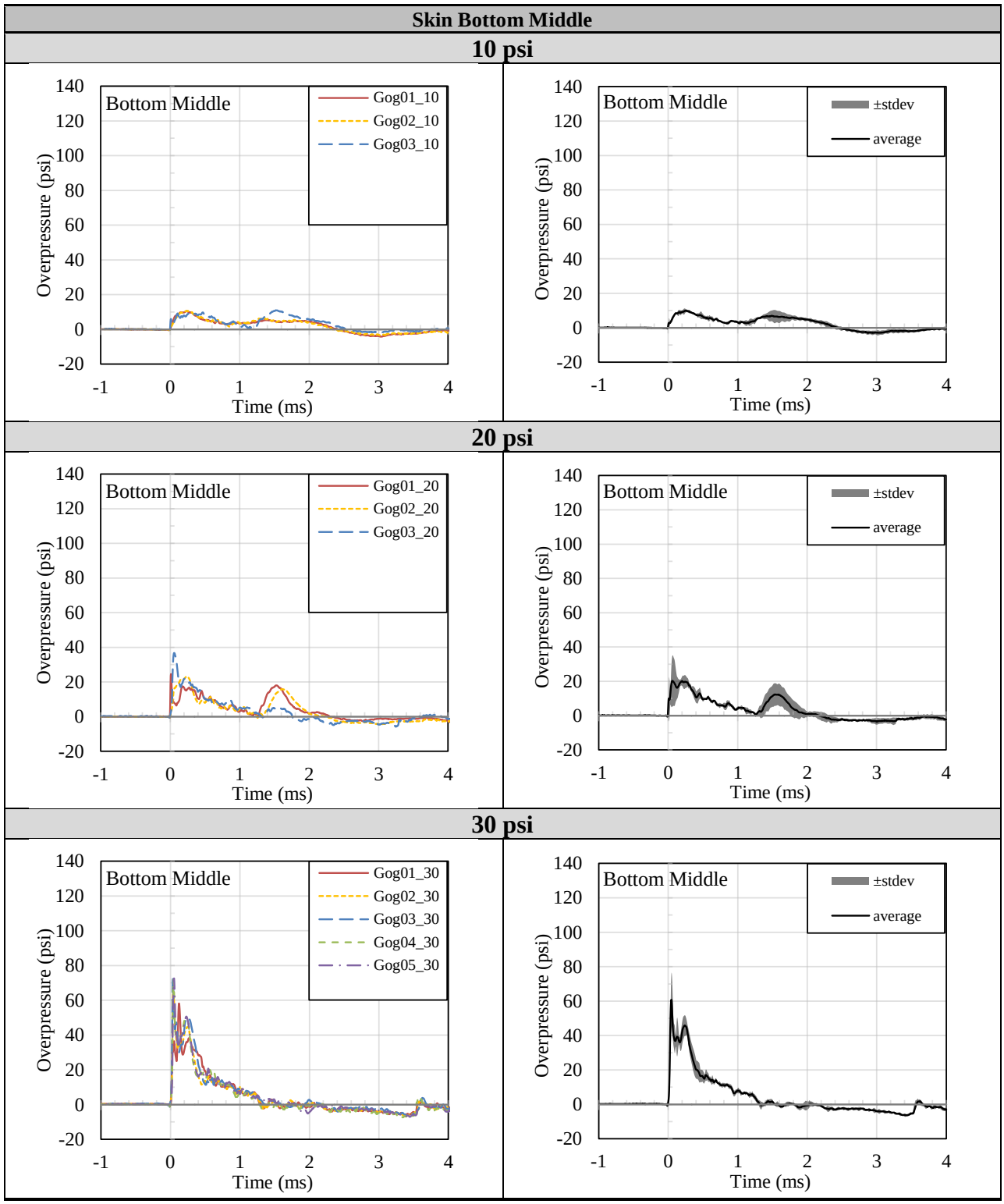

Figure A64. Skin Bottom Middle 3D Orbit – Goggles.
Note: Sensor covered by Goggles.

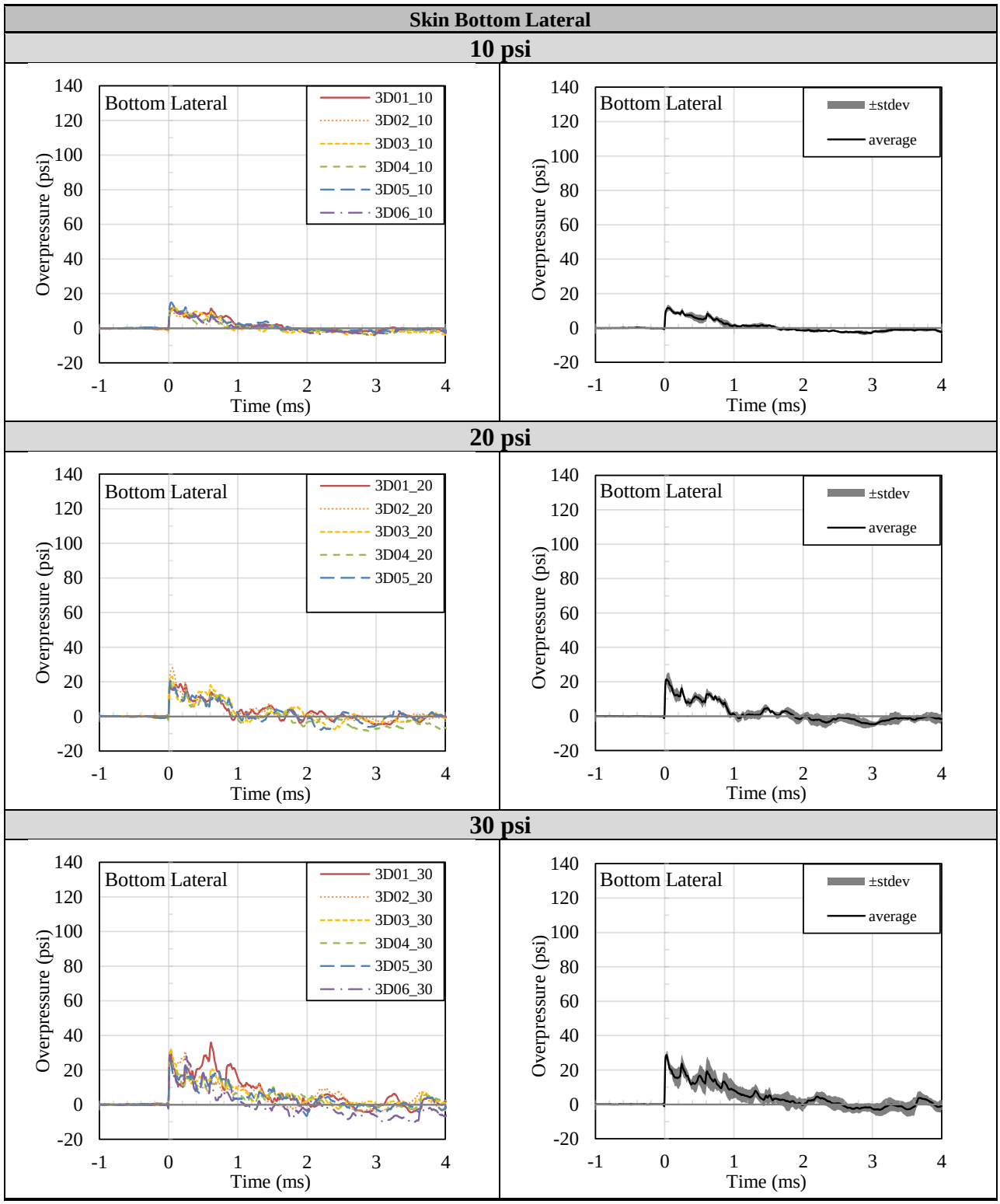

Figure A65. Skin Bottom Lateral 3D Orbit – Unprotected Eye.

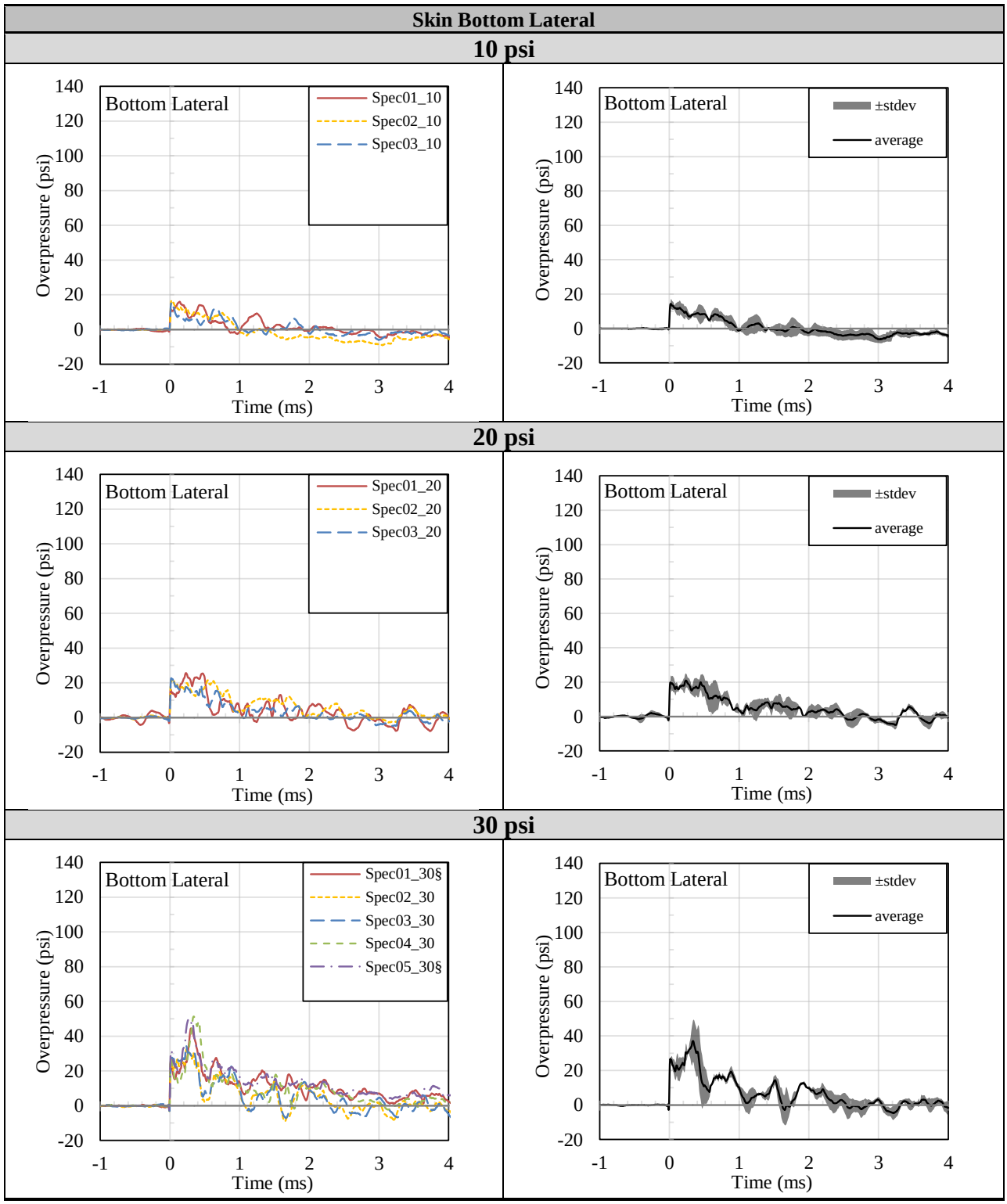

Figure A66. Skin Bottom Lateral 3D Orbit – Spectacles.

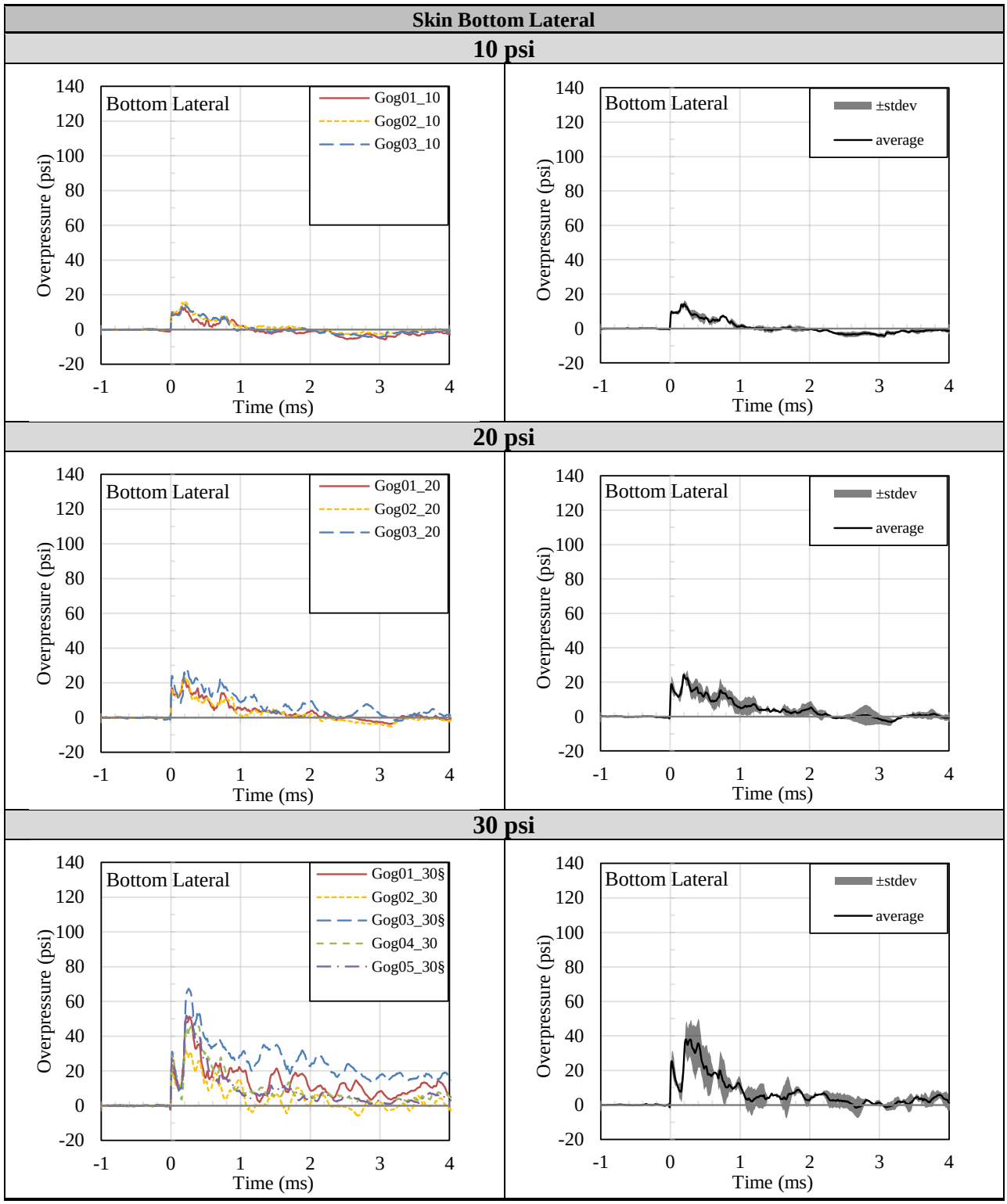

Figure A67. Skin Bottom Lateral 3D Orbit – Goggles.
Note: Sensor covered by Goggles.

Appendix B
Shock Wave Parameters for Porcine Eye Tests

Table B1. Average shock wave parameters for static sensors – empty tube. 214
Table B2. Average shock wave parameters for static sensors – isolated eye. 215
Table B3. Average shock wave parameters for static sensors – synthetic orbit. 215
Table B4. Average shock wave parameters for static sensors – unprotected 3D orbit..... 216
Table B5. Average shock wave parameters for static sensors – 3D orbit with spectacles. 216
Table B6. Average shock wave parameters for static sensors – 3D orbit with goggles. 217
Table B7. Average shock wave parameters for IOP – all conditions. 217
Table B8. Average shock wave parameters for intraorbital sensors - synthetic orbit. 218
Table B9. Average shock wave parameters for intraorbital sensors - unprotected 3D orbit. 218
Table B10. Average shock wave parameters for intraorbital sensors - 3D orbit with spectacles219
Table B11. Average shock wave parameters for intraorbital sensors - 3D orbit with goggles. . 219
Table B12. Average shock wave parameters for facial sensors - unprotected 3D orbit. 220
Table B13. Average shock wave parameters for facial sensors - 3D orbit with spectacles. 221
Table B14. Average shock wave parameters for facial sensors - 3D orbit with goggles. 222
Table B15. Average driver rupture pressure. 223

Table B1. Average shock wave parameters for static sensors – empty tube.

Pressure	Test Condition	10 psi	20 psi	30 psi
Peak Overpressure (psi)				
Static	Wall 01	10.64 ± 1.55	23.71 ± 1.30	34.04 ± 2.05
	Wall 02	10.04 ± 1.06	19.05 ± 1.16	28.24 ± 1.19
	Wall 03	9.24 ± 1.07	17.45 ± 0.91	25.90 ± 1.35
Time of Arrival (ms)				
Static	Wall 01	2.89 ± 0.10	2.15 ± 0.07	1.88 ± 0.05
	Wall 02	3.59 ± 0.12	2.74 ± 0.08	2.41 ± 0.06
	Wall 03	4.31 ± 0.14	2.91 ± 1.45	2.96 ± 0.07
Positive Duration (ms)				
Static	Wall 01	1.77 ± 0.13	1.81 ± 0.10	1.86 ± 0.07
	Wall 02	2.06 ± 0.18	2.29 ± 0.03	2.34 ± 0.01
	Wall 03	1.59 ± 0.10	1.72 ± 0.31	1.73 ± 0.31
Positive Impulse (psi*ms)				
Static	Wall 01	8.32 ± 1.03	15.25 ± 0.79	21.40 ± 0.69
	Wall 02	8.62 ± 1.14	16.11 ± 0.91	23.04 ± 0.73
	Wall 03	7.43 ± 0.91	13.85 ± 0.96	19.40 ± 1.07

Table B2. Average shock wave parameters for static sensors – isolated eye.

Pressure	Test Condition	10 psi	20 psi	30 psi
Peak Overpressure (psi)				
Static	Wall 01	11.49 ± 0.39	24.00 ± 3.15	32.79 ± 4.06
	Wall 02	10.41 ± 0.37	18.68 ± 2.34	25.81 ± 3.99
	Wall 03	10.13 ± 0.14	18.44 ± 2.71	24.95 ± 2.99
	Fluid Flow	10.59 ± 0.34	19.48 ± 2.65	27.05 ± 3.40
Time of Arrival (ms)				
Static	Wall 01	2.79 ± 0.03	2.15 ± 0.15	1.94 ± 0.10
	Wall 02	3.48 ± 0.03	2.74 ± 0.17	2.47 ± 0.12
	Wall 03	4.17 ± 0.04	3.35 ± 0.20	3.03 ± 0.14
	Fluid Flow	3.43 ± 0.03	2.70 ± 0.18	2.44 ± 0.12
Positive Duration (ms)				
Static	Wall 01	1.93 ± 0.02	1.90 ± 0.01	1.87 ± 0.02
	Wall 02	2.12 ± 0.04	2.23 ± 0.12	2.41 ± 0.10
	Wall 03	1.70 ± 0.01	1.81 ± 0.20	2.31 ± 0.09
	Fluid Flow	2.07 ± 0.02	2.17 ± 0.04	2.24 ± 0.03
Positive Impulse (psi*ms)				
Static	Wall 01	8.84 ± 0.18	15.30 ± 1.88	20.38 ± 1.89
	Wall 02	9.23 ± 0.25	16.18 ± 2.08	22.17 ± 2.10
	Wall 03	7.95 ± 0.15	13.61 ± 1.73	19.42 ± 1.85
	Fluid Flow	8.91 ± 0.18	15.79 ± 2.27	21.39 ± 2.02

Table B3. Average shock wave parameters for static sensors – synthetic orbit.

Pressure	Test Condition	10 psi	20 psi	30 psi
Peak Overpressure (psi)				
Static	Wall 01	9.34 ± 1.09	27.66 ± 4.30	34.41 ± 2.48
	Wall 02	9.25 ± 0.88	22.75 ± 3.27	29.18 ± 1.68
	Wall 03	8.96 ± 0.25	19.55 ± 2.48	24.79 ± 0.67
	Fluid Flow	12.39 ± 5.28	28.77 ± 4.14	38.78 ± 2.59
Time of Arrival (ms)				
Static	Wall 01	2.93 ± 0.07	2.01 ± 0.11	1.87 ± 0.05
	Wall 02	3.64 ± 0.08	2.57 ± 0.14	2.46 ± 0.17
	Wall 03	4.36 ± 0.10	3.16 ± 0.16	2.95 ± 0.07
	Fluid Flow	3.58 ± 0.08	2.51 ± 0.15	2.36 ± 0.06
Positive Duration (ms)				
Static	Wall 01	1.99 ± 0.03	1.95 ± 0.02	1.88 ± 0.03
	Wall 02	1.76 ± 0.01	1.81 ± 0.01	1.89 ± 0.07
	Wall 03	1.55 ± 0.08	2.13 ± 0.41	2.00 ± 0.48
	Fluid Flow	2.36 ± 0.32	3.04 ± 0.81	5.53 ± 3.05*
Positive Impulse (psi*ms)				
Static	Wall 01	7.90 ± 0.73	18.88 ± 2.56	23.20 ± 1.01
	Wall 02	7.75 ± 0.62	18.20 ± 2.34	22.67 ± 1.01
	Wall 03	6.63 ± 0.64	16.77 ± 3.19	20.44 ± 2.62
	Fluid Flow	9.22 ± 1.84	24.15 ± 5.73	40.33 ± 11.28*

*Only four tests because one test maxed out sensor in the middle of the positive duration.

Table B4. Average shock wave parameters for static sensors – unprotected 3D orbit.

Pressure	Test Condition	10 psi	20 psi	30 psi
Peak Overpressure (psi)				
Static	Wall 01	9.56 ± 0.64	24.46 ± 1.31	33.55 ± 1.42
	Wall 02	9.20 ± 0.59	19.61 ± 2.35	28.63 ± 2.55
	Wall 03	8.80 ± 0.37	17.74 ± 0.46	25.05 ± 1.17
	Fluid Flow	13.08 ± 0.70	28.91 ± 2.01	40.84 ± 2.13
Time of Arrival (ms)				
Static	Wall 01	2.96 ± 0.05	2.14 ± 0.07	1.90 ± 0.03
	Wall 02	3.67 ± 0.06	2.73 ± 0.08	2.43 ± 0.04
	Wall 03	4.39 ± 0.06	3.34 ± 0.10	2.98 ± 0.05
	Fluid Flow	3.62 ± 0.06	2.68 ± 0.08	2.39 ± 0.04
Positive Duration (ms)				
Static	Wall 01	1.97 ± 0.05	1.94 ± 0.06	1.90 ± 0.03
	Wall 02	1.69 ± 0.04	1.78 ± 0.02	1.92 ± 0.05
	Wall 03	1.56 ± 0.11	2.15 ± 0.40	1.87 ± 0.40
	Fluid Flow	1.83 ± 0.12	2.40 ± 0.20	2.51 ± 0.39
Positive Impulse (psi*ms)				
Static	Wall 01	7.80 ± 0.53	15.91 ± 0.87	22.21 ± 0.79
	Wall 02	7.66 ± 0.43	15.29 ± 0.66	21.78 ± 0.95
	Wall 03	6.69 ± 0.51	14.67 ± 1.23	19.35 ± 1.32
	Fluid Flow	8.00 ± 0.52	17.85 ± 1.15	27.09 ± 2.94

Table B5. Average shock wave parameters for static sensors – 3D orbit with spectacles.

Pressure	Test Condition	10 psi	20 psi	30 psi
Peak Overpressure (psi)				
Static	Wall 01	12.87 ± 1.06	20.83 ± 0.75	31.41 ± 2.03
	Wall 02	12.34 ± 0.81	17.64 ± 0.32	29.26 ± 0.75
	Wall 03	11.79 ± 0.76†	17.19 ± 0.65	23.27 ± 0.38*
	Fluid Flow	16.01 ± 1.68	24.57 ± 0.31	38.62 ± 1.56
Time of Arrival (ms)				
Static	Wall 01	2.61 ± 0.06	2.22 ± 0.01	1.96 ± 0.04
	Wall 02	3.32 ± 0.11	2.81 ± 0.01	2.50 ± 0.04
	Wall 03	3.98 ± 0.16†	3.44 ± 0.02	3.09 ± 0.05*
	Fluid Flow	3.26 ± 0.10	2.77 ± 0.02	1.70 ± 0.72
Positive Duration (ms)				
Static	Wall 01	1.99 ± 0.12	2.34 ± 0.01	2.42 ± 0.03
	Wall 02	1.72 ± 0.06	1.86 ± 0.08	1.96 ± 0.01
	Wall 03	1.40 ± 0.00†	1.78 ± 0.09	1.54 ± 0.10*
	Fluid Flow	1.81 ± 0.04	2.49 ± 0.02	3.24 ± 0.87
Positive Impulse (psi*ms)				
Static	Wall 01	10.35 ± 0.77	15.35 ± 0.16	23.11 ± 0.64
	Wall 02	9.93 ± 0.67	14.69 ± 0.11	21.90 ± 0.60
	Wall 03	8.42 ± 0.80†	12.29 ± 0.04	17.36 ± 0.80*
	Fluid Flow	10.43 ± 1.45	16.75 ± 0.41	28.30 ± 4.22

†Only two tests because insufficient DAS available for one test.
*Only two tests because insufficient DAS available for three tests.

Table B6. Average shock wave parameters for static sensors – 3D orbit with goggles.

Pressure	Test Condition	10 psi	20 psi	30 psi
Peak Overpressure (psi)				
Static	Wall 01	10.32 ± 0.16	20.29 ± 1.56	30.86 ± 1.19
	Wall 02	10.16 ± 0.28	17.44 ± 1.10	30.11 ± 1.52
	Wall 03	9.70 ± 0.18	16.20 ± 1.20	26.70 ± 3.18*
	Fluid Flow	14.63 ± 0.07	29.10 ± 2.99	50.08 ± 4.01
Time of Arrival (ms)				
Static	Wall 01	2.80 ± 0.06	2.21 ± 0.03	1.94 ± 0.04
	Wall 02	3.50 ± 0.06	2.88 ± 0.09	2.48 ± 0.05
	Wall 03	4.22 ± 0.03	3.52 ± 0.10	3.05 ± 0.04*
	Fluid Flow	3.45 ± 0.02	2.83 ± 0.09	1.95 ± 0.69
Positive Duration (ms)				
Static	Wall 01	1.90 ± 0.01	1.94 ± 0.07	2.39 ± 0.02
	Wall 02	1.71 ± 0.03	1.82 ± 0.07	1.96 ± 0.02
	Wall 03	1.49 ± 0.06	1.53 ± 0.07	1.74 ± 0.22*
	Fluid Flow	1.78 ± 0.04	2.31 ± 0.41	2.90 ± 0.81
Positive Impulse (psi*ms)				
Static	Wall 01	8.70 ± 0.15	14.20 ± 1.18	23.05 ± 0.22
	Wall 02	8.51 ± 0.12	13.84 ± 1.33	21.91 ± 0.23
	Wall 03	6.98 ± 0.08	11.43 ± 0.75	18.79 ± 1.98*
	Fluid Flow	9.04 ± 0.14	16.34 ± 2.13	28.87 ± 4.58

*Only two tests at this test level because insufficient DAS available for one test.

Table B7. Average shock wave parameters for IOP – all conditions.

Pressure	Test Condition	10 psi	20 psi	30 psi
Peak Overpressure (psi)				
IOP	Isolated	18.69 ± 5.42	37.03 ± 7.99	57.98 ± 10.44
	Synthetic Orbit	21.62 ± 3.38	67.45 ± 13.31	85.73 ± 7.51
	3D Orbit - unprotected	19.51 ± 3.04	49.71 ± 10.67	89.40 ± 28.16
	3D Orbit - spectacles	24.99 ± 2.13	36.15 ± 3.86	68.85 ± 16.53
	3D Orbit - goggles	12.68 ± 1.22	32.84 ± 4.76	68.04 ± 24.88
Time of Arrival (ms)				
IOP	Isolated	3.55 ± 0.22	2.71 ± 0.17	2.45 ± 0.11
	Synthetic Orbit	3.59 ± 0.08	2.54 ± 0.14	2.37 ± 0.06
	3D Orbit - unprotected	3.62 ± 0.06	2.69 ± 0.09	2.39 ± 0.04
	3D Orbit - spectacles	3.29 ± 0.11	2.78 ± 0.01	2.47 ± 0.04
	3D Orbit - goggles	3.51 ± 0.03	2.89 ± 0.09	2.08 ± 0.94
Positive Duration (ms)				
IOP	Isolated	1.62 ± 0.83	1.50 ± 0.32	1.13 ± 0.39
	Synthetic Orbit	1.40 ± 0.04	1.68 ± 0.47	1.96 ± 0.71
	3D Orbit - unprotected	1.43 ± 0.14	1.82 ± 0.43	1.57 ± 0.30
	3D Orbit - spectacles	0.96 ± 0.14	0.80 ± 0.19	1.43 ± 0.87
	3D Orbit - goggles	0.93 ± 0.45	0.99 ± 0.47	1.32 ± 0.87
Positive Impulse (psi*ms)				
IOP	Isolated	11.27 ± 2.18	25.26 ± 7.23	30.34 ± 9.93
	Synthetic Orbit	9.48 ± 0.86	28.95 ± 4.69	39.79 ± 4.60
	3D Orbit - unprotected	8.87 ± 0.50	23.21 ± 5.76	34.08 ± 3.05
	3D Orbit - spectacles	9.69 ± 0.72	13.21 ± 1.50	37.21 ± 20.54
	3D Orbit - goggles	5.11 ± 2.92	10.82 ± 6.26	29.32 ± 16.70

Table B8. Average shock wave parameters for intraorbital sensors - synthetic orbit.

Pressure	Test Condition	10 psi	20 psi	30 psi
Peak Overpressure (psi)				
Orbital	Synthetic – Maxilla	24.63 ± 2.95	74.34 ± 13.77	96.08 ± 8.98
	Synthetic – Lacrimal	23.08 ± 3.37	73.38 ± 15.39	99.45 ± 10.28
	Synthetic – Frontal A.	23.28 ± 1.62	72.89 ± 18.48	103.40 ± 20.93
	Synthetic – Frontal P.	27.73 ± 3.21	79.90 ± 16.46	96.97 ± 7.65
Time of Arrival (ms)				
Orbital	Synthetic – Maxilla	3.61 ± 0.09	2.56 ± 0.13	2.39 ± 0.06
	Synthetic – Lacrimal	3.61 ± 0.08	2.55 ± 0.13	2.39 ± 0.06
	Synthetic – Frontal A.	3.61 ± 0.08	2.55 ± 0.13	2.38 ± 0.06
	Synthetic – Frontal P.	3.63 ± 0.09	2.56 ± 0.14	2.39 ± 0.06
Positive Duration (ms)				
Orbital	Synthetic – Maxilla	1.30 ± 0.17	1.56 ± 0.39	1.73 ± 0.39
	Synthetic – Lacrimal	1.32 ± 0.17	1.33 ± 0.19	1.56 ± 0.41
	Synthetic – Frontal A.	1.30 ± 0.23	1.37 ± 0.27	1.22 ± 0.31
	Synthetic – Frontal P.	1.37 ± 0.02	1.33 ± 0.26	1.38 ± 0.56
Positive Impulse (psi*ms)				
Orbital	Synthetic – Maxilla	9.30 ± 1.46	28.05 ± 4.76	38.20 ± 2.42
	Synthetic – Lacrimal	9.20 ± 1.32	26.58 ± 4.60	35.88 ± 2.43
	Synthetic – Frontal A.	9.49 ± 1.35	27.13 ± 6.65	35.24 ± 5.80
	Synthetic – Frontal P.	10.35 ± 1.04	26.78 ± 5.67	34.83 ± 6.72

Table B9. Average shock wave parameters for intraorbital sensors - unprotected 3D orbit.

Pressure	Test Condition	10 psi	20 psi	30 psi
Peak Overpressure (Avg ± Stdev)				
Orbital	3D – Maxilla	16.17 ± 2.38	43.66 ± 4.13	79.10 ± 13.07
	3D – Lacrimal	17.33 ± 1.85	39.54 ± 6.39	85.76 ± 10.67
	3D – Frontal A.	16.62 ± 2.75	41.03 ± 4.96	80.36 ± 13.89
	3D – Frontal Post.	20.09 ± 3.62	46.77 ± 3.70	95.12 ± 12.68
Time of Arrival (ms)				
Orbital	3D – Maxilla	3.63 ± 0.05	2.70 ± 0.09	2.42 ± 0.03
	3D – Lacrimal	3.67 ± 0.09	2.70 ± 0.08	2.42 ± 0.04
	3D – Frontal A.	3.65 ± 0.07	2.70 ± 0.09	2.42 ± 0.03
	3D – Frontal Post.	3.66 ± 0.07	2.71 ± 0.09	2.43 ± 0.04
Positive Duration (ms)				
Orbital	3D – Maxilla	1.33 ± 0.30	0.43 ± 0.24	0.72 ± 0.29
	3D – Lacrimal	0.96 ± 0.54	0.87 ± 0.44	0.60 ± 0.32
	3D – Frontal A.	1.15 ± 0.52	0.69 ± 0.45	0.70 ± 0.43
	3D – Frontal Post.	1.04 ± 0.41	0.81 ± 0.21	0.62 ± 0.39
Positive Impulse (psi*ms)				
Orbital	3D – Maxilla	8.87 ± 1.04	8.10 ± 4.30	21.79 ± 7.19
	3D – Lacrimal	6.24 ± 3.83	15.19 ± 6.60	19.25 ± 10.55
	3D – Frontal A.	8.44 ± 3.36	13.08 ± 8.15	21.71 ± 10.60
	3D – Frontal Post.	8.23 ± 3.59	16.35 ± 4.03	19.56 ± 13.11

Table B10. Average shock wave parameters for intraorbital sensors - 3D orbit with spectacles.

Pressure	Test Condition	10 psi	20 psi	30 psi
Peak Overpressure (Avg ± Stdev)				
Orbital	3D – Maxilla	29.52 ± 11.57	41.80 ± 5.62	88.20 ± 9.06
	3D – Lacrimal	19.43 ± 3.29*	44.77 ± 5.34	82.65 ± 28.17
	3D – Frontal A.	29.60 ± 4.78	43.08 ± 5.51*	82.26 ± 11.77
	3D – Frontal Post.	35.00 ± 4.03	73.45 ± 19.52	106.34 ± 12.66
Time of Arrival (ms)				
Orbital	3D – Maxilla	3.33 ± 0.11	2.84 ± 0.02	2.51 ± 0.03
	3D – Lacrimal	3.49 ± 0.06*	2.87 ± 0.03	2.55 ± 0.03
	3D – Frontal A.	3.32 ± 0.10	2.82 ± 0.03	2.49 ± 0.04
	3D – Frontal Post.	3.37 ± 0.12	2.85 ± 0.06	2.54 ± 0.04
Positive Duration (ms)				
Orbital	3D – Maxilla	0.38 ± 0.25	0.66 ± 0.16	0.49 ± 0.40
	3D – Lacrimal	0.69 ± 0.45*	0.56 ± 0.32	0.54 ± 0.39
	3D – Frontal A.	0.71 ± 0.23	0.83 ± 0.06	0.62 ± 0.37
	3D – Frontal Post.	1.11 ± 0.45	0.88 ± 0.00*	2.22 ± 1.86
Positive Impulse (psi*ms)				
Orbital	3D – Maxilla	3.92 ± 2.21	10.40 ± 2.84	11.09 ± 10.69
	3D – Lacrimal	6.32 ± 5.10*	10.68 ± 7.55	17.60 ± 15.34
	3D – Frontal A.	8.58 ± 1.27	14.66 ± 0.52*	18.09 ± 12.69
	3D – Frontal Post.	16.56 ± 3.57	25.46 ± 8.71	63.71 ± 37.35

*Only two tests because one test maxed out this sensor.

Table B11. Average shock wave parameters for intraorbital sensors - 3D orbit with goggles.

Pressure	Test Condition	10 psi	20 psi	30 psi
Peak Overpressure (Avg ± Stdev)				
Orbital	3D – Maxilla	17.74 ± 4.62	35.28 ± 11.61	66.80 ± 19.57*
	3D – Lacrimal	25.76 ± 12.64	63.72 ± 18.03	70.39 ± 14.38
	3D – Frontal A.	17.49 ± 0.92	38.73 ± 2.79	75.91 ± 22.10
	3D – Frontal Post.	22.84 ± 2.97	54.44 ± 16.03	101.41 ± 19.05
Time of Arrival (ms)				
Orbital	3D – Maxilla	3.81 ± 0.33	3.47 ± 0.33	3.64 ± 0.31*
	3D – Lacrimal	3.86 ± 0.02	3.18 ± 0.17	2.74 ± 0.10
	3D – Frontal A.	3.68 ± 0.06	3.04 ± 0.13	2.66 ± 0.07
	3D – Frontal Post.	3.75 ± 0.07	1.87 ± 2.08	2.66 ± 0.09
Positive Duration (ms)				
Orbital	3D – Maxilla	0.90 ± 0.18	0.91 ± 0.11	1.06 ± 0.39*
	3D – Lacrimal	0.72 ± 0.19	0.58 ± 0.54	0.70 ± 0.31
	3D – Frontal A.	0.71 ± 0.38	0.88 ± 0.16	0.67 ± 0.08
	3D – Frontal Post.	1.48 ± 0.91	1.35 ± 0.08	2.32 ± 1.88
Positive Impulse (psi*ms)				
Orbital	3D – Maxilla	7.17 ± 0.26	13.24 ± 1.55	25.27 ± 14.19*
	3D – Lacrimal	8.11 ± 2.74	13.27 ± 5.73	19.96 ± 6.79
	3D – Frontal A.	5.29 ± 3.44	13.11 ± 2.24	19.29 ± 3.73
	3D – Frontal Post.	11.45 ± 6.36	31.21 ± 12.40	63.52 ± 33.62

*Only three tests because insufficient DAS available for two tests.

Table B12. Average shock wave parameters for facial sensors - unprotected 3D orbit.

Pressure	Test Condition	10 psi	20 psi	30 psi
Peak Overpressure (psi)				
Facial	3D – Nasal	25.73 ± 1.65	68.47 ± 3.33	101.16 ± 12.34
	3D – Top Medial	19.40 ± 1.30	48.10 ± 4.12	76.08 ± 7.66
	3D – Top Middle	15.17 ± 0.93	36.47 ± 4.92	56.49 ± 6.91
	3D – Top Lateral	13.33 ± 1.50	29.06 ± 5.31	51.84 ± 11.02
	3D – Bot. Medial	20.41 ± 0.83	49.33 ± 5.81	81.94 ± 7.47
	3D – Bot. Middle	17.35 ± 1.18	44.85 ± 3.06	66.99 ± 3.73
	3D – Bot. Lateral	12.02 ± 1.71	22.17 ± 3.60	30.36 ± 3.53
Time of Arrival (ms)				
Facial	3D – Nasal	3.61 ± 0.06	2.68 ± 0.09	2.38 ± 0.04
	3D – Top Medial	3.60 ± 0.06	2.67 ± 0.08	2.37 ± 0.04
	3D – Top Middle	3.63 ± 0.06	2.69 ± 0.09	2.39 ± 0.04
	3D – Top Lateral	3.69 ± 0.06	2.74 ± 0.09	1.85 ± 1.41
	3D – Bot. Medial	3.60 ± 0.06	2.67 ± 0.09	2.38 ± 0.04
	3D – Bot. Middle	3.63 ± 0.06	2.70 ± 0.09	2.40 ± 0.04
	3D – Bot. Lateral	3.71 ± 0.06	2.76 ± 0.09	2.46 ± 0.04
Positive Duration (ms)				
Facial	3D – Nasal	1.52 ± 0.19	1.82 ± 0.31	1.60 ± 0.30
	3D – Top Medial	1.15 ± 0.52	1.18 ± 0.36	1.20 ± 0.30
	3D – Top Middle	1.25 ± 0.22	1.04 ± 0.25	1.02 ± 0.36
	3D – Top Lateral	0.92 ± 0.28	1.22 ± 0.24	1.54 ± 0.33
	3D – Bot. Medial	1.52 ± 0.56	1.29 ± 0.20	1.59 ± 0.29
	3D – Bot. Middle	1.33 ± 0.07	1.39 ± 0.18	1.32 ± 0.04
	3D – Bot. Lateral	1.37 ± 0.40	1.16 ± 0.44	1.86 ± 0.49
Positive Impulse (psi*ms)				
Facial	3D – Nasal	10.89 ± 1.73	23.61 ± 2.33	34.73 ± 3.12
	3D – Top Medial	8.42 ± 2.85	18.69 ± 3.66	29.35 ± 5.74
	3D – Top Middle	7.90 ± 1.20	15.29 ± 2.42	22.98 ± 4.93
	3D – Top Lateral	6.45 ± 1.42	15.59 ± 2.60	32.59 ± 5.14
	3D – Bot. Medial	10.40 ± 2.80	19.10 ± 1.48	35.42 ± 4.34
	3D – Bot. Middle	7.09 ± 0.43	14.99 ± 1.09	21.92 ± 1.36
	3D – Bot. Lateral	6.89 ± 1.23	10.88 ± 1.59	19.51 ± 4.85

Table B13. Average shock wave parameters for facial sensors - 3D orbit with spectacles.

Pressure	Test Condition	10 psi	20 psi	30 psi
Peak Overpressure (psi)				
Facial	3D – Nasal	26.37 ± 2.70	37.50 ± 0.78	62.22 ± 2.14
	3D – Top Medial	27.16 ± 2.41	45.67 ± 2.57	79.18 ± 2.28
	3D – Top Middle	20.52 ± 1.31	32.26 ± 1.11	52.77 ± 1.36
	3D – Top Lateral	24.87 ± 1.50	40.13 ± 3.50	67.72 ± 25.25§
	3D – Bot. Medial	29.22 ± 2.42	42.82 ± 2.45	73.96 ± 2.39
	3D – Bot. Middle	27.32 ± 2.96	45.19 ± 1.29	73.65 ± 3.54
	3D – Bot. Lateral	15.93 ± 0.74	23.31 ± 2.05	42.64 ± 8.75*
Time of Arrival (ms)				
Facial	3D – Nasal	3.27 ± 0.11	2.77 ± 0.01	2.46 ± 0.05
	3D – Top Medial	3.19 ± 0.12	2.78 ± †	1.72 ± 1.52
	3D – Top Middle	3.19 ± 0.05	2.77 ± 0.02	2.45 ± 0.04
	3D – Top Lateral	3.27 ± 0.24	2.80 ± 0.05	2.47 ± 0.09
	3D – Bot. Medial	3.12 ± 0.01	2.69 ± 0.13	2.40 ± 0.10
	3D – Bot. Middle	3.21 ± 0.14	2.78 ± 0.02	2.46 ± 0.04
	3D – Bot. Lateral	3.35 ± 0.11	2.85 ± 0.01	2.54 ± 0.04*
Positive Duration (ms)				
Facial	3D – Nasal	1.09 ± 1.00	1.20 ± 0.14	1.48 ± 0.34
	3D – Top Medial	1.46 ± 0.89	1.17 ± †	1.83 ± 0.43‡
	3D – Top Middle	1.48 ± 0.44	1.07 ± 0.44	1.38 ± 0.47
	3D – Top Lateral	0.90 ± 0.44	1.53 ± 0.54	1.57 ± 0.29‡
	3D – Bot. Medial	1.07 ± 0.48¦	1.45 ± 0.07	1.46 ± 0.27
	3D – Bot. Middle	1.29 ± 0.16‡	1.29 ± 0.03	1.41 ± 0.20
	3D – Bot. Lateral	0.93 ± 0.08	1.39 ± 0.47	1.30 ± 0.39*
Positive Impulse (psi*ms)				
Facial	3D – Nasal	7.83 ± 3.90	14.02 ± 2.16	24.09 ± 2.59
	3D – Top Medial	16.10 ± 9.57	16.74 ± †	35.58 ± 5.21
	3D – Top Middle	11.47 ± 3.04	13.10 ± 2.52	24.22 ± 3.95
	3D – Top Lateral	8.66 ± 4.16	25.41 ± 16.05	25.10 ± 1.49‡
	3D – Bot. Medial	11.09 ± 3.76¦	21.99 ± 2.78	35.21 ± 2.39
	3D – Bot. Middle	9.36 ± 0.69‡	14.48 ± 1.27	22.19 ± 2.05
	3D – Bot. Lateral	7.50 ± 0.80	16.50 ± 5.70	22.15 ± 5.85*

*Only three tests at this level because two tests do not return to zero after initial peak.
†Only one test at this level because two tests do not return to zero after initial peak.
‡Only four tests at this level because one test did not return to zero after initial peak.
§Only four tests at this level because one test did not return to zero after initial peak.
¦Only two tests at this test level because one test recorded an uncharacteristic response after initial peak.

Table B14. Average shock wave parameters for facial sensors - 3D orbit with goggles.

Pressure	Test Condition	10 psi	20 psi	30 psi
Peak Overpressure (psi)				
Facial	3D – Nasal	10.30 ± 0.84	18.63 ± 4.02	30.90 ± 2.69
	3D – Top Medial	13.97 ± 3.70	28.77 ± 6.05	35.28 ± 4.06
	3D – Top Middle	11.06 ± 0.65	22.74 ± 1.86	39.24 ± 1.50
	3D – Top Lateral	14.91 ± 0.34	24.87 ± 3.91	63.33 ± 22.67
	3D – Bot. Medial	18.83 ± 3.63	37.47 ± 10.35	105.33 ± 61.19
	3D – Bot. Middle	10.72 ± 0.23	29.96 ± 10.47	68.54 ± 6.21
	3D – Bot. Lateral	14.62 ± 1.49	23.78 ± 0.93	50.01 ± 12.36*
Time of Arrival (ms)				
Facial	3D – Nasal	3.49 ± 0.03	2.88 ± 0.08	2.45 ± 0.07
	3D – Top Medial	3.39 ± 0.11	2.82 ± 0.09	2.40 ± 0.10
	3D – Top Middle	3.33 ± 0.15	2.76 ± 0.18	2.43 ± 0.07
	3D – Top Lateral	3.50 ± 0.12	2.82 ± 0.03	2.51 ± 0.05
	3D – Bot. Medial	3.48 ± 0.02	2.56 ± 0.38	2.39 ± 0.11
	3D – Bot. Middle	3.50 ± 0.03	2.97 ± 0.09	2.47 ± 0.04
	3D – Bot. Lateral	3.55 ± 0.03	2.91 ± 0.09	2.50 ± 0.05*
Positive Duration (ms)				
Facial	3D – Nasal	1.65 ± 0.07	2.07 ± 0.08	1.53 ± 0.39
	3D – Top Medial	1.12 ± 0.46	1.12 ± 0.98	1.54 ± 0.18
	3D – Top Middle	0.77 ± 0.19	0.98 ± 0.57	1.32 ± 0.12
	3D – Top Lateral	0.81 ± 0.19	1.37 ± 0.59	2.18 ± 1.07
	3D – Bot. Medial	1.52 ± 1.59†	1.49 ± 0.12	1.51 ± 0.99
	3D – Bot. Middle	2.43 ± 0.09	1.63 ± 0.58	1.38 ± 0.14
	3D – Bot. Lateral	1.35 ± 0.55	2.43 ± 0.42	2.02 ± 1.32*
Positive Impulse (psi*ms)				
Facial	3D – Nasal	7.99 ± 0.28	14.61 ± 2.00	20.59 ± 2.60
	3D – Top Medial	6.84 ± 1.25	11.19 ± 3.86	22.52 ± 3.83
	3D – Top Middle	4.89 ± 0.63	9.25 ± 4.38	19.34 ± 1.13
	3D – Top Lateral	5.91 ± 1.04	12.54 ± 3.03	52.04 ± 34.65
	3D – Bot. Medial	8.71 ± 8.04†	23.89 ± 2.85	33.65 ± 17.95
	3D – Bot. Middle	12.42 ± 1.77	14.88 ± 3.24	24.18 ± 1.15
	3D – Bot. Lateral	7.28 ± 1.37	17.70 ± 6.18	26.26 ± 13.91*

*Only two tests at this level because one test did not return to zero after initial peak.

Table B15. Average driver rupture pressure.

Pressure	Test Condition	10 psi	20 psi	30 psi
Peak Overpressure (psi)				
Driver	Empty Tube	63.57 ± 10.63	158.51 ± 11.72	262.59 ± 13.34
	Isolated Eye	67.17 ± 1.69	155.28 ± 29.47	243.78 ± 33.40
	Synthetic Orbit	53.18 ± 5.58	191.75 ± 34.51	267.34 ± 18.27
	3D Orbit - Unprotected	54.12 ± 6.26	155.07 ± 14.97	258.83 ± 13.82
	3D Orbit - Spectacles	80.04 ± 9.05	137.70 ± 1.60	247.74 ± 8.38
	3D Orbit - Goggles	63.63 ± 1.72	128.43 ± 15.88	250.94 ± 8.92

Appendix C
Porcine Eye Injury Summary

Table C1. Eye injuries upon dissection - control eyes. 225
Table C2. Eye injuries upon dissection - sham eyes (isolation). 225
Table C3. Eye injuries upon dissection - sham eyes (gelatin). 226
Table C4. Eye injuries upon dissection - unprotected isolated eye tests. 227
Table C5. Eye injuries upon dissection - unprotected synthetic orbit eye tests. 227
Table C6. Eye injuries upon dissection - 3D orbit eye tests (unprotected). 228
Table C7. Eye injuries upon dissection - 3D orbit eye tests (spectacles). 228
Table C8. Eye injuries upon dissection - 3D orbit eye tests (goggles). 229

Note: The following tables include all injuries recorded during eye dissections. Some of these injuries were caused during the dissection and cannot be correlated to primary blast overpressure exposure. The tube used to pressurize the eye sometimes penetrated the posterior half of the lens. This resulted in a characteristic three-pronged star-shaped "poke" in the posterior half the the lens, and resulted in capsule tearing. The pressurization tube penetrated the ciliary body in some extreme cases. This resulted in small holes in the ciliary body and tears in the zonules. Lens capsule tear or rupture is marked with an asterik. Injuries caused by the dissection process are marked with a cross. Injuries that could potentially be caused by primary blast overpressure exposure are marked in bold.

Legend	Comment
---	No injury data available.
*	Lens capsule tear/rupture.
†	Injury likely happened during dissection.
bold	Injuries potentially caused by primary blast overpressure exposure.

Table C1. Eye injuries upon dissection - control eyes.

Control Eyes					
	Corneal Abrasion	**Zonular Damage**	**Lens Damage**	**Ciliary Body Damage**	**Retinal Damage**
Day 1					
PE14	N	---	---	---	---
PE24	N	N	---	---	**Y**
PE40	N	N	N	N	**Y**
PE41	N	N	N	N	**Y**
PE42	N	N	N	Y†	**Y**
PE45	N	N	N	Y†	**Y**
PE60	N	N	N	N	**Y**
PE171	N	N	N	N	**Y**
PE179	N	N	N	N	**Y**
PE192	N	N	N	**Y**	**Y**
Day 2					
PE18	N	N	N	---	**Y**
PE46	N	N	N	N	**Y**
PE47	N	N	N	N	**Y**
PE48	N	N	N	Y†	---
PE168	N	N	N	N	**Y**
PE174	N	N	N	N	**Y**
PE196	N	N	N	N	**Y**
Day 3					
PE07	N	---	---	---	---
PE09	N	---	---	---	---
PE101	N	N	N	N	**Y**
PE158	N	N	N	N	**Y**
PE159	N	N	N	N	**Y**
PE170	N	N	N	N	**Y**
PE189	N	N	N	**Y**	**Y**

Table C2. Eye injuries upon dissection - sham eyes (isolation).

Sham Eyes (Isolated)					
	Corneal Abrasion	**Zonular Damage**	**Lens Damage**	**Ciliary Body Damage**	**Retinal Damage**
Day 1					
PE133	N	---	N	N	**Y**
PE152	N	N	N	N	**Y**
PE153	N	N	N	N	**Y**
Day 3					
PE143	N	N	N	N	**Y**
PE144	N	N	N	N	**Y**
PE156	N	N	N	N	**Y**
PE157	N	N	N	N	**Y**
PE160	N	N	N*	**Y**	**Y**

Table C3. Eye injuries upon dissection - sham eyes (gelatin).

Sham Eyes (Gelatin)					
	Corneal Abrasion	**Zonular Damage**	**Lens Damage**	**Ciliary Body Damage**	**Retinal Damage**
Day 1					
PE92	N	---	N	**Y**	**Y**
PE93	N	---	N	N	**Y**
PE94	N	N	N	**Y**	**Y**
PE104	N	N	N	**Y**	**Y**
PE109	N	N	N	N	**Y**
PE110	N	**Y**	N	**Y**	**Y**
PE163	N	N	N	--	**Y**
Day 2					
PE13	N	N	---	---	**Y**
PE95	N	---	Y*†	**Y**	**Y**
PE96	N	N	N	N	**Y**
PE106	N	N	**Y***	N	**Y**
PE166	N	N	N	N	**Y**
Day 3					
PE88	N	N	N	**Y***	**Y**
PE89	N	N	N	N	**Y**
PE90	N	N	N*	**Y**	**Y**
PE98	N	N	N	**Y**	**Y**
PE99	N	N	N	N	**Y**
PE100	N	N	N	N	**Y**
PE188	N	**Y**	N	**Y**	**Y**

Table C4. Eye injuries upon dissection - unprotected isolated eye tests.

Unprotected Isolated Eye						
		Corneal Abrasion	**Zonular Damage**	**Lens Damage**	**Ciliary Body Damage**	**Retinal Damage**
10 psi						
PE119	Day 2	N	N	---	N	**Y**
PE124	Day 1	N	N	N	N	**Y**
PE120	Day 2	N	N	N*	**Y**	**Y**
PE122	Day 3	N	N	N	N	**Y**
PE123	Day 3	N	N	N	N	**Y**
20 psi						
PE118	Day 1	---	---	---	---	---
PE145	Day 1	N	N	Y†	**Y**	**Y**
PE147	Day 2	N	N	N	N	**Y**
PE154	Day 2	N	N	N	N	**Y**
PE150	Day 3	N	N	**Y*†**	N	**Y**
PE151	Day 3	N	N	Y†	N	**Y**
30 psi						
PE125	Day 2	N	N	Y†	N	**Y**
PE126	Day 2	N	N	Y†	N	**Y**
PE132	Day 3	N	N	N	N	**Y**
PE137	Day 3	N	N	N	N	**Y**

Table C5. Eye injuries upon dissection - unprotected synthetic orbit eye tests.

Synthetic Orbit with Unprotected Eye						
		Corneal Abrasion	**Zonular Damage**	**Lens Damage**	**Ciliary Body Damage**	**Retinal Damage**
10 psi						
PE80	Day 1	N	N	Y†	N	**Y**
PE85	Day 1	N	N	N	**Y**	**Y**
PE82	Day 2	N	N	N	N	**Y**
PE06	Day 3	---	N	N	---	**Y**
PE08	Day 3	---	N	---	---	**Y**
20 psi						
PE21	Day 1	---	N	---	---	**Y**
PE23	Day 1	---	N	Y†	---	**Y**
PE25	Day 2	---	N	N	**Y**	**Y**
PE105	Day 2	N	**Y**	N*	**Y**	**Y**
PE75	Day 3	N	N	N	**Y**	**Y**
PE79	Day 3	N	N	N*	N	**Y**
30 psi						
PE15	Day 2	---	---	Y†	---	**Y**
PE103	Day 2	N	N	Y†	N	**Y**
PE111	Day 2	N	N	N	**Y**	**Y**
PE17	Day 3	---	N	Y†	---	**Y**
PE20	Day 3	---	**Y**	Y†	N	**Y**

Table C6. Eye injuries upon dissection - 3D orbit eye tests (unprotected).

3D Orbit with Unprotected Eye						
		Corneal Abrasion	**Zonular Damage**	**Lens Damage**	**Ciliary Body Damage**	**Retinal Damage**
10 psi						
PE01	Day 1	---	N	N	---	**Y**
PE84	Day 1	N	N	---	**Y**	**Y**
PE03	Day 2	---	N	---	---	**Y**
PE81	Day 2	---	N	N	N	**Y**
PE05	Day 3	---	N	Y†	---	**Y**
PE83	Day 3	N	N	Y†	**Y**	**Y**
20 psi						
PE86	Day 1	N	N	N*	N	**Y**
PE37	Day 2	---	N	Y†	N	**Y**
PE38	Day 3	---	N	Y*†	N	**Y**
PE39	Day 3	---	N	N	N	**Y**
PE148	Day 3	N	N	Y*†	N	**Y**
30 psi						
PE102	Day 1	N	N	N	N	**Y**
PE16	Day 2	---	N	Y†	---	**Y**
PE26	Day 2	---	N	N	N	**Y**
PE97	Day 3	---	**Y**	Y*†	**Y**	**Y**
PE107	Day 3	N	N	N*	**Y**	**Y**
PE112	Day 3	N	**Y**	Y*†	**Y**	**Y**

Table C7. Eye injuries upon dissection - 3D orbit eye tests (spectacles).

3D Orbit with Spectacles						
		Corneal Abrasion	**Zonular Damage**	**Lens Damage**	**Ciliary Body Damage**	**Retinal Damage**
10 psi						
PE172	Day 2	N	N	Y†	N	**Y**
PE173	Day 2	N	N	N	**Y**	**Y**
PE185	Day 2	N	N	Y*†	**Y**	**Y**
20 psi						
PE175	Day 1	N	N	N*	N	**Y**
PE177	Day 1	N	N	N	**Y**	**Y**
PE178	Day 2	N	N	N*	---	**Y**
30 psi						
PE184	Day 1	N	N	N	N	**Y**
PE194	Day 2	N	N	Y*†	---	**Y**
PE195	Day 2	N	**Y**	Y*†	**Y**	**Y**
PE186	Day 3	N	N	**Y***†	**Y**	**Y**
PE187	Day 3	N	**Y**	**Y***†	---	**Y**

Table C8. Eye injuries upon dissection - 3D orbit eye tests (goggles).

3D Orbit with Goggles						
		Corneal Abrasion	**Zonular Damage**	**Lens Damage**	**Ciliary Body Damage**	**Retinal Damage**
10 psi						
PE161	Day 1	N	N	Y*†	N	**Y**
PE162	Day 1	N	**Y**	**Y***	**Y**	**Y**
PE165	Day 2	N	N	Y*†	N	**Y**
20 psi						
PE169	Day 1	N	N	N	N	**Y**
PE190	Day 1	N	**Y**	Y*	N	**Y**
PE167	Day 3	N	---	Y*†	**Y**	**Y**
30 psi						
PE183	Day 1	N	N	N	**Y**	**Y**
PE193	Day 1	N	N	Y*†	**Y**	**Y**
PE191	Day 2	N	N	Y*†	**Y**	**Y**
PE181	Day 3	N	N	N*	**Y**	**Y**
PE182	Day 3	N	N	N	N	**Y**

Appendix D
MATLAB Script

```
% ---------------------------------------------------------------------
%                        Eye Blast Data Processing
%                                vda@vt.edu                Update: 31Aug15
% ---------------------------------------------------------------------
close all; clear all; clc;
%% User Inputs
   cd('J:\Blast Work\01 Final Data\01 Pig Eye Data\0 - Empty Tube');
           file  = 'Spec'; %Test ID
   pressureLevel = '30_5'; %Test Pressure Level
         channel = 5;      %Channel to process
          thresh = 0.5;    %Threshold for slope
      channelStr = num2str(channel);
%% Background
    samplingRate = 301.887; %kHz
           sheet = 'TDAS Ch 1-255';
        fileName = [file,pressureLevel,'.XLS'];
         rawData = xlsread(fileName,sheet,'A23:R45023');
   %Channel Names (based on test type)
       channelNames  = {'Time' 'Driver' ...
                        'Stat01' 'Stat02' 'Stat03' ...
                        'Pencil' 'IOP' ...
                        'OrbBot' 'OrbSide' 'OrbTopAnt' 'OrbTopPost' ...
                        'Reflected' ...
                        'TopMed' 'TopMid' 'TopTemp' ...
                        'BotMed' 'BotMid' 'BotTemp'};
%% Prep Data for Processing
for q = channel
    %Raw Data for Channel to be Analyzed
      channelName = channelNames{1,q};
      str = sprintf([file,' ',pressureLevel,'psi',' ','\n',channelName]);
    %Start Time at t=0ms
      for n = 2:length(rawData)
              channelData(1,1) = 0;
              channelData(n,1) = channelData(n-1,1) + 1/samplingRate;
      end
     %Zero Channel (based on avg of first 10k pts)
        n = 10000;
        channelData(:,2) = rawData(:,q) - mean(rawData(1:n,q));
end
%% Quantify Shock Wave Paramenters (using max slope)
   slope(1,1) = 0;
   slope(length(channelData),1) = 0;
        %Find slope of all points
        for j = 2:length(channelData)-1
            slope(j,1) = (channelData(j+1,2)-channelData(j-1,2))/...
                         (2*(1/samplingRate));
        end
        slopeThreshold = thresh*max(slope(:,1));

        for l = 1:length(channelData)
            if (slope(l,1) > slopeThreshold)
                slope(l,2) = slope(l,1);
```

```
            else
                slope(l,2) = 0;
            end
        end

    %ToA = Beg (+) Duration
     maxSlope(1) = find(slope(:,2),1,'first');
     maxSlope(2) = maxSlope(1)/samplingRate;

     for h = 1:maxSlope(1)
         if channelData(h,2) < channelData(h+1,2)
             ToAcheck(h,1) = 0;
         else
             ToAcheck(h,1) = 1;
         end
     end

     begPosDur(1) = find(ToAcheck(1:maxSlope(1),1) > 0,1,'last')+1;
     begPosDur(2) = maxSlope(2);
     begPosDur(3) = channelData(begPosDur(1),2);

     %Ensure begPosDur is a (+) value
     while channelData(begPosDur(1),2) < 0
             begPosDur(1) = begPosDur(1) + 1;
     end

     %Temporally Zero (for corridor plots)
     for n = 1:length(channelData)
         channelData(n,3) = channelData(n,1) - begPosDur(2);
     end

    %Peak Overpressure
     [pkPsiY,pkPsiX] = max(channelData(:,2));
     peakOverpressure(1) = pkPsiX;
     peakOverpressure(2) = pkPsiX/samplingRate;
     peakOverpressure(3) = pkPsiY;

     %(+) Duration
     endPosDur(1,1) = find(channelData(begPosDur(1):length(channelData),2) <
0,1,'first')-2;
     endPosDur(1,2) = endPosDur(1)/samplingRate;
      endPosDur(2,1) = begPosDur(1)+endPosDur(1);
      endPosDur(2,2) = endPosDur(2,1)/samplingRate;
      endPosDur(2,3) = channelData(endPosDur(2,1),2);
       posDuration(1) = endPosDur(1,2);

     %(+) Impulse
     posImpulse(1) =
(1/samplingRate)*trapz(channelData(begPosDur(1):endPosDur(2,1),2));
%% Plot
     %Impulse Patch
      impulsePatch(1:endPosDur(1)+1,1) =
channelData(begPosDur(1):endPosDur(2,1),1);
       impulsePatch(endPosDur(1)+2:2*length(1:endPosDur(1))+2,1) =
flipud(channelData(begPosDur(1):endPosDur(2,1),1));
```

```
     impulsePatch(1:endPosDur(1)+1,2) =
channelData(begPosDur(1):endPosDur(2,1),2);
      impulsePatch(endPosDur(1)+2:2*length(1:endPosDur(1))+2,2) = 0;
       impulseX = impulsePatch(:,1);
       impulseY = impulsePatch(:,2);
       impulseZ = ones(length(impulseX),1);
    %Plot Impulse
     figure(1)
      %Raw Data
       plot(channelData(:,1),channelData(:,2),'k','LineWidth',1) %RawData
       hold on

plot(channelData(begPosDur(1):begPosDur(1)+endPosDur(1),1),channelData(begPos
Dur(1):begPosDur(1)+endPosDur(1),2),'ko','LineWidth',0.5,'MarkerSize',2)

plot(channelData(pkPsiX(1),1),channelData(pkPsiX(1),2),'ro','LineWidth',0.5,'
MarkerSize',2)

plot(channelData(begPosDur(1),1),channelData(begPosDur(1),2),'go','LineWidth'
,0.5,'MarkerSize',2)

plot(channelData(begPosDur(1)+endPosDur(1),1),channelData(begPosDur(1)+endPos
Dur(1),2),'go','LineWidth',0.5,'MarkerSize',2)
      %Impulse Patch (Raw)
       p3 =
patch(impulseX,impulseY,impulseZ,'k','EdgeColor','none','facealpha',0.2);
       zeroLine = refline(0,0); %Zero
        set(zeroLine,'Color','k');
      %Figure Details
       axis([peakOverpressure(2)-5 peakOverpressure(2)+10 -10 130])
       xlabel('Time (ms)')
       ylabel('Overpressure (psi)')
       title(str)
      %Legend
       legend('Raw Data')
       str2 =
sprintf(['Ch',channelStr,'_',channelName,'_',file,pressureLevel]);
       saveas(figure(1),str2,'fig')
%% Structure of Summary Results
    AllResults{1,1}      = 'Pk Pressure (psi)';
    AllResults{1,2}      = 'ToA (ms)';
    AllResults{1,4}      = '(+) Dur (ms)';
    AllResults{1,5}      = '(+) Imp (psi*ms)';
        AllResults{2,1}  = peakOverpressure(3);
        AllResults{2,2}  = begPosDur(2);
        AllResults{2,4}  = posDuration(1);
        AllResults{2,5}  = posImpulse(1);
    AllResults{4,1}      = 'Time';
    AllResults{4,2}      = 'Data';
        AllResults{5,1}  = channelData(:,3);
        AllResults{5,2}  = channelData(:,2);
%% Save .mat file and Play Sound to Indicate Complete Run
   clearvars -except AllResults channelData thresh rawData begPosDur ...
                     endPosDur maxSlope peakOverpressure samplingRate str2
   save(str2);
```